

Targeting Mitochondria in Cancer Cells Using Nano Platforms

**A Thesis submitted to partial fulfilment of the degree of
Doctor of Philosophy**

By

**Abhik Mallick
ID: 20123200**

Research Supervisor

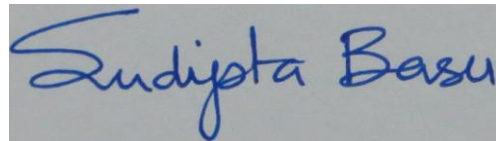
**Dr. Sudipta Basu
Ramalingaswami Fellow
Indian Institute of Science Education and Research, Pune**



Certificate

This is to certify that the work incorporated in this entitled "**Targeting Mitochondria in Cancer Cells Using Nano Platforms**" submitted by **Abhik Mallick** carried out by candidate at Indian Institute of Science Education and Research (IISER), Pune, under my supervision. The work presented here or any part of it has not been included in any other thesis submitted previously for the award of any degree or diploma from any other university or institution.

Date: 09/02/2018



Dr. Sudipta Basu
(Research Supervisor)
Ramalingaswami Fellow
IISER, Pune - 411008
India.

Declaration

I hereby declare that the thesis entitled "**Targeting Mitochondria in Cancer Cells Using Nano Platforms**" submitted for Doctor of Philosophy in chemistry at Indian Institute of Science Education and Research (IISER), Pune, has not been submitted by me to any other university or institution. This work presented here was carried out at the Indian Institute of Science Education and Research, Pune, India under the supervision of Dr. Sudipta Basu.

Date: 09.02.2018



Abhik Mallick
ID-20123200
(Senior Research Fellow)
Department of Chemistry
IISER, Pune- 411008
India.

Dedicated to
Ma and Baba

ACKNOWLEDGEMENT

I would like to take the opportunity to express my deep sense of gratitude to my respected faculty advisor Dr. Sudipta Basu for his careful guidance, support and encouragement throughout my research career. Starting from an order to training juniors, I have learnt everything from him.

I would like to thank Dr. S Britto and Dr. BLV Prasad for being my research advisory committee (RAC) members and providing me valuable comments during RAC meetings, which enabled me to notice the shortcomings of work and make necessary improvements.

A special mention of Dr. K.N.Ganesh (our former director), Dr. M. Jayakanan and Dr. H. Chakrapani who had given us the privilege to work in the biology laboratory. I would also like to mention about Dr. Srinivas Hotha. Without his encouragement, I wouldn't have entered into research field.

I express my sincere thanks to all lab-mates(Aditi, Chandra, Aman, Sandeep, Sohan ,Shalini, Ankur, Deepali, Nikunj, Kamil, Jyoti, Sumer, Suhas and Naresh) for their suggestion for betterment of my performance in every aspect. A special thanks to Piyush More and Meenu Kuman for teaching me the biological tools, which helped me a lot . I also want to thank Dhrubojyoti Dutta for his valuable suggestions for my research work A special mention of Aditi, Aman, Chandra and Meenu for the good times we had outside the lab. I also want to thank Poulomi Sengupta (NCL Pune) and Ayantika Sengupta (IISER Pune) for the help in emergency when we performed the biological experiments.

I am also thankful to all my collaborators (Dr. Balu Chopade, Dr. Pramod Pillai,, Dr. Mayurika Lahiri, Dr. Sujit Ghosh, Dr. Soumyo Sinha Roy, Dr. K.N.Ganesh, Dr.B.Das) for the immense trust they have shown on me. and faculties (both from Chemistry and Biology department) and lab-technicians for helping me throughout in their own special ways. I would like to thank CSIR-UGC and IISER PUNE for funding and providing a high quality research atmosphere.

I also want to thank Tushar sir and all other people from the administrative department, IISER Pune for enormous help they do day after day after without any expectations.

I also want to thank my friends (Arindamda, Supratik. Sudebda, Parthada, Rejaul, Avishek, Susnata, Saptaswa, Arunava, Koushik, Soumya, Tanmoy, Unmesh, Hasanda, Maidul, Barun and Biplab) for the wonderful time I have spent in IISER Pune and back in home.

Finally I would like to thank my Ma and Baba because they are my life.

Abhik Malllick

Abstract

Cancer is one of the leading causes of morbidity and mortality worldwide. To understand the characteristics of cancer cells, the hallmarks of cancer are outlined by Hanahan and Weinberg. Resisting cell death and deregulation of cellular energetics are the two imperative hallmarks of cancer which are tightly governed by an important sub-cellular organelle, mitochondrion. The mitochondrion is known to be "the power house of the cell" since it produces energy in the form of ATP. Although, mitochondria is called "the power house of the cell", its roles in cancer progression are very well highlighted in recent studies and made it an alternative and interesting target for cancer therapy. However, there are three major challenges in targeting mitochondria in next generation cancer therapy: (a) selective targeting of mitochondria in cellular milieu, (b) specific targeting of mitochondria in cancer tissues and (c) overcome drug resistance. To address these, we have developed lipidic nanoparticle for specific targeting of Bcl-2 protein on mitochondria in cancer cells to overcome drug resistance. Moreover, we also developed Cerberus and graphene oxide based nanoplatfoms to target the mitochondrial DNA and associated proteins in cancer cells. Furthermore, mitochondria show complex cross-talk with the nucleus and endoplasmic reticulum(ER) for protein and lipid supply. Hence, simultaneous targeting of nucleus and mitochondria would lead to the augmented therapeutic outcome. To address this, we have developed dual-drug conjugated nanoparticles to target nucleus and mitochondria in cancer cells. We envision that the here presented unique approaches can be easily translated into clinics as platform technologies to inhibit multiple diverse targets concurrently into mitochondria, improve the therapeutic efficacy, reduce the off-target toxicity, overcome drug resistance and finally, offer a better quality of life to the cancer patients.

TABLE OF CONTENT

<i>Chapter 1: Introduction</i>	<i>1-19</i>
1.1 Cancer	2
1.2 Hallmarks of Cancer	2-3
1.3 Mitochondria and cancer	3-8
1.3.1 Mitochondrial biogenesis and turnover	
1.3.2 Mitochondrial fission and fusion dynamics	
1.3.3 Evading cell death	
1.3.4 Metabolism and bioenergetics	
1.3.5 Signalling pathway	
1.3.6 Mitochondrial DNA	
1.4 Specific targeting of mitochondria in the sub-cellular milieu	8-12
1.4.1 Delocalised lipophilic cation	
1.4.2 Heterocyclic aromatic cations	
1.4.3 Mitochondria targeting peptides	
1.5 Selective targeting of mitochondria in cancer cells	12-15
1.5.1 Passive targeting	
1.5.2 Active targeting	
1.5.3 Targeting subcellular organelles with nanoparticles	
1.6 Aim of thesis	15-16
1.7 References	16-19
<i>Chapter 2: Nanoparticle mediated targeting of mitochondria induces apoptosis in cancer cells</i>	
<i>20-67</i>	
2.1 Introduction	21-22
2.2 Results and Discussion	22-48
2.2.1 Engineering of TOS-TPP-Obt NPs.	

2.2.2 Cellular internalization.	
2.2.3 Mechanism of endocytosis.	
2.2.4 Mitochondria localization.	
2.2.5 Mitochondrial outer membrane permeabilization.	
2.2.6 Cytotoxicity, apoptosis and mechanism.	
2.2.7 Mitochondria targeting and cytotoxicity in drug resistant cancer cell.	
2.3 Conclusions	48
2.4 Materials and methods	48-57
2.4.1 Materials	
2.4.2 Synthesis of conjugate (2)	
2.4.3 Characterization of conjugate 2	
2.4.5 Characterization of α -tocopheryl succinate-TPP conjugate (3)	
2.4.6 Engineering of TOS-TPP-Obt-NPs	
2.4.7 Determination of size, surface charge and shape of α -TOS-TPP-Obt nanoparticle	
a. Dynamic light scattering (DLS)	
b. Field-Emission Scanning Electron Microscopy (FESEM) of α -TOS-TPP-Obt nanoparticles	
c. Atomic Force Microscopy (AFM) of α -TOS-TPP-Obt nanoparticles	
d. Transmission Electron Microscopy (TEM) of α -TOS-TPP-Obt nanoparticles	
2.4.8 Determination of drug loading	
2.4.9 Stability of the α -TOS-TPP-Obt nanoparticles at 4 ⁰ C and 37 ⁰ C by DLS.	
2.4.10 Release kinetics	
2.4.11 Cellular internalization by CLSM.	
2.4.12 Endocytosis mechanism by CLSM	
2.4.13 Endocytosis mechanism by fluorescence activated cell sorting (FACS)	
2.4.14 Lysosome permeabilization by acridine orange assay	

2.4.15 Mitochondria localization	
2.4.16 Drug content in mitochondria fraction by FACS	
2.4.17 JC1 assay	
2.4.18 Calcein AM assay	
2.4.19 Apoptosis detection by FACS	
2.4.20 General procedure for Immunostaining assay	
2.4.21 General procedure for Western blot analysis	
2.4.22 Cell viability assay	
2.5 Appendices	58-62
2.6 References	63-67

***Chapter 3 a : Targeting mitochondrial DNA and associated proteins by Cerberus nanoparticle
67-98***

3 a.1 Introduction	69-70
3.a.2 Results and Discussion	70-86
3a.2.1 Engineering mitochondria targeting Cerberus nanoparticle (mt-CN).	
3a.2.2. Mitochondrial homing of Cerberus nanoparticle	
3a.2.3. Mitochondrial DNA damage and inhibition of mitochondrial Topoisomerase I	
3a.2.4. Impairing mitochondria by mt-CN	
3a.2.4.1 Mitochondrial outer membrane permeabilization (MOMP)	
3a.2.4.2 Mitochondrial transition pore (MTP) Formation by mt-CN	
3a.2.4.3 Mitochondrial damage by mt-CN	
3a.2.5. Cytochrome c release and ROS generation	
3a.2.6. Induction of apoptosis and Cell death	
3a.3 Conclusions	86
3a.4 Experimental methods	86-92

3a.4.1 Materials	
3a.4.2. Synthesis of α -TOS-TPP conjugate (1)	
3a.4.3. Synthesis of α -TOS-CDDP conjugate (2)	
3a.4.4 Engineering of Cerberus Nanoparticle (mt-CN)	
3a.4.5 Dynamic light scattering and FESEM	
3a.4.6 Determination of drug loading in mt-CN	
3a.4.7 Stability of mt-CN	
3a.4.8 Mitochondria localization	
3a.4.9 Quantification of mt-DNA by polymerase chain reaction (PCR)	
3.a.4.10 Analysis of electron transport chain proteins	
3a.4.11 Detection of Mitochondrial Topoisomerase 1 (Top1mt) by immunostaining	
3a.4.12 Determination of mitochondrial outer membrane permeabilisation (MOMP):	
3a.4.12.1 JC 1 assay	
3a.4.12.2 TMRM assay	
3a.4.12.3 Calcein AM assay	
3a.4.13 Generation of Reactive oxygen species (ROS)	
3a.4.14 Release of Cytochrome C	
3a.4.15 Apoptosis detection by flow cytometry	
3a.4.16 Caspase 9 activity	
3a.4.17 Cell viability assay	
3a.5 References	97

Chapter 3 b : Targeting Mitochondrial DNA and associated proteins by Graphene oxide nanomaterials **98-110**

3b.1 Introduction	99-100
3b.2 Results and Discussion	100-106
3b.2.1 Synthesis of mitochondria targeting graphene oxide conjugate	
3b.2.2 Characterisation of mitochondria targeting graphene oxide	

nanoparticle	
3b.2.3 Mitochondrial outer membrane permeabilisation (MOMP)	
3b.2.3.1 JC1 and TMRM assay	
3b.2.3.2 Calcein AM assay	
3b.2.4. Generation of Reactive Oxygen Species (ROS)	
3b.2.5 Cell viability assay	
3b.3 Conclusions	106-107
3b.4 Experimental methods	107-109
3b.4.1 Materials	
3b.4.2 Synthesis of mitochondria targeting graphene oxide nanomaterial	
3b.4.3 Determination of surface charge and shape of mitochondria targeting graphene oxide nanomaterial	
3b.4.3.1 Dynamic light scattering (DLS)	
3b.4.3.2 Field-Emission Scanning Electron Microscopy (FESEM) of mitochondria targeting graphene oxide nanomaterial	
3b.4.4 Raman Spectroscopy.	
3b.4.5 Fluorescence Spectroscopy	
3b.4.6 Determination of drug loading	
3b.4.7 Determination of mitochondrial outer membrane permeabilisation (MOMP):	
3b.4.7.1 JC 1 assay	
3b.4.7.2 TMRM assay	
3b.4.7.3 Calcein AM assay	
3b.4.8 Generation of Reactive Oxygen Species (ROS)	
3b.4.9 Cell Viability assay	
3b.5 References	109-110

Chapter 4: Dual Drug Conjugated Nanoparticle for Simultaneous Targeting of Mitochondria and Nucleus in Cancer Cells ***111-164***

4..1 Introduction	112-114
-------------------	---------

4.2 Results and Discussion	114-143
4.2.1 Synthesis and characterization of dual-drug conjugated nanoparticles	
4.2.1.1 Synthesis of dual-drug conjugates	
4.2.1.2 Engineering of dual drug conjugated nanoparticles	
4.2.1.3 Stability of dual drug conjugated nanoparticles	
4.2.1.4 Release of dual drugs from nanoparticles	
4.2.2 <i>In vitro</i> cytotoxicity assay of dual-drug conjugated nanoparticles	
4.2.2.1 Cell viability assay	
4.2.2.2 Apoptosis assay by FACS	
4.2.2.3 Caspase assay	
4.2.2.4 Cell cycle analysis	
4.2.3 Cellular internalization of dual drug conjugated nanoparticles	
4.2.4 Targeting mitochondria by dual drug conjugated nanoparticles	
4.2.5 Targeting nucleus and microtubule by dual drug conjugated nanoparticle	
4.3 Conclusions	143
4.4 Experimental methods	143-153
4.4.1 Materials	
4.4.2 Synthesis of α -tocopherol succinate-doxorubicin conjugate (2)	
4.4.3 Synthesis of α -tocopherol succinate-paclitaxel conjugate (3)	
4.4.4 Synthesis of aquated cisplatin (4)	
4.4.5 Synthesis of α -tocopherol succinate-cisplatin conjugate (5)	
4.4.6 General procedure of synthesizing dual drug conjugated nanoparticles and rhodamine loaded nanoparticles	
4.4.7 General procedure for quantification of drug loading	
4.4.8 Determination of size distribution of nanoparticles by dynamic light scattering (DLS)	
4.4.9 Field-Emission Scanning Electron Microscopy (FESEM) of dual-drug conjugated nanoparticles	
4.4.10 Atomic Force Microscopy (AFM) of dual-drug conjugated	

nanoparticles

4.4.11 Transmission Electron Microscopy (TEM) of dual-drug conjugated nanoparticles

4.4.12 Stability of the nanoparticles at 4°C and 37°C by dynamic light scattering (DLS)

4.4.13 General procedure for determining the drug release profile.

4.4.14 Cell viability assay.

4.4.15 FACS analysis for apoptosis detection.

4.4.16 Caspase activity assay

4.4.17 Cell cycle analysis

4.4.18 Confocal laser scanning microscopy (CLSM) studies.

4.4.18.1 Cellular internalization

4.4.18.2 Mitochondrial imaging

4.4.18.3 General procedure for immunostaining to visualize cytochrome c, γ H2AX, PARP and tubulin.

4.4.19 General procedure for Western blot analysis.

4.2.5 Appendices

153-158

4.2.6 References

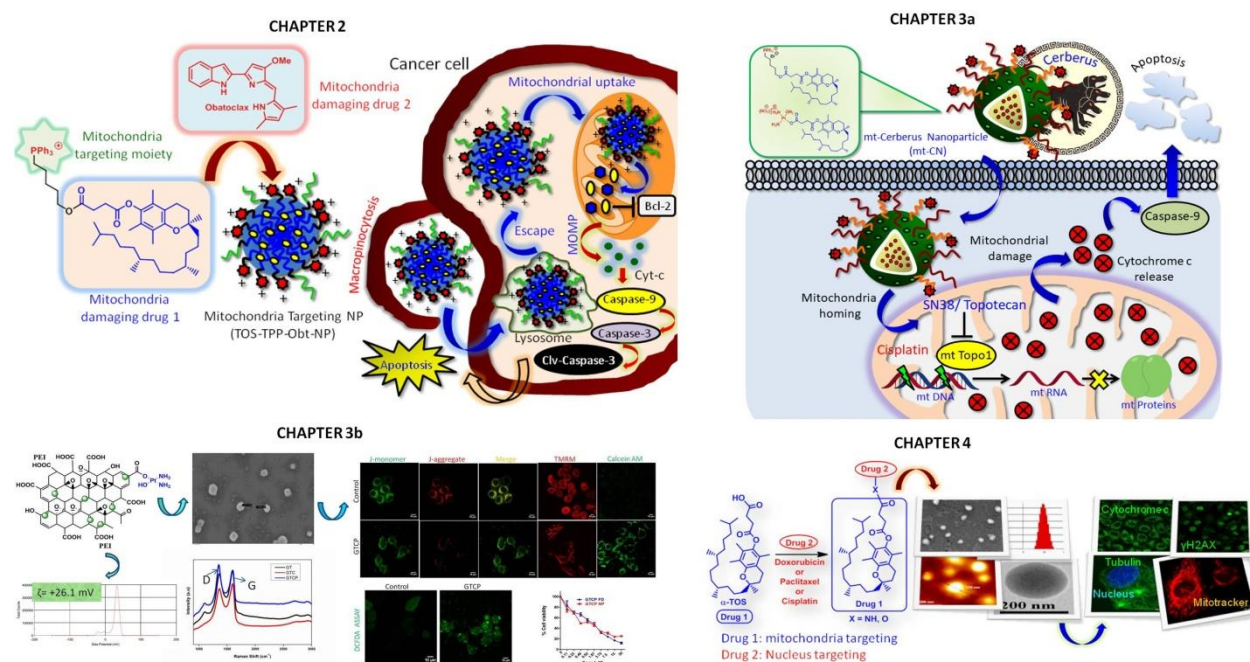
158-164

List of Publications

- (1) **Abhik Mallick**, Piyush More, Sougata Ghosh, Rohan Chipalkatti, Balu A. Chopade, Mayurika Lahiri, and Sudipta Basu. Dual drug conjugated nanoparticle for simultaneous targeting of mitochondria and nucleus in cancer cells. *ACS Appl. Mater. Interface*, **2015**, *7*, 7584-7598. **[Impact Factor: 7.504]**
- (2) **Abhik Mallick**, Piyush More, Muhammed Muazzam Kamil Syed, and Sudipta Basu. Nanoparticle Mediated Mitochondrial Damage Induces Apoptosis in Cancer. *ACS Appl. Mater. Interface*, **2016**, *8*, 13218-13231. **[Impact Factor: 7.504]**
- (3) **Abhik Mallick**, Meenu Kuman, Arijit Ghosh, Benubrata Das and Sudipta Basu. Targeting mitochondrial DNA and associated proteins by Cerberus nanoparticles. (Manuscript under review)
- (4) **Abhik Mallick**, Aditi Nandi and Sudipta Basu. Simultaneous Targeting of Mitochondrial DNA and Mitochondrial Topoisomerase I by Graphene Oxide Nanomaterials. (Manuscript under preparation)
- (5) Aditi Nandi, **Abhik Mallick**, Piyush More, Poulomi Sengupta, Nirmalya Ballav and Sudipta Basu. Cisplatin-induced self-assembly of graphene oxide sheets into spherical nanoparticles for damaging sub-cellular DNA. *Chem. Commun.* **2017**, *53*, 1409-1412. **[Impact Factor: 6.567]**
- (6) Avishek Karmakar, Biplab Joarder, **Abhik Mallick (second author)**, Partha Samanta, Aamod V. Desai, Sudipta Basu and Sujit K. Ghosh Aqueous phase sensing of cyanide ions using a hydrolytically stable metal–organic framework. *Chem. Commun.* **2017**, *53*, 1253-1256. **[Impact Factor: 6.567]**
- (7) Chandramouli Ghosh, Neha Gupta, Piyush More, Poulomi Sengupta, **Abhik Mallick**, Manas Kumar Santra and Sudipta Basu. Engineering and In Vitro Evaluation of Acid Labile Cholesterol Tethered MG132 Nanoparticle for Targeting Ubiquitin-Proteasome System in Cancer. *Chemistry Select*, **2016**, *1*, 5099-5106.
- (8) Gayathri Devatha, Soumendu Roy, Anish Rao, **Abhik Mallick**, Sudipta Basu and Pramod P Pillai. Electrostatically Driven Resonance Energy Transfer in “Cationic” Biocompatible Indium Phosphide Quantum Dots. *Chem. Sci.* **2017**, *8*, 3879-3884. **[Impact Factor: 9.144].**

Synopsis

Cancer is one of the leading causes of morbidity and mortality worldwide. To understand the characteristics of cancer cells, the hallmarks of cancer are outlined by Hanahan and Weinberg. Resisting cell death and deregulation of cellular energetics are the two imperative hallmarks of cancer which are tightly governed by an important sub-cellular organelle, mitochondrion. The mitochondrion is known to be "the power house of the cell" since it produces energy in the form of ATP. Although, mitochondrion is called "the power house of the cell", its roles in cancer progression are very well highlighted in recent studies and made it an alternative and interesting target for cancer therapy. However, there are three major challenges in targeting mitochondria for next generation cancer therapy: (a) selective targeting of mitochondria in sub-cellular milieu, (b) specific targeting of mitochondria in cancer cells keeping them intact in healthy and (c) overcome drug resistance (**Chapter 1**). We have addressed these challenges by merging organic synthesis, chemical biology and nanotechnology based platforms in this thesis (Scheme 1).



Scheme 1: Targeting mitochondria in cancer cells using chemical biology and nanotechnology platforms.

In **Chapter 2**, we have developed lipidic nanoparticle for specific targeting of Bcl-2 protein on mitochondria in cancer cells to overcome drug resistance. Detouring of conventional DNA damaging anti-cancer drugs into mitochondria to damage mitochondrial DNA is evolving as a

promising strategy in chemotherapy. Inhibiting single target in mitochondria would eventually lead to emergence of drug resistance. Herein, triphenylphosphine (TPP) coated positively charged 131.6 nm spherical nanoparticles (NPs) comprised of-tocopheryl succinate (TOS, inhibitor of complex II in electron transport chain) and obatoclax (Obt, inhibitor of Bcl-2) were engineered. The TOS-TPP-Obt-NPs entered into acidic lysosomes via macropinocytosis followed by lysosomal escape and finally homed into mitochondria over a period of 24 h. Subsequently, these TOS-TPP-Obt-NPs triggered mitochondrial outer membrane permeabilization (MOMP) by inhibiting anti-apoptotic Bcl-2, leading to cytochrome c release. These TOS-TPP-Obt-NPs mediated mitochondrial damage induced cellular apoptosis through caspase-9 and caspase-3 cleavage to show improved efficacy in HeLa cells. Moreover, TOS-TPP-Obt-NPs induced MOMP in drug resistant triple negative breast cancer cells (MDA-MB-231) leading to remarkable efficacy compared to the combination of free drugs in higher drug concentrations.

In **Chapter 3**, we have developed lipidic and graphene oxide based nanoplatfroms to target the mitochondrial DNA and associated proteins in cancer cells. Chapter 3 was subdivided in to two chapters:

Chapter 3a discusses targeting mitochondrial DNA and associated proteins by Cerberus nanoparticle. Mitochondrion contains circular DNA responsible for the protein synthesis required in oxidative phosphorylation. However, spatial targeting of mitochondrial DNA keeping nuclear DNA intact in cancer cells is highly challenging task. In this chapter, we have engineered triphenylphosphine (TPP) coated mitochondrial targeting positively charged sub 200 nm Cerberus Nanoparticle (mt-CN). These nanoparticles can contain cisplatin (DNA damaging drug) and SN38 or Topotecan (Topoisomerase I inhibitor) simultaneously in a single nanoparticle. Confocal laser scanning microscopy confirmed that mt-CN can home into mitochondria in MCF7 breast cancer cells within 12 h. A combination of polymerase-chain reaction (PCR) and gel electrophoresis on isolated mitochondria from MCF7 cells exhibited that mt-CN damaged mitochondrial DNA leading to reduction in synthesis of mitochondria-encoded cytochrome c oxidase subunit 1 (MTCO1), while keeping nuclear DNA unperturbed. This mt-CN-mediated co-targeting of mt-DNA and mitochondrial Topoisomerase I (Top1mt) impaired mitochondria through outer membrane permeabilization (MOMP) followed by sequestration of cytochrome c and reactive oxygen species (ROS). Finally, mt-CN induced early and late apoptosis in MCF7 cells by cleavage of caspase-9 to trigger improved cell death compared to free drug combination.

Chapter 3b demonstrates the simultaneous targeting of mitochondrial DNA and mitochondrial Topoisomerase I by graphene oxide nanomaterials. Inspired by the biomedical applications of graphene oxide and the targeting ability of polyethyleneimine directing nanomaterials to mitochondria, we have successfully developed mitochondria targeting graphene oxide nanoparticle of size $< 200\text{nm}$ which was characterized by electron microscopy and Raman spectroscopic methods. These mitochondria targeting graphene oxide nanoparticles (mt-GO-NPs) damaged the mitochondrial DNA (mt-DNA) and mitochondrial Topoisomerase I (Top1mt) leading to mitochondrial outer membrane permeabilization (MOMP) and ROS generation. These mitochondria targeting graphene oxide nanoparticles (mt-GO-NPs) induced enhanced cell death compared to the free drug combination.

Finally in **Chapter 4**, we synthesized dual drug conjugated nanoparticles for simultaneous targeting of mitochondria and nucleus in cancer cells. Although, specific targeting of mitochondria emerged as an interesting strategy to alter the bioenergetics of cancer cells, mitochondria depend on the nucleus and other cellular organelles for most of their proteins and lipids as well as their cellular functions. Therefore, simultaneous targeting of mitochondria and nucleus is very important to achieve better therapeutic efficacy against cancer. To achieve this goal, we have developed sub 200 nm particles from dual-drug conjugates derived from direct tethering of mitochondria damaging drug (α -tocopheryl succinate) and nucleus damaging drugs (cisplatin, doxorubicin and paclitaxel). These dual drug conjugated nanoparticles internalized into the acidic lysosomal compartments of the HeLa cervical cancer cells through endocytosis and induced apoptosis through cell cycle arrest. These nanoparticles damaged mitochondrial morphology and triggered the release of cytochrome c. Moreover, these nanoparticles targeted nucleus to induce DNA damage, fragment the nuclear morphology and damage the cytoskeletal protein tubulin. Therefore, these dual-drug conjugated nanoparticles can be successfully used as platform technology to simultaneously target multiple subcellular organelles in cancer cells to improve the therapeutic efficacy of the free drugs.

We envision that the here presented unique approaches can be used as tools to understand mitochondrial biology in more details with the promise of unravelling new functions. Moreover, these platforms also have potential to be translated into clinics to inhibit multiple diverse targets concurrently into mitochondria, improve the therapeutic efficacy, reduce the off-target toxicity, overcome drug resistance and finally, offer a better quality of life to the cancer patients.

Chapter 1: Introduction

1.1 Cancer

Cancer is the generic term for a large group of diseases that can affect any part of the body. Rapid formation of abnormal cells that grow beyond their usual boundaries is called cancer.¹

According to International Union Against Cancer (UICC) 2017 report, over 7 million people die from cancer and more than 11 million cases are diagnosed worldwide per year. Tobacco kills more than 5 million people, of whom 1.5 million die of lung cancer. Also, more than 160,000 cases of childhood cancer are diagnosed and at least 90,000 children die of cancer. In 2020, if current trends continue, new cases of cancer will increase to 16 million per year and more than 10 million people will die annually. According to World Health Organization (WHO), globally, nearly 1 in 6 deaths is caused by cancer.²

Cancer arises from the transformation of normal cells into tumor cells in a multistage process. It is as a result of persons' genetic factors or 3 categories of external factors namely physical carcinogens, chemical carcinogens, biological carcinogens. Also, the incidence of cancer rises dramatically with age with the tendency of less effective cellular repair mechanisms.¹

An accurate cancer diagnosis is important for effective treatment. Every cancer type requires a specific treatment regimen that constitutes surgery, radiotherapy, and chemotherapy.¹

Palliative care improves the quality of life of patients and their families.³

1.2 Hallmarks of Cancer

To understand the complexities in the characteristics of cancer cell, in the year 2000, Hanahan and Weinberg outlined the hallmarks of cancer, namely, sustaining proliferative signaling, evading growth suppressors, resisting cell death, enabling replicative immortality, induction of angiogenesis and activating invasion and metastasis.⁴ Later, after a decade, they added another two enabling characteristics, i.e., genome instability/mutation and tumor-promoting inflammation and two other emerging hallmarks, namely, deregulating cellular energetics and avoiding immune destruction (**Figure 1**).⁵ Out of these ten hallmarks, resisting cell death and deregulation of cellular energetics are the two imperative hallmarks of cancer which are tightly governed by an important sub-cellular organelle, mitochondrion.

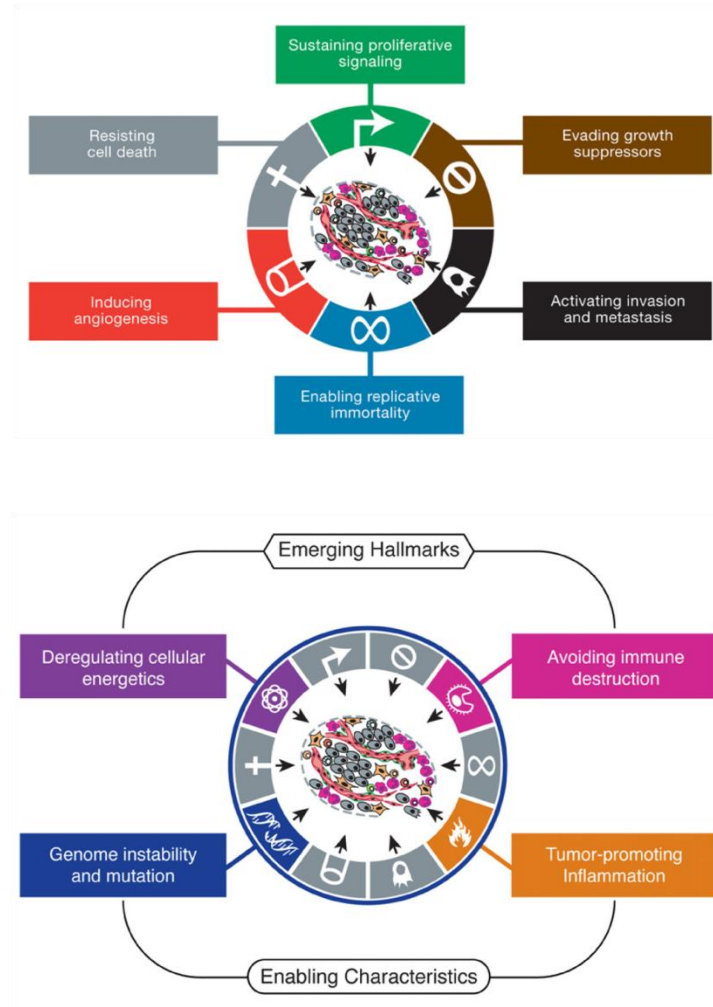


Figure 1: Hallmarks of cancer (adapted from Hanahan et al. *Cell*, **2011**, *144*, 646-674)

1.3 Mitochondria and Cancer

Mitochondrion is known to be the "power house" of the cell. Mitochondrion controls the bioenergetics and biosynthesis inside the cells to regulate stress sensing for allowing the cells to adapt to the environment.⁶

Mitochondria are endosymbiotic in origin. The endosymbiotic hypothesis suggested that mitochondria descended from specialized bacteria (cyanobacterium) that was endocytosed by another species of prokaryote, and became incorporated into the cytoplasm for survival.⁷

The major function of mitochondria is the production of energy in the form of ATP. However the role of mitochondria extends beyond energy production. Mitochondria are the modulators of

oxidation–reduction (redox) status, generators of reactive oxygen species (ROS), controls cytosolic calcium (Ca^{2+}) levels, contribute to the cytosolic biosynthetic precursors such as acetyl-CoA and pyrimidines, and initiator of programmed cell death through intrinsic pathway of apoptosis. Any change in these functions can intervene the biosynthetic pathways, cellular signal transduction pathways, transcription factors and chromatin structure to shift the cell from a quiescent, differentiated state to an actively proliferating one leading to neoplasm.⁸⁻⁹ Moreover, mitochondrial biogenesis and turnover, fission and fusion dynamics, cell death, oxidative stress, metabolism and bioenergetics, signaling and mitochondrial DNA can contribute immensely in each steps of tumorigenesis (**Figure 2**).^{8,10} As a result, mitochondrion has emerged as one of the unconventional, alternative targets for next-generation cancer therapy.

Mitochondrial biogenesis and turnover: Mitochondrial biogenesis and turnover are the two pathways which are responsible for dictating the mitochondrial mass emerging as a positive and negative regulator of tumorigenesis. Mitochondrial biogenesis is defined as the growth and division of pre-existing mitochondria. Thus the role of mitochondrial biogenesis is regulated by many factors such as metabolic state, tumor heterogeneity, tissue type, microenvironment, and tumor stage.¹¹ Mitophagy is the selective autophagy pathway for mitochondrial turnover, which maintains healthy mitochondrial populations.¹² Thus these two pathways are the key players of oncogenic signaling pathways.

Mitochondrial fission and fusion dynamics: Mitochondrial fission and fusion dynamics are of great importance since their balance dictates the morphology of the mitochondria.¹³ The recruitment of dynamin-related protein-1(Drp1) to mitochondria is an important step in mitochondrial membrane fission. The receptors causing membrane constriction on interaction with its outer mitochondria membrane (OMM) are catalyzed by GTPase activity. This process is regulated by phosphorylation mediated by multiple kinases as response of the cell-cycle arrest and stress conditions.¹⁴ The mitochondrial fusion is mediated by mitofusins (Mfn1 and Mfn2) along with optic atrophy-1 (Opa1).¹⁵ Mitochondria exist as either fused, tubular networks or as fragmented granules depending on cellular state. The imbalance of fission and fusion activities in cancer, with increased fission activity and/or decreased fusion activity results in the production of fragmented mitochondrial network.¹⁶

Evading cell death: Evading cell death is an imperative hallmark of cancer which is tightly governed by mitochondria.⁵ Apoptosis is the programmed cell death and mitochondria are directly involved in the intrinsic pathway of apoptosis.¹⁷ The pro-apoptotic Bcl-2 family members Bax and Bak are translocated to the outer mitochondria membrane where their oligomerization takes place. This thereby results in mitochondrial outer membrane permeabilization (MOMP), mitochondrial transition pore formation and generation of cytochrome c from mitochondria into the cytosol followed by activation of caspases, the executors of apoptosis.¹⁸ During normal physiological condition, anti-apoptotic Bcl-2 family members such as Bcl-2 and Bcl-XL bind and inhibit Bax/Bak. Tumor cells can escape the process of apoptosis by downregulation of pro-apoptotic Bcl-2 genes and/or upregulation of anti-apoptotic Bcl-2 genes. The balance of pro- and anti-apoptotic proteins affects a cancer cell's susceptibility to apoptotic stimuli and may predict how a tumor will respond to chemotherapy.¹⁹⁻

21

Metabolism and bioenergetics: Metabolic reprogramming is another most important hallmark of cancer which is involved in macromolecule synthesis, bioenergetic demand, and cellular survival. Mitochondrion is the hub of such metabolic reactions and drives this reprogramming through multiple mechanisms such as alterations in glucose utilization, reprogramming of amino acid metabolism and alteration in lipid metabolism.²²

Signaling pathways: The overlap of signaling pathways of tumorigenesis and mitochondrial biology is well established at multiple levels. Firstly, the alteration of mitochondrial functions to support tumorigenesis is well dictated by the classical oncogenic signaling pathways. Secondly, there are direct signals from mitochondria affecting the cellular physiology and tumorigenesis. Finally, mutations in mitochondrial enzymes are responsible of onco-metabolite production, a novel set of mitochondrial signaling molecules that is involved in tumor initiation.²³

Mitochondrial DNA: Other than nucleus, mitochondrion is one of the most important organelles which contains the genomic material.²⁴ The mitochondrial genome of a mammalian cell (MtDNA) is double stranded, circular, supercoiled consisting of 16,568 base pairs. It produces proteins required for oxidative phosphorylation (OXPHOS) through mitochondrial transcriptional and translational machinery. and any mutation in the mitochondrial genome is

responsible for a great impact on diseases like cancer, ageing and neurodegenerative diseases.²⁵ Thus MtDNA has evolved to be an essential target for the diseased state in recent years.²⁶⁻²⁷ However, strategies for targeting mitochondria by delivering single DNA damaging drug would eventually lead drug resistance through mitochondrial DNA damage repair mechanisms.²⁸

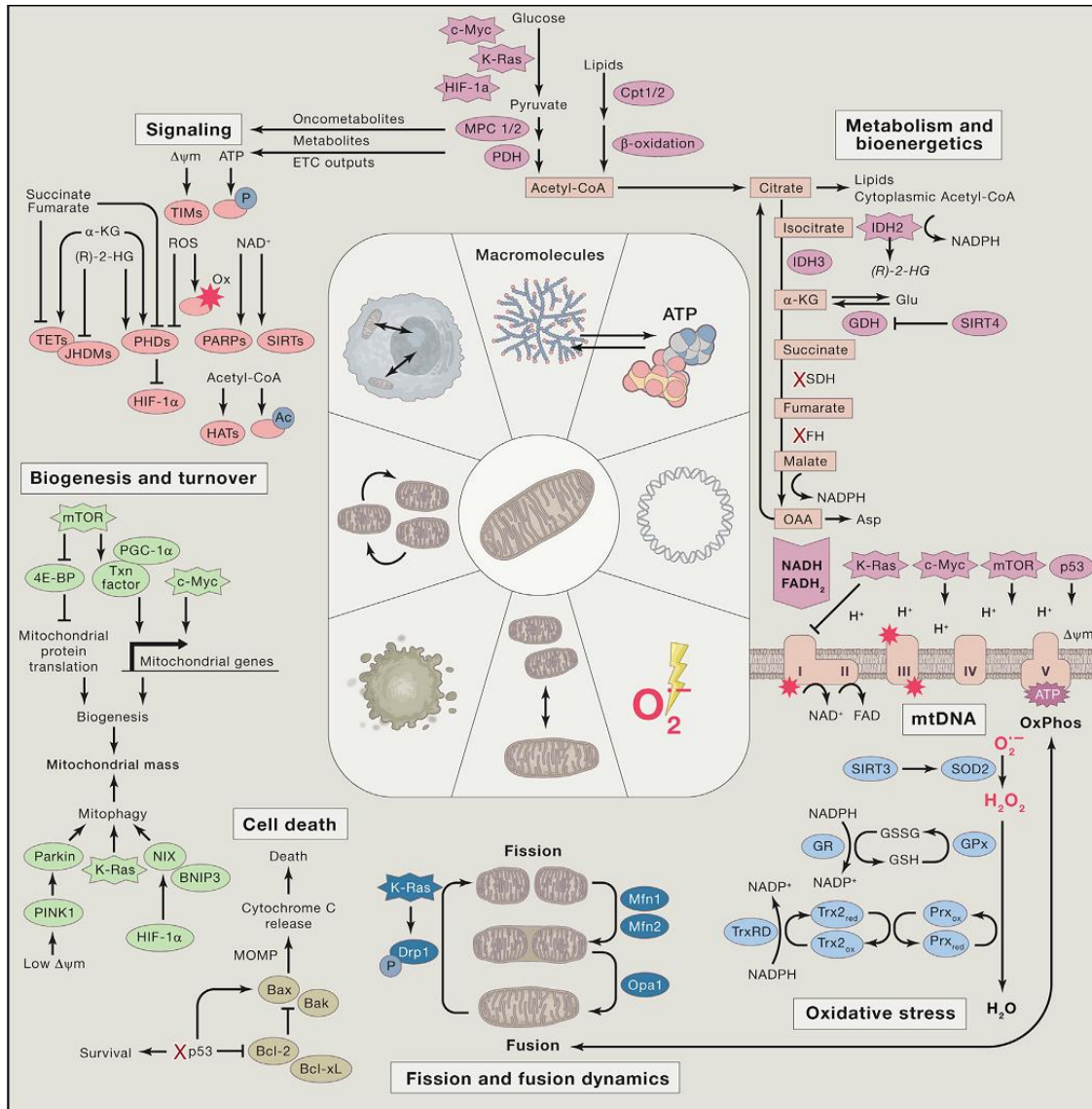


Figure 2: Mitochondria and Cancer (adapted from Haigis et al. *Cell*, 2016, 166, 555-566)

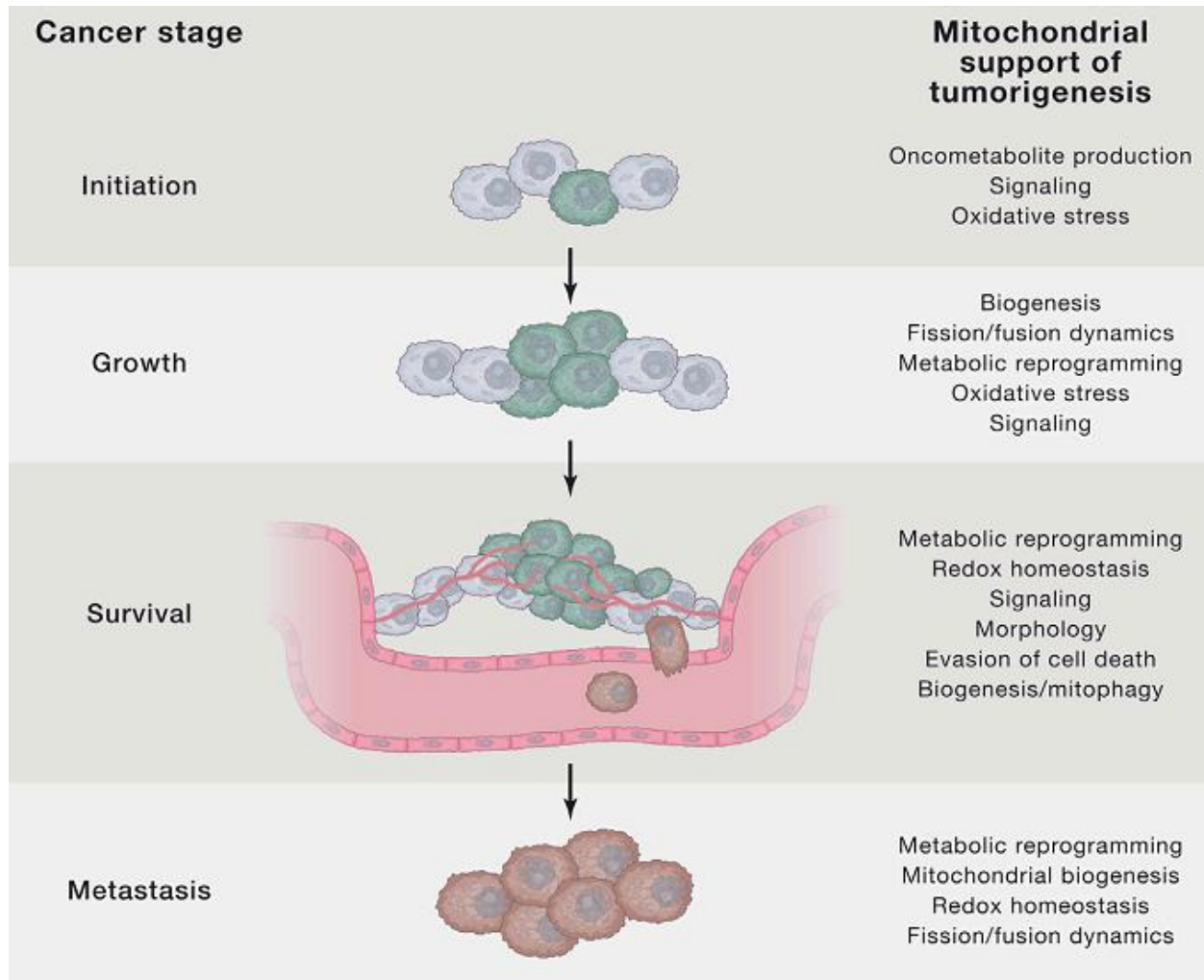


Figure 3: Mitochondria and Stages of tumorigenesis (adapted from Haigis et al. *Cell*, 2016, 166, 555-566)

Thus, it is essential to target the proteins associated to the mitochondrial genome and since mitochondrial DNA has a bidirectional mode of replication and transcription with organized nucleoids in the mitochondrial inner membrane, the presence of mitochondrial topoisomerase 1 (TOP1MT) is very essential for mitochondrial replication and transcription.²⁹ Thus targeting MtDNA as well as TOP1MT thus can be a very important tool to explore mitochondrial DNA biology in cancer cells.

Thus the role of mitochondria in cancer is well established in recent years (**Figure 2**) and mitochondrial support for tumorigenesis in the different stages of cancer is outlined in the **Figure 3**.⁸

1.4 Specific targeting of mitochondria in the sub-cellular milieu

The importance of maintenance of a tight regulated interface with other sub-cellular compartments dictates the structural features of the mitochondria. They are bounded by a double membrane structure having an outer and inner membrane. The inner membrane is composed of a closely packed hydrophobic combination of phospholipid molecules and is highly impermeable. The protein complexes of the electron transport chain (ETC) generate a highly electronegative (140 to 180 mV) potential across this inner membrane in the mitochondria. The active transport of H⁺ ions from the mitochondrial matrix to the inter membrane space maintains the gradient and creates a pH difference across the inner membrane. The ATP synthesis is governed by the electromotive force which is due to potential and concentration gradients and is essential for maintenance of mitochondrial function.³⁰

This mitochondrial membrane potential is responsible for the uptake of the lipophilic cations by the mitochondria where the positively charged species gets accumulated. The lipophilic cations, in order to reach the mitochondria, should cross the plasma and mitochondrial membrane and since both have a negative membrane potential (30-40 mV for plasma membrane and 120-180 mV for mitochondrial membrane respectively), can penetrate through the cytosol and finally to the mitochondria. The higher accumulation of lipophilic cations to the mitochondria is due to the higher negative membrane potential compared to the cytosol. Thus, on comparison to the extracellular matrix, the lipophilic cations can be 100-1000 fold or more accumulated in the mitochondria. The entry of the lipophilic cations extravagating through inner membrane is a multi-step process where firstly they bind to the intermembrane space (IMS) and once they remain inside the phospholipid membrane, they get transferred to the matrix side of the membrane where finally they get dissociated. Thus the perfect balance of charge and hydrophobicity of any molecule are the major requirements of accumulation into the mitochondria (**Figure 4 and 5**).³¹ Several vectors have been extensively used to deliver any therapeutic molecule into mitochondria:

Delocalised lipophilic cation: One of the most important examples of delocalized lipophilic cation is triphenylphosphonium (TPP) cation. Murphy and coworkers were the first to conjugate TPP group to bioactive molecules for the successful accumulation to the mitochondria. TPP is used for the delivery of probes, imaging agents, pharmacophores and anti-oxidants to mitochondria.³² The main advantage of the usage of TPP over any other targeting moiety for driving any cargo to mitochondria are as follows: (a) TPP is stable in biological systems, (b) it has a perfect balance of hydrophobicity (lipophilic character) and hydrophilicity (positive charge), (c) easy to synthesize and purify, (d) low chemical reactivity in the cellular milieu and (e) the absence of light absorption or fluorescence in the visible or near-infrared (NIR) region. The basic skeleton of any TPP based mitochondrial targeting agent consists of a targeting moiety (lipophilic cation), a linker sequence and a functional moiety. There are numerous examples (**Figure 6**) of TPP based mitochondria targeting agents. One interesting example is Mito Q (**Figure 6**) which is relatively safe in human thereby having a great clinical and translational importance in this class of molecules.³³

Heterocyclic aromatic cations: Small molecule heterocyclic aromatic cations (e.g., rhodamine, pyridinium, and cyanine derivatives) were also used as targeting moieties to drive any cargo to mitochondria. Cationic fluorophores such as rhodamine and cyanine dyes are extensively used for mitochondrial staining and monitoring mitochondrial membrane potential. Some of the examples of heterocyclic compounds used as mitochondria-targeting agents are berberin, rhodamine, indolium, pyridinium, and guanidinium cations (**Figure 7**).³³

Mitochondrial targeting peptides: In 2005, Szeto-Schiller (SS) had first designed peptides that can deliver antioxidant cargo to the mitochondria. The SS peptide is a tetrapeptide comprised of aromatic and basic residues containing three positive charges at physiological pH.³⁴ In 2008, Shana O'Kelly designed mitochondria-penetrating peptides (MPPs), a new generation of peptides, which deliver a diverse set of cargoes into the mitochondrial matrix. The peptides are composed of short six amino sequences with alternate cationic and hydrophobic residues. Thus the delocalization of the cationic charge over a large surface area made it more specific for mitochondria. The fluorescent dyes and therapeutic drugs could be easily directed to the mitochondria for successful delivery (**Figure 8**).³⁵

In our work, we have mainly focused on the use of TPP since it is easy to synthesize and characterize.

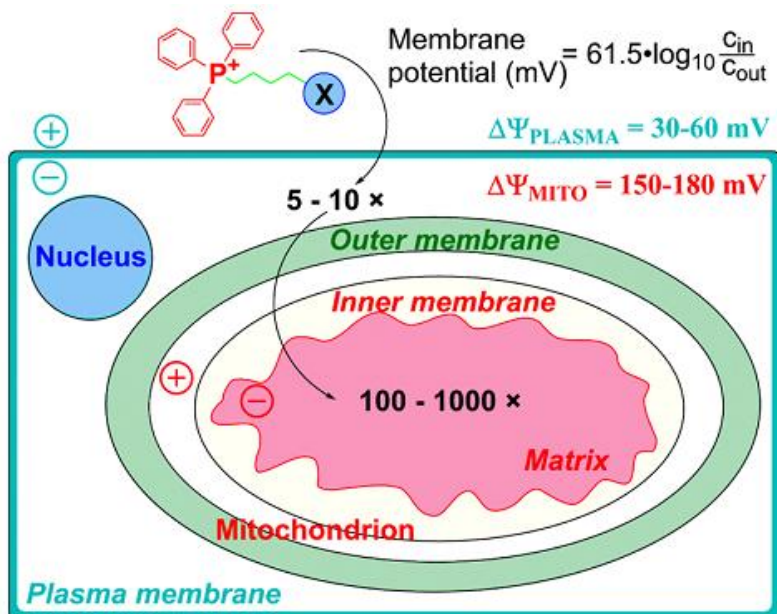


Figure 4: TPP-linked compounds driven by plasma membrane and mitochondrial membrane potentials in the cell. (adapted from Murphy et al. *PNAS*. **2003**, *100*, 5407–5412)

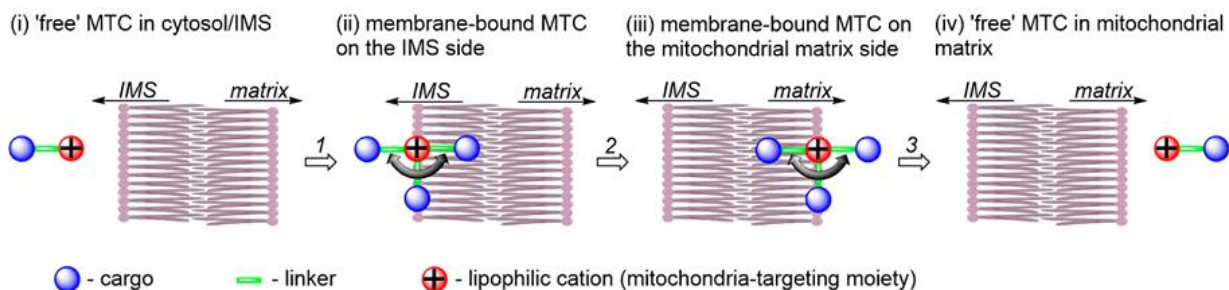


Figure 5: Schematic representation of the entry of the lipophilic cation extravagating through inner mitochondrial membrane (adapted from Kalyanaraman et al. *Chem. Rev.***2017**, *117*, 10043–10120)

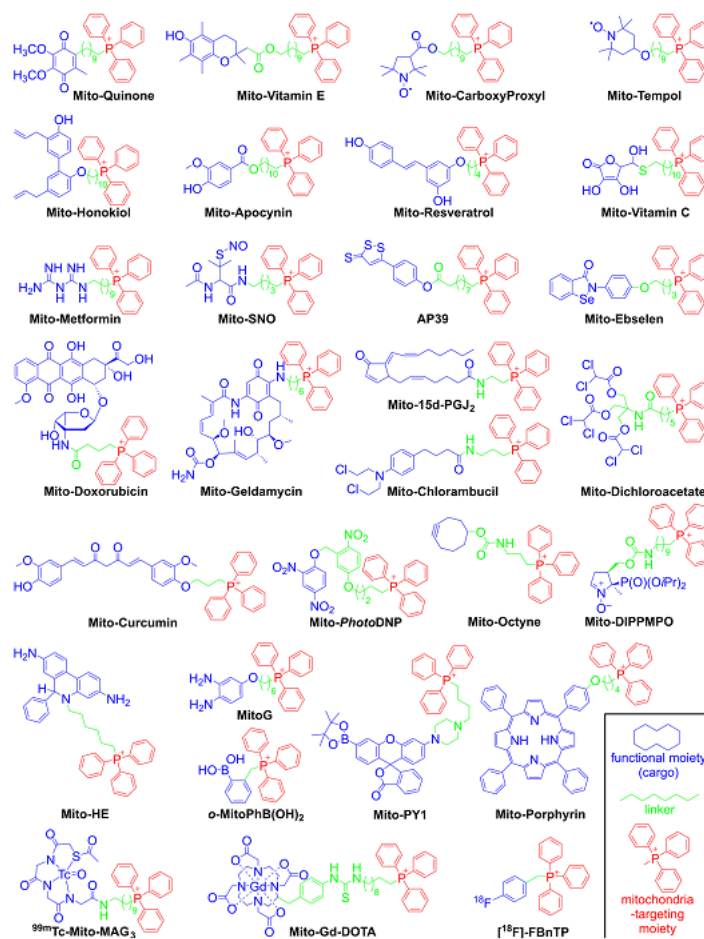


Figure 6: Examples of mitochondria targeting TPP conjugated compounds (adapted from Kalyanaraman et al. *Chem. Rev.* **2017**, *117*, 10043–10120)

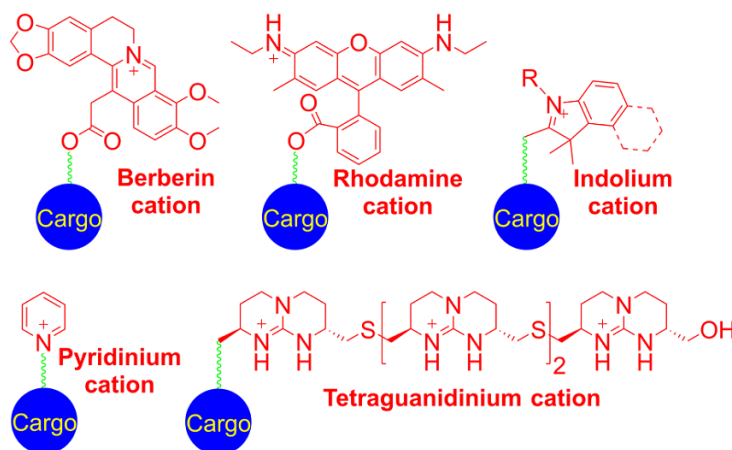


Figure 7: Examples of mitochondria targeting heterocyclic aromatic cations (adapted from Kalyanaraman et al. *Chem. Rev.* **2017**, *117*, 10043–10120)

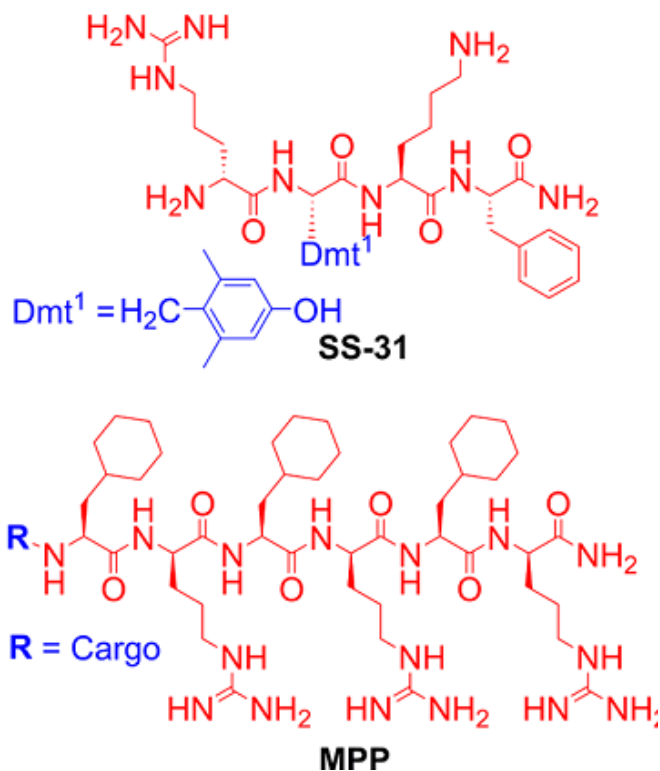


Figure 8: Examples of mitochondria targeting peptides (adapted from Kalyanaraman et al. *Chem. Rev.* **2017**, *117*, 10043–10120)

1.5 Selective targeting of mitochondria in cancer cells

Mitochondria are the ubiquitous powerhouses of the healthy as well as cancer cells. Hence, selective sub-cellular targeting of mitochondria in cancer cells, keeping them unperturbed in healthy cells, could be of central importance for the development of cancer therapeutics and therefore demanding nanotechnology-based toolkits.³⁶

Nanotechnology based platforms have revolutionized cancer therapeutics in last decade. Several nanovectors including liposomes, polymeric nanoparticles, nanocell, layer-by-layer nanoparticles, graphene oxide, gel-liposome and carbon nanotubes (**Figure 9**) have been demonstrated to deliver small molecule drugs, nucleic acids (genes and siRNAs) and therapeutic proteins successfully into tumor tissues through passive [enhanced permeability and retention (EPR) effect] and active targeting (cancer biomarker driven) (**Figure 10**).³⁷⁻³⁸

Passive targeting: To effectively deliver drugs to the targeted site, the delivery system must remain in the bloodstream for a considerable time without being eliminated by means of

metabolism and phagocytosis. The delivery vehicles are usually caught in the blood circulation by body's defense mechanism, the reticulo-endothelial system (RES) present in spleen and liver. Passive targeting involves designing drug carrier systems to evade reticulo-endothelial system. Fast growing tumor cells require recruitment of new vessels for oxygen and nutrient supply. That results in growth factor imbalance and leads to highly disorganized tumor vessels contributing to passive targeting. Unique microenvironment surrounding tumor cells differs from normal cells, also contributes to the passive targeting. Hyperproliferating tumor cells show high metabolic rate utilizing the energy obtained through glycolysis, resulting in acidic environment. Delivery vehicles are designed to remain stable at physiological pH (pH = 7.4) and to release the drugs at acidic pH. Cancer cells even express unique biological macromolecules such as matrix metalloproteinases, which can be used in passive targeting. Fast growing vascularization, leakiness and defective lymphatic drainage contribute to the passive targeting. Molecular weight, size, surface properties of the vector play role in passive targeting.³⁹⁻⁴⁰

Enhanced permeability and retention (EPR) effect: It is an effective strategy to selectively deliver nanosize anticancer drugs/drug carriers to the tumor tissue. This effect was first noticed by Maeda and coworkers in studying the inflammation induced by microbial infections.⁴¹ The nanovectors having size < 200 nm were found to be most effective in cancer therapy and diagnosis. This due to their preferential accumulation into tumor tissues through the unique leaky vasculature compared to the tight endothelial junctions of the healthy tissues. This mechanism is termed as enhanced permeability and retention (EPR) effect and is the basis for selectively targeting tumor tissues via passive targeting.⁴² Recent research focuses on delivery of polymer conjugates, micellar or liposomal drugs of anticancer agents via this mechanism and along with active targeting, the EPR effect is becoming an attractive strategy for such drug designs.⁴³

Active Targeting: Active targeting involves attaching specific ligands to the drug delivery vehicle which will interact with their complementary receptors over-expressed on specific tumor tissues. Active targeting makes use of specific surface exposed receptor and ligand interaction to deliver the drug at specific site. The conjugated ligands can be antibodies, peptides or glycans. However, capacity of delivering drug at particular concentration is compromised in active targeting. Most of the cancer cells express specific molecular markers, which are not expressed by normal cells, serve as site for active targeting. The target cell, usually, accumulate the drug

through receptor-mediated endocytosis. Endocytosed drug carriers are then transported to endosomes and lysosomes, where these are processed to release the drug by lysosomal enzymes. Since resistance inducing proteins such as P-glycoprotein cannot pump out nanoparticle-associated drug or drug-polymer conjugates that have entered the cell *via* the endocytic mechanism, active targeting mechanisms provide an alternative way to combat multi-drug resistance.⁴⁴⁻⁴⁶

Targeting subcellular organelles with nanoparticles: Inside the cells, biomolecules (nucleic acids, proteins, carbohydrates, lipids) are compartmentalized into different sub-cellular organelles and their spatial localizations determine their biological functions. Hence, perturbing specific functional biomolecules localized in selective organelles is a real challenge in cancer therapeutics and is in its infancy. Dhar et al. developed lipophilic cationic triphenylphosphine (TPP) coated nanoparticles to deliver DNA damaging drug (cisplatin) or metabolic inhibitor (3-bromopyruvate) into mitochondria by exploiting their higher membrane potential compared to cell membrane.⁴⁷⁻⁴⁸ Similarly, several other nanovectors were also developed to deliver therapeutic molecules into mitochondria through TPP, cationic peptide or other cationic moiety-mediated targeting.

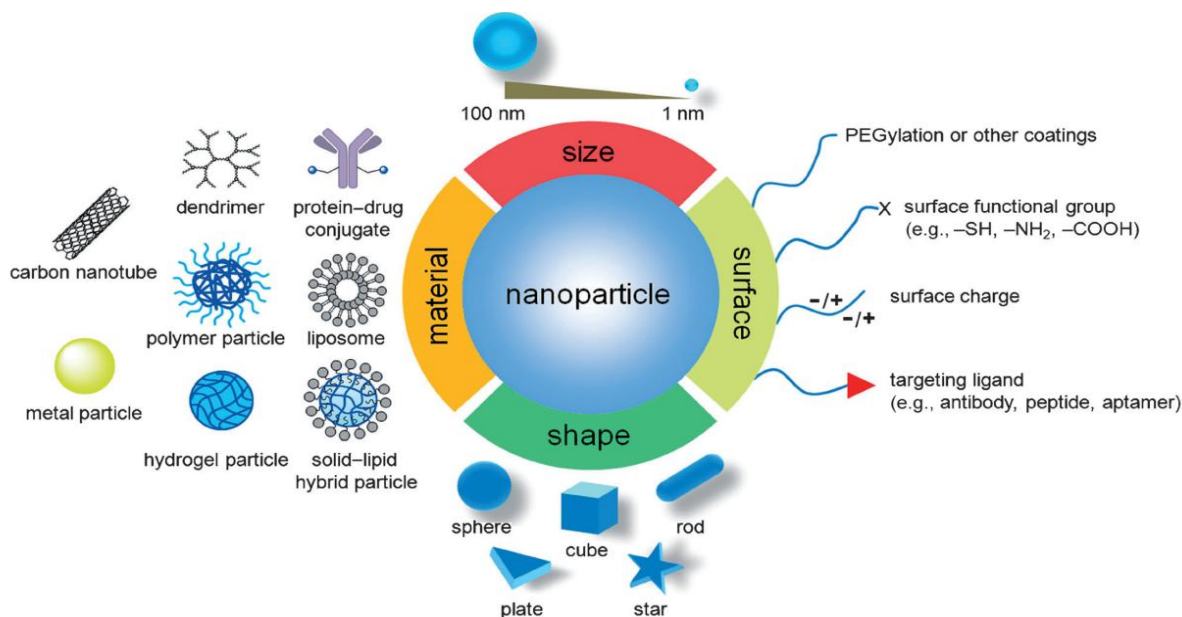


Figure 9: Characteristics of nanoparticles in a nut shell (adapted from Xia et al. *Angew. Chem. Int. Ed.* **2014**, 53, 12320-12364., **2007**, 2, 751-760)

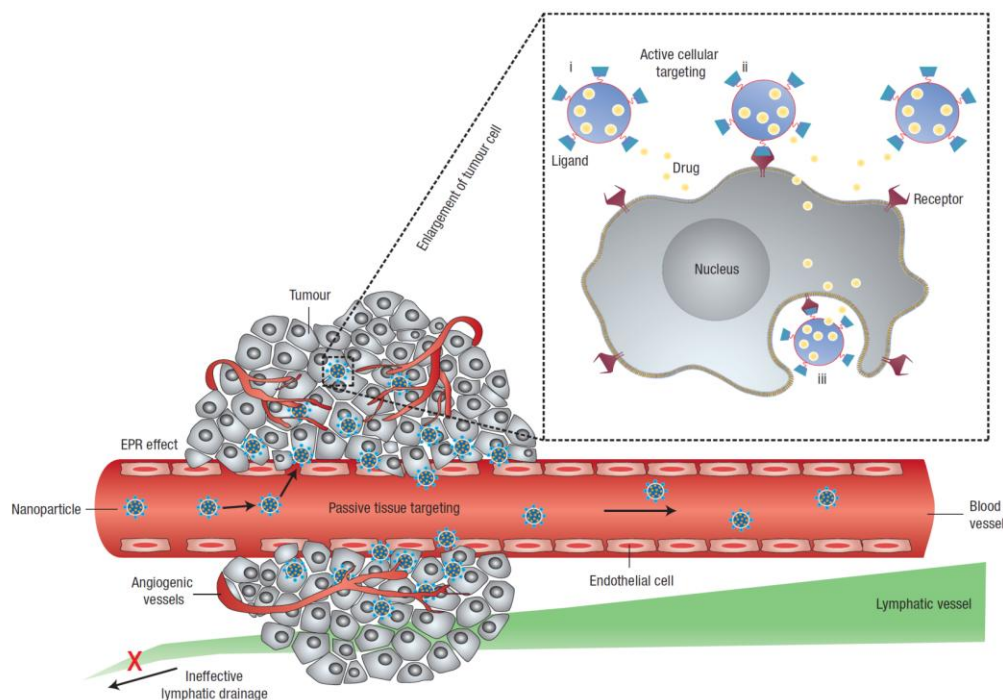


Figure 10: Schematic representation of passive and active targeting (adapted from Peer et al. *Nat. Nanotechnol.*, 2007, 2, 751-760)

1.6 Aim of thesis

Mitochondria have emerged as novel, alternative targets for next generation cancer therapy. However, there are three major challenges in targeting mitochondria: (a) *selective targeting of mitochondria in cellular milieu*, (b) *specific targeting of mitochondria in cancer tissues keeping mitochondria in healthy cells intact* and (c) *overcome drug resistance*. To address these, we have developed cationic lipidic nanoparticle for specific targeting of anti-apoptotic Bcl-2 protein on mitochondria in cancer cells to overcome drug resistance (Chapter 2). Further, we also developed Cerberus Nanoparticles and graphene oxide based nanoplatfroms to specifically target the mitochondrial DNA (mt-DNA) and mitochondrial topoisomerase I (mt-TOP1) in cancer cells (Chapter 3). Moreover, mitochondria show complex cross-talk with the nucleus and endoplasmic reticulum (ER) for protein and lipid supply. Hence, simultaneous targeting of nucleus and mitochondria would lead to the augmented therapeutic outcome. Hence, we have developed dual-drug conjugated nanoparticles to target nucleus and mitochondria simultaneously in cancer cells (Chapter 4). We envision that the here presented unique

approaches can be translated into clinics in future as platform technologies to inhibit multiple diverse targets concurrently into mitochondria, improve the therapeutic efficacy, reduce the off-target toxicity, overcome drug resistance and finally, offer a better quality of life to the cancer patients.

1.7 References

- (1) WHO. WHO | Cancer <http://www.who.int/cancer/en/>.
- (2) Siegel, R. L.; Miller, K. D.; Jemal, A. Cancer Statistics, 2017. *CA. Cancer J. Clin.* **2017**, *67*, 7–30.
- (3) WHO. Definition of Palliative Care.
- (4) Hanahan, D.; Weinberg, R. a. The Hallmarks of Cancer. *Cell* **2000**, *100*, 57–70.
- (5) Hanahan, D.; Weinberg, R. A. Review Hallmarks of Cancer : The Next Generation. *Cell* **2011**, *144*, 646–674.
- (6) Goodsell, D. S. Mitochondrion. *Biochem. Mol. Biol. Educ.* **2010**, *38*, 134–140.
- (7) Martin, W. F.; Garg, S.; Zimorski, V. Endosymbiotic Theories for Eukaryote Origin. *Philos. Trans. R. Soc. B Biol. Sci.* **2015**, *370*, 20140330.
- (8) Vyas, S.; Zaganjor, E.; Haigis, M. C. Mitochondria and Cancer. *Cell* **2016**, *166*, 555–566.
- (9) Wallace, D. C. Mitochondria and Cancer. *Nat. Rev. Cancer* **2012**, *12*, 685–698.
- (10) Fulda, S.; Galluzzi, L.; Kroemer, G. Targeting Mitochondria for Cancer Therapy. *Nat. Rev. Drug Discov.* **2010**, *9*, 447–464.
- (11) Diaz, F.; Moraes, C. Mitochondrial Biogenesis and Turnover. *Cell Calcium* **2008**, *44*, 24–35.
- (12) Youle, R. J.; Narendra, D. P. Mechanisms of Mitophagy. *Nat. Rev. Mol. Cell Biol.* **2011**, *12*, 9–14.
- (13) Youle, R. J.; van der Bliek, A. M. Mitochondrial Fission, Fusion, and Stress. *Science* , **2012**, *337*, 1062–1065.
- (14) Szabadkai, G.; Simoni, A. M.; Chami, M.; Wieckowski, M. R.; Youle, R. J.; Rizzuto, R. Drp-1-Dependent Division of the Mitochondrial Network Blocks Intraorganellar Ca²⁺ Waves and Protects against Ca²⁺-Mediated Apoptosis. *Mol. Cell* **2004**, *16*, 59–68.

- (15) Zhang, Y.; Chan, D. C. New Insights into Mitochondrial Fusion. *FEBS Lett.* **2007**, *581*, 2168–2173.
- (16) Westermann, B. Mitochondrial Fusion and Fission in Cell Life and Death. *Nat. Rev. Mol. Cell Biol.* **2010**, *11*, 872–884.
- (17) Elmore, S. Apoptosis: A Review of Programmed Cell Death. *Toxicol. Pathol.* **2007**, *35*, 495–516.
- (18) Youle, R. J.; Strasser, A. The BCL-2 Protein Family: Opposing Activities That Mediate Cell Death. *Nat. Rev. Mol. Cell Biol.* **2008**, *9*, 47–59
- (19) Chipuk, J. E.; Moldoveanu, T.; Llambi, F.; Parsons, M. J.; Green, D. R. The BCL-2 Family Reunion. *Mol. Cell* **2010**, *37*, 299–310.
- (20) Tait, S. W. G.; Green, D. R. Mitochondria and Cell Death: Outer Membrane Permeabilization and beyond. *Nat. Rev. Mol. Cell Biol.* **2010**, *11*, 621–632.
- (21) Ichim, G.; Tait, S. W. G. A Fate Worse than Death: Apoptosis as an Oncogenic Process. *Nat. Rev. Cancer* **2016**, *16*, 539–548.
- (22) Weinberg, S. E.; Chandel, N. S. Targeting Mitochondria Metabolism for Cancer Therapy. *Nat. Chem. Biol.* **2015**, *11*, 9–15.
- (23) Tait, S. W. G.; Green, D. R. Mitochondria and Cell Signalling. *J. Cell Sci.* **2012**, *125*, 807–815.
- (24) Schon, E. A.; DiMauro, S.; Hirano, M. Human Mitochondrial DNA: Roles of Inherited and Somatic Mutations. *Nat. Rev. Genet.* **2012**, *13*, 878–890.
- (25) Chatterjee, A.; Mambo, E.; Sidransky, D. Mitochondrial DNA Mutations in Human Cancer. *Oncogene* **2006**, *25*, 4663–4674.
- (26) Berridge, M. V.; Dong, L.; Neuzil, J. Mitochondrial DNA in Tumor Initiation, Progression, and Metastasis: Role of Horizontal mtDNA Transfer. *Cancer Res.* **2015**, *75*, 3203–3208.
- (27) Chatterjee, A.; Mambo, E.; Sidransky, D. Mitochondrial DNA Mutations in Human Cancer. *Oncogene* **2006**, *25*, 4663–4674.
- (28) Kazak, L.; Reyes, A.; Holt, I. J. Minimizing the Damage: Repair Pathways Keep Mitochondrial DNA Intact. *Nat. Rev. Mol. Cell Biol.* **2012**, *13*, 659–671.

- (29) Zhang, H.; Barcelo, J. M.; Lee, B.; Kohlhagen, G.; Zimonjic, D. B.; Popescu, N. C.; Pommier, Y. Human Mitochondrial Topoisomerase I. *Proc. Natl. Acad. Sci.* **2001**, *98*, 10608–10613.
- (30) Wisnovsky, S.; Lei, E. K.; Jean, S. R.; Kelley, S. O. Mitochondrial Chemical Biology: New Probes Elucidate the Secrets of the Powerhouse of the Cell. *Cell Chem. Biol.* **2016**, *23*, 917–927.
- (31) Smith, R. A. J.; Hartley, R. C.; Cochemé, H. M.; Murphy, M. P. Mitochondrial Pharmacology. *Trends Pharmacol. Sci.* **2012**, *33*, 341–352.
- (32) Smith, R. a J.; Porteous, C. M.; Gane, A. M.; Murphy, M. P. Delivery of Bioactive Molecules to Mitochondria in Vivo. *Proc. Natl. Acad. Sci. U. S. A.* **2003**, *100*, 5407–5412.
- (33) Zielonka, J.; Joseph, J.; Sikora, A.; Hardy, M.; Ouari, O.; Vasquez-Vivar, J.; Cheng, G.; Lopez, M.; Kalyanaraman, B. Mitochondria-Targeted Triphenylphosphonium-Based Compounds: Syntheses, Mechanisms of Action, and Therapeutic and Diagnostic Applications. *Chem. Rev.* **2017**, *117*, 10043–10120.
- (34) Szeto, H. H. Mitochondria-Targeted Peptide Antioxidants: Novel Neuroprotective Agents. *AAPS J.* **2006**, *8* (3), E521–E531.
- (35) Jean, S. R.; Ahmed, M.; Lei, E. K.; Wisnovsky, S. P.; Kelley, S. O. Peptide-Mediated Delivery of Chemical Probes and Therapeutics to Mitochondria. *Acc. Chem. Res.* **2016**, *49* (9), 1893–1902.
- (36) Pathak, R. K.; Kolishetti, N.; Dhar, S. Targeted Nanoparticles in Mitochondrial Medicine. *Wiley Interdiscip. Rev. Nanomedicine Nanobiotechnology* **2015**, *7*, 315–329.
- (37) Ferrari, M. Cancer Nanotechnology: Opportunities and Challenges. *Nat. Rev. Cancer* **2005**, *5*, 161–171.
- (38) Peer, D.; Karp, J. M.; Hong, S.; Farokhzad, O. C.; Margalit, R.; Langer, R. Nanocarriers as an Emerging Platform for Cancer Therapy. *Nat. Nanotechnol.* **2007**, *2*, 751–760.
- (39) Sun, T.; Zhang, Y. S.; Pang, B.; Hyun, D. C.; Yang, M.; Xia, Y. Engineered Nanoparticles for Drug Delivery in Cancer Therapy. *Angew. Chemie - Int. Ed.* **2014**, *53*, 12320–12364.
- (40) Jiang, W.; Huang, Y.; An, Y.; Kim, B. Y. S. Remodeling Tumor Vasculature to Enhance Delivery of Intermediate-Sized Nanoparticles. *ACS Nano* **2015**, *9*, 8689–8696.
- (41) Matsumura, Y.; Maeda, H. A New Concept for Macromolecular Therapeutics in Cancer Chemotherapy: Mechanism of Tumoritropic Accumulation of Proteins and the Antitumor Agent

Smancs. *Cancer Res.* **1986**, *46* (8), 6387–6392.

(42) Maeda, H.; Nakamura, H.; Fang, J. The EPR Effect for Macromolecular Drug Delivery to Solid Tumors: Improvement of Tumor Uptake, Lowering of Systemic Toxicity, and Distinct Tumor Imaging in Vivo. *Adv. Drug Deliv. Rev.* **2013**, *65*, 71–79.

(43) Rajora, A.; Ravishankar, D.; Osborn, H.; Greco, F. Impact of the Enhanced Permeability and Retention (EPR) Effect and Cathepsins Levels on the Activity of Polymer-Drug Conjugates. *Polymers* **2014**, *6*, 2186–2220.

(44) Wang, M.; Thanou, M. Targeting Nanoparticles to Cancer. *Pharmacol. Res.* **2010**, *62*, 90–99.

(45) Bazak, R.; Hourri, M.; El Achy, S.; Kamel, S.; Refaat, T. Cancer Active Targeting by Nanoparticles: A Comprehensive Review of Literature. *J. Cancer Res. Clin. Oncol.* **2015**, *141*, 769–784.

(46) Byrne, J. D.; Betancourt, T.; Brannon-Peppas, L. Active Targeting Schemes for Nanoparticle Systems in Cancer Therapeutics. *Adv. Drug Deliv. Rev.* **2008**, *60*, 1615–1626.

(47) Marrache, S.; Pathak, R. K.; Dhar, S. Detouring of Cisplatin to Access Mitochondrial Genome for Overcoming Resistance. *Proc. Natl. Acad. Sci.* **2014**, *111*, 10444–10449.

(48) Marrache, S.; Dhar, S. The Energy Blocker inside the Power House: Mitochondria Targeted Delivery of 3-Bromopyruvate. *Chem. Sci.* **2015**, *6*, 1832–1845.

Chapter 2: Nanoparticle mediated targeting of mitochondria induces apoptosis in cancer cells

This chapter has been published as:

Abhik Mallick, Piyush More, Muhammed Muazzam Kamil Syed, and Sudipta Basu. Nanoparticle Mediated Mitochondrial Damage Induces Apoptosis in Cancer. *ACS Appl. Mater. Interface*, **2016, 8, 13218-13231.**

2.1. Introduction

One of the most important hallmarks of cancer is evading cell death.¹ Programmed cell death is defined as apoptosis and mitochondria play an important role in the intrinsic pathway of apoptosis.² Bcl-2 family proteins are the key players of apoptosis. Bcl-2 family proteins can be divided into anti-apoptotic Bcl-2 proteins (Bcl-2, Bcl-W, Bcl-XL, A1 & Mcl1) and pro-apoptotic Bcl-2 proteins (Effectors [BAK, BAX, BOK] and BH3-only proteins [BID, BIM, BAD, BIK, BMF, BNIP3, HRK, NOXA & PUMA]).³⁻⁴ The pro-apoptotic Bcl-2 family members Bax and Bak are translocated to the outer mitochondria membrane where their oligomerization takes place. This thereby results in mitochondrial outer membrane permeabilization (MOMP), mitochondrial transition pore formation and generation of cytochrome c from mitochondria into the cytosol followed by activation of caspases, the executors of apoptosis. The anti-apoptotic Bcl-2 family members bind and inhibit the oligomerization of Bax/Bak. The down-regulation of pro-apoptotic Bcl-2 proteins and/or upregulation of anti-apoptotic Bcl-2 proteins are the main causes of evading cell death in tumor. The BH3-only proteins can also bind with the anti-apoptotic Bcl-2 protein and the oligomerization of the pro-apoptotic proteins can occur followed by apoptosis.⁵⁻⁶ As a result small molecule Bcl-2 inhibitors have evolved as interesting class of anti-cancer agents.⁷⁻⁸ Interestingly, Bcl-2 protein is also located in other sub-cellular organelles like endoplasmic reticulum (ER) and nucleus.⁹ Hence, small molecules would inhibit Bcl-2 proteins non-specifically into all possible locations leading to a global effect on the cells.¹⁰ Subsequently, spatial targeting of Bcl-2 proteins in each organelle is a real challenge to understand its functions in different sub-cellular locations.¹¹ Moreover, mitochondrial Bcl-2 protein is mainly responsible for inducing apoptosis in cancer cells. Hence, selective targeting of Bcl-2 on mitochondrial membrane would effectively lead programmed cell death.

To address this, herein we have engineered nanoparticles (NPs) comprised of triphenylphosphine (TPP), α -tocopheryl succinate (TOS, mitochondrial electron transport chain inhibitor) and obatoclax (Obt, small molecule Bcl-2 inhibitor) moieties. These TOS-TPP-Obt-NPs were internalized into the lysosomal compartments by macropinocytosis in a time dependent manner within 1 h followed by lysosomal escape in 6 h. Finally TOS-TPP-Obt-NPs homed into mitochondria over 24 h. These TOS-TPP-Obt-NPs activated mitochondrial outer membrane permeabilization (MOMP) through anti-apoptotic Bcl-2 inhibition, followed by cytochrome c

release. This nanoparticle mediated MOMP lead the cleavage of caspase-9 and caspase-3 to induce apoptosis in cervical cancer cells (HeLa). Interestingly, these TOS-TPP-Obt-NPs demonstrated improved efficacy in drug resistant breast cancer cells (MDA-MB-231) by damaging mitochondria. These nanoparticles could be used as a platform to deliver multiple drugs into mitochondria of cancer cells to damage different targets simultaneously.

2.2. Results and discussion

2.2.1 Engineering of TOS-TPP-Obt NPs. We have chosen α -tocopheryl succinate (α -TOS) as mitochondria damaging drug due to its ability to bind with mitochondrial complex II of electron transport chain and induce apoptosis in different types of cancer through mitochondrial outer membrane permeabilization (MOMP).^{12,13} Moreover, α -TOS demonstrated improved therapeutic efficacy in combination with traditional chemotherapeutic drugs.¹⁴⁻¹⁶ Herein, we appended a linker with α -TOS by conjugating 5-bromopentane-1-ol by ester linkage using DCC and DMAP as coupling reagents to obtain conjugate **2** in 65 % yield (**Figure 1**). We further introduced mitochondria targeting TPP group by reacting compound **2** with triphenylphosphine in presence of potassium carbonate (K_2CO_3) as base in refluxing condition to afford α -TOS-TPP conjugate **3** in 34 % yield.¹⁷ We characterized conjugate **2** by 1H , ^{13}C nuclear magnetic resonance spectroscopy (NMR), high-resolution mass spectroscopy (HR-MS) and matrix assisted laser adsorption/ionization-time of flight (MALDI-TOF) mass spectroscopy. In 1H -NMR spectra of conjugate **2**, appearance of triplate peaks at $\delta = 4.11$ - 4.14 ppm (2H) and 3.37 - 3.41 ppm (2H) confirmed the presence of $Br-(CH_2)_4-\underline{CH_2}-OCO-TOS$ protons and $Br-\underline{CH_2}-(CH_2)_4-OCO-TOS$ protons respectively (**Figure A1**). Also multiplate peaks at $\delta = 1.84$ - 1.91 ppm (2H), 1.74 - 1.81 ppm (2H) and 1.64 - 1.69 ppm (2H) confirmed the presence of $Br-CH_2-(CH_2)_3-CH_2-OCO-TOS$ protons. Moreover, the presence of triplate peaks at $\delta = 2.92$ - 2.95 ppm (2H), 2.74 - 2.78 ppm (2H) and 2.57 - 2.60 ppm (2H) represented $Br-(CH_2)_5-OCO-CH_2-\underline{CH_2}-COO-TOS$, $Br-(CH_2)_5-OCO-\underline{CH_2}-CH_2-COO-TOS$ and benzylic $-CH_2-$ protons on tetrahydropyran moiety in TOS respectively (**Figure A1**). Finally, the aromatic $-CH_3$ protons were confirmed by singlate peaks $\delta = 2.09$ ppm (3H), 2.02 ppm (3H) and 1.98 ppm (3H) in the TOS moiety (**Figure A1**). ^{13}C NMR spectra of conjugate **2** revealed characteristic peaks at $\delta = 172.2$ ppm and 170.9 ppm for the ester functionality (*a* and *b* peaks in **Figure A2**). All six aromatic carbon atoms appeared at

characteristic δ values of 149.6, 141.3, 126.7, 124.9, 123.0, and 117.4 ppm (*d, e, f* and *g* peaks in **Figure A2**). The quaternary carbon atom in the tetrahydropyran moiety and Br-(CH₂)₄-CH₂-OCO-TOS carbon atom in the linker were characterized by the peaks at $\delta = 75.1$ ppm and 64.5 ppm respectively. Finally, conjugate **2** was confirmed by HR-MS and MALDI-TOF spectroscopy by having molecular ion peak [M]⁺ at $m/z = 679.3929$ (**Figure A3**), [M+Na]⁺ at $m/z = 701.3763$ and [M+K]⁺ at $m/z = 717.3459$ respectively (**Figure A4**). Conjugate **3** was also characterized by ¹H, ¹³C NMR spectroscopy, HR-MS and MALDI-TOF mass spectrometry. The appearance of aromatic peaks as multiplets in ¹H NMR spectra of conjugate **3** at $\delta = 7.67$ -7.85 ppm (15H) confirmed the presence of phenyl groups (*j* peaks in **Figure A5**). The remaining characteristic proton peaks appeared in the respected positions as in conjugate **2** (*a, b, c, d, e, f, g, h* and *i* peaks in **Figure A5**). Similarly, in ¹³C NMR spectra, new aromatic carbon peaks appeared at $\delta = 134.9, 133.6, 130.5, 118.8, 117.9$ and 117.4 ppm confirmed the presence of phenyl groups in conjugate **3** (*F* peaks in **Figure A6**). The other peaks remained in the same position as in conjugate **2** (*a, b, c, d, e, f, g, h* peaks in **Figure A6**). Conjugate **3** was also characterized by molecular ion peaks [M]⁺ at $m/z = 861.5582$ by HR-MS (**Figure A7**) as well as by MALDI-TOF mass spectrometry (**Figure A8**). We also characterized the presence of TPP group in conjugate **3** by ³¹P NMR spectroscopy having characteristic peak at $\delta = 24.3$ ppm (**Figure A9**). We finally evaluated the purity of the conjugates **2** and **3** by reverse phase high-performance liquid chromatography (RP-HPLC). Conjugate **2** and conjugate **3** showed 93.4 % and 95.6 % purity respectively in RP-HPLC (**Figure A10**).

All these ¹H, ¹³C, ³¹P NMR, HR-MS, MALDI-TOF and RP-HPLC data clearly confirmed the presence of conjugate **2** and conjugate **3** in high purity. We have engineered mitochondria targeted dual drug loaded TOS-TPP-Obt-NPs by solvent evaporation-lipid film formation-hydration-extrusion method (**Figure 1b**).¹⁸ We have chosen obatoclox as the second drug to be entrapped into the nanoparticle. Obatoclox is a red fluorescent small molecule, BH3-domain binding pan-Bcl-2 inhibitor, already in a clinical trial as monotherapy as well as in combination with other drugs for different types of cancers.¹⁹⁻²¹ Moreover, obatoclox is highly hydrophobic in

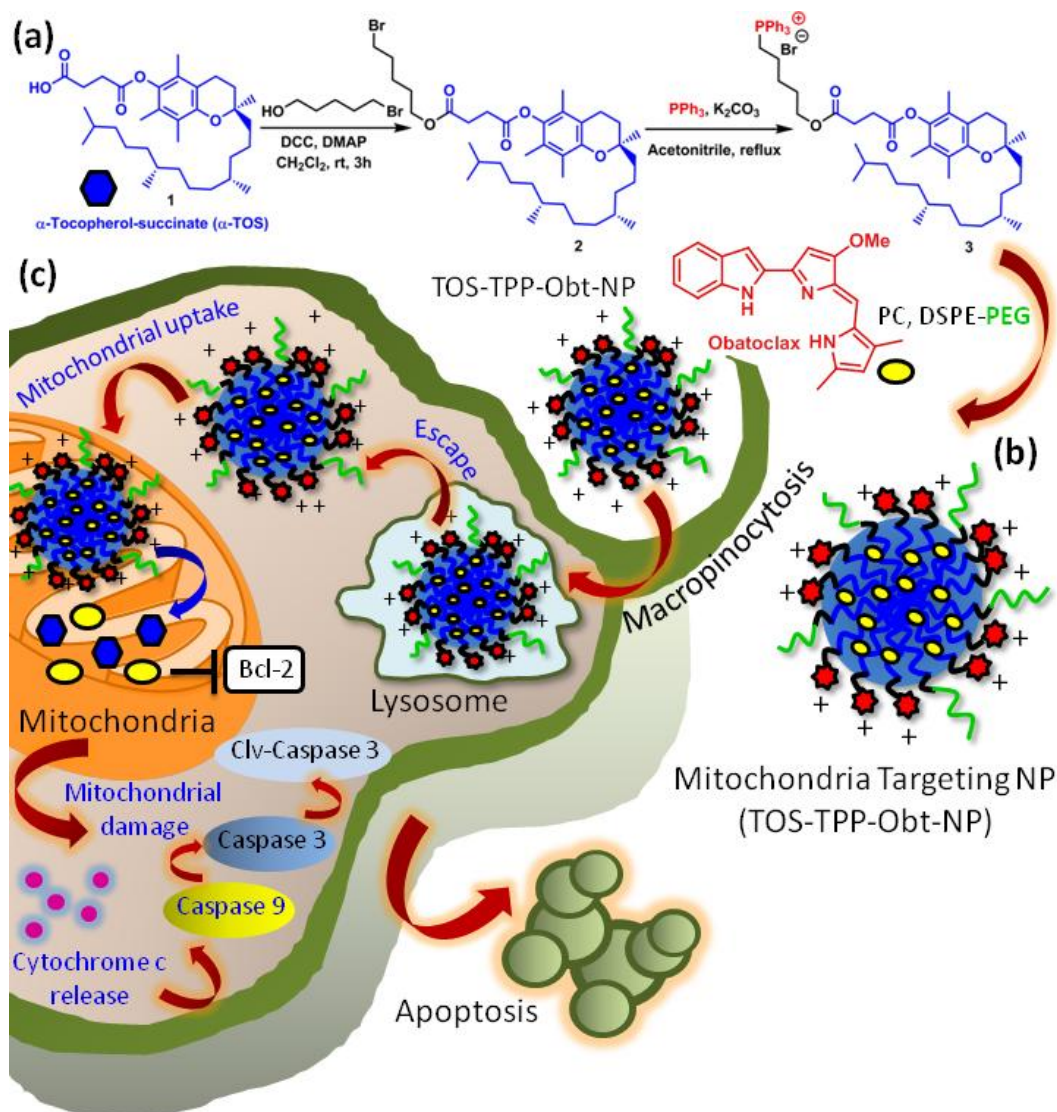


Figure 1. (a) Synthetic scheme of TOS-TPP conjugate (**3**) from α -tocopheryl succinate (α -TOS). (b) Engineering of mitochondria targeting TOS-TPP-Obt-NPs. (c) Schematic representation of cellular internalization and mitochondrial homing of TOS-TPP-Obt-NPs leading to apoptosis.

nature leading to erratic biodistribution to bind with its actual target on mitochondrial outer membrane.²² We synthesized TOS-TPP-Obt-NPs by mixing phosphatidylcholine (PC), α -TOS-TPP conjugate **3** and free obatoclax in 2:1:0.2 weight ratios. We used DSPE-PEG to surface coat the nanoparticles with polyethylene glycol to evade the mononuclear phagocytic systems (MPS) to ensure prolonged blood circulation.²³

The size of the nanoparticles is one of the important determining factors to be successfully accumulated into the tumor tissues by unique leaky vasculature.²⁴ In a recent report, it was shown that the nanoparticles having optimal diameter range of 100-160 nm had improved blood circulation and tumor accumulation by enhanced permeability and retention (EPR) effect.²⁵ The mean hydrodynamic diameter of the TOS-TPP-Obt-NPs was determined to be 131.6 ± 1.62 nm (mean \pm SEM, n = 3) (**Figure 2a**) by dynamic light scattering (DLS). Hence, we expect our TOS-TPP-Obt-NPs will also have better blood circulation half-life as well as improved tumor tissue homing by EPR effect. For effective mitochondria trafficking, the nanoparticles should bear high positive charge on the surface. We also evaluated the surface charge of the TOS-TPP-Obt-NPs by DLS, which was found to be $+42.9 \pm 1.20$ mV (mean \pm SEM, n = 3) (**Figure 2b**). The positive charge on the TOS-TPP-Obt-NPs is the function of both TOS-TPP as well as PEG. Since the conc. of PEG is kept very low, the positive charge of the TOS-TPP-Obt-NPs is dictated by the conc. of TOS-TPP conjugate which is the basic requirement of targeting mitochondria. Secondly, the arrangement of TOS-TPP and PEG is in such a way that we get such high positive zeta potential value. The results had been reported in triplicate. Therefore, this highly positively charged sub 200 nm TOS-TPP-Obt-NPs should effectively home into tumor tissues followed by mitochondria localization. Size, shape and morphology of the nanoparticles play critical role to be recognized by body's innate immune system.²⁶ Thus, we visualized the size, shape and morphology of the nanoparticles by field-emission scanning electron microscopy (FESEM) (**Figure 2c**), transmission electron microscopy (TEM) (**Figure 2d**) and atomic force microscopy (AFM) (**Figure 3b**). The FESEM and TEM images clearly showed that TOS-TPP-Obt-NPs were mono-dispersed in nature having spherical in shape with smooth surface morphology and less than 200 nm in diameter. The spherical shape and smooth surface morphology were also confirmed by AFM images with little aggregation in nature. We also determined the presence of nitrogen in obatoclax and phosphorus in triphenylphosphine (TPP) in the same TOS-TPP-Obt-NPs by energy dispersive X-ray spectroscopy (EDX) (**Figure 3a**). We evaluated the dual drug loading in the nanoparticle by UV-Vis spectroscopy from concentration versus absorbance graph at characteristic $\lambda_{\max} = 287$ nm (for α -TOS) and $\lambda_{\max} = 488$ nm (for obatoclax) (**Figure 3d**). The mean loading of α -TOS and obatoclax was calculated to be = 1035 μ g/mL (loading efficiency = 20.7%, loading content = 6.4 %) and 222 μ g/mL (loading efficiency = 22.2%, loading content =

1.3%) respectively (**Figure 3c**). In our previous study, we have observed that dual-drug conjugated nanoparticles engineered from α -TOS formed 10 nm hydrophobic shells with hydrophilic core.²⁷

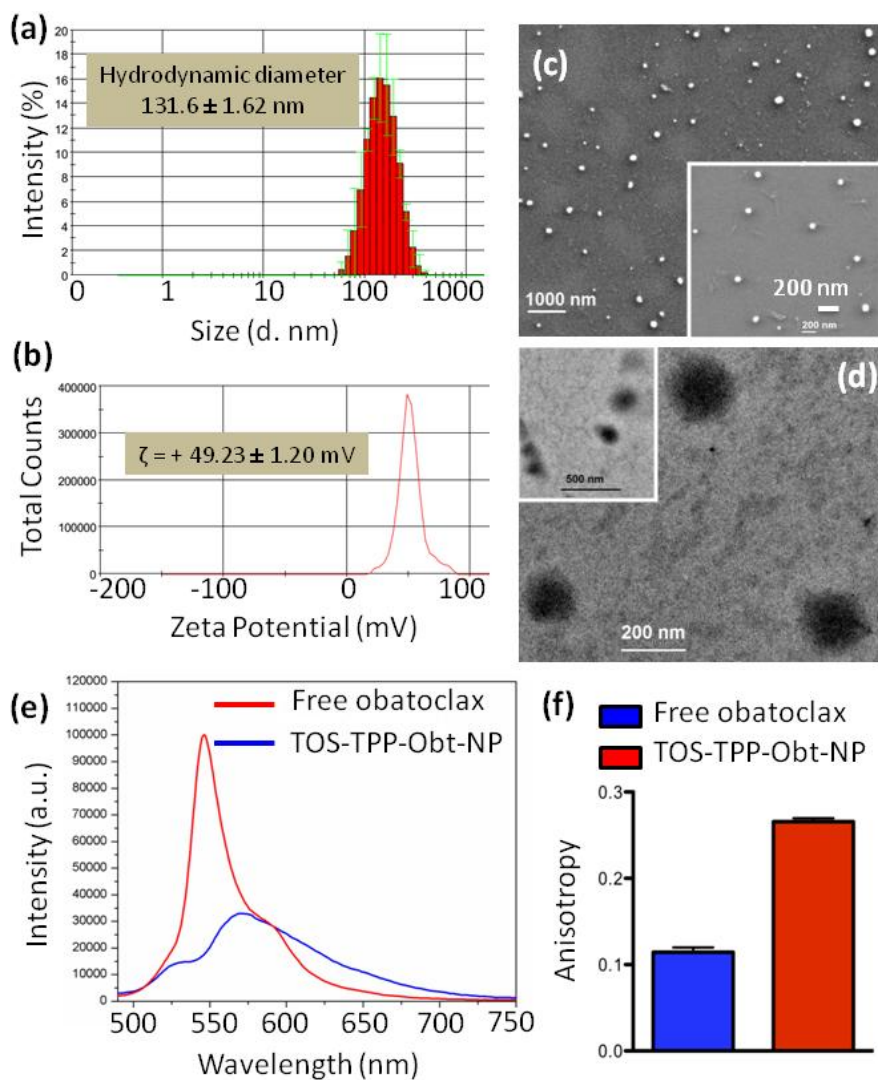


Figure 2. (a) Hydrodynamic diameter and (b) zeta potential of TOS-TPP-Obt-NPs determined by DLS. All the values were determined as mean \pm SEM ($n = 3$). (c) FESEM (inset scale bar = 200 nm) and (d) TEM (inset scale bar = 500 nm) images of TOS-TPP-Obt-NPs. (e) Fluorescence emission quenching of obatoclax in TOS-TPP-Obt-NPs compared to free obatoclax at $\lambda_{\text{max}} = 546$ nm. (f) Steady state fluorescence anisotropy of free obatoclax and obatoclax encapsulated in TOS-TPP-Obt-NPs.

To understand the location of hydrophobic obatoclax molecules in our TOS-TPP-Obt-NP, we evaluated the fluorescence emission spectra of free obatoclax and compared with the fluorescence emission spectra of encapsulated obatoclax in TOS-TPP-Obt-NPs (**Figure 2e**).

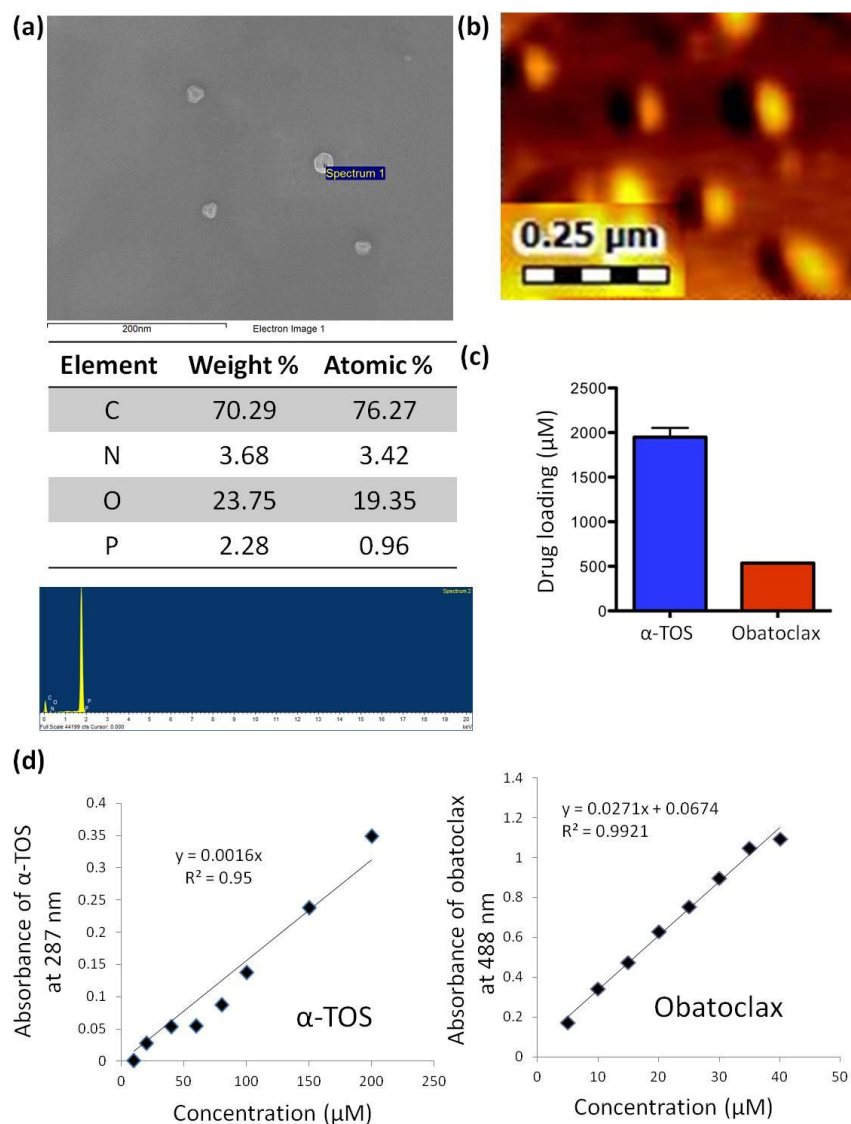


Figure 3. (a) AFM images of TOS-TPP-Obt-NPs.(b) EDX spectra of TOS-TPP-Obt-NPs determined from FESEM.(c) Loading of α -TOS and obatoclax in TOS-TPP-Obt-NPs. (d) Concentration versus absorbance calibration graph of α -TOS and obatoclax determined by UV-Vis spectroscopy. All the data presented here were determined as mean \pm SEM (n = 3).

It was observed that the characteristic peak of obatoclax at $\lambda_{\max} = 546$ nm was completely quenched in TOS-TPP-Obt-NP which clearly indicated the π - π stacking of highly aromatic planner obatoclax with the aromatic ring of α -TOS in the hydrophobic region. Moreover, fluorescence steady state anisotropy study showed a 3 folds increase in fluorescent anisotropy of encapsulated obatoclax in TOS-TPP-Obt-NPs compared to free obatoclax (**Figure 2f**), which conclusively demonstrated that obatoclax resides in the hydrophobic shells in the TOS-TPP-Obt-NPs.

For successful clinical translation, the TOS-TPP-Obt-NPs should have shelf stability at storage condition (4 °C) as well as in blood circulation (37 °C). We evaluated the stability of the TOS-TPP-Obt-NPs at 4 °C by DLS. The hydrodynamic diameter was changed from 133.9 ± 0.5 nm (PDI = 0.141 ± 0.01) to 164.7 ± 2.4 nm (PDI = 0.39 ± 0.007) over 7 days (**Figure 4 a-b**).

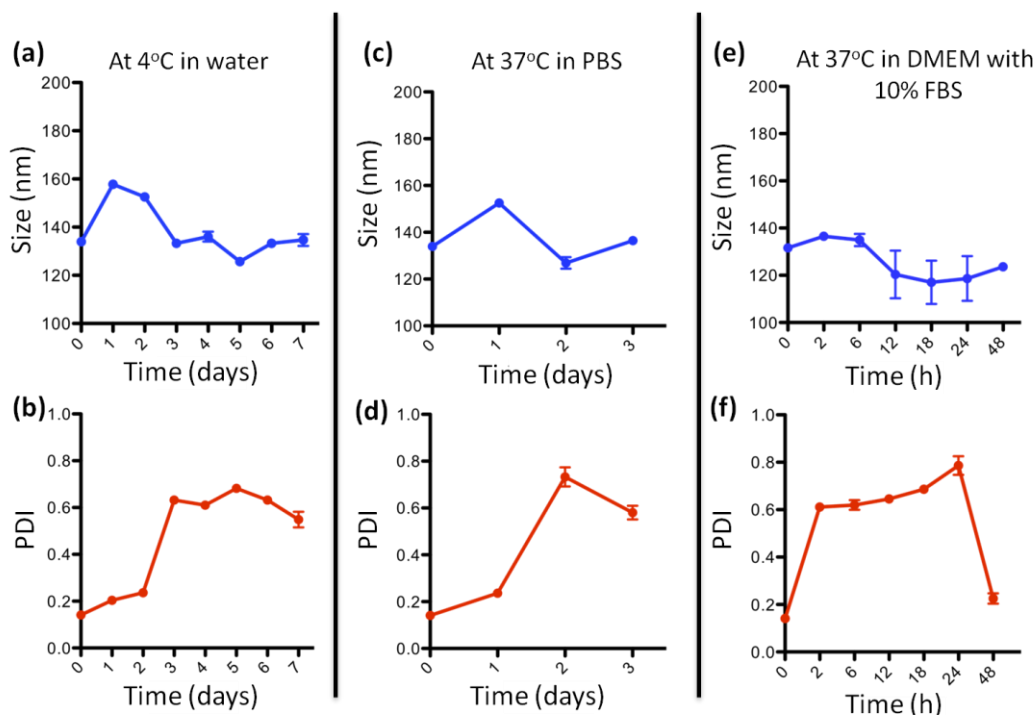


Figure 4. Stability of TOS-TPP-Obt-NPs (a-b) at 4°C in water for 7 days, (c-d) at 37°C in PBS for 3 days and (e-f) at 37°C in DMEM media with 10% FBS for 48h determined by DLS.

We also evaluated the stability of TOS-TPP-Obt-NPs at 37 °C in phosphate buffer saline (PBS). The diameter of the nanoparticles changed from 133.9 ± 0.5 nm (PDI = 0.141 ± 0.01) to 166.5 ± 1.2 nm (PDI = 0.348 ± 0.029) over 3 days (**Figure 4 c-d**). Finally, the stability of these TOS-

TPP-Obt-NPs were determined in DMEM cell culture media in presence of 10 % fetal bovine serum (FBS) to mimic blood circulation milieu in which cell culturing is done at 37 °C. The hydrodynamic diameter of the nanoparticles were changed negligibly from 131.6 ± 1.6 nm with $PDI = 0.141 \pm 0.01$ to 163.6 ± 1.2 nm with $PDI = 0.392 \pm 0.018$ over 48 h (**Figure 4 e-f**) which is enough to be accumulated in tumor tissues by passive targeting. These stability data clearly demonstrated that TOS-TPP-Obt-NPs were stable in storage condition for a week and in blood circulation mimic for 2 days.

2.2.2 Cellular internalization. Despite the development of different nano-vectors to deliver the traditional chemotherapeutic drugs to mitochondria, the actual mechanism of mitochondria homing of those nano-vectors is not very well understood.^{28,29} To address this, we first evaluated the cellular uptake mechanism of our TOS-TPP-Obt-NPs in HeLa cervical cancer cells in time dependent manner using confocal laser scanning microscopy (CLSM). Our previous understanding revealed that α -TOS-drug nanoparticles home into acidic lysosomes in a time dependent manner.²⁷ Inspired by those observations, we stained the acidic lysosomes of HeLa cells with green fluorescent LysoTracker DND-153 and incubated the cells with red fluorescent TOS-TPP-Obt-NPs for 1 h, 3 h and 6 h time points. We co-stained the nucleus by blue fluorescent DAPI. The merging of green and red fluorescence leading to yellow color in CLSM images (**Figure 5**) confirmed that the TOS-TPP-Obt-NPs localized into the lysosomes within 1 h. Further quantification from CLSM through Pearson's coefficient and Mander's coefficients revealed that the volume of overlapping regions of green and red fluorescence gradually decreased from 84.9 % to 80.7 % to 47.4 % from 1 h to 3 h to 6 h respectively (**Table 1**). This temporal reduction of colocalization volume unmistakably indicated that the TOS-TPP-Obt-NPs escaped from lysosomal compartments in time dependent manner. Besides, in a high resolution CLSM imaging (**Figure 6 a-b**) revealed green fluorescence regions at 6 h, which clearly confirmed that TOS-TPP-Obt-NPs were no longer present in some of the lysosomes. These CLSM images exhibited that TOS-TPP-Obt-NPs would quickly internalize and localize into lysosomes within 1 h but would escape over a period of time leading to the reduction of colocalization over 6 h. As control, we treated the HeLa cells with free obatoclax and imaged the cells at 1 h and 3 h time points. Contrast to TOS-TPP-Obt-NPs, free obatoclax internalized into

the cells and localized into lysosomes as well as nucleus in a non-specific manner (**Figure 7**). The overlapping of red and blue colors yielded purple color, which showed the co-localization of free obatoclax in nucleus.

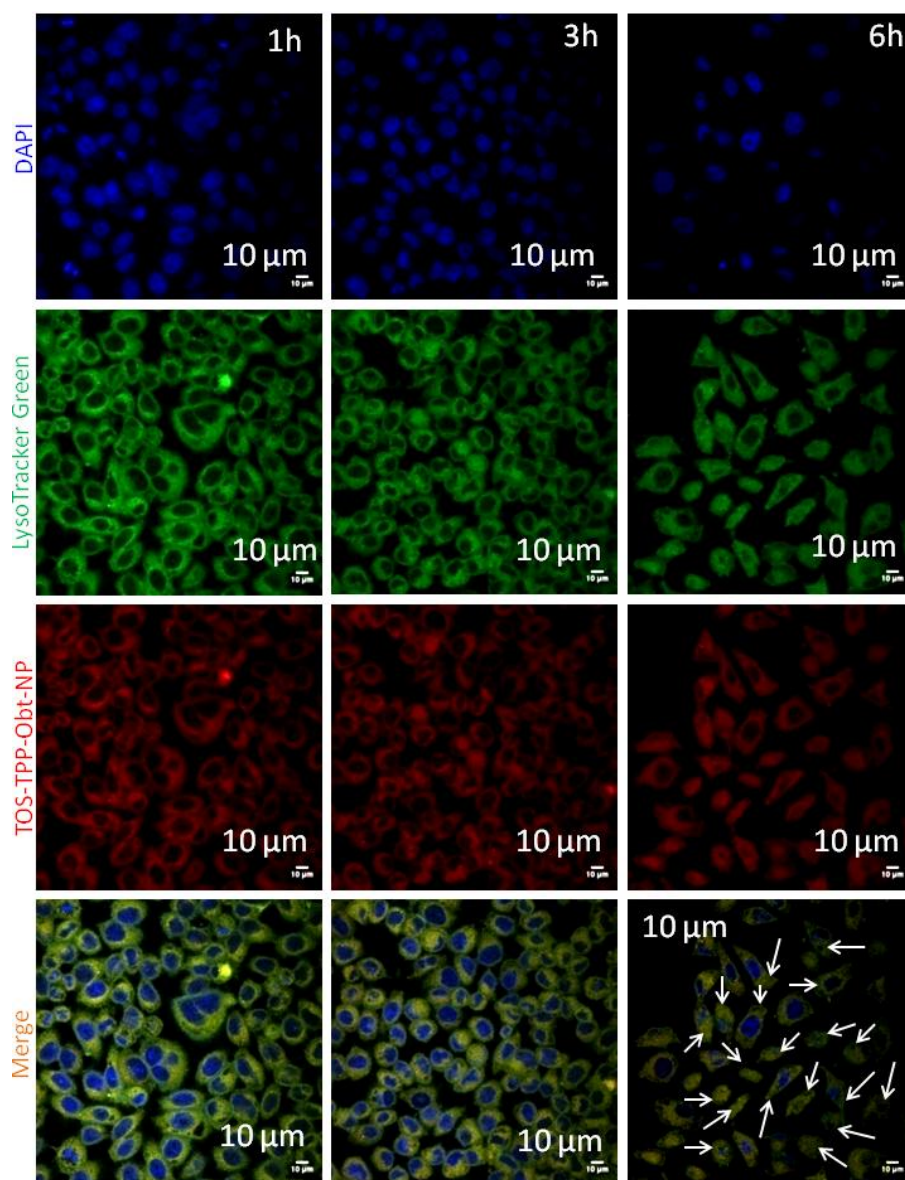


Figure 5. Confocal laser scanning microscopy images of internalization of TOS-TPP-Obt-NPs in HeLa cells in 1 h, 3 h and 6 h time points. Nucleus and lysosomes were stained by DAPI (blue) and LysoTracker (green) dyes. The yellow regions in merged images showed the co-localization of TOS-TPP-Obt-NPs (red) into lysosomes. Scale bar = 10 μm.

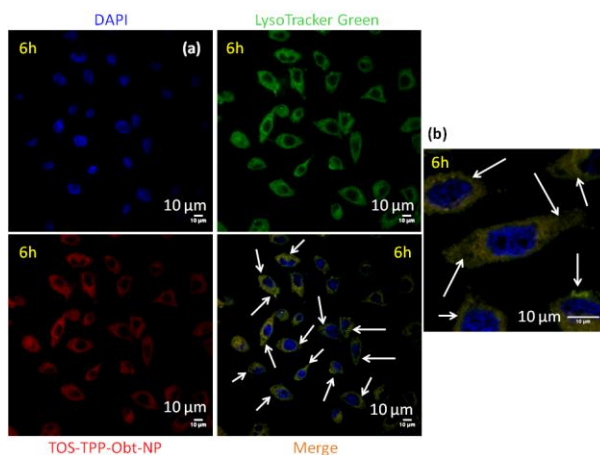


Figure 6. (a-b) CLSM images of HeLa cells after incubating with TOS-TPP-Obt-NPs for 6h. Nucleus and lysosomes were stained with DAPI and LysoTracker Green. Overlapping of green and red fluorescence showed the localization of TOS-TPP-Obt-NPs into lysosomes. Green colors in the merged images indicated by arrows demonstrated the escape of TOS-TPP-Obt-NPs from lysosomes at 6 h. (b) Magnified CLSM images of few cells showed more prominent green regions indicated the lysosomes without red TOS-TPP-Obt-NPs. Scale bar = 10 μ m.

Treatment Time		1 h	3h	6h
Image Channels		C2(green) C3(red)	C2(green) C3(red)	C2(green) C3(red)
Pearsons' Correlation Coefficient	r	0.8538	0.868	0.916
Manders Coefficient	M1 (fraction of C2 overlapping C3)	0.9756	0.9646	0.8656
	M2 (fraction of C3 overlapping C2)	0.9816	0.9777	0.9489
Percent volume colocalized		84.92%	80.76%	47.45%

Table 1: Quantification of localization of TOS-TPP-Obt-NPs into acidic lysosomes from CLSM.

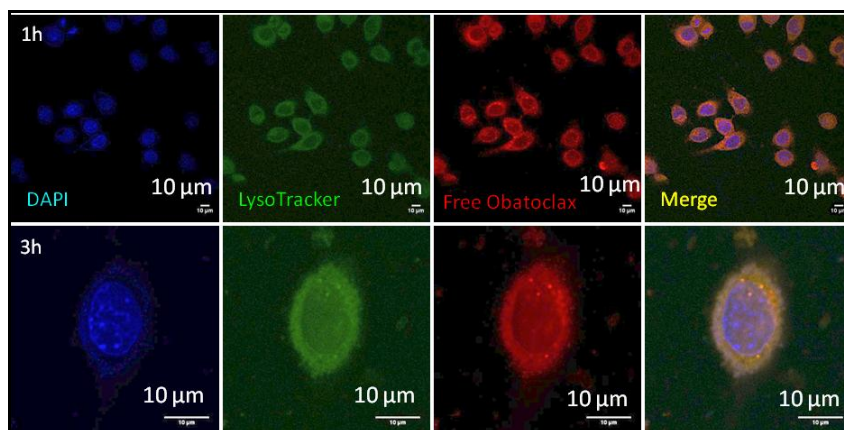


Figure 7. CLSM images of cellular internalization of free obatoclax in HeLa cells at 1h and 3h. Nucleus and lysosomal compartments were stained by DAPI (blue) and LysoTracker (green) dyes. Overlap of blue and red fluorescence yielded purple color showed TOS-TPP-Obt-NPs localized into nucleus. Merging of green and red lead to yellow color showed the localization of TOS-TPP-Obt-NPs in lysosomes. Scale bar = 10 μ m.

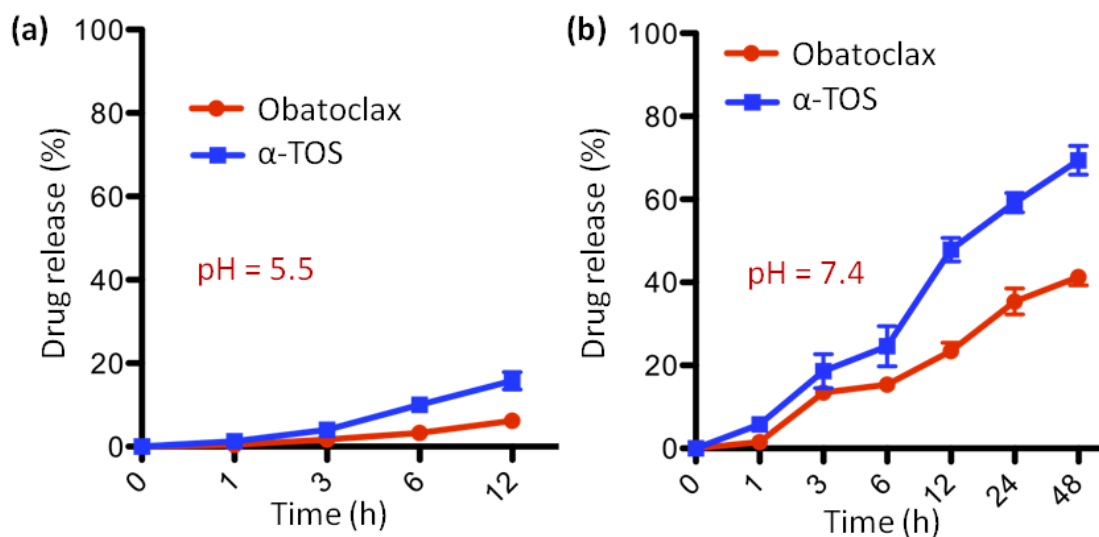


Figure 8. Release of obatoclax and α -TOS from TOS-TPP-Obt-NPs at (a) pH = 5.5 mimicking lysosomes and at (b) pH = 7.4 mimicking mitochondrial environment at different time points. All the data presented were calculated as mean \pm SEM (n = 3).

To be effective in mitochondria targeting, the TOS-TPP-Obt-NPs should not release their payloads in lysosomal acidic environment. Therefore, we evaluated the release profile of dual

drugs from the nanoparticles at pH = 5.5 (absence of ions/salts and serum mimicking protein) which mimics the lysosomes. We incubated TOS-TPP-Obt-NPs in pH = 5.5 buffer and quantified the release of obatoclax and α -TOS at 1 h, 3 h, 6 h and 12 h time points. We calculated the amount of drug released in each time points by UV-Vis spectroscopy at $\lambda_{\text{max}} = 287$ nm (for α -TOS) and $\lambda_{\text{max}} = 488$ nm (for obatoclax) (**Figure 8**). Interestingly, at 6 h, only 3.27 ± 0.43 % obatoclax and 10.03 ± 1.52 % α -TOS were released (**Figure 8**). Moreover, at 12 h, only 6.20 ± 1.0 % and 15.78 ± 2.09 % of obatoclax and α -TOS were found to be released respectively. This release kinetics data obviously demonstrated that very less amounts of dual drugs were released in lysosomes even after 12 h, which would lead to deployment of the major amount of drugs into mitochondria. All the data presented here were determined to be as mean \pm SEM (n = 3).

2.2.3 Mechanism of endocytosis. The cells can engulf different molecules through myriad of endocytosis mechanisms.³⁰ To evaluate the mechanism of cellular internalization we treated the HeLa cells with caveolae-mediated endocytosis inhibitor (genistein), clathrin-mediated endocytosis inhibitor (chlorpromazine) and macropinocytosis inhibitor (amiloride) for 30 min followed by treatment with TOS-TPP-Obt-NPs for 2 h. We have incubated the inhibitor treated cells with TOS-TPP-Obt-NPs for 2 h as we have observed that the highest amount of internalization of nanoparticles occurred within 1 h to 3 h. We evaluated the cellular internalization of TOS-TPP-Obt-NPs by CLSM. **Figure 9a** demonstrated that chlorpromazine and genistein pre-treated cells endocytosed TOS-TPP-Obt-NPs in the same extent as non-inhibitor treated control cells and localized into lysosomes (yellow color formed from overlapping of green and red color). However, amiloride treated cells internalized the TOS-TPP-Obt-NPs significantly less compared to the non-inhibitor treated control cells. Further quantification through Pearson's coefficient and Mander's coefficients from CLSM images revealed that amiloride treated cells lead to remarkable reduction of volume of overlapping to 26.8% compared to 76.4 %, 65.5 % and 68.8 % for genistein treated, chlorpromazine treated and no-inhibitor treated control cells (**Table 2**). The nanoparticles due to its size range in around approximately above 150 nm are generally endocytosed by macropinocytosis . These CLSM

images and quantification unambiguously confirmed that TOS-TPP-Obt-NPs internalized into the lysosomes through macropinocytosis mediated endocytic mechanism.

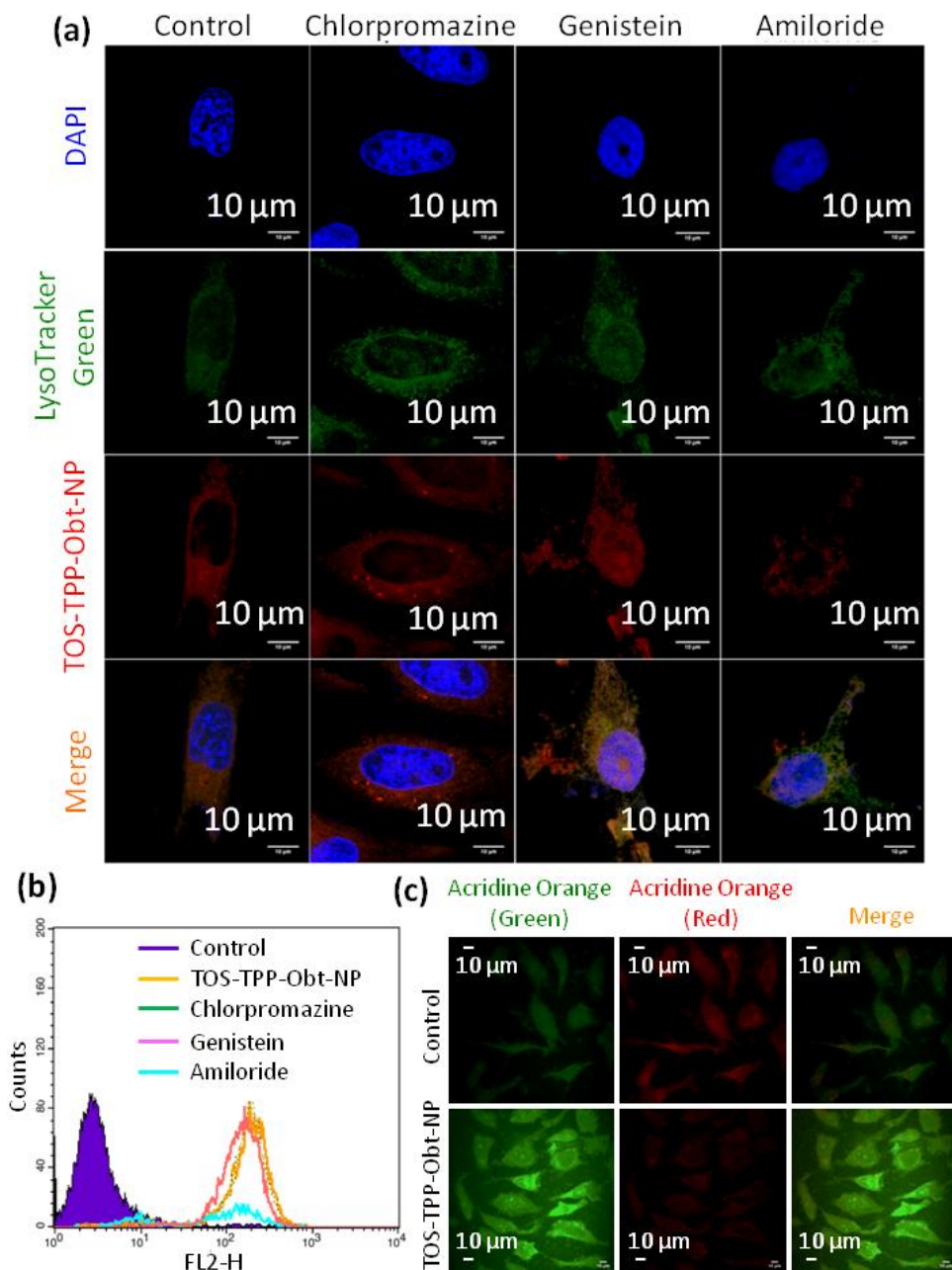


Figure 9. (a) Confocal laser scanning microscopy images of HeLa cells pre-treated with chlorpromazine, genistein and amiloride followed by treatment with TOS-TPP-Obt-NPs. Nucleus and lysosomes were stained by DAPI (blue) and LysoTracker (green) dyes. Scale bar = 10 μm. (b) Fluorescence activated cell sorting analysis of HeLa cells pre-treated with chlorpromazine, genistein and amiloride followed by treatment with TOS-TPP-Obt-NPs. (c)

Acridine orange assay in HeLa cells after treatment with TOS-TPP-Obt-NPs which showed much increased green/red ratio compared to non-nanoparticle treated control cells. Scale bar = 10 μm .

We further pre-treated the HeLa cells with genistein, chlorpromazine and amiloride for 30 min followed by TOS-TPP-Obt-NPs for 2 h and evaluated the number of fluorescently labelled cells by fluorescence activated cell sorting (FACS) method (**Figure 9b**). The FACS data clearly demonstrated that the number of fluorescently labeled cells was significantly reduced in amiloride pre-treated cells, whereas the number of cells was negligibly different in genistein treated and chlorpromazine treated cells compared to non-inhibitor treated cells or non-nanoparticle treated cells as control. This FACS data obviously supported the mechanism of endocytosis determined by CLSM images.

Treatment Time		Control	Genistein	Chlorpromazine	Amiloride
Image Channels		C2(green) C3 (red)	C2(green) C3 (red)	C2(green) C3(red)	C2(green) C3 (red)
Pearsons' Correlation Coefficient	r	0.52	0.3570	0.5109	0.7797
Manders Coefficients	M1 (fraction of C2 overlapping C3)	0.8578	0.9539	0.8664	0.4010
	M2 (fraction of C3 overlapping C2)	0.9355	0.9607	0.8871	0.8750
Percent volume colocalized		68.81%	76.39%	65.56%	26.77%

Table 2: Quantification of localization of TOS-TPP-Obt-NPs into HeLa cells in presence of different endocytosis pathway inhibitors.

After accumulating into the acidic lysosomes, the TOS-TPP-Obt-NPs must escape lysosomes before trafficking to mitochondria. To evaluate the lysosomal permeabilization, we treated the

HeLa cells with TOS-TPP-Obt-NPs for 12 h followed by acridine orange dye and imaged the cells by CLSM. Acridine orange is a lipophilic amine dye, which shows red color while inside the intact lysosomes in acidic condition. However, after lysosomes are permeabilized, acridine orange releases into the cytosol leading to the change in its color from red to green.³¹ Post-treatment of HeLa cells with TOS-TPP-Obt-NPs showed much intense increase in green fluorescence than red fluorescence compared to the non-nanoparticle treated control cells (**Figure 9c**). This acridine orange assay clearly delineated that TOS-TPP-Obt-NPs induced degradation of lysosomal integrity after 12 h.

2.2.4 Mitochondria localization. After lysosomal escape, the TOS-TPP-Obt-NPs should be trafficked to mitochondria to deliver their payloads. To visualize the localization into mitochondria, we treated HeLa cells with TOS-TPP-Obt-NPs for 12 h and 24 h followed by staining the mitochondria with MitoTracker green dye. We imaged the cells by CLSM. **Figure 10a** exhibited that the red fluorescent TOS-TPP-Obt-NPs co-localized into green fluorescent-tagged mitochondria leading to merge yellow color in both 12 h and 24 h time points. Pearson's coefficient and Mander's coefficients based quantification of volume of co-localization demonstrated 77.5 % and 75.6 % overlapping regions in 12 h and 24 h time points which corroborated that TOS-TPP-Obt-NPs localized into mitochondria over 24 h (**Table 3**).

To further confirm the localization of TOS-TPP-Obt-NPs into mitochondria, we treated the HeLa cells with the nanoparticles for 24 h (as substantial amount of nanoparticles accumulated into mitochondria at 24 h) and isolated the mitochondria using mitochondria isolation kit.³² As control we isolated the mitochondria from non-nanoparticle treated HeLa cells. We evaluated the presence of red fluorescent obatoclax into mitochondria by flow cytometry analysis. The FACS data in **Figure 10b** demonstrated remarkable increase in red fluorescent intensity in mitochondria compared to non-treated control cells due to the accumulation of TOS-TPP-Obt-NPs into mitochondria. From these CLSM and FACS analysis, it was apparent that TOS-TPP-Obt-NPs successfully trafficked into mitochondria in time dependent manner over 24 h. After being localized into the mitochondria, the TOS-TPP-Obt-NPs should release their cargoes at pH = 7.4 (absence of ions/salts and serum mimicking protein) which mimics the mitochondrial outer membrane.³³ Hence, we incubated TOS-TPP-Obt-NPs at pH = 7.4 buffer and quantified the

release of obatoclax ($\lambda_{\max} = 488 \text{ nm}$) and α -TOS ($\lambda_{\max} = 287 \text{ nm}$) by UV-Vis spectroscopy at different time points. We found that after localization into mitochondria at 12 h, $23.48 \pm 1.95 \%$ and $47.91 \pm 2.8 \%$ obatoclax and α -TOS were released respectively (**Figure 8b**).

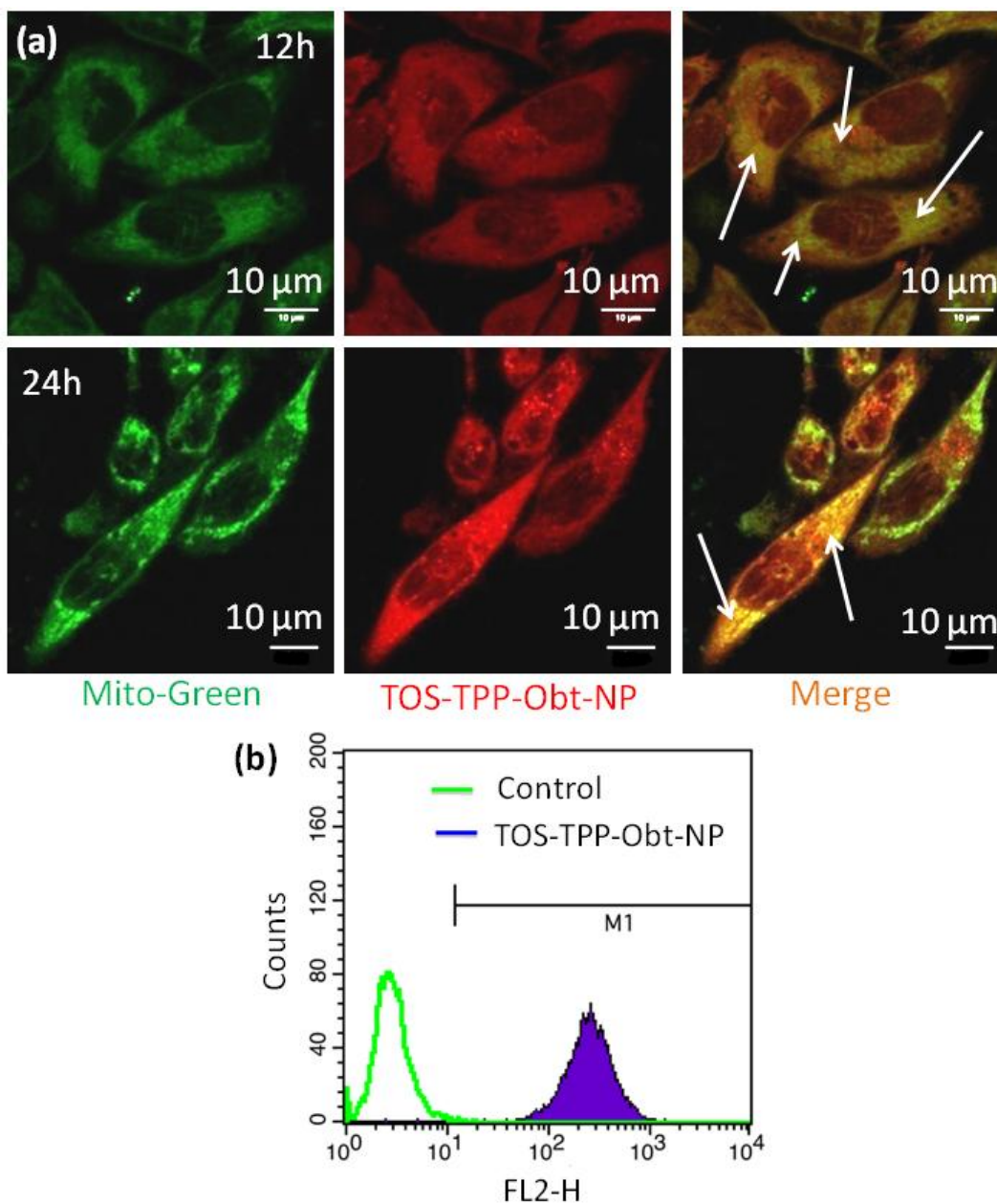


Figure 10. (a) Confocal microscopy images of HeLa cells showing the homing of TOS-TPP-Obt-NPs into mitochondria for 12 h and 24 h time points. Mitochondria were stained with MitoTracker green dyes. The yellow regions in the merged images indicate the co-localization of TOS-TPP-Obt-NPs in mitochondria. Scale bar = 10 μm . (b) Flow cytometry analysis of

mitochondria fraction isolated from HeLa cells after treatment with TOS-TPP-Obt-NPs for 24 h showing the localization of red fluorescent obatoclax into mitochondria.

Treatment Time		12 h	24h
Image Channels		C2(green) C3(red)	C2(green) C3(red)
Pearsons' Correlation Coefficient	r	0.82	0.6115
Manders Coefficient	M1 (fraction of C2 overlapping C3)	0.9686	0.9395
	M2 (fraction of C3 overlapping C2)	1.0	0.9183
Percent volume colocalized		77.49%	75.65%

Table 3: Quantification of co-localization of TOS-TPP-Obt-NPs into mitochondria in HeLa cells by CLSM

We also observed that at 24 h, substantial amount of obatoclax (35.41 ± 3.15 %) and α -TOS (59.17 ± 2.32 %) were released from the nanoparticles into mitochondria. Furthermore, highest amount of obatoclax (41.25 ± 1.9 %) and α -TOS ($69.38 \pm 3.4\%$) were released from TOS-TPP-Obt-NPs at pH = 7.4 at 48 h. This release experiment evidently showed that significantly high amount of dual drugs were released after localization of TOS-TPP-Obt-NPs into mitochondria at 12 h, 24 h and 48 h due to diffusion controlled release, which would lead to the effective inhibition of multiple mitochondrial targets. **The sequential release of both the drugs cannot be controlled.** All the data presented here were determined to be as mean \pm SEM (n = 3).

2.2.5 Mitochondrial outer membrane permeabilization. After trafficking into mitochondria and successfully released their dual drugs, we further investigated the effect of TOS-TPP-Obt-NPs on mitochondrial membrane potential ($\Delta\psi_m$) using a cationic dye 5,5',6,6'-tetrachloro-1,1',3,3' tetraethylbenzimidazolylcarbocyanine iodide (JC1). JC1 shows potential reliant accumulation in the mitochondria with fluorescent emission alteration from green (~ 525 nm) to red (~ 590 nm) due to formation of red fluorescent J-aggregates. Mitochondrial depolarization

can be measured by the increase in the ratio of green/red fluorescent intensity.³⁴ HeLa cells were treated with TOS-TPP-Obt-NPs for 24 h followed by staining with JC1 and the live cells were imaged by CLSM. **Figure 11a** revealed significant increase in green/red ratio (green: red = 3.44 ± 0.06) in TOS-TPP-Obt-NP treated cells compared to much less green/red ratio (green: red = 1.27 ± 0.01) in the non-nanoparticle treated control cells as well as only free obatoclox treated cells (green: red = 1.89 ± 0.08) (**Figure 12 and 11b**). This JC1 assay exhibited that TOS-TPP-Obt-NPs induced mitochondrial depolarization much significantly (2 times more) compared to free obatoclox.

Mitochondrial depolarization results the opening of mitochondrial permeability transition pores (MTP). We further evaluated the opening of MTPs by Calcein *O,O'*-diacetate tetrakis (acetoxymethyl) ester (Calcein AM) dye.³⁵ Calcein AM passively diffuses into the cells and accumulates into cytosol and mitochondria. Inside cells, esterases cleave the ester functionality leading to the release of green fluorescent calcein dye, which is quenched by addition of CoCl_2 , whereas mitochondrial Calcein AM remains intact. After opening of MTPs, mitochondrial Calcein AM will be released into cytosol leading to conversion into fluorescent Calcein. We treated HeLa cells with TOS-TPP-Obt-NPs for 24 h, followed by treatment with calcein AM and CoCl_2 . The live cells were visualized by confocal microscopy. As control, we treated HeLa cells with Calcein AM and CoCl_2 without any nanoparticles. CLSM images in **Figure 11c** clearly confirmed that TOS-TPP-Obt-NPs induced opening of mitochondrial transition pores leading to increase in green fluorescence intensity compared to no-nanoparticle treated control cells. This Calcein AM assay demonstrated that TOS-TPP-Obt-NPs induced permeabilization of mitochondrial outer membrane (MOMP).

Mitochondrial outer membrane permeabilization leads to the release of cytochrome c from inter membrane space (IMS).⁵ To visualize the cytochrome c release after mitochondrial damage, we treated HeLa cells with TOS-TPP-Obt-NPs for 24 h. The cells were then stained with cytochrome c antibody tagged with green fluorescent dye Alexa Fluor 488 and imaged through CLSM. **Figure 11d** explicitly showed highly increased expression of cytochrome c in TOS-TPP-Obt-NPs treated cells compared to the non-nanoparticle treated cells. Hence, from these experiments it was confirmed that after localization into mitochondria and releasing dual drugs

after 24 h, TOS-TPP-Obt-NPs triggered mitochondrial depolarization, followed by opening of mitochondrial transition pores leading to release of cytochrome c as pro-apoptotic molecule.

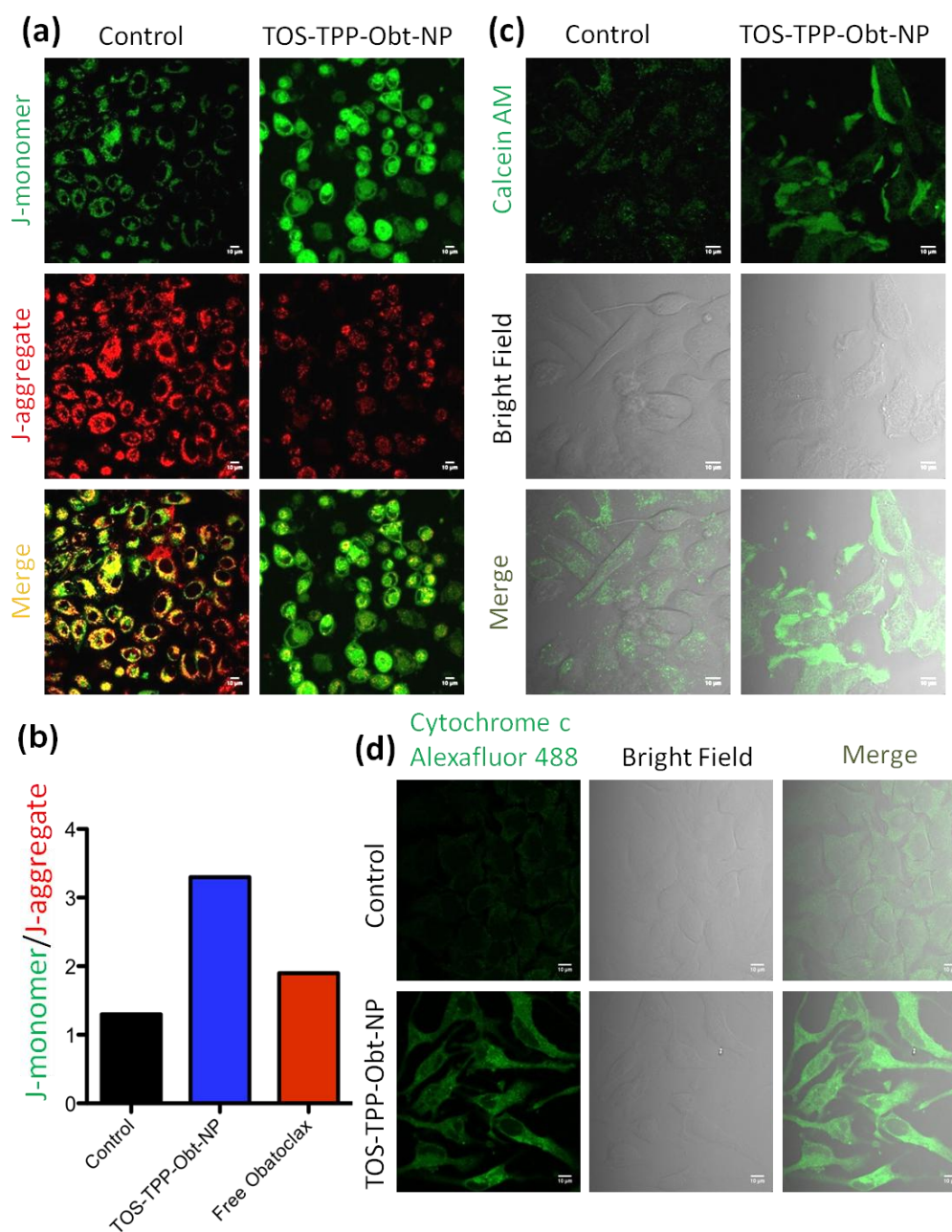


Figure 11. (a) Confocal images of HeLa cells treated with TOS-TPP-Obt-NPs followed by JC1 dye to observe mitochondrial depolarization compared to control cells. The green and red colors were generated by JC1 dye in monomeric and aggregated forms respectively. (b) J-monomer/J-aggregate quantification of TOS-TPP-Obt-NPs in HeLa cells compared to free obatoclax and

non-treated control cells. (c) Confocal images of HeLa cells stained with green fluorescent calcein AM for mitochondrial transition pore (MTP) opening induced by TOS-TPP-Obt-NPs. (d) CLSM images of HeLa cells treated with TOS-TPP-Obt-NPs for 24 h. Cells were stained with cytochrome c Alexa Fluor 488 antibody (green). Scale bar = 10 μm .

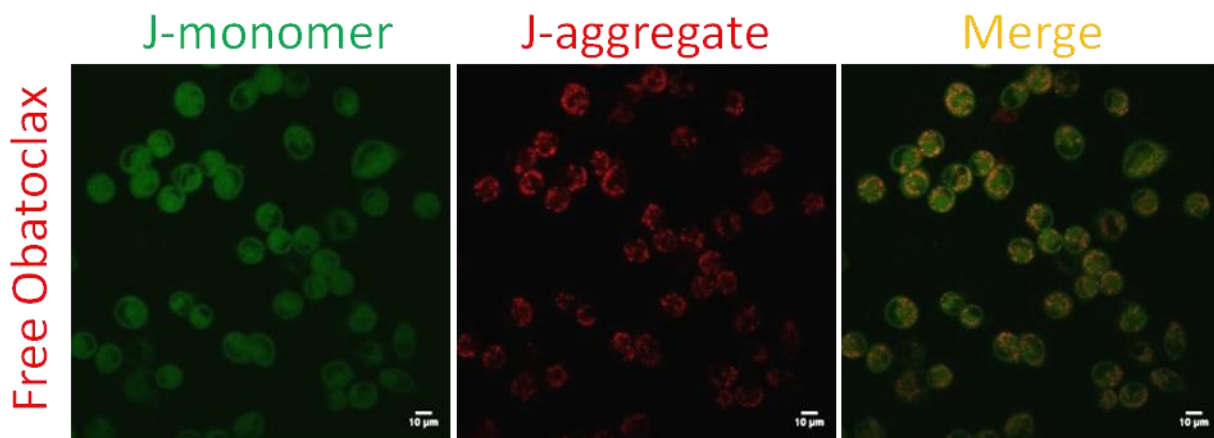


Figure 12. CLSM images of J-monomer and J-aggregate in free obatoclax treated HeLa cells.

2.2.6. Cytotoxicity, apoptosis and mechanism. Mitochondrial outer membrane permeabilization (MOMP) and release of cytochrome c as pro-apoptotic molecule induce apoptosis leading to the cellular death.⁵ To understand the effect of nanoparticle mediated mitochondrial damage in cancer cells, we treated HeLa cells by TOS-TPP-Obt-NPs for 24 h and 48 h evaluated the cell viability by MTT assay. As a control, we treated the cells with free α -TOS and free obatoclax in combination present in the nanoparticle formulation. At 24 h, TOS-TPP-Obt-NPs demonstrated much lower $\text{IC}_{50} = 6.30 \pm 0.22 \mu\text{M}$ (cell viability = $40.4 \pm 2.7 \%$ at $25 \mu\text{M}$ concentration of obatoclax) compared to $\text{IC}_{50} = 13.09 \pm 0.48 \mu\text{M}$ (cell viability = $42.37 \pm 1.54 \%$ at $25 \mu\text{M}$ concentration of obatoclax) for free drug cocktail (**Figure 14a**). Also, at 48 h, TOS-TPP-Obt-NPs showed even more improved efficacy of $\text{IC}_{50} = 3.7 \pm 0.07 \mu\text{M}$ compared to $\text{IC}_{50} = 6.7 \pm 0.1 \mu\text{M}$ for free drugs combination (**Figure 13a**). Moreover, TOS-TPP-Obt-NPs induced more cancer cell death (cell viability = 11% at $25 \mu\text{M}$ concentration of obatoclax) compared to free drug combination in the same α -TOS/obatoclax ratio (cell viability = 14% at $25 \mu\text{M}$ concentration of obatoclax). We rationalized that TOS-TPP-Obt-NPs showed much improved effect in cell death at 48 h compared to 24 h due to their improved accumulation in mitochondria at 48 h as well as the enhanced release of dual drugs at 48 h at $\text{pH} = 7.4$ compared to 24 h. In

addition, at 24 h, the nanoparticles started to accumulate into the mitochondria which would take another 24 h to release considerable amount of drugs into mitochondria for enhanced efficacy at 48 h (**Figure 8b**). We also evaluated the effects of free α -TOS, free α -TOS-TPP and free obatoclox in HeLa cells by MTT assay after 48 h of incubation. Free α -TOS, free α -TOS-TPP and free obatoclox illustrated much higher $IC_{50} = 25.26 \pm 2.96 \mu\text{M}$, $33.97 \pm 0.87 \mu\text{M}$ and $13.38 \pm 0.2 \mu\text{M}$ respectively (**Figure 14 b-d**). These cell viability data clearly delineated that dual drug loaded TOS-TPP-Obt-NPs were much more efficacious compared to free single drug treatments as well as drug combinations. All the data presented here were calculated as mean \pm SEM (n = 3).

To investigate the mechanism triggering HeLa cell death, we evaluated the induction of apoptosis by TOS-TPP-Obt-NPs by FACS analysis. We treated the cells with TOS-TPP-Obt-NPs in their IC_{50} value for 24 h followed by staining the externalized phosphatidylserine in the apoptotic cell surface by green fluorescent Annexin V-FITC. We counter stained the cells by red fluorescent propidium iodide (PI) to differentiate apoptotic and necrotic cells. Indeed, TOS-TPP-Obt-NPs induced early apoptosis in 61.3 % cells and late apoptosis in 17.4 % cells compared to 1.8 % and 0.1 % cells were found in early and late apoptotic stages in non-treated control cells (**Figure 14b**). Hence, it was evident that TOS-TPP-Obt-NPs induced early apoptosis leading to the cell death in HeLa cells.

Obatoclox inhibits anti-apoptotic Bcl-2 in its BH3 domain, triggers the polymerization of BAK-BAX leading to MOMP.²⁰ To evaluate the effect of TOS-TPP-Obt-NPs on Bcl-2, we treated HeLa cells with mitochondria targeting nanoparticles for 24 h and evaluated the expression of Bcl-2 by western blot analysis. **Figure 13c** demonstrated that TOS-TPP-Obt-NPs successfully inhibited Bcl-2 expression (2.2 folds reduction, **Figure 15a**) on mitochondrial outer membrane to induce MOMP. Activating MOMP through Bcl-2 inhibition, followed by cytochrome c release triggers initiator caspase-9 which upon cleavage activates executioner caspase-3 leading to cellular apoptosis through intrinsic mechanism.^{36,37} To evaluate the effect of MOMP in apoptosis, we treated the cells with TOS-TPP-Obt-NPs for 24 h and evaluated the expression of pro-caspase-9, cleaved caspase-3 and pro-caspase-3 by western blot analysis. Fig. 13c, showed the reduction of expression of pro-caspase-9 (2.1 folds, **Figure 15b**) and pro-caspase-3 (1.9 folds, **Figure 15d**) in TOS-TPP-Obt-NPs treated cells compared to no-treated control cells. On

the other hand, the expression of cleaved caspase-3 was increased (1.9 folds, **Figure 15c**) in TOS-TPP-Obt-NPs treated cells compared to control cells (**Figure 13c**). From this western blot analysis,

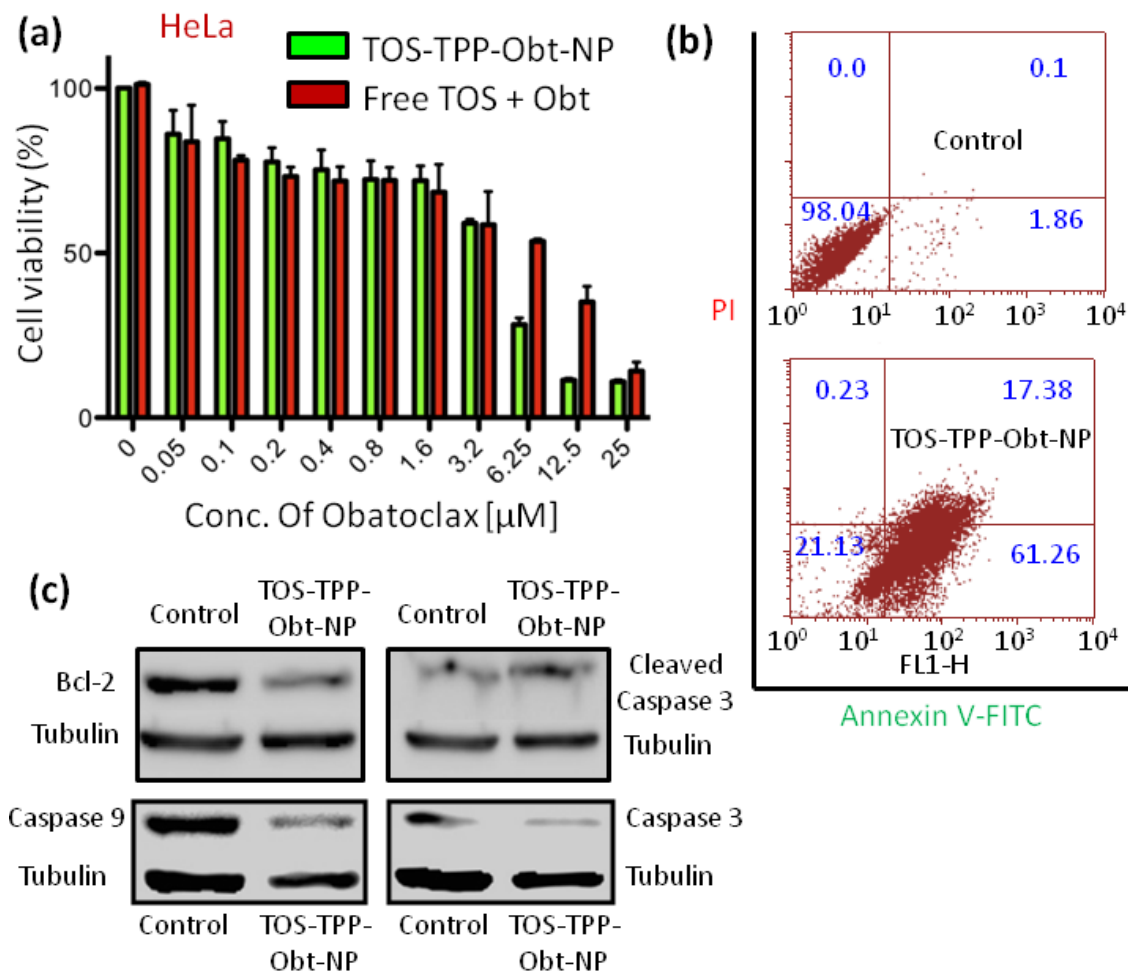


Figure 13. (a) Cell viability assay of TOS-TPP-Obt-NPs in HeLa cells after 48 h incubation respectively ($p < 0.001$, Two-way ANOVA test). (b) Flow cytometric analysis of apoptosis induced by TOS-TPP-Obt-NPs in HeLa cells. Lower left, lower right, upper right and upper left quadrants represent the % of healthy, early apoptotic, late apoptotic and necrotic cells after treatment with TOS-TPP-Obt-NPs for 24 h. (c) Western blot analysis to visualize the expression of Bcl-2, caspase-9, cleaved caspase-3 and caspase-3 after treatment of HeLa cells with TOS-TPP-Obt-NPs for 24 h.

it was evident that TOS-TPP-Obt-NPs inhibited Bcl-2 on mitochondrial outer membrane leading to apoptosis through caspase-9 and caspase-3 mediated intrinsic mechanism

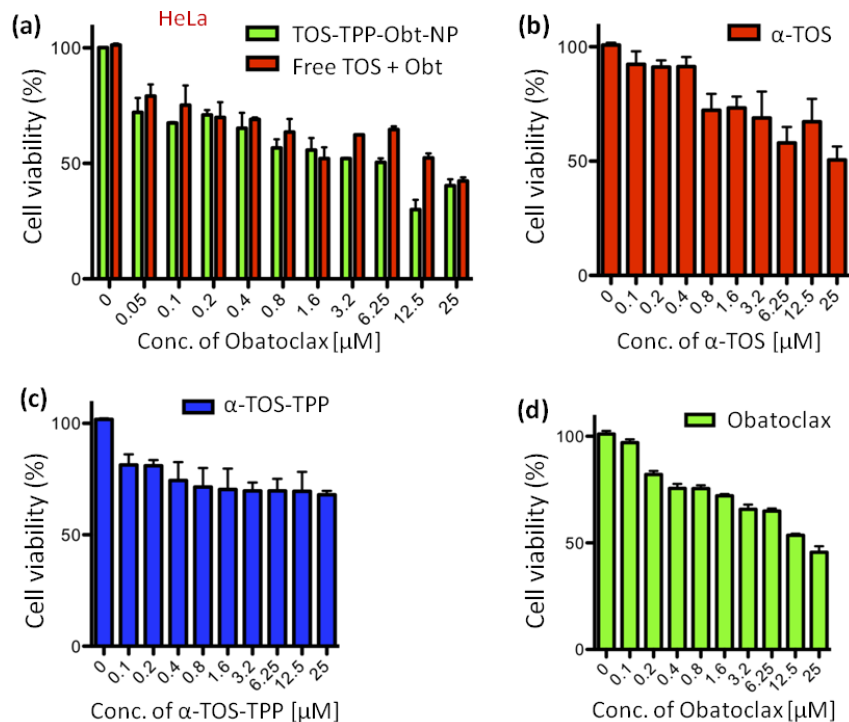


Figure 14. Cell viability determination by MTT assay in HeLa cells treated by (a) TOS-TPP-Obt-NPs and free drug combinations for 24 h, (b) free α -TOS for 48 h, (c) free α -TOS-TPP conjugate for 48 h and (d) free obatoclax for 48 h.

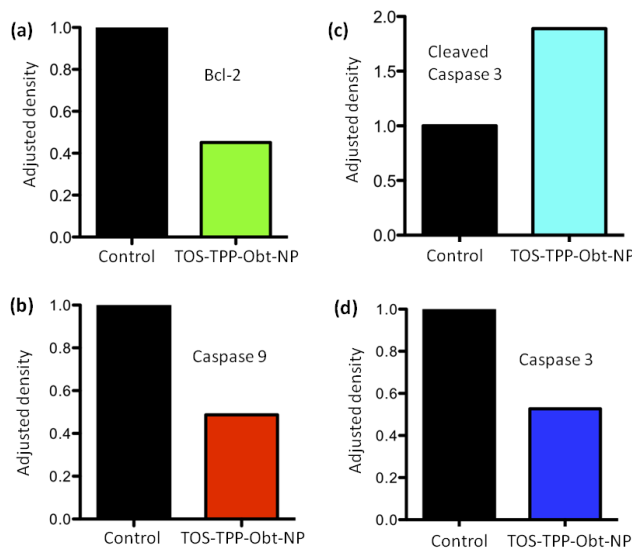


Figure 15: Quantification of (a) Bcl-2 (b) caspase-9 (c) cleaved caspase-3 and (d) caspase-3 expressions in HeLa cells after treatment with TOS-TPP-Obt-NPs for 24 h from western blot.

2.2.7 Mitochondria targeting and cytotoxicity in drug resistant cancer cell. One of the major advantages to target mitochondrial proteins and genomic materials by conventional chemotherapeutic drugs is to overcome the emergence of drug resistance.³⁸⁻⁴⁰ Hence, we evaluated the effect of TOS-TPP-Obt-NPs in drug resistant MDA-MB-231 triple negative breast cancer cells. To visualize the co-localization of TOS-TPP-Obt-NPs in mitochondria, we treated MDA-MB-231 cells with the nanoparticles for 12 h and 24 h time points, followed by staining the mitochondria with MitoTracker green dye and imaged the cells by CLSM. The emergence of yellow color by overlapping green and red fluorescent in **Figure 16a** explicitly demonstrated that TOS-TPP-Obt-NPs homed into mitochondria in a time dependent manner over 24 h. Furthermore, quantification of percent volume co-localization by Pearsons' Correlation Coefficient and Manders Coefficients revealed that 13.55 % and 59.49 % co-localization of TOS-TPP-Obt-NPs took place in mitochondria at 12 h and 24 h time points respectively (Table 4).

To assess the effect of TOS-TPP-Obt-NPs in mitochondrial membrane potential, we treated the MDA-MB-231 cells with the nanoparticles for 24 h and stained the cells with JC1 dye. The live cells were visualized by confocal microscopy. **Figure 16b** confirmed substantial increase in green/red ratio (green: red = 2.95 ± 0.07) in TOS-TPP-Obt-NP treated cells compared to much decreased green/red ratio (green: red = 0.85 ± 0.04) in the non-nanoparticle treated control cells as well as only free obatoclax treated cells (green: red = 0.58 ± 0.04) (**Figure 17 a-b**).

Finally, we evaluated the efficacy of TOS-TPP-Obt-NPs in drug resistant triple negative breast cancer MDA-MB-231 cells. We treated the cells with TOS-TPP-Obt-NPs in a dose dependent manner at 48 h and quantified the cell viability by MTT assay. TOS-TPP-Obt-NPs showed $IC_{50} = 1.06 \pm 0.06 \mu\text{M}$ comparable to $IC_{50} = 0.78 \pm 0.17 \mu\text{M}$ for free drug combination (**Figure 16c**). Furthermore, TOS-TPP-Obt-NPs induced much less cell viability ($3.2 \pm 1.8 \%$ in $25 \mu\text{M}$ concentration of obatoclax) compared to the cell viability ($35.4 \pm 7.0 \%$ at $25 \mu\text{M}$ concentration of obatoclax) induced by the free drug cocktails. More interestingly, TOS-TPP-Obt-NPs showed much improved efficacy in drug resistance triple negative breast cancer MDA-MB-231 cells ($IC_{50} = 1.06 \pm 0.06 \mu\text{M}$) compared to drug sensitive cervical cancer HeLa cells ($IC_{50} = 3.7 \pm$

0.07 μM) (**Figure 16c**) at 48 h. We anticipate that our TOS-TPP-Obt-NPs would target Bcl-2 in mitochondria very specifically in cancer cells. It is well know that, Bcl-2 can be localized into

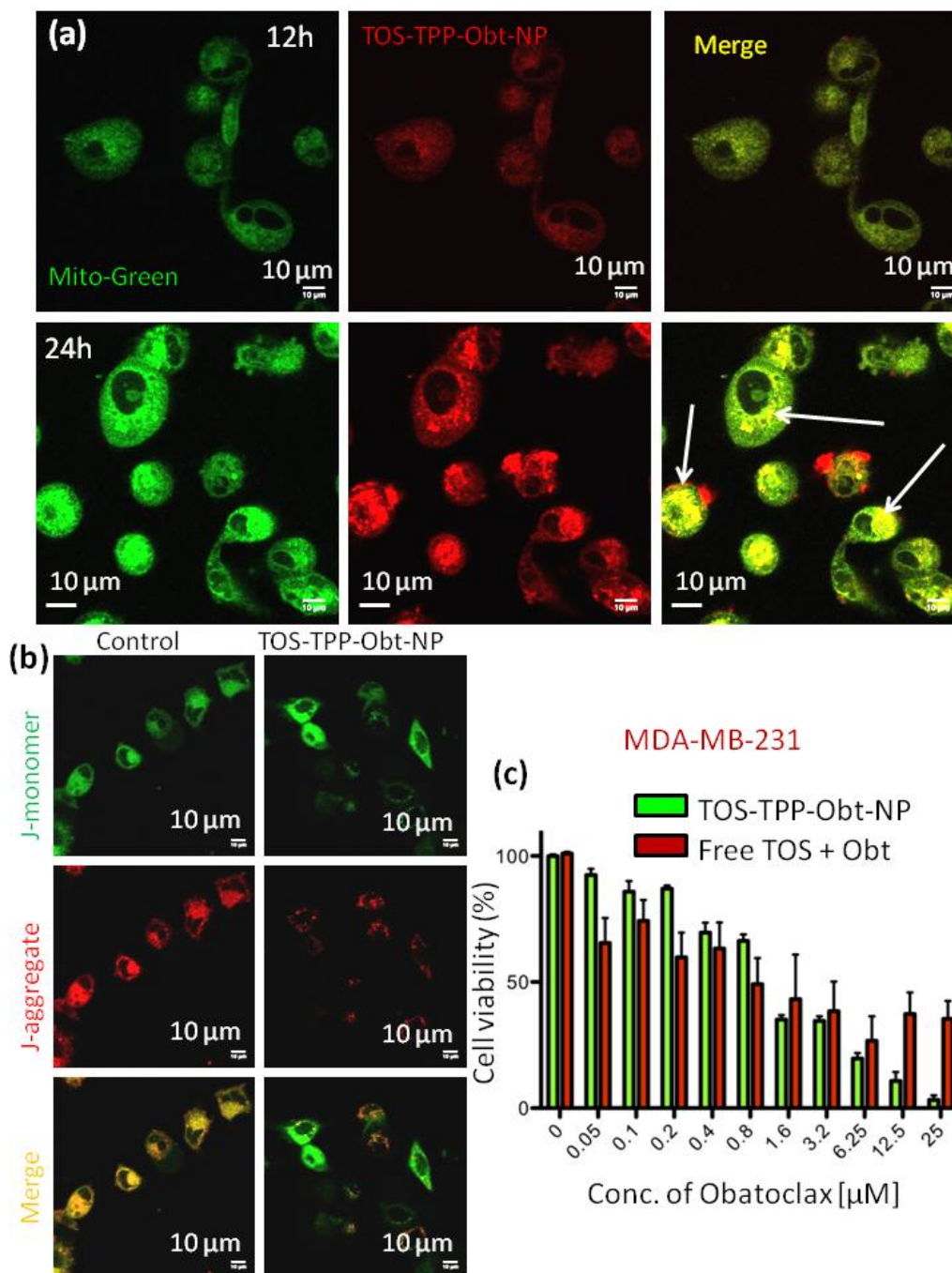


Figure 16. (a) Confocal microscopy images of MDA-MB-231 cells showing the homing of TOS-TPP-Obt-NPs into mitochondria for 12 h and 24 h time points. Mitochondria were stained with MitoTracker green dyes. The yellow regions in the merged images indicate the co-localization of TOS-TPP-Obt-NPs and mitochondria. Scale bars: 10 μm . (b) Confocal microscopy images of MDA-MB-231 cells showing the homing of TOS-TPP-Obt-NPs into mitochondria for 12 h and 24 h time points. Mitochondria were stained with MitoTracker green dyes. The yellow regions in the merged images indicate the co-localization of TOS-TPP-Obt-NPs and mitochondria. Scale bars: 10 μm . (c) Bar graph showing Cell viability (%) versus Conc. of Obatoclax [μM] for MDA-MB-231 cells. The legend indicates TOS-TPP-Obt-NP (green) and Free TOS + Obt (red). Error bars represent standard deviation.

localization of TOS-TPP-Obt-NPs in mitochondria. (b) Confocal images of MDA-MB-231 cells treated with TOS-TPP-Obt-NPs followed by JC1 dye to observe mitochondrial depolarization compared to control cells. The green and red colors were generated by JC1 dye in monomeric and aggregated forms respectively. (c) Cell viability assay of TOS-TPP-Obt-NPs in MDA-MB-231 cells after 48h incubation respectively ($p < 0.001$, Two-way ANOVA test).

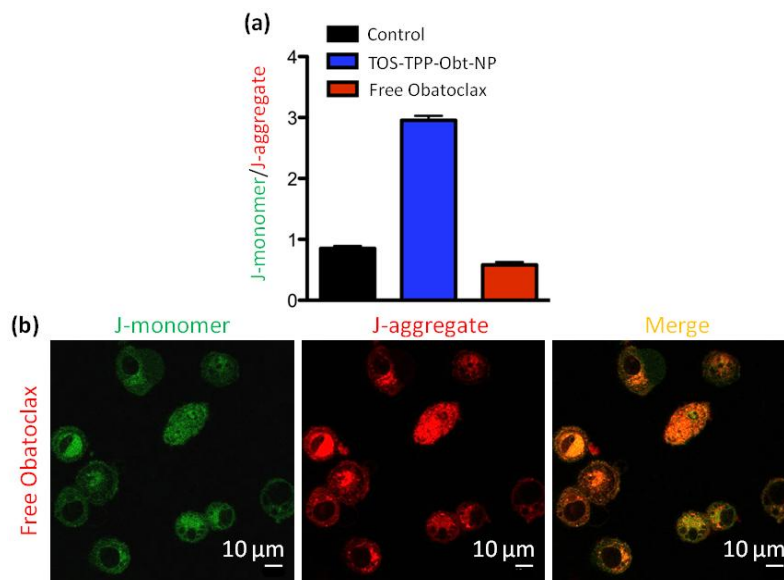


Figure 17. (a) J-monomer/J-aggregate quantification of TOS-TPP-Obt-NPs in MDA-MB-231 cells compared to free obatoclox and non-treated control cells. (b) CLSM images of J-monomer and J-aggregate in free obatoclox treated MDA-MB-231 cells.

Treatment Time		12 h	24h
Image Channels		C2(green) C3(red)	C2(green) C3(red)
Pearsons' Correlation Coefficient	r	0.753	0.4774
Manders Coefficient	M1 (fraction of C2 overlapping C3)	0.6693	0.8901
	M2 (fraction of C3 overlapping C2)	0.3354	0.8277
Percent volume colocalized		13.55%	59.49%

Table 4 :Quantification of co-localization of TOS-TPP-Obt-NPs into mitochondria in MDA-MB-231 cells by CLSM.

mitochondrial outer membrane, nuclear envelop and endoplasmic reticulum to have diverse functions.⁴¹ Our novel TOS-TPP-Obt-NPs showed advantage over free drugs (**Figure 16c**) to target specifically mitochondrial Bcl-2 without inhibiting them in other sub-cellular compartments. This nanoparticles mediated spatial targeting of Bcl-2 in mitochondria would reveal interesting properties and behavior in cancer cells. We also envision that, TOS-TPP-Obt-NPs would show much improved efficacy in *in vivo* models to increase the effective drug loading inside the tumor tissue hence increasing maximum tolerated dose (MTD), whereas free drug combination at higher concentration would lead off-target systemic toxicity.¹⁸ Finally from these cell viability and apoptosis assay, it was clear that TOS-TPP-Obt-NPs showed much-improved efficacy in cervical cancer cells as well as drug-resistant triple negative breast cancer cells compared to free drug combination through the induction of apoptosis.

2.3. Conclusion

In conclusion, we have developed a novel dual-drug loaded nanoparticle entity with positive surface charge for specific targeting of mitochondria in cancer cell. The so called spherical TOS-TPP-Obt-NPs are expected to be accumulated into the tumor tissues through unique enhanced permeability and retention effect. These NPs were found to be endocytosed into the cancer cells by macropinocytosis followed by localization into mitochondria in time dependent manner. In mitochondria, TOS-TPP-Obt-NPs triggered mitochondrial outer membrane permeabilization (MOMP) by inhibiting anti-apoptotic Bcl-2. This nanoparticle targeted mitochondrial damage lead to higher cancer cell death through caspase-9 and caspase-3 mediated apoptosis. We envision that the here presented unique approach can be easily translated into clinics as a platform technology to inhibit multiple diverse targets concurrently into mitochondria, improve the therapeutic efficacy, reduce the off-target toxicity, overcome drug resistance and finally, offer better quality of life to the cancer patients.

2.4. Materials and methods

2.4.1 Materials: Solvents, α -tocopherol succinate, 5-bromopentanol, triphenylphosphine, Calcein AM, cobalt(II) chloride (CoCl_2), chlorpromazine, amiloride, genistein, L- α -phosphatidylcholine (PC), sephadex G-25, sodium dodecyl sulfate (SDS), Hanks' balanced solution without phenol red and sodium bicarbonate, 4-(2-Hydroxyethyl)piperazine-1-ethanesulfonic acid sodium salt (HEPES), acridine orange, lab tek chamber slide 8 wells, 5,5',6,6'-tetrachloro-1,1',3,3'-tetraethylbenzimidazolylcarbocyanine iodide (JC 1 dye) and silicon wafer for field emission scanning electron microscopy (FE-SEM) were bought from Sigma-Aldrich. Obatoclox mesylate was bought from Selleck Chemicals. 1,2-Distearoyl-*sn*-Glycero-3-Phosphoethanolamine-N-[Amino(Polyethylene Glycol)2000] (DSPE-PEG) and the mini handheld extruder kit (including 0.2 nm Whatman Nucleopore Track-Etch Membrane, whatman filter supports and 1.0 mL Hamiltonian syringes) were bought from Avanti Polar Lipids Inc. Dulbecco's Modified Eagle's Medium (DMEM) and 3-(4,5-dimethylthiazol-2-yl)-2,5-diphenyltetrazolium bromide (MTT), propidium iodide and 4',6-Diamidino-2-phenylindole dihydrochloride (DAPI) were purchased from Gibco. LysoTrackerTM Green DND-153, MitoTracker Green[®] FM, *SlowFade*[®] diamond antifade reagent and were obtained from Life Technologies. HeLa and MDA-MB 231 cells were obtained from National Centre for Cell Science (NCCS), Pune. Primary antibodies: Anti-Caspase-3 antibody, anti-Bcl-2 antibody, Anti-Caspase-9 antibody, Anti-cleaved caspase-3 antibody and Anti tubulin antibody ; Secondary antibodies: HRP Goat anti-rat IgG, HRP Goat anti-mouse IgG, and Annexin V-FITC labeling solution were bought from biolegend. ; Cytochrome c rabbit mAb, anti-rabbit IgG and HRP-linked antibody were obtained from CST. Rabbit anti-chicken IgG antibody and alexa fluor[®] 488 goat anti-rabbit IgG (H+L) antibody were purchased from Life technologies. The mitochondria isolation kit for cultured cells was bought from the Thermo Scientific.

2.4.2 Synthesis of conjugate (2). α -tocopherol succinate (**1**) (200 mg, 0.3773 mmol, 1 equiv.) was dissolved in 3 mL dry dichloromethane (DCM) under inert atmosphere and cooled to 0 °C. Subsequently, N,N'-dicyclohexylcarbodiimide (DCC) (93 mg, 0.4524 mmol, 1.2 equiv) and 4-(dimethylamino) pyridine (DMAP) (22 mg, 0.1885 mmol, 0.5 equiv) were added to the reaction mixture with continuous stirring under inert condition. After 30 min, 5-bromopentanol (91.26 μL , 0.754 mmol, 2 equiv) was added into the reaction mixture. The reaction was monitored by thin layer chromatography (TLC) at room temperature. After 3 h, the reaction was filtered with Whatman filter paper to remove the excess solid dicyclohexylurea (by product). The filtrate was then evaporated using rotary evaporator and the crude product was purified using silica gel (100-

200 mesh size) column chromatography with 1 % ethyl acetate in petroleum ether to obtain the pure compound **2** (Yield = 50.75 %).

2.4.3 Characterization of conjugate 2:

¹H NMR (400 MHz, CDCl₃): δ = 4.11-4.14 (t, 2H, J = 8Hz), 3.37-3.41 (t, 2H, J = 8Hz), 2.92-2.95 (t, 2H, J = 8Hz), 2.76-2.78 (t, 2H, J = 8Hz), 2.57-2.60 (t, 2H, J = 8Hz), 2.09 (s, 3H), 2.02-2.05 (s, 3H), 1.98-1.99 (s, 3H), 1.64-1.91 (m, 7H), 1.47-1.57 (m, 5H), 1.03-1.57 (m, 19H), 0.84-0.88(m, 11H).

¹³C NMR (100 MHz, CDCl₃): δ = 172.18, 170.94, 149.63, 141.27, 126.67, 124.92, 123.03, 117.39, 100.27, 76.73, 75.05, 64.48, 39.40, 37.47, 33.31, 32.72, 32.79, 32.29, 29.17, 27.99, 24.81, 22.73, 21.03, 19.77, 12.94, 11.81.

HR-MS: m/z: for C₃₈H₆₄BrO₅⁺ [M+H]⁺: calculated = 679.3859, observed = 679.3929.

MALDI-TOF: m/z: for C₃₈H₆₃BrO₅Na⁺ [M+Na]⁺: calculated = 701.3859, observed = 701.3763.

m/z: for C₃₈H₆₃BrO₅K⁺ [M+K]⁺: calculate = 717.3859, observed = 717.3459.

2.4.4 Synthesis of TOS-TPP conjugate (3). Conjugate **2** (124 mg, 0.1825 mmol, 1 equiv), triphenylphosphine (95.74 mg, 0.365 mmol, 2 equiv), and 70 mg of potassium carbonate (K₂CO₃) were taken in a round bottom flask, dissolved in 5 mL of acetonitrile (CH₃CN) and refluxed for 24 h. After the reaction was over (monitored by TLC), K₂CO₃ was filtered and rinsed with CH₃CN. The filtrate was evaporated using rotary evaporator and then treated with diethylether to remove the excess triphenylphosphine. The crude product was purified using silica gel column chromatography with 2 % methanol in dichloromethane to obtain the pure compound **3**. (Yield = 35 %).

2.4.5 Characterization of α -tocopheryl succinate-TPP conjugate (3):

¹H NMR (400 MHz, CDCl₃): δ = 7.67-7.85 (m, 15H), 4.05-4.08 (t, 1H), 3.74-3.81 (m, 1H), 2.89-2.92 (t, 1H), 2.68-2.72 (t, 1H), 2.56-2.59 (t, 2H), 1.97-2.07 (m, 7H), 1.65-1.84 (m, 9H), 1.35-1.55 (m, 7H), 1.23-1.30 (m, 18H), 1.04-1.17 (m, 8H), 0.84-0.91 (m, 13H).

¹³C NMR (100 MHz, CDCl₃): δ = 172.15, 171.07, 149.40, 139.25, 134.99, 134.96, 133.70, 133.60, 130.54, 130.42, 126.68, 124.97, 122.94, 118.79, 117.93, 117.38, 75.06, 64.15, 39.37,

37.45, 37.28, 33.80, 32.79, 29.68, 27.96, 24.78, 22.70, 22.61, 19.75, 19.64, 14.09, 12.94, 12.10, 11.80.

^{31}P NMR (CDCl_3): $\delta = 24.29$

HR-MS: m/z: for $\text{C}_{56}\text{H}_{78}\text{O}_5\text{P}^+[\text{M}]^+$: calculated=861.5587, observed= 861.5582

MALDI-TOF: m/z: for $\text{C}_{56}\text{H}_{78}\text{O}_5\text{P}^+[\text{M}]^+$: calculated=861.5587, observed = 861.5600.

2.4.6 Engineering of TOS-TPP-Obt-NPs. 10.0 mg of L- α -phosphatidylcholine (PC), 5.0 mg of α -tocopheryl succinate-TPP conjugate (**3**), 1 mg of 1,2-distearoyl-*sn*-glycero-3-phosphoethanolamine-N-[amino(polyethylene glycol)2000] (DSPE-PEG) and 1 mg of obatoclax (Obt) were dissolved in 5.0 mL DCM. DCM was evaporated thoroughly to form thin uniform lipid film. The obatoclax containing lipid film was aquated with 1 mL water for 1 h at 60 °C. The self-assembled nanoparticles formed were passed through Sephadex G-25 followed by extrusion through Whatmann membrane having 200 nm porosity. The nanoparticles were stored at 4 °C for further use.²⁷

2.4.7 Determination of size, surface charge and shape of α -TOS-TPP-Obt nanoparticles

a. Dynamic light scattering (DLS)

The mean particle size and surface charge (zeta potential) of the α -TOS-TPP-Obt nanoparticles was measured by dynamic light scattering (DLS) method using Zetasizer Nano2590 (Malvern, UK). 50 μl of α -TOS-TPP-Obt nanoparticles solution was diluted to 1ml using DI water and 3 sets of 10 measurements each were performed at 90 degree scattering angle to get the average particle size.

b. Field-Emission Scanning Electron Microscopy (FESEM) of α -TOS-TPP-Obt nanoparticles:

5 μl of α -TOS-TPP-Obt nanoparticles in water was placed on a silicon chip without any dopant and it was allowed to dry at room temperature under vacuum desiccators for 2 hours. The silicon chip was then gold coated (30-40 nm thickness) using Quorum, Q150T- E5. The FESEM measurements were done using Carl Zeiss, Ultra plus, scanning electron microscope at an operating voltage of 4.0 KV.

c. Atomic Force Microscopy (AFM) of α -TOS-TPP-Obt nanoparticles:

5 μ l of α -TOS-TPP-Obt nanoparticles in water was placed on mica sheet and dried under the vacuum desiccators for 2 h. Shape and size of these nanoparticles were determined using Nano Wizard Atomic Force Microscopy (AFM).

d. Transmission Electron Microscopy (TEM) of α -TOS-TPP-Obt nanoparticles:

15 μ l of α -TOS-TPP-Obt nanoparticles in water was placed on a TEM copper grid. After 30 min this sample drop was wicked off by using filter paper and then 15 μ L of freshly prepared 0.25% uranyl acetate (2.5 mg uranyl acetate in 1 mL dd water) solution was placed on the TEM copper grid. After 1 min, uranyl acetate solution was wicked off and the sample was washed three times with 15 μ l dd water each time. The sample was dried overnight on a clean dust free surface under a funnel. The α -TOS-TPP-Obt nanoparticles were imaged using Tecnai T300 HR-TEM and Tecnai G2 20-Twin LR-TEM instruments.

2.4.8 Determination of drug loading. A Calibration curve was plotted in the concentration range of 2.5 to 200 μ M (for α -TOS) and 5-40 μ M (for obatoclax mesylate) by diluting the 1 mM standard stock solution of drugs in dimethyl sulfoxide (DMSO). The absorbance was measured at 287 nm and 488 nm for α -TOS and obatoclax mesylate respectively with respect to the corresponding solvent blank. The linearity was plotted for absorbance (A) against concentration (C). For drug loading in nanoparticles, prepared nanoparticles were dissolved in spectroscopic grade DMSO in 1 % dilution (done in triplicate). Absorbance was measured at characteristic wavelength against the corresponding solvent blank in 200 μ L quartz cuvette and from the calibration curve drug loading was measured in triplicate. Drug loading efficiency and drug loading content were calculated by the equations below.

Drug loading efficiency = Amount of drug loaded into nanoparticle \div Amount of drug used X 100 %.

Drug loading content = Amount of drug loaded into nanoparticle \div Amount of nanoparticle X 100 %.

2.4.9 Stability of the α -TOS-TPP-Obt nanoparticles at 4°C and 37°C by DLS. The stability of the nanoparticles was checked at 4°C and 37°C by Dynamic Light Scattering method using Zetasizer Nano2590 (Malvern, UK). 50 μ L of nanoparticles solution was diluted to 1 mL using DI water and 3 sets of 10 measurements each were performed at 90 degree scattering angle to get

the average particle size. This was done for 14 days keeping the nanoparticles at 4°C (refrigerator) and 37°C (incubator) to check its stability at shelf (for storage purpose) as well as in blood circulation temperature. Similarly, the nanoparticles were incubated in DMEM cell culture media containing 10% FBS (or in PBS) at 37°C for 3 days and size and PDI values were measured in predetermined time points.

2.4.10 Release kinetics. Concentrated 250 µL dual-drug conjugated nanoparticles were suspended in 250 µL pH = 5.5 solution (or pH = 7.4 solution) and sealed in a dialysis membrane (MWCO = 2000 Dalton for alpha tocopherol succinate and obatoclax release). The dialysis bags were incubated in 10 mL pH = 5.5 solution (or pH = 7.4 solution) at room temperature with gentle shaking. A 400 µL portion of the aliquot was collected from the incubation medium at predetermined time intervals and the released dual drugs were quantified by UV-VIS spectrophotometer.

2.4.11 Cellular internalization by CLSM. 5×10^4 HeLa cells were seeded on a cover slip in a 6 well plate and incubated overnight in a 5% CO₂ incubator at 37°C for attachment. Cells were then first washed with PBS (pH = 7.4) and then treated with α-TOS-TPP-Obt nanoparticles (at a concentration equivalent to 2 µg ml⁻¹ of obatoclax) and free obatoclax (2 µg ml⁻¹) for 1, 3 and 6 h. Cells were then washed twice with PBS and fixed with 500 µL of paraformaldehyde (3.7% in PBS, pH = 6.9) by incubating for 10 min at 4°C. The paraformaldehyde was aspirated and cells are washed trice with PBS. Low pH lysosomes were stained with 1 µM LysoSensorTM Green DND-153 (Invitrogen) by incubating the cells at 37°C for 45 min. The cells were then washed three times to remove the unbound LysoSensorTM followed by staining the cells for nuclei with 2 µg mL⁻¹ DAPI (HiMedia) by incubating at 37°C for 20 min. Then cells were washed three times with PBS and mounted on a glass slide using 5 µL diamond antifed-mounting medium. The slides were subjected to fluorescence imaging using a CLSM (Zeiss LSM 710).

2.4.12 Endocytosis mechanism by CLSM. 5×10^4 HeLa cells were seeded on a cover slip in a 6 well plate and incubated overnight in a 5 % CO₂ incubator at 37 °C for attachment. Cells were first washed with phosphate buffered saline (PBS) (pH = 7.4) and then pre-incubated with following inhibitors: Chlorpromazine (10 µg mL⁻¹), 5-(N-ethyl-N-isopropyl)-Amiloride (1 mM) and Genistein (200 µM) for 30 min. Control cells were treated without inhibitors. After 30 min, the inhibitor solutions were removed, and TOS-TPP-Obt-NPs (2 µg mL⁻¹) in media were added

and incubated for 2 h. Cells were then washed twice with PBS and fixed with 500 μL of paraformaldehyde (3.7 % in PBS, pH = 6.9) by incubating for 10 min at 4 °C. The paraformaldehyde was aspirated and cells were washed thrice with PBS. Low pH lysosomes were stained with 1 μM LysoTrackerTM Green DND-153 (Invitrogen) by incubating the cells at 37 °C for 45 min. Cells were washed three times with PBS followed by staining the cells for nuclei with 2 $\mu\text{g mL}^{-1}$ DAPI (HiMedia) by incubating at 37 °C for 20 min. After three more washings with PBS, cells were mounted on a glass slide using 5 μL antifade-mounting medium. The slides were subjected to fluorescence imaging using a confocal laser scanning microscopy (CLSM) (Zeiss LSM 710).

2.4.13 Endocytosis mechanism by fluorescence activated cell sorting (FACS). 5×10^4 HeLa cells were seeded on a 6 well plate and incubated overnight in a 5 % CO_2 incubator at 37 °C for attachment. Cells were first washed with PBS (pH = 7.4) and then pre-incubated with Chlorpromazine, 5-(N-ethyl-N-isopropyl)-Amiloride and Genistein in the same concentrations described before for 30 min. After 30 min, the inhibitor solutions were removed and TOS-TPP-Obt-NPs were added and incubated for 2 h. A control was kept without adding the nanoparticle. After 2 h, the cells were washed with three times PBS, trypsinized and washed twice with media by means of centrifugation at 750 rpm for 4 min. Then the cells were suspended in PBS and passed through cell strainer to get individual cells and analyzed using BD FACS CaliburTM.

2.4.14 Lysosome permeabilization by acridine orange assay. 5×10^4 HeLa cells were seeded on a 6 well plate and incubated overnight in a 5 % CO_2 incubator at 37 °C for attachment. The cells were then treated with TOS-TPP-Obt-NPs ($10 \mu\text{g mL}^{-1}$) for 12 h. A control was kept without adding the nanoparticle. Cells were then washed thrice with PBS (pH = 7.4) and treated with acridine orange ($5 \mu\text{g mL}^{-1}$) and incubated in dark at 37 °C for 15 min. Staining solution was aspirated and cells were washed thrice with PBS and then fixed with 3.7 % paraformaldehyde at 37 °C for 15 min. Fixing solution was discarded and the cells were washed thrice with PBS and mounted on a glass slide using *SlowFade*® diamond antifade reagent. The slides were subjected to fluorescence imaging using a CLSM (Zeiss LSM 710).

2.4.15 Mitochondria localization. 1.5×10^4 HeLa (or MDA-MB 231) cells were seeded in a lab tek chamber slide 8 well (per well) and incubated overnight in a 5 % CO_2 incubator at 37 °C for attachment. Cells were then treated with TOS-TPP-Obt-NPs at a concentration corresponding to

the IC₅₀ value of respective drugs for 12 h and 24 h. Cells were then washed thrice with PBS (pH = 7.4) and treated with MitoTracker Green® FM at a concentration of 200 nM in PBS and incubated in dark at 37 °C for 25 min. Staining solution was aspirated and cells are washed thrice with PBS. The lab tek chamber slide 8 wells were subjected to fluorescence imaging using a CLSM (Zeiss LSM 710).

2.4.16 Drug content in mitochondria fraction by FACS. 3×10^8 HeLa cells were incubated in T75 flask overnight for attachment and then treated with TOS-TPP-Obt-NPs for 24 h at their respective IC₅₀ values. A control was kept without adding the nanoparticle. After the treatment, media was removed and cells were trypsinized and washed twice with PBS by means of centrifugation at 750 rpm for 4 min to obtain a cell pellet. The mitochondria was isolated from the cell pellet by the mitochondria isolation kit for cultured cells (Thermo Scientific) using the protocol described by the manufacturer. Briefly, protease inhibitor was added into the Reagent A and Reagent C. 800 µL of mitochondria isolation Reagent A was added to the cell pellet and vortexed at a medium speed for 5 sec and the tube was incubated into ice for 2 min. Into it, 800 µL mitochondria isolated Reagent B was added and mixed them by vortexing for 5 sec followed by incubation in ice for 5 min. Again 800 µL of mitochondria isolation Reagent C was added into the mixture and mix thoroughly without vortexing. The tube was centrifuged at 700 Xg for 10 min at 4 °C. The supernatant was transferred into new 2 mL tube and centrifuged at 12000 Xg for 15 min at 4 °C. The supernatant was transferred into new tube (cytosolic fraction) and the pellet contained mitochondria. Finally, 500 µL mitochondria isolation Reagent C was added to the pellets and centrifuged at 12000 Xg for 5 min. The supernatant was discarded and mitochondria pellet was isolated. The drug content in the isolated mitochondrial fraction was measured by BD FACS Calibur™ with 10000 total even collected.

2.4.17 JC1 assay. 1.5×10^4 HeLa (or MDA-MB 231) cells were seeded in a lab tek chamber slide 8 well (per well) and incubated overnight in a 5 % CO₂ incubator at 37 °C for attachment. Cells were then treated with TOS-TPP-Obt-NPs at a concentration corresponding to the IC₅₀ value of respective drugs for 24 h. A control was kept without adding the nanoparticle. Cells were then washed twice with PBS (pH = 7.4) and incubated with JC1 dye (10 µg mL⁻¹) at 37 °C for 20 min. Before adding JC1 dye, cells were visualized using CLSM at 590 nm fluorescence emission wave length and the red fluorescence signal obtained from the nanoparticles were

calculated to be deducted from JC1 fluorescence emission signal as base line correction. The excess dye was aspirated and cells are washed thrice with PBS. The lab tek chamber slide 8 wells were subjected to fluorescence imaging using a CLSM (Zeiss LSM 710).

2.4.18 Calcein AM assay. 1.5×10^4 HeLa cells were seeded in a lab tek chamber slide 8 well (per well) and incubated overnight in a 5 % CO₂ incubator at 37 °C for attachment. Cells were then treated with TOS-TPP-Obt-NPs at a concentration corresponding to the IC₅₀ value of respective drugs for 24 h. A control was kept without adding the nanoparticle. Cells were then washed twice with PBS (pH = 7.4) and incubated with 1 μM Calcein AM and 1 mM CoCl₂ in modified Hanks' balanced solution supplemented with 10 mM Na-HEPES (pH = 7.4) without phenol red and sodium bicarbonate at 37 °C for 30 min. The excess dye was aspirated and cells are washed thrice with PBS for the complete removal of Calcein AM and CoCl₂. The lab tek chamber slide 8 well was subjected to fluorescence imaging using a CLSM (Zeiss LSM 710).

2.4.19 Apoptosis detection by FACS. For apoptosis detection, 2×10^6 HeLa cells were incubated in 6 well plates overnight for attachment and then treated with TOS-TPP-Obt-NPs for 24 hours. After the treatment, media was removed and cells were trypsinized and washed twice with PBS by means of centrifugation at 750 rpm for 4 min. Cell pellet was then resuspended in 100 μL of Annexin-V-FLUOS labeling solution (Annexin-V-FLUOS Staining Kit from Roche) and incubated in 500 μL of incubation buffer at 25°C for 15 mins. Cells were then passed through cell strainer to get individual cells and analyzed using BD FACS Calibur to detect the apoptosis.

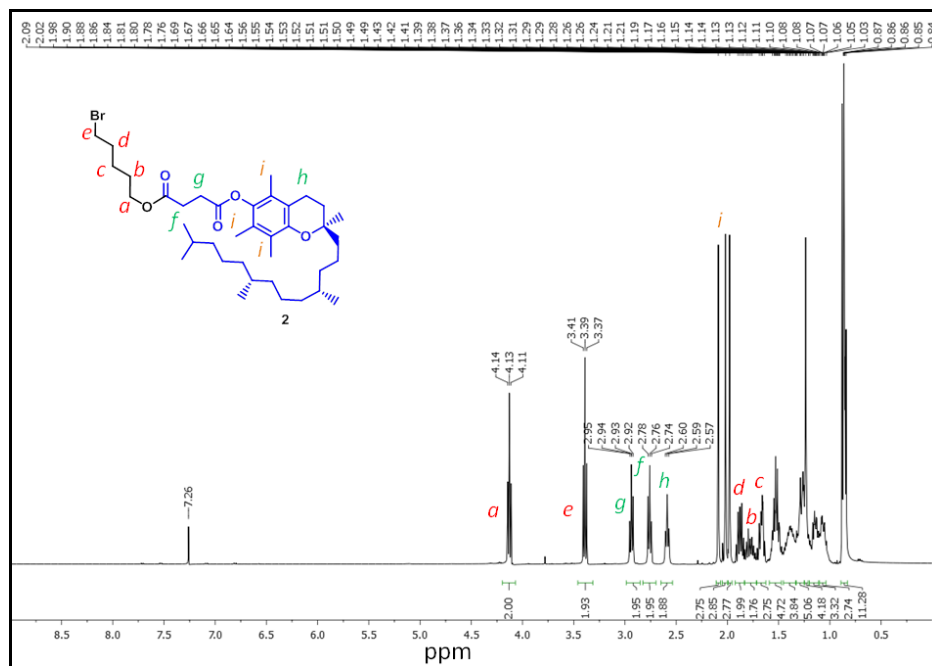
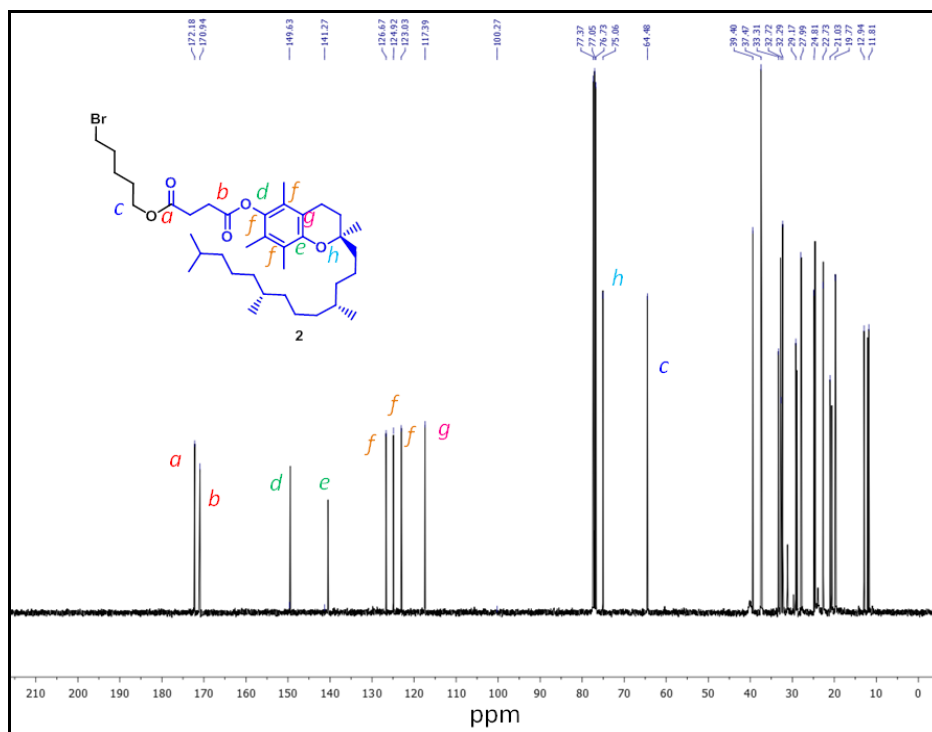
2.4.20 General procedure for Immunostaining assay. 5×10^4 HeLa cells were seeded on a coverslip in a 6 well plate and incubated overnight in a 5% CO₂ incubator at 37°C for attachment. Cells were then treated with TOS-TPP-Obt-NPs at corresponding IC₅₀ concentration for 24 h. Cells were washed once with PBS and then fixed with 3.7% paraformaldehyde at 37°C for 15 min. Cells were then washed twice with PBS (pH = 7.4) and were permeabilized by incubating in blocking buffer (PBS containing 0.3% tween and 5% FBS) at room temperature. Cells were then incubated in primary antibody solution (cytochrome c 1:100 dilution) at 37°C for 3 hr. Cells are washed thrice with blocking buffer. Then cells were incubated in fluorochrome conjugated secondary antibody solution (1:500 dilution) at 37°C for 40 min in dark. Cells were

washed thrice with PBS and mounted on a glass slide using SlowFade® gold antifade reagent. The slides were subjected to fluorescence imaging using a CLSM (Zeiss LSM 710).

2.4.21 General procedure for Western blot analysis. After 24 hours of TOS-TPP-Obt-NPs treatment in their corresponding IC₅₀ concentrations, HeLa cells were lysed and suspended in sample buffer. Proteins were separated using SDS-polyacrylamide gel electrophoresis (SDS-PAGE) and then proteins were transferred onto the membrane (electroblotting). Blotted membrane was then blocked in freshly prepared TBS containing nonfat dry milk (5%) for 1 hour with constant agitation at room temperature. Membrane was then rinsed once with TBST and then incubated in the primary antibody solution (1:1000 dilution, except 1:2500 for GAPDH) overnight at 4°C with gentle agitation (except 4 hours for GAPDH). Membrane was then washed 3 times (15 min each) with TBST and then incubated in HRP conjugated secondary antibody solution (1:500 dilution) for 45 min at room temperature with gentle agitation. Membrane was again washed thrice with TBST (5 min each). Protein detection was then followed by using Immobilon Western Chemiluminescent HRP Substrate (membrane was incubated in the substrate for 1 min). Images were acquired using GE Healthcare Lifesciences ImageQuant LAS 4000. After the acquisition, membrane was boiled in distilled water for 5 min and again was re-probed for GAPDH gene. Further image processing and intensity calculations were performed using ImageJ software.

2.4.22 Cell viability assay. 5×10^3 HeLa (or MDA-MB 231) cells were seeded per well in 96-well microlitre plate and incubated overnight in a 5% CO₂ incubator at 37°C for attachment. Cells were then treated with α -TOS-TPP-Obt nanoparticles and free drug combinations in different concentrations (0.1, 0.2, 0.4, 0.8, 1.6, 3.2, 6.4, 12.5, 25, 50 μ M) for 48 h. 20 μ L of MTT reagent (5 mg/mL) was added to each well and incubated for 4 h at 37°C. Formazan crystals were then solubilized in 100 μ L of the solubilization buffer (10 gm SDS in 0.1 N HCl) and incubated overnight. Absorbance was measured by spectrophotometer at 550 nm. The percent cell viability was calculated considering the untreated cells as 100 percent viability and the effectiveness of α -TOS-TPP-Obt nanoparticles was compared with the free drug combinations.

2.5. Appendices

Figure A1: ^1H NMR spectra of conjugate 2

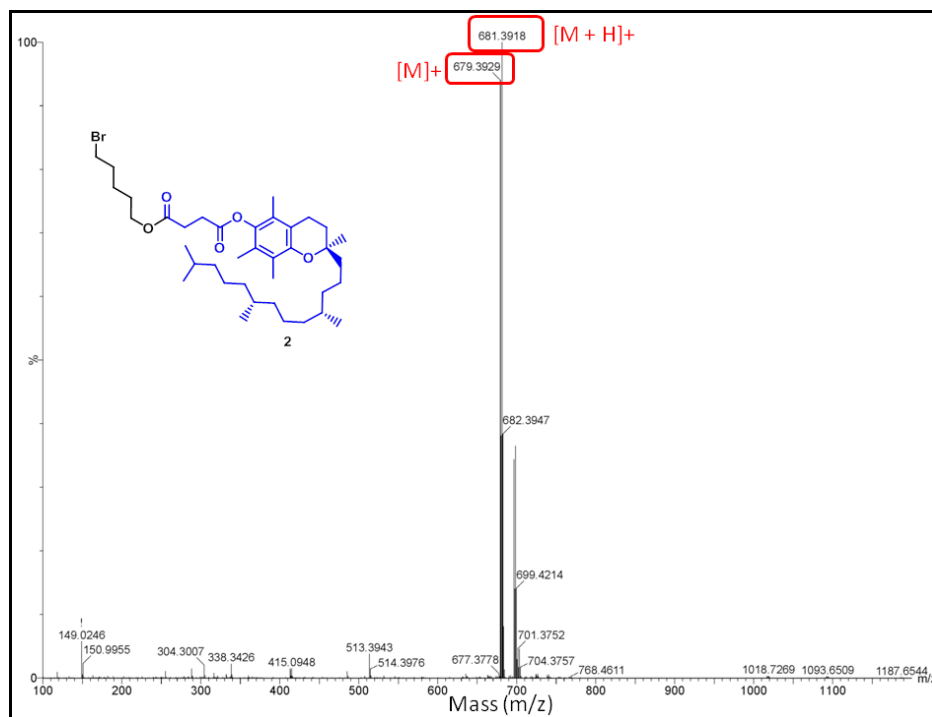


Figure A3: HR-MS spectra of conjugate 2.

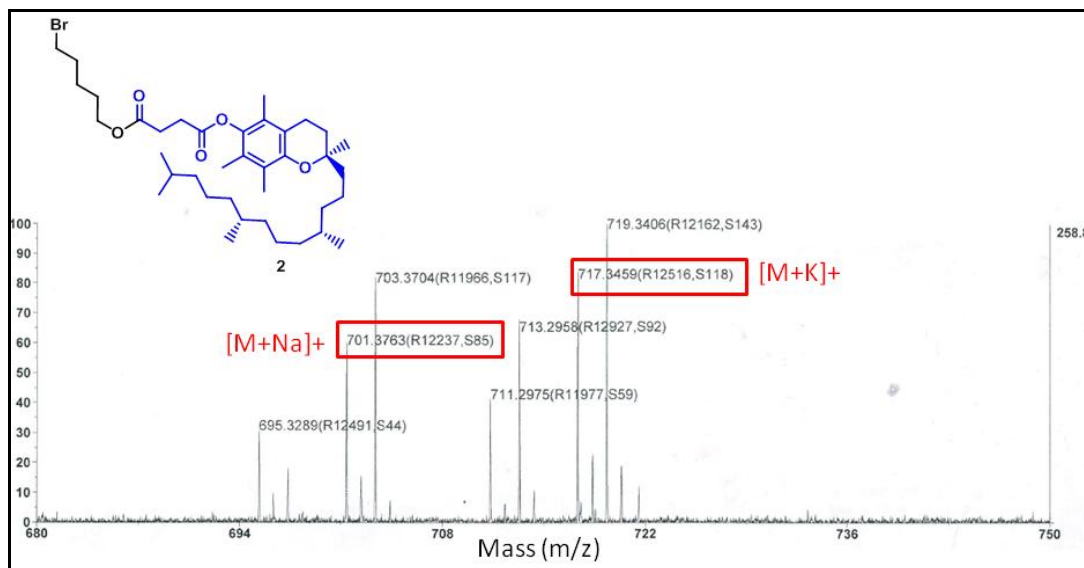


Figure A4: MALDI-TOF spectra of conjugate 2

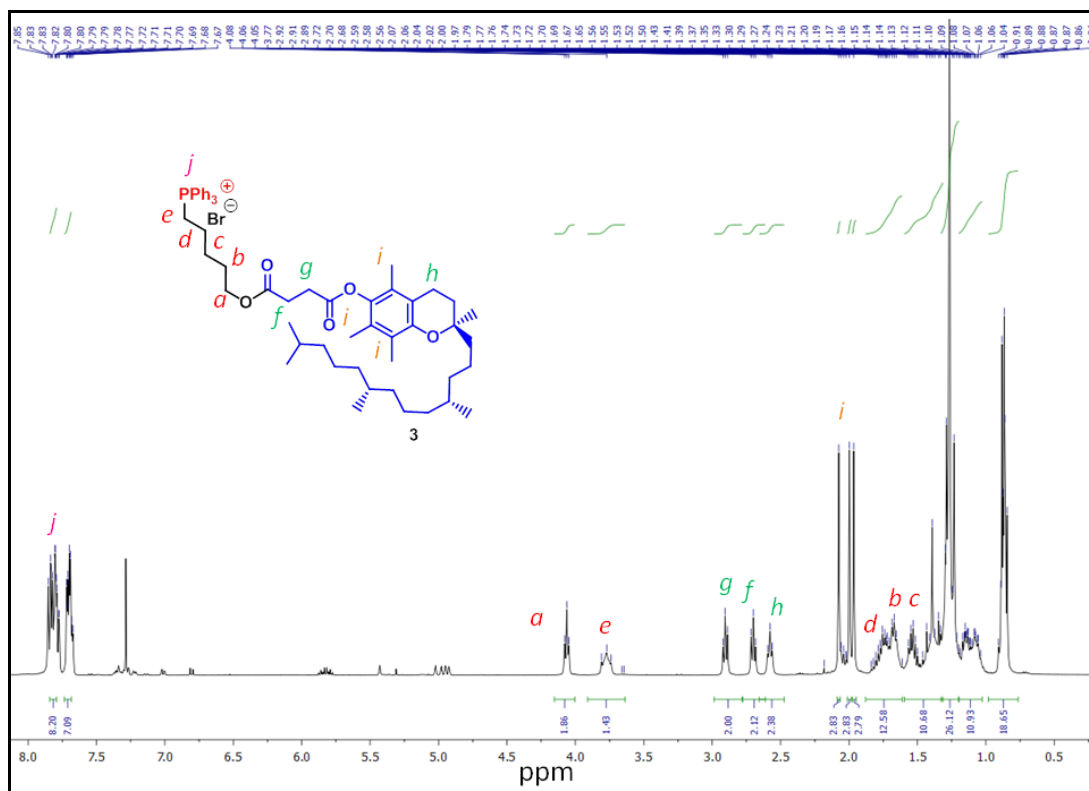


Figure A5: ^1H NMR spectra of α -TOS-TPP conjugate **3**

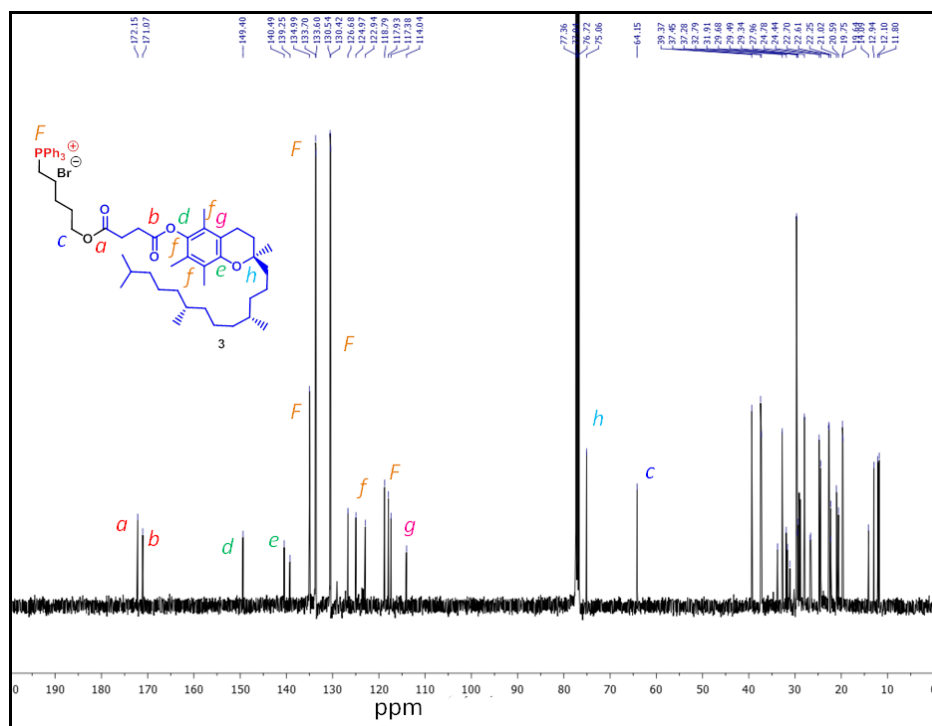


Figure A6: ^{13}C NMR spectra of α -TOS-TPP conjugate **3**.

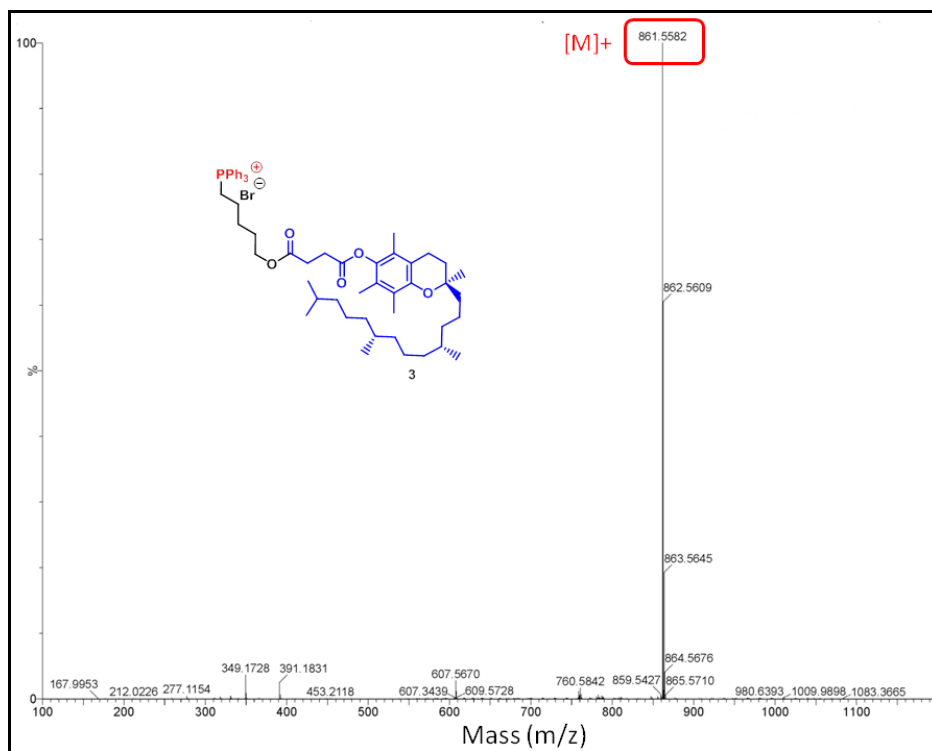


Figure A7: HR-MS spectra of α -TOS-TPP conjugate **3**

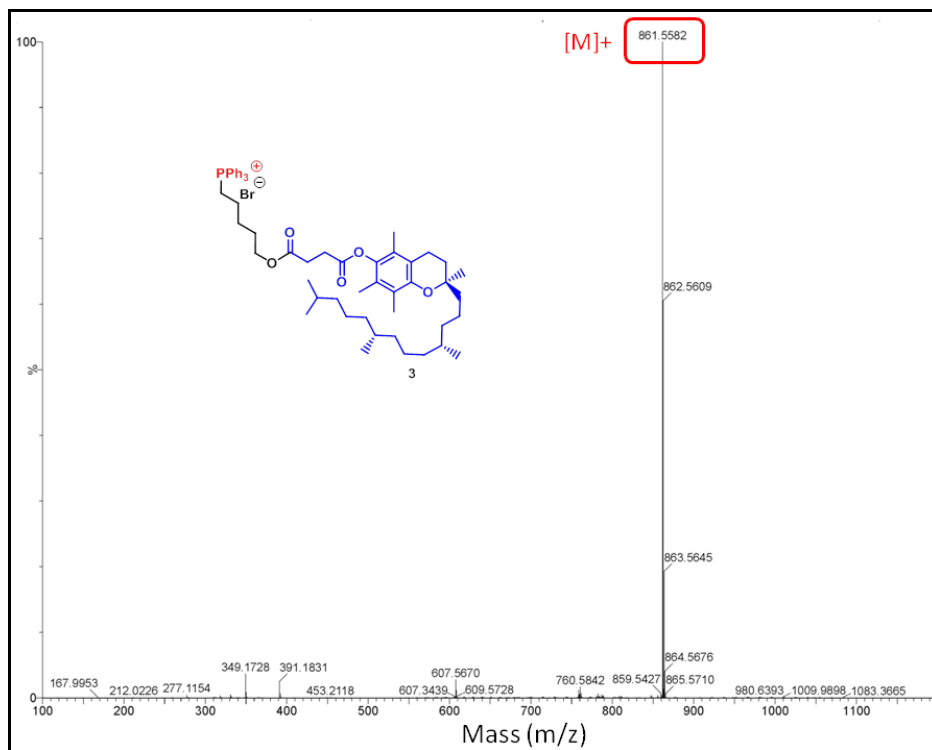


Figure A8: MALDI-TOF spectra of α -TOS-TPP conjugate **3**

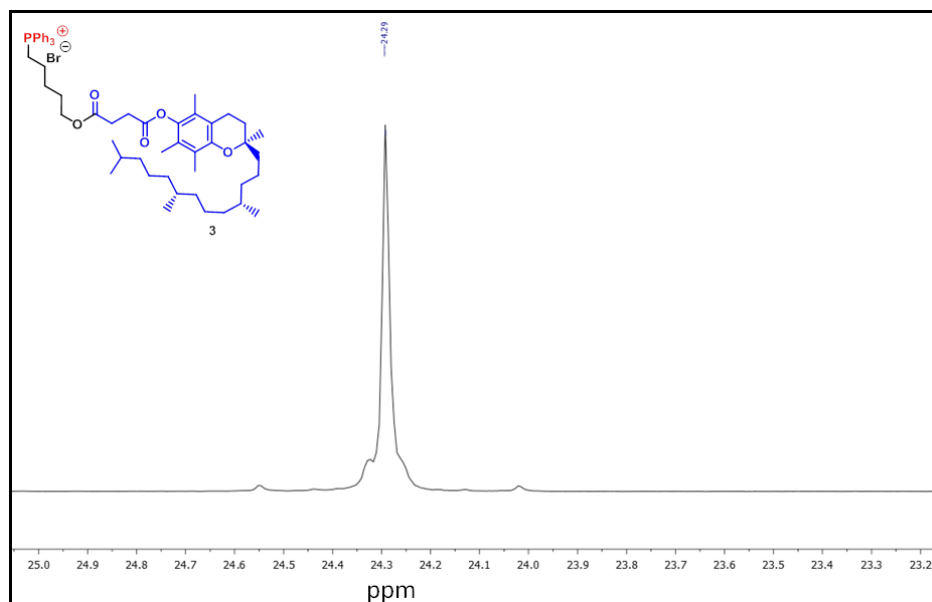


Figure A9: ^{31}P NMR spectra of α -TOS-TPP conjugate **3**.

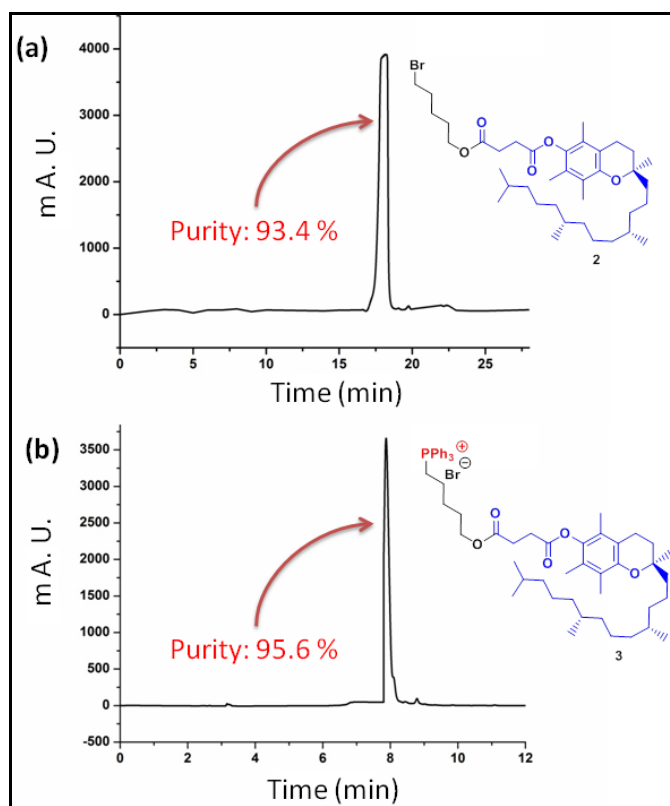


Figure A10: RP-HPLC traces of (a) conjugate **2** and (b) conjugate **3**.

2.6. References

- (1) Hanahan, D.; Weinberg, R. A. Hallmarks of Cancer: The next Generation. *Cell* **2011**, *144*, 646–674.
- (2) Elmore, S. Apoptosis: A Review of Programmed Cell Death. *Toxicol. Pathol.* **2007**, *35*, 495–516.
- (3) Youle, R. J.; Strasser, A. The BCL-2 Protein Family: Opposing Activities That Mediate Cell Death. *Nat. Rev. Mol. Cell Biol.* **2008**, *9*, 47–59
- (4) Chipuk, J. E.; Moldoveanu, T.; Llambi, F.; Parsons, M. J.; Green, D. R. The BCL-2 Family Reunion. *Mol. Cell* **2010**, *37*, 299–310.
- (5) Tait, S. W. G.; Green, D. R. Mitochondria and Cell Death: Outer Membrane Permeabilization and beyond. *Nat. Rev. Mol. Cell Biol.* **2010**, *11*, 621–632.
- (6) Ichim, G.; Tait, S. W. G. A Fate Worse than Death: Apoptosis as an Oncogenic Process. *Nat. Rev. Cancer* **2016**, *16*, 539–548.
- (7) Delbridge, A.; Strasser, A. The BCL-2 Protein Family, BH3-Mimetics and Cancer Therapy. *Cell Death Differ.* **2015**, *22*, 1071–1080.
- (8) Kang, M. H.; Reynolds, C. P. Bcl-2 Inhibitors: Targeting Mitochondrial Apoptotic Pathways in Cancer Therapy. *Clin. Cancer Res.* **2009**, *15*, 1126–1132.
- (9) Thomenius, M. J. Bcl-2 on the Endoplasmic Reticulum: Protecting the Mitochondria from a Distance. *J. Cell Sci.* **2003**, *116*, 4493–4499.
- (10) Montero, J.; Letai, A. Why Do BCL-2 Inhibitors Work and Where Should We Use Them in the Clinic? *Cell Death Differ.* **2017**, *25*, 56–64.
- (11) Giorgi, C.; De Stefani, D.; Bononi, A.; Rizzuto, R.; Pinton, P. Structural and Functional Link between the Mitochondrial Network and the Endoplasmic Reticulum. *Int. J. Biochem. Cell Biol.* **2009**, *41*, 1817–1827.
- (12) Dong, L. F.; Low, P.; Dyason, J. C; Wang, X. F.; Prochazka, L.; Witting, P. K.; Freeman, R.; Swettenham, E.; Valis, K.; Liu, J.; Zobalova, R.; Turanek, J.; Spitz, D. R.; Domann, F. E.; Scheffler, I. E.; Ralph, S. J.; Neuzil, J. Alpha-Tocopheryl Succinate Induces Apoptosis by Targeting Ubiquinone-Binding Sites in Mitochondrial Respiratory Complex II. *Oncogene* **2008**, *27*, 4324–4335.

- (13) Dong, L. F.; Freeman, R.; Liu, J.; Zobalova, R.; Marin-Hernandez, A.; Stantic, M.; Rohlena, J.; Valis, K.; Rodriguez-Enriquez, S.; Butcher, B.; Goodwin, J.; Brunk, U. T.; Witting, P. K.; Moreno-Sanchez, R.; Scheffler, I. E.; Ralph, S. J.; Neuzil, J. Suppression of Tumor Growth in vivo by the Mitocan Alpha-Tocopheryl Succinate Requires Respiratory Complex II. *Clin. Cancer Res.* **2009**, *15*, 1593-1600.
- (14) Kruspig, B.; Zhivotovsky, B.; Gogvadze, V. Contrasting Effects of α -Tocopheryl Succinate on Cisplatin- and Etoposide-Induced Apoptosis. *Mitochondrion*, **2013**, *13*, 533-538.
- (15) Zhang, X.; Peng, X.; Yu, W.; Hou, S.; Zhao, Y.; Zhang, Z.; Huang, X.; Wu, K. Alpha Tocopheryl Succinate Enhances Doxorubicin-Induced Apoptosis in Human Gastric Cancer Cell via Promotion of Doxorubicin Influx and Suppression of Doxorubicin Efflux. *Cancer Lett.* **2011**, *307*, 174-181.
- (16) Kanai, K.; Kikuchi, E.; Mikami, S.; Suzuki, E.; Uchida, Y.; Kodaira, K.; Miyajima, A.; Ohigashi, T.; Nakashima, J.; Oya, M. Vitamin E Succinate Induced Apoptosis and Enhanced Chemosensitivity to Paclitaxel in Human Bladder Cancer Cells in vitro and in vivo. *Cancer Sci.* **2010**, *101*, 216-223.
- (17) Mavanoff, B. E.; Reitz, A. B.; Duhl-Emswiler, B. A. Stereochemistry of the Wittig reaction. Effect of Nucleophilic Groups in the Phosponium Ylide. *J. Am. Chem. Soc.*, **1985**, *107*, 217-226.
- (18) Sengupta, P.; Basu, S.; Soni, S.; Pandey, A.; Roy, B.; Oh, M. S.; Chin, K. T.; Paraskar, A. S.; Sarangi, S.; Connor, Y.; Sabbisetti, V. S.; Kopparam, J.; Kulkarni, A.; Muto, K.; Amarasiriwardena, C.; Jayawardene, I.; Lupoli, N.; Dinulescu, D. M.; Bonventre, J. V.; Mashelkar, R. A.; Sengupta, S. Cholesterol-Tethered Platinum II-Based Supramolecular Nanoparticle Increases Antitumor Efficacy and Reduces Nephrotoxicity. *Proc. Natl. Acad. Sci. USA.* **2012**, *109*, 11294-11299.
- (19) Schimmer, A. D.; O'Brien, S.; Kantarjian, H.; Brandwein, J.; Cheson, B. D.; Minden, M. D.; Yee, K.; Ravandi, F.; Giles, F.; Schuh, A.; Gupta, V.; Andreeff, M.; Koller, C.; Chang, H.; Kamel-Reid, S.; Berger, M.; Viallet, J.; Borthakur, G. A Phase I Study of the Pan Bcl-2 Family Inhibitor Obatoclax Mesylate in Patients with Advanced Hematologic Malignancies. *Clin. Cancer Res.* **2008**, *14*, 8295-8301.

- (20) O'Brien, S. M.; Claxton, D. F.; Crump, M.; Faderl, S.; Kipps, T.; Keating, M. J.; Viallet, J.; Cheson, B. D. Phase I Study of Obatoclox Mesylate (GX15-070), a Small Molecule Pan-Bcl-2 Family Antagonist, in Patients with Advanced Chronic Lymphocytic Leukemia. *Blood* **2009**, *113*, 299-305.
- (21) Paik, P. K.; Rudin, C. M.; Brown, A.; Rizvi, N. A.; Takebe, N.; Travis, W.; James, L.; Ginsberg, M. S.; Juergens, R.; Markus, S.; Tyson, L.; Subzwari, S.; Kris, M. G.; Krug, L. M. A Phase I Study of Obatoclox Mesylate, a Bcl-2 Antagonist, Plus Topotecan in Solid Tumor Malignancies. *Cancer Chemother. Pharmacol.* **2010**, *66*, 1079-1085.
- (22) Nguyen, M.; Marcellus, R. C.; Roulston, A.; Watson, M.; Serfass, L.; Murthy Madiraju, S. R.; Goulet, D.; Viallet, J.; Bélec, L.; Billot, X.; Acoca, S.; Purisima, E.; Wiegmanns, A.; Cluse, L.; Johnstone, R. W.; Beauparlant, P.; Shore, G. C. Small Molecule Obatoclox (GX15-070) Antagonizes MCL-1 and Overcomes MCL-1-Mediated Resistance to Apoptosis. *Proc. Natl. Acad. Sci. USA.* **2007**, *104*, 19512-19517.
- (23) Harris, J. M.; Chess, R. B. Effect of Pegylation on Pharmaceuticals. *Nat. Rev. Drug Discov.* **2003**, *2*, 214-221.
- (24) Matsumura, Y.; Maeda, H. A New Concept for Macromolecular Therapeutics in Cancer Chemotherapy: Mechanism of Tumoritropic Accumulation of Proteins and the Antitumor Agent Smancs. *Cancer Res.* 1986, **46**, 6387-6392.
- (25) Wang, J.; Mao, W.; Lock, L. L.; Tang, J.; Sui, M.; Sun, W.; Cui, H.; Xu, D.; Shen, Y. The Role of Micelle Size in Tumor Accumulation, Penetration, and Treatment. *ACS Nano* **2015**, *9*, 7195-7206.
- (26) Champion, J. A.; Mitragotri S. Role of Target Geometry in Phagocytosis. *Proc. Natl. Acad. Sci. U S A.* **2006**, *103*, 4930-4934.
- (27) Mallick, A.; More, P.; Ghosh, S.; Chippalkatti, R.; Chopade, B. A.; Lahiri, M.; Basu, S. Dual Drug Conjugated Nanoparticle for Simultaneous Targeting of Mitochondria and Nucleus in Cancer Cells. *ACS Appl. Mater. Interfaces* **2015**, *7*, 7584-7598.
- (28). Qu, Q.; Ma, X.; Zhao, Y. Targeted Delivery of Doxorubicin to Mitochondria Using Mesoporous Silica Nanoparticle Nanocarriers. *Nanoscale* **2015**, *7*, 16677–16686.

- (29) Wang, L.; Liu, Y.; Li, W.; Jiang, X.; Ji, Y.; Wu, X.; Xu, L.; Qiu, Y.; Zhao, K.; Wei, T.; Li, Y.; Zhao, Y.; Chen, C. Selective Targeting of Gold Nanorods at the Mitochondria of Cancer Cells: Implications for Cancer Therapy. *Nano Lett.* **2011**, *11*, 772-780.
- (30) Doherty, G. J.; McMahon, H. T. Mechanisms of Endocytosis. *Annu. Rev. Biochem.* **2009**, *78*, 857-902.
- (31) Boya, P.; Kroemer, G. Lysosomal Membrane Permeabilization in Cell Death. *Oncogene* **2008**, *27*, 6434-6451.
- (32) Zhou, J.; Zhao, W. Y.; Ma, X.; Ju, R. J.; Li, X. Y.; Li, N.; Sun, M. G.; Shi, J. F.; Zhang, C. X.; Lu, W. L. The Anticancer Efficacy of Paclitaxel Liposomes Modified with Mitochondrial Targeting Conjugate in Resistant Lung Cancer. *Biomaterials* **2013**, *34*, 3626-3638.
- (33) Rin Jean, S.; Tulumello, D. V.; Wisnovsky, S. P.; Lei, E. K.; Pereira, M. P.; Kelley, S. O. Molecular Vehicles for Mitochondrial Chemical Biology and Drug Delivery. *ACS Chem. Biol.* **2014**, *9*, 323-333.
- (34) Pathak, R. K.; Marrache, S.; Harn, D. A.; Dhar, S. Mito-DCA: a Mitochondria Targeted Molecular Scaffold for Efficacious Delivery of Metabolic Modulator Dichloroacetate. *ACS Chem. Biol.* **2014**, *9*, 1178-1187
- (35) Petronilli, V.; Miotto, G.; Canton, M.; Brini, M.; Colonna, R.; Bernardi, P.; Di Lisa, F. Transient and Long-Lasting Openings of the Mitochondrial Permeability Transition Pore can be Monitored Directly in Intact Cells by Changes in Mitochondrial Calcein Fluorescence. *Biophys. J.* **1999**, *76*, 725-734.
- (36) Mariño, G.; Niso-Santano, M.; Baehrecke, E. H.; Kroemer, G. Self-Consumption: the Interplay of Autophagy and Apoptosis. *Nat. Rev. Mol. Cell Biol.* **2014**, *15*, 81-94.
- (37) Samali, A.; Cai, J.; Zhivotovsky, B.; Jones, D. P.; Orrenius, S. Presence of a Pre-Apoptotic Complex of Pro-Caspase-3, Hsp60 and Hsp10 in the Mitochondrial Fraction of Jurkat Cells. *EMBO J.* **1999**, *18*, 2040-2048.
- (38) Marrache, S.; Pathak, R. K.; Dhar, S. Detouring of Cisplatin to Access Mitochondrial Genome for Overcoming Resistance. *Proc. Natl. Acad. Sci. USA.*, **2014**, *111*, 10444-10449.

- (39) Fonseca, S. B.; Pereira, M. P.; Mourtada, R.; Gronda, M.; Horton, K. L.; Hurren, R.; Minden, M. D.; Schimmer, A. D.; Kelley, S. O. Rerouting Chlorambucil to Mitochondria Combats Drug Deactivation and Resistance in Cancer Cells. *Chem. Biol.* **2011**, *18*, 445-453.
- (40) Chamberlain, G. R.; Tulumello, D. V.; Kelley, S. O. Targeted Delivery of Doxorubicin to Mitochondria. *ACS Chem. Biol.* **2013**, *8*, 1389-1395.
- (41) Akao, Y.; Otsuki, Y.; Kataoka, S.; Ito, Y.; Tsujimoto, Y. Multiple Subcellular Localization of bcl-2: Detection in Nuclear Outer Membrane, Endoplasmic Reticulum Membrane, and Mitochondrial Membranes. *Cancer Res.* **1994**, *54*, 2468-2471.

Chapter 3a :Targeting mitochondrial DNA and associated proteins by Cerberus nanoparticle

Sections of this chapter represent the following work in progress:

Abhik Mallick, Meenu Kuman, Arijit Ghosh, Benubrata Das and Sudipta Basu. Cerberus Nanoparticle: Co-targeting of Mitochondrial DNA and Mitochondrial Topoisomerase-I in Breast Cancer Cells.
(Manuscript under review)

3a.1. Introduction

Breast cancer is one of the leading causes of death among women in the whole world.¹ Chemotherapeutic regimen using small molecule cytotoxic drugs for treatment of breast cancer gained huge success over last couple of decades.²⁻⁵ However, most chemotherapeutic drugs impairing traditional targets like nuclear DNA (cisplatin, 5-fluorouracil, doxorubicin) or tubulin (paclitaxel and docetaxel) remained ineffective in longer run due to heterogeneous nature of tumor and emergence of drug resistance through intrinsic or extrinsic mechanisms.⁶⁻¹⁰ Hence, searching for alternative targets for traditional chemotherapeutic drugs emerged as interesting strategy for next-generation cancer therapy.¹¹⁻¹³ In this context, mitochondrion has emerged as non-conventional target for cancer therapy.¹⁴⁻¹⁷ Mitochondrion, the powerhouse of the cells, not only produces ATP as energy currency, but plays crucial roles in biosynthesis, stress signaling, programmed cell death (apoptosis) and autophagy.¹⁸⁻²² Consequently, perturbation in mitochondrial functions is implicated as one of the emerging hallmarks of cancer progression and metastasis.^{17, 23} Interestingly, mitochondrion contains circular DNA which produces proteins required for oxidative phosphorylation (OXPHOS) through mitochondrial transcriptional and translational machinery.²⁴⁻²⁶ As a result, detouring conventional chemotherapeutic drugs into mitochondria to damage mitochondrial DNA (mt-DNA) instead of nuclear DNA helped in improving therapeutic efficacy and overcoming drug resistance.^{27, 28} Considering the ubiquitous nature in healthy and cancerous cells, selective spatial targeting of mitochondria in cancerous cells remained a major challenge. Nano-scale platforms have shown promise to address this challenge.^{29, 30}

Nanoplatfroms have changed the paradigm of cancer chemotherapy in last couple of decades by packaging and delivering therapeutic materials (small molecule drugs, antibodies, siRNAs, genes) safely into tumor tissues by either passive or active targeting.³¹⁻³³ However, delivering drugs into specific organelles especially into mitochondria is still in its infancy. Recently, different cationic moieties including lipophilic triphenylphosphine (TPP),³⁴⁻³⁹ amphiphilic peptides⁴⁰⁻⁴⁵ and other quaternary pyridine based moieties were used to route DNA damaging anti-cancer drugs into mitochondria for improved efficacy and overcome drug resistance.⁴⁶ Interestingly, similar to nucleus, mitochondria contain several DNA damage repair mechanisms which can overcome the effect of DNA damaging drugs in mitochondria.^{47, 48} Hence, it is

necessary to impair multiple targets inside mitochondria for enhanced and optimal therapeutic effect. In this context, mitochondrial DNA Topoisomerase I (Top1mt) is an interesting candidate due to its role in maintaining mitochondrial DNA homeostasis, integrity and repair.^{49,50} Moreover, Top1mt is shown to be implicated in cancer and drug resistance.⁵¹ Although several efforts have been made to damage nuclear DNA simultaneously with the inhibition of nuclear Topoisomerase I, co-targeting of their counterparts in mitochondria remained completely unexplored for effective cancer therapy.

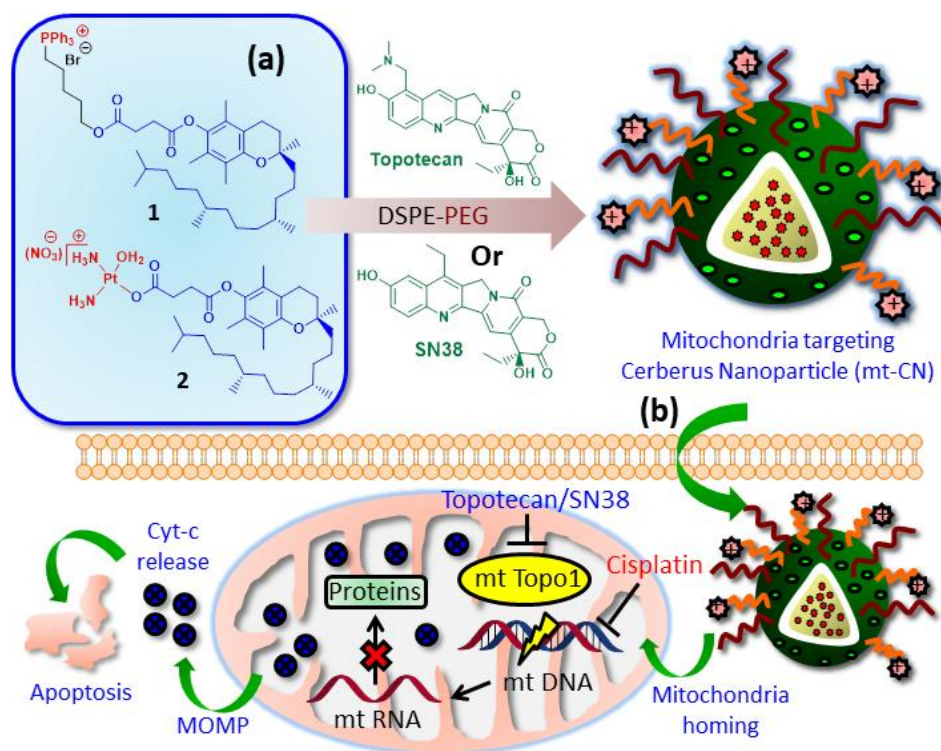
To address this, herein, we have engineered triphenylphosphine (TPP) coated cationic mitochondria targeted Cerberus Nanoparticle (mt-CN) which comprises α -tocopheryl succinate (TOS; complex II inhibitor in electron transport chain), cisplatin (DNA damaging drug) and topotecan or SN38 (Topoisomerase I inhibitor). These nanoparticles were localized into mitochondria of MCF7 breast cancer cells visualized by confocal laser scanning microscopy (CLSM). Inhibition of mitochondrial Topoisomerase I (Top1mt) and damage of mitochondrial DNA (mt-DNA) were simultaneously achieved by mt-CNs leading to inhibition of mitochondrial protein synthesis. These co-targeting of Top1mt and mt-DNA damaged mitochondria through mitochondrial outer membrane permeabilization (MOMP) followed by release of pro-apoptotic cytochrome c and generation of reactive oxygen species (ROS). This mt-CN-mediated mitochondrial impairment triggered programmed cell death (apoptosis) through cleavage of caspase-9, leading to improved cell death in MCF7 breast cancer cells. These mt-CNs can be further explored as platform for damaging multiple targets spatially and selectively in mitochondria of cancer cells to overcome drug resistance in clinics.

3a.2. Result and Discussion

3a.2.1 Engineering mitochondria targeting Cerberus nanoparticle (mt-CN):

Spatial targeting of mitochondria in sub-cellular milieu as well as in cancer tissues keeping them intact in healthy tissues remained a major challenge. High negative potential of mitochondrial membrane compared to cell membrane was exploited to develop lipophilic triphenylphosphine (TPP) labeled molecules for routing them to mitochondria.⁵² Using this strategy, several groups engineered TPP coated nanoparticles to deliver DNA damaging drugs into the mitochondria of cancer cells for improved therapeutic effect.³⁴⁻³⁷ In a recent study, we have demonstrated that

TPP coated α -tocopheryl succinate (α -TOS) based nanoparticle comprising obatoclox (Bcl-2 inhibitor) can target mitochondria to induce apoptosis in cancer cells.⁵³ Herein, we have blended α -TOS-TPP conjugate (1) with α -TOS-cisplatin conjugate (α -TOS-CDDP, 2) and encapsulated either topotecan or SN38 (Topoisomerase I inhibitor) to engineer Cerberus Nanoparticle (inspired by a Greek mythological three headed dog called Cerberus) (**Scheme 1a**). We mixed phosphatidylcholine (PC), α -TOS-TPP (1), α -TOS-CDDP (2) and SN38 or topotecan in 6:1:1:1 weight ratios to obtain mt-CN [CDDP-SN38] and mt-CN [CDDP-Topo] respectively. We induced stealth nature into mt-CN by using DSPE-PEG₂₀₀₀ to overcome phagocytic system and longer blood circulation half-life for future translational ease.



Scheme 1: (a) Engineering mitochondria targeting Cerberus Nanoparticle (mt-CN) from TOS-TPP and TOS-CDDP conjugate encapsulating Topotecan or SN38. (b) Schematic representation of mechanism of action of mt-CN to induce mitochondrial DNA damage and inhibition of mitochondrial Topoisomerase I to impair mitochondrial protein synthesis.

The size and shape of the nano-scale particles are determinant factors for effective accumulation into tumor tissues by passive targeting.⁵⁴ We determined the size of mt-CNs by dynamic light scattering (DLS). The hydrodynamic diameters of mt-CN [CDDP-SN38] and mt-CN [CDDP-

Topo] were found to be 185.6 nm and 175.4 nm (**Figure 1a, b**) which were ideal for accumulation into tumor tissues through passive targeting.⁵⁵ The size and shape of the mt-CNs were further visualized by field-emission scanning electron microscopy (FESEM). The electron microscopy images (**Figure 1c, d**) evidently showed that both mt-CN [CDDP-SN38] and mt-CN [CDDP-Topo] were spherical in shape and sub 200 nm in diameter, confirming the hydrodynamic diameter determined by DLS. For effective spatial targeting of mitochondria in sub-cellular milieu, the nano-scale platform must contain positive surface charge.⁵² We assessed the surface charge of the mt-CNs by measuring zeta potential through light scattering (DLS). Both mt-CN [CDDP-SN38] and mt-CN [CDDP-Topo] showed zeta potential = + 35 mV and + 23 mV respectively (**Figure 1e, f**). These high positive surface charges on mt-CNs indicated their potential for successful mitochondria localization.

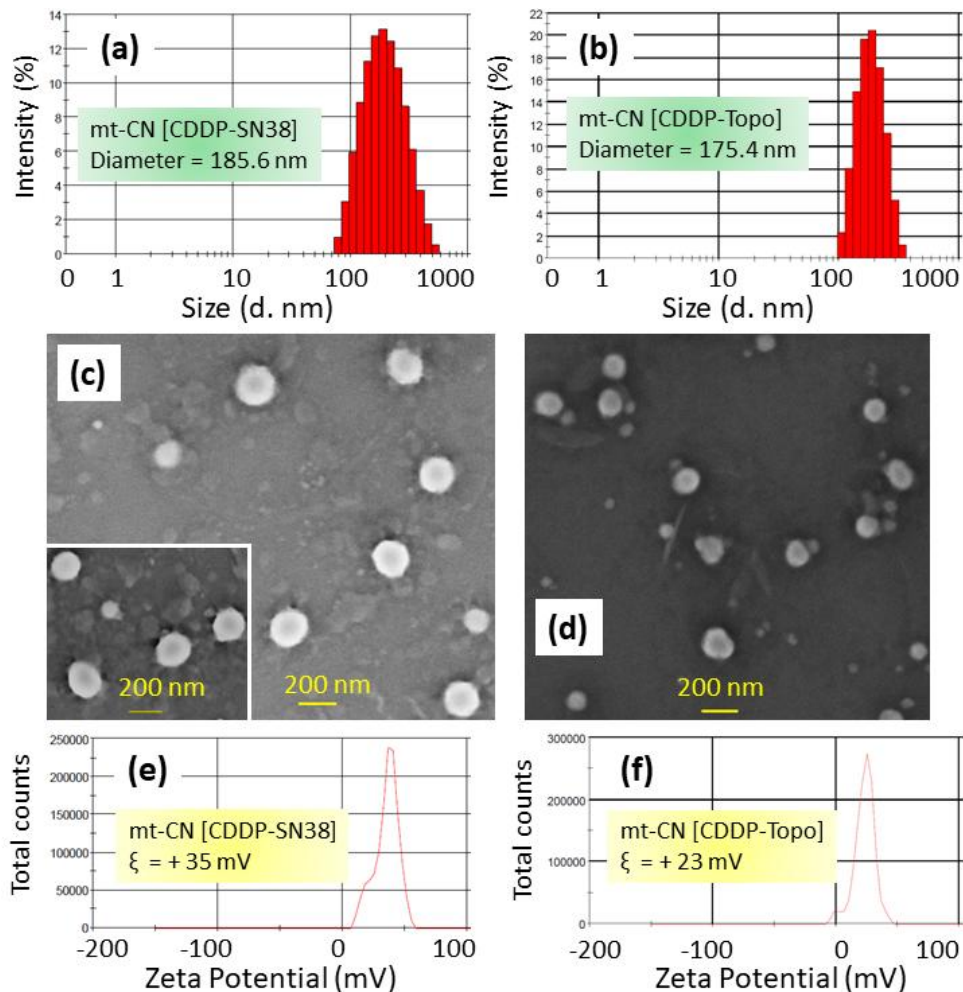


Figure 1: Characterization of size, shape, morphology and surface charge of mt-CN by (a,b) dynamic light scattering, (c,d) FESEM and (e,f) zeta potential.

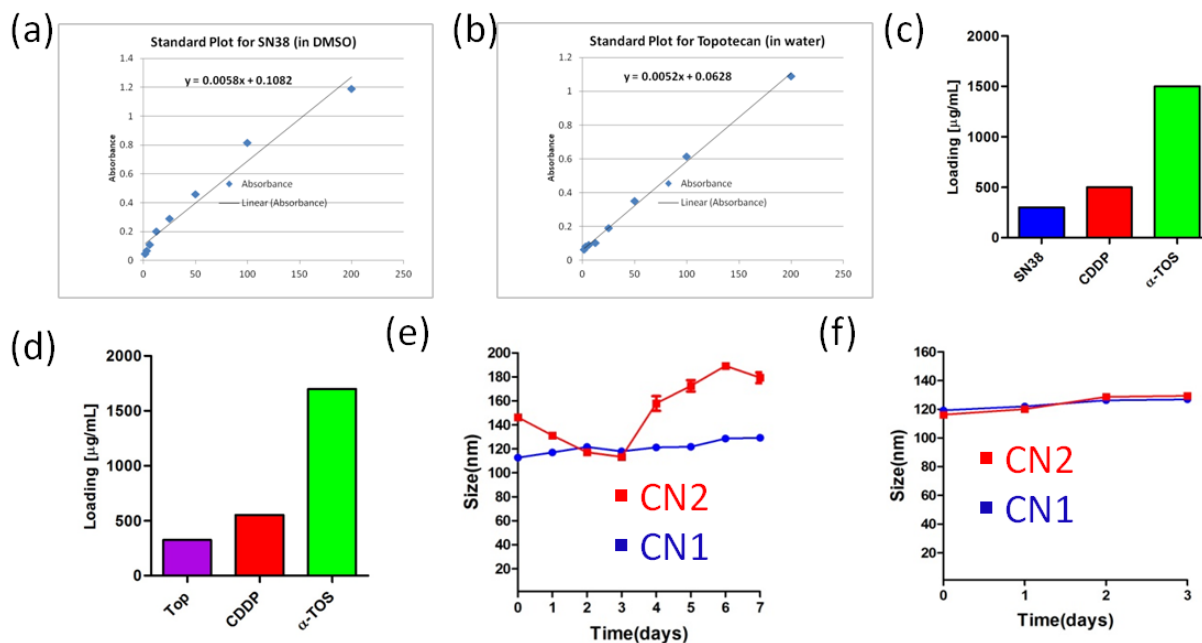


Figure 2: (a-b) Concentration versus absorbance calibration graph of SN38 and topotecan determined by UV-Vis spectroscopy. (c-d) Loading of α -TOS, CDDP, SN38 and α -TOS, CDDP, topotecan in Cerberus nanoparticles (CN1 and CN2). (e) Stability of Cerberus nanoparticles (CN1 and CN2) at 4°C in water for 7 Days and (f) at 37°C in DMEM media with 10% FBS for 3 days determined by DLS.

Further, the loading of all three drugs into mt-CN was evaluated by UV-Vis spectroscopy through concentration versus absorbance calibration curve at characteristic $\lambda_{\text{max}} = 387$ nm, 405 nm, 287 nm and 706 nm for SN38, topotecan, α -TOS and cisplatin respectively (**Figure 2 a,b**). It was observed that mt-CN [CDDP-SN38] contained 303 $\mu\text{g/mL}$, 560 $\mu\text{g/mL}$ and 1584 $\mu\text{g/mL}$ of SN38, cisplatin and α -TOS respectively (**Figure 2c**). On the other hand, mt-CN [CDDP-Topo] contained the loading of topotecan, cisplatin and α -TOS in 321 $\mu\text{g/mL}$, 509 $\mu\text{g/mL}$ and 1704 $\mu\text{g/mL}$ respectively (**Figure 2d**).

For future applications into clinics, the mt-CN should be stable in storage condition. Hence, we assessed the stability of the mt-CN at 4 °C for a week. It was observed that the size of the mt-CN [CDDP-SN38] was increased marginally from 112.7 nm to 129.3 nm over 7 days (**Figure 2e**). On the other hand, the size of the mt-CN [CDDP-topo] was increased from 146.3 nm to 179.3 nm over 7 days. Moreover, the mt-CN should be highly stable in biological environment for successful localization into mitochondria as well as tumor tissues after travelling through

blood circulation. To evaluate the stability in biological milieu, we incubated mt-CNs in DMEM cell culture media containing 10 % fetal bovine serum (FBS) at 37 °C over 3 days and measured the change in size by DLS. It was observed that the size of mt-CN [CDDP-SN38] was increased minimally from 119.3 nm to 126.9 nm over 3 days (**Figure 2f**). Similarly, the size of mt-CN [CDDP-Topo] was also changed from 116.2 nm to 129.3 nm after 72 h. These stability data clearly showed that mt-CNs were stable in storage condition over 7 days and highly stable in biological environment for 3 days which is considerable enough to be localized into mitochondria as well as tumor tissues through blood circulation.

3a.2.2. Mitochondrial homing of Cerberus nanoparticle:

Spherical, sub 200 nm size with highly positive surface charge, the mt-CNs should localize into mitochondria of cancer cells. It was shown in a previous study that TPP coated α -TOS based nanoparticle containing obatoclax (Bcl-2 inhibitor) can enter into cancer cells by macropinocytosis and localize into acidic lysosomes followed by homing into mitochondria within 12 h.⁵³ Hence, to visualize the localization of mt-CNs into mitochondria, we treated MCF7 breast cancer cells with green fluorescent mt-CN [CDDP-SN38] and mt-CN [CDDP-Topo] for 12 h. The mt-CNs were green fluorescently labeled due to the inherent green fluorescence nature of SN38 and Topotecan. We counter stained the mitochondria of MCF7 cells by red fluorescent MitoTracker™ Red CMXRos and visualized the live cells under confocal laser scanning microscopy (CLSM). Fluorescent microscopy images (**Figure 3**) evidently showed that green fluorescent mt-CNs localized into red fluorescently labeled mitochondria to yield yellow merged areas over 12 h. On the other hand, no merged yellow signal was seen in non-nanoparticle treated control cells. Further quantification from CLSM through Pearson's and Mander's correlation coefficients revealed that mt-CN [CDDP-SN38] and mt-CN [CDDP-Topo] showed 67.7 % and 55.4 % volume co-localization respectively by overlapping green and red fluorescence signals inside the cells (**Table 1**). These confocal microscopy images and quantification clearly exhibited that mt-CNs homed into mitochondria of MCF7 cells within 12 h.

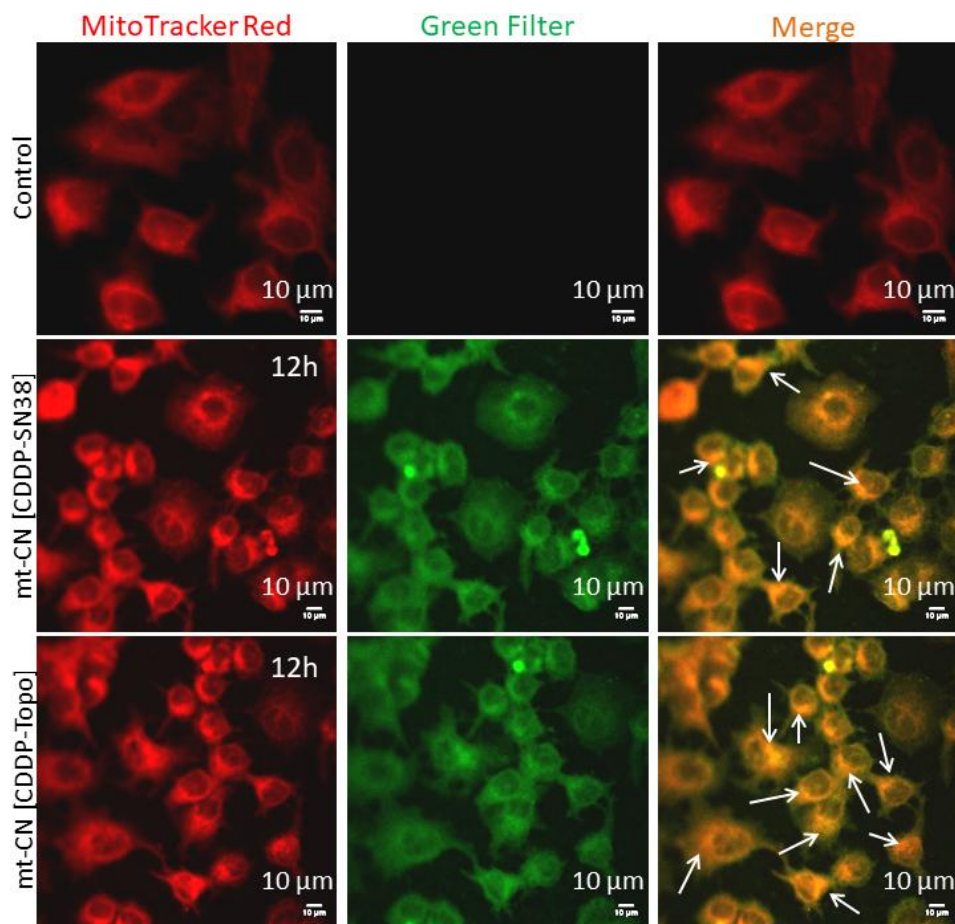


Figure 3: Confocal laser scanning microscopy (CLSM) images of mt-CN in MCF7 cells showing the homing of mt-CN into mitochondria after 12 h of post-incubation. Mitochondria are stained with MitoTracker Red. Scale = 10 μm .

Nanoparticles		CN1	CN2
Image Channels		C1 (green) C2 (red)	C1 (green) C2 (red)
Pearsons' Correlation Coefficient	r	0.7735	0.6299
Manders Coefficients	M1 (fraction of C2 overlapping C3)	0.8657	0.9725
	M2 (fraction of C3 overlapping C2)	0.9018	1.0
Percent volume colocalized		67.69%	55.35%

Table 1 : Quantification of co-localization of Cerberus nanoparticles (CN1 and CN2) into mitochondria in MCF7 cells by CLSM after 12 hours.

3a.2.3. Mitochondrial DNA damage and inhibition of mitochondrial Topoisomerase I:

After homing into mitochondria mt-CNs would be able to damage mitochondrial DNA (mt-DNA) in combination with mitochondrial topoisomerase inhibition by the effect of cisplatin and SN38 or topotecan. We further evaluated the effect of cisplatin in damaging mt-DNA. We treated MCF7 cells with mt-CN [CDDP-SN38] and mt-CN [CDDP-Topo] for 24 h and isolated mitochondrial DNA from nuclear DNA. We used polymerase chain reaction (PCR) to amplify the long segment of the mitochondrial DNA (10 kbp) which clearly showed that both the mt-CNs induced significant mitochondrial DNA damage compared to non-nanoparticle treated control cells (**Figure 4a**). On the other hand, the short segment of the mitochondrial DNA remained nearly unaffected as expected.⁴⁰ Further quantification from PCR revealed that mt-CN [CDDP-SN38] and mt-CN [CDDP-Topo] reduced the long segment of mt-DNA by 4 folds and 2.8 folds compared to the control cells respectively (**Figure 5a**).

Mitochondrial DNA encodes the proteins necessary for oxidative phosphorylation (OXPHOS) inside mitochondria.²⁶ One of the mt-DNA encoded mitochondrial proteins is respiratory chain component mitochondria-encoded cytochrome c oxidase subunit 1 (MTCO1).⁵⁶ To assess the effect of mt-DNA damage on mitochondrial protein synthesis, we treated MCF7 cells with mt-CNs for 24 h and isolated the mitochondria. We evaluated the expression of MTCO1 in isolated mitochondria by gel electrophoresis. From the gel image (**Figure 4b**), it was visually evident that both mt-CNs reduced the expression of MTCO1 compared to no-nanoparticle treated control cells. Further quantification from western blot exhibited that, mt-CN [CDDP-SN38] and mt-CN [CDDP-Topo] reduced the expression of MTCO1 by 3.3 folds and 2 folds respectively (**Figure 5b**). We also evaluated the expression of nuclear DNA encoded protein succinate dehydrogenase subunit A (SDHA) in mitochondria by western blot analysis. The gel electrophoresis of mitochondrial extract of MCF7 cells after treatment with mt-CNs for 24 h showed negligible change in the expression of SDHA (**Figure 4b**). Further quantification from western blot also confirmed that both the mt-CNs reduced the expression of SDHA marginally (**Figure 5c**). These PCR and western blot results clearly demonstrated that mt-CNs spatially damaged mitochondrial DNA keeping nuclear DNA intact leading to mitochondrial translation blockage.

Furthermore, we also evaluated the inhibition of mitochondrial topoisomerase I (Top1mt) by mt-CNs. We treated the MCF7 cells with both mt-CNs for 24 h and fixed the cells followed by treatment with primary antibody specific for Top1mt. The cells were further visualized by CLSM

after staining with Alexa Fluor 488-labelled secondary antibody (green fluorescent) selective for Top1mt. From the CLSM images, it was evident that both mt-CNs reduced the expression of Top1mt significantly compared to non-nanoparticle treated control cells (**Figure 4c**). Quantification from CLSM images revealed that mt-CN [CDDP-SN38] and mt-CN [CDDP-Topo] reduced the mean fluorescence intensity by 2.1 folds and 1.4 folds respectively (**Figure 5d**). These fluorescence microscopy images and quantification indicated that mt-CNs inhibited mitochondrial Topoisomerase I.

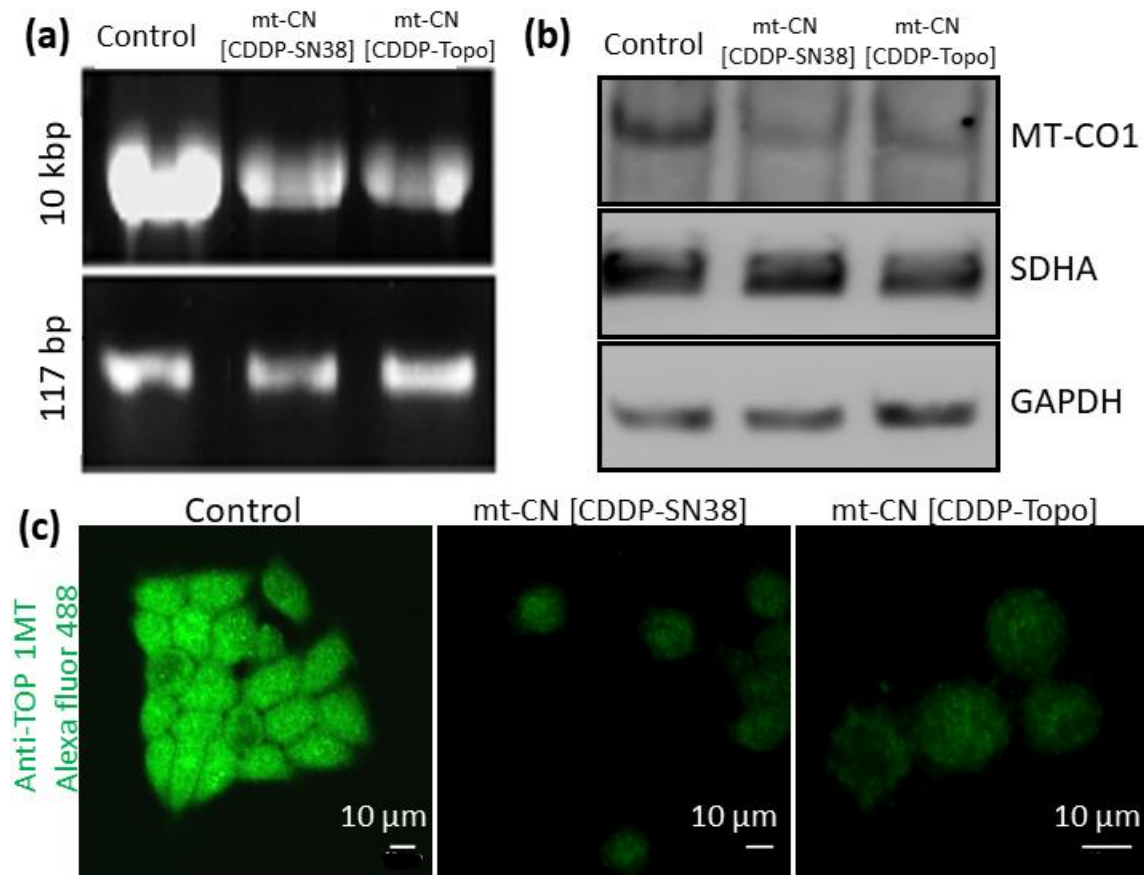


Figure 4: (a) Long and short range PCR in isolated mitochondria from MCF7 cells after treatment with mt-CN for 24 h to show the mitochondrial DNA damage. (b) Western blot analysis of isolated mitochondrial fraction of MCF7 cells after treatment with mt-CN to visualize the expression of MT-CO1 and SDHA. (c) CLSM images of mitochondrial Topoisomerase I in MCF7 cells after treatment with mt-CN for 24 h followed by staining with Anti-Top1MT-Alexa Fluor 488 antibody (green fluorescent). Scale = 10 μm.

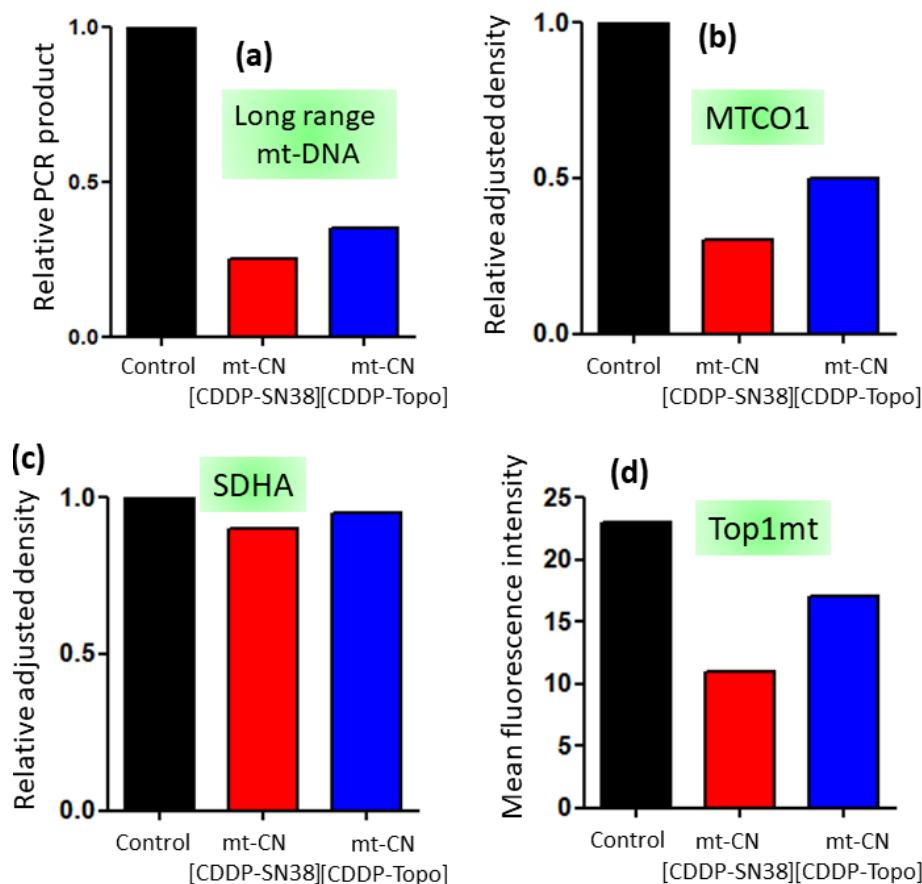


Figure 5: Quantification of (a) long-range mt-DNA fragments from PCR assay, (b) expression of MTCO-1 (c) expression of SDHA and (d) expression of Top1mt from Western blot analysis after treating MCF7 cells with mt-CN for 24 h.

3a.2.4. Impairing mitochondria by mt-CN:

3a.2.4.1 Mitochondrial outer membrane permeabilization (MOMP):

Cerberus nanoparticle (mt-CN)-mediated co-targeting of DNA and Topoisomerase-I in mitochondria would lead to mitochondrial damage through mitochondrial outer membrane permeabilization (MOMP).⁵⁷ The mitochondrial membrane permeabilization was measured by JC1 assay. JC1 (a cationic carbocyanine dye) shows remarkable fluorescence emission shift from monomeric green (~ 529 nm) at outside mitochondria to aggregated red (~ 590 nm) state inside the healthy mitochondrial. As a result, the green and red fluorescence intensity ratio can be used as the marker for mitochondrial damage. To evaluate the MOMP, we treated MCF7 cells with mt-CN for 24 h followed by staining with JC1 dye and the cells were visualized through confocal microscopy. CLSM images in **Figure 6a** clearly exhibited that mt-CN [CDDP-SN38] and mt-CN

[CDDP-Topo] induced much increased green fluorescence intensity compared to red fluorescence indicating the existence of JC1 dye in increased monomeric form outside the mitochondria compared to aggregated form inside the mitochondria. This phenomena leads to more increased green fluorescence regions in merged images. In contrast, non-nanoparticle treated control cells showed nearly comparable green and red fluorescence intensity leading to merged yellow regions indicating that JC1 dye remained in both monomeric and aggregated forms outside and inside mitochondria respectively. Further quantification from the confocal images revealed that mt-CN [CDDP-SN38] and mt-CN [CDDP-Topo] induced 1.57 folds and 1.27 folds in increase in green: red fluorescence intensity respectively compared to control cells (**Figure 7a**). These microscopy images and quantification clearly demonstrated that mt-CNs triggered the mitochondrial damage through outer membrane permeabilization (MOMP).

3a.2.4.2 Mitochondrial transition pore (MTP) formation by mt-CN:

Mitochondrial outer membrane permeabilization by mt-CN triggers the transition pore (MTP) formation. Nanoparticle-mediated MTP formation was further evaluated by Calcein methylester (Calcein AM) assay. Non-fluorescent Calcein AM can enter into the cells to be localized into cytosol and mitochondria.⁵⁸ However, the cytosolic esterases can hydrolyze the ester linkage in Calcein AM into carboxylic acid moiety to release green fluorescent Calcein which can be quenched by CoCl_2 added externally. In contrast, the non-fluorescent Calcein AM in mitochondria remain intact. After MOMP, mitochondrial Calcein AM can be sequestered into cytosol through the formation of MTPs followed by esterase cleavage into green fluorescent Calcein. Hence, to evaluate the MTP formation, we treated MCF7 cells by both mt-CNs for 24 h followed by treatment with Calcein AM and CoCl_2 . The green fluorescence signal from Calcein was visualized by confocal microscopy. The CLSM images in **Figure 6b** evidently showed that mt-CN[CDDP-SN38] and mt-CN[CDDP-Topo] significantly increased the release of green fluorescent Calcein from mitochondria into cytosol indicating the formation of mitochondrial transition pores after MOMP. In contrast, the untreated control cells showed weak fluorescence signals indicating mitochondria without transition pores through MOMP. We also quantified the formation of green fluorescent Calcein from the confocal images. It was observed that mt-CN [CDDP-SN38] and mt-CN [CDDP-Topo] increased 1.5 folds and 1.4 folds mean fluorescence intensity respectively compared to non-treated control cells (**Figure 7b**). These CLSM images

and quantification indicated that mt-CNs induced transition pore formation into mitochondrial after outer membrane permeabilization.

3a.2.4.3 Mitochondrial damage by mt-CN:

Nanoparticle-mediated MOMP and MTP formation would weaken mitochondrial

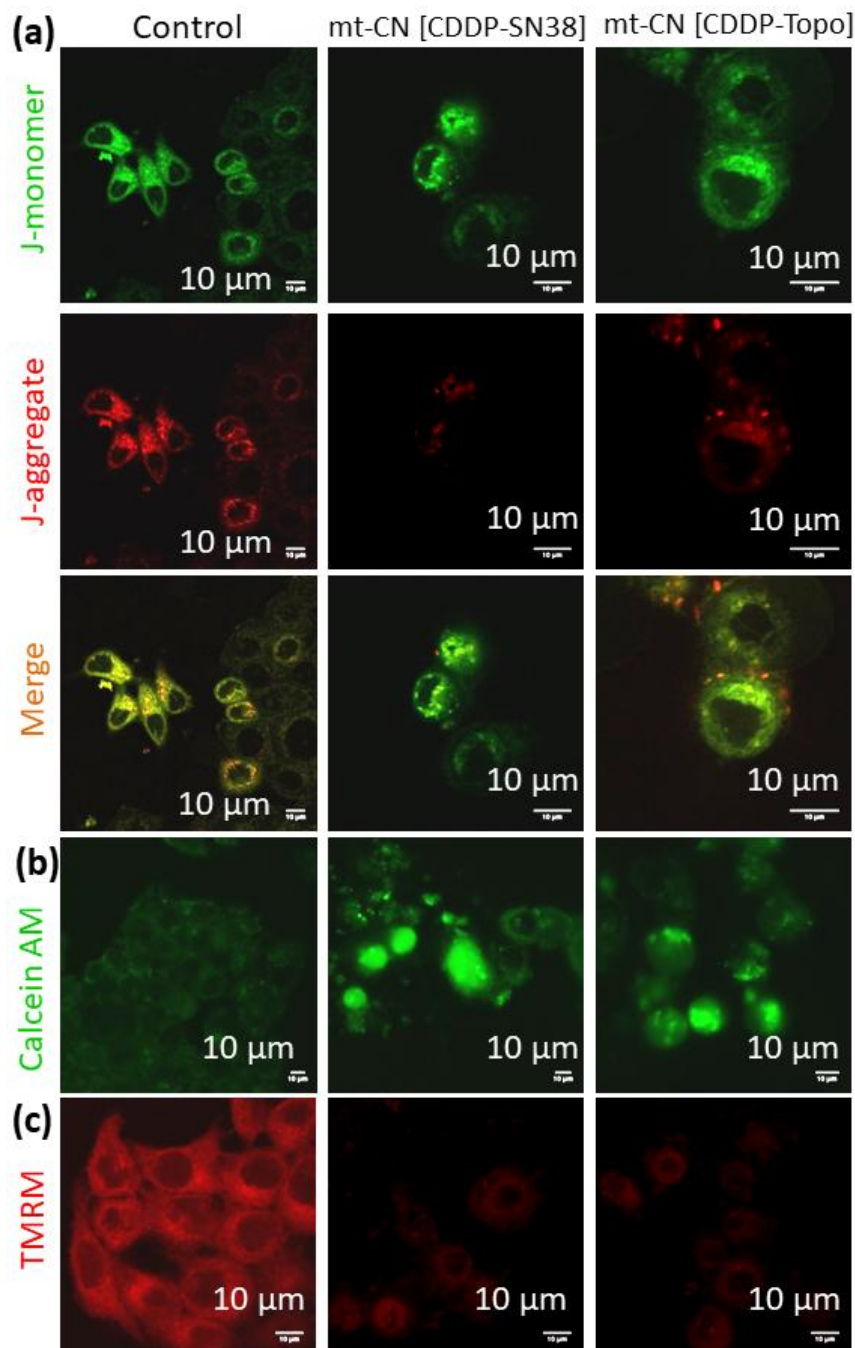


Figure 6: Mitochondrial damage induced by mt-CN in MCF7 cells was visualized by confocal microscopy through (a) JC1 assay (b) Calcein AM assay and (c) TMRM assay. Scale = 10 μm.

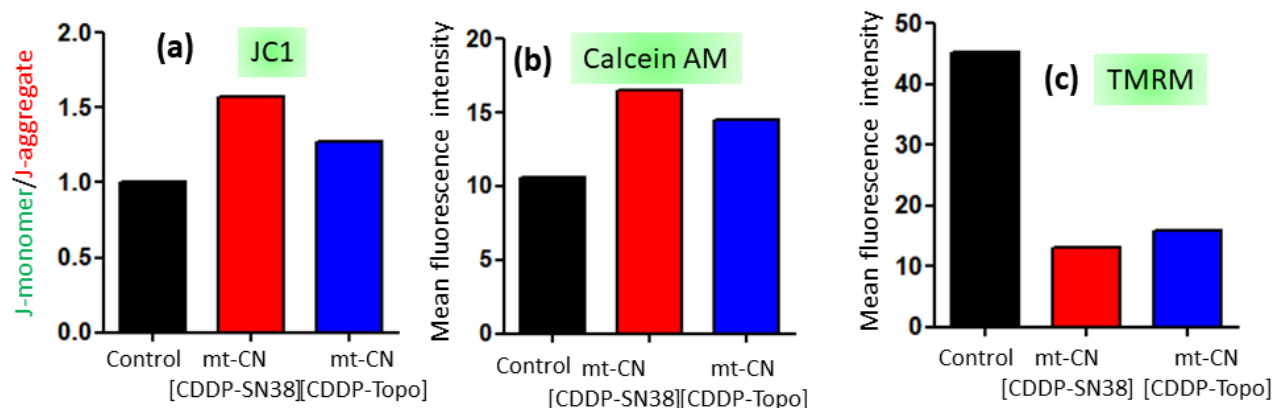


Figure 7: Confocal laser scanning microscopy based quantification of (a) J-monomer/J-aggregate in JC1 assay, (b) mean fluorescence intensity of Calcein AM and (c) mean fluorescence intensity of TMRM from MCF7 cells after treatment with mt-CNs for 24 h.

hyperpolarization. Mitochondria damage induced by mt-CNs was evaluated by tetramethyl rhodamine methyl ester (TMRM) assay,⁵⁹ where red fluorescent cationic TMRM would be accumulated into undamaged hyperpolarized mitochondria for their higher $\Delta\Psi_m$. MCF7 cells were treated with both mt-CNs for 24 h and red fluorescence inside the cells was visualized by confocal fluorescence microscopy. The confocal microscopy images in **Figure 6c** demonstrated that mt-CN [CDDP-SN38] and mt-CN [CDDP-Topo] reduced the sub-cellular intensity of red fluorescent TMRM significantly compared to control cells. We also quantified the TMRM retained inside the cells from confocal images, which revealed that mt-CN [CDDP-SN38] and mt-CN [CDDP-Topo] reduced 3.5 folds and 2.8 folds mean fluorescence intensity respectively compared to non-nanoparticle treated cells (**Figure 7c**). The fluorescence imaging exhibited that mt-CNs induced mitochondrial damage by MOMP and MTP formation.

3a.2.5. Cytochrome c release and ROS generation:

Mitochondrial outer membrane permeabilization triggers the sequestration of pro-apoptotic molecule cytochrome c into cytosol to induce apoptosis.^{57, 60} The expression of cytochrome c after mt-CN-mediated MOMP was visualized by confocal fluorescence microscopy. MCF7 cells were treated with mt-CNs for 24 h and cytochrome c was stained with green fluorescently labeled Alexa Fluor 488 anti-cytochrome c antibody. The fluorescence confocal microscopy images (**Figure 8a**) evidently confirmed that mt-CN [CDDP-SN38] and mt-CN [CDDP-Topo] increased the expression of cytochrome c in MCF7 cells compared to control cells. Moreover, it

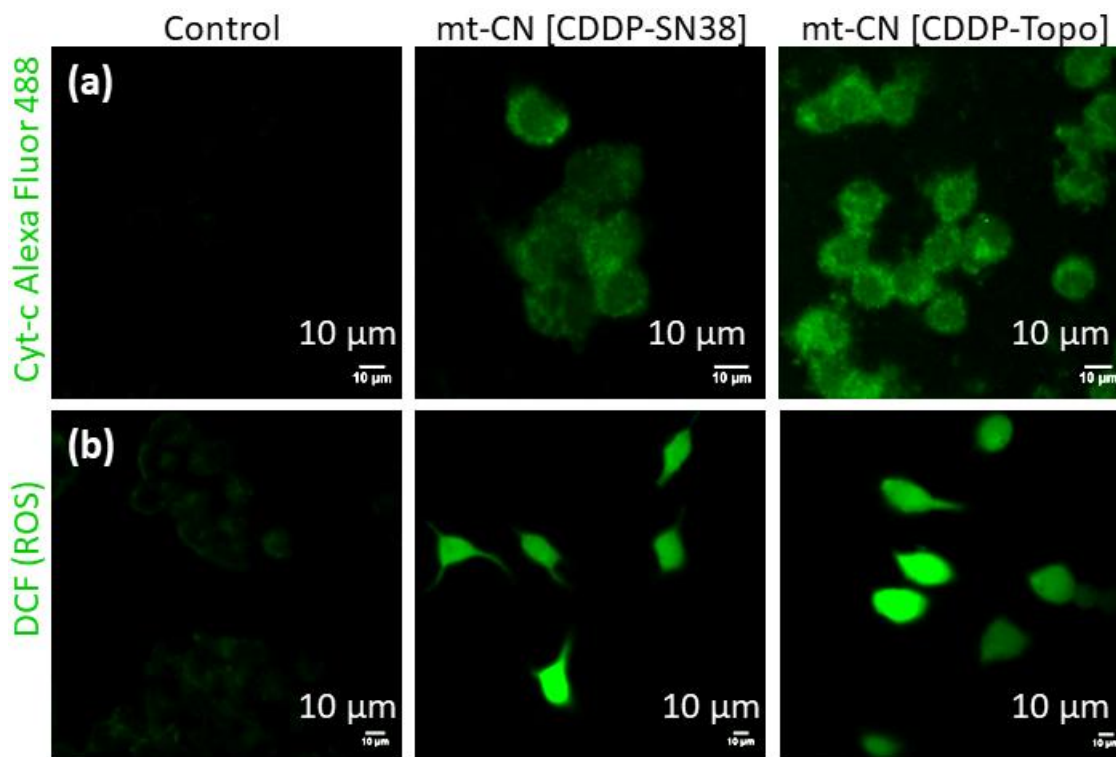


Figure 8: CLSM images of MCF7 cells after treatment with mt-CN for 24 h to visualize (a) the expression of cytochrome c stained with green fluorescent Alexa Fluor 488 labeled anti-cytochrome c antibody (b) generation of reactive oxygen species (ROS) by DCF assay. Scale = 10 μm.

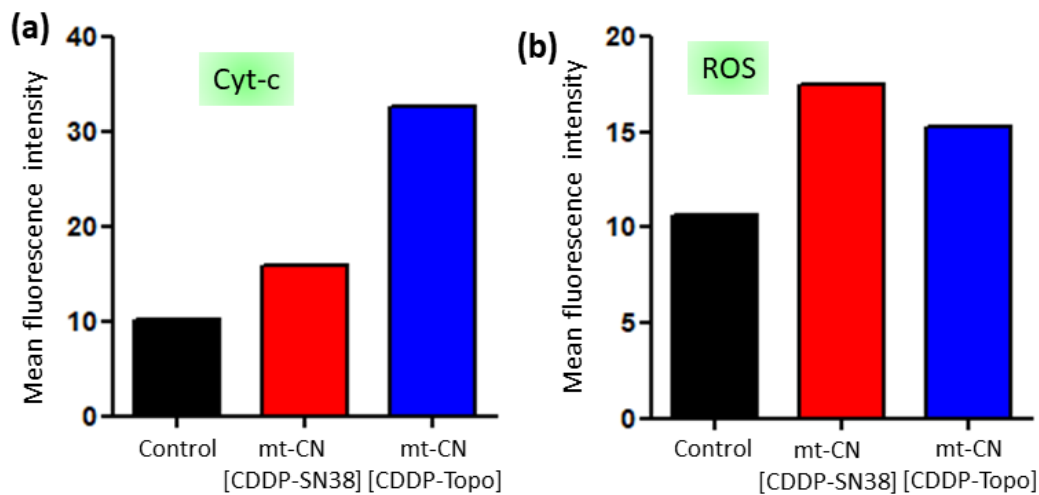


Figure 9 : Quantification of mean fluorescence intensity from confocal microscopy of (a) cytochrome c and (b) reactive oxygen species (ROS) in MCF7 cells after treatment with mt-CN for 24 h.

was also observed that mt-CN [CDDP-SN38] and mt-CN [CDDP-Topo] increased the fluorescent intensity from green fluorescent Alexa Fluor 488 anti-cytochrome antibody into 1.5 folds and 3.2 folds respectively (**Figure 9a**). From this microscopy study and quantification, it was evident that mt-CN-mediated mitochondrial damage released cytochrome c from mitochondria into cytosol to induce further cell death.

Furthermore, mitochondrial damage leads to the formation of reactive oxygen species (ROS) into the cells to trigger cell death⁵⁹. Hence, we assessed the production of ROS after mitochondrial damage by mt-CN by dichlorodihydrofluorescein diacetate (H₂DCFDA) assay.⁶¹ In the sub-cellular milieu, non-fluorescent H₂DCFDA gets hydrolyzed into the corresponding dicarboxylic acid, which is further oxidized by the reactive-oxygen species inside the cells to afford green fluorescent dichlorofluorescein (DCF). Hence, we treated MCF7 cells with mt-CN for 24 h and the cells were stained with H₂DCFDA. The live cells were further visualized by fluorescence confocal microscopy to evaluate the ROS generation. **Figure 8b** clearly demonstrated both the mt-CN induced the generation of ROS by remarkable increase in green fluorescence intensity into MCF7 cells compared to no-nanoparticle treated control cells. Subsequent quantification from fluorescence microscopy revealed that mt-CN [CDDP-SN38] and mt-CN [CDDP-Topo] increased the mean fluorescence intensity by 1.6 folds and 1.4 folds respectively (**Figure 9b**). These confocal imaging and quantification, it was evident that mt-CN-mediated mitochondrial damage lead to generation of reactive-oxygen species (ROS) in MCF7 breast cancer cells.

3a.2.6. Induction of apoptosis and cell death:

Cerberus nanoparticle-mediated mitochondrial damage and subsequent release of cytochrome c and generation of ROS would trigger the cells into apoptosis (programmed cells death).⁶² Induction of apoptosis was assessed by flow cytometry analysis. MCF7 cells were treated with mt-CN for 24 h and cells were stained by FITC-labeled Annexin V (green fluorescent) to evaluate the flipped phosphatidylserines on the outer surface of early apoptotic cells. The cells were further treated with red fluorescent propidium iodide (PI) to stain the DNA of the late apoptotic and necrotic cells. From the flow cytometry data, it was observed that mt-CN [CDDP-SN38] triggered 71.9 %, 6.8 % and 0.1 % cells into early apoptosis, later apoptosis and necrosis respectively (**Figure 10a**). On the other hand, mt-CN [CDDP-Topo] treated cells were found in 64.3 %, 10.6 % and 0.1 % in early apoptotic, late apoptotic and necrotic stages respectively

(**Figure 10a**) compared to non-treated control cells. From this flow cytometry data, it was confirmed that mt-CNs induced early and late apoptosis in MCF7 cells through mitochondrial damage.

Apoptosis in cancer cells is initiated by caspase-9, which is cleaved to trigger the programmed cell death.⁶³ To evaluate the expression of caspase-9, MCF7 cells were treated with mt-CNs for 24 h and the cells were successively treated by caspase-9 antibody. The expression of caspase-9 was visualized by confocal microscopy after staining the cells with red fluorescently labeled Alexa Fluor 567-anti-caspase-9 antibody. The CLSM images in **Figure 10b** indicated that both mt-CNs reduced the expression of caspase-9 significantly in MCF7 cells compared to control cells. Fluorescence confocal microscopy based quantification also revealed that mt-CN [CDDP-SN38] and mt-CN [CDDP-Topo] reduced the red fluorescent intensity by 2.5 folds and 1.4 folds respectively (**Figure 11a**). We further measure the expression of caspase-9 by Western blot analysis. MCF7 cells were treated with mt-CNs for 24 h caspase-9 was visualized and quantified by gel electrophoresis. Figure 6c convincingly indicated that both mt-CNs reduced the expression of caspase-9 in MCF7 cells. The quantification of protein expression from Western blot also showed that mt-CN [CDDP-SN38] and mt-CN [CDDP-Topo] reduced the expression of caspase-9 by 1.3 folds and 1.2 folds respectively (**Figure 11b**). These confocal microscopy and gel electrophoresis convincingly showed that mt-CNs induced apoptosis in MCF7 cells by cleavage of caspase-9.

Finally, we assessed the effect of mitochondrial damage over cancer cell's death. We treated MCF7 cells by mt-NPs in a dose dependent manner over 48 h and evaluated the cell viability by MTT assay. As control, MCF7 cells were treated with the cocktail of α -TOS, cisplatin and SN38 or Topotecan in the same ratio present in the nanoparticles. At 48 h, post-incubation, mt-CN [CDDP-SN38] showed much lower $IC_{50} = 5.9 \mu\text{M}$ with 8.4 % cell viability at 30 μM (concentration of SN38 in nanoparticle) (**Figure 10d**). In contrast, the free drug cocktail showed much higher $IC_{50} = 9.6 \mu\text{M}$ with much higher cell viability = 22.4 % at 30 μM (concentration of SN38 in the cocktail). Interestingly, mt-CN [CDDP-Topo] showed almost similar $IC_{50} = 7.7 \mu\text{M}$ (cell viability = 13.2 % at 30 μM Topotecan concentration in the nanoparticle) compared to the $IC_{50} = 8.1 \mu\text{M}$ (cell viability = 19.7 % at 30 μM Topotecan concentration in the cocktail) shown by the free drug cocktail (**Figure 10e**). These cell viability data clearly demonstrated that mt-CN [CDDP-SN38] showed much improved cell killing efficacy compared to the free drug cocktails.

However, mt-CN [CDDP-Topo] showed comparable efficacy towards MCF7 cells in comparison to free drug combination. We anticipate that these mt-CN can serve as tools to spatially inhibit multiple targets into mitochondria for enhanced efficacy towards cancer cells.

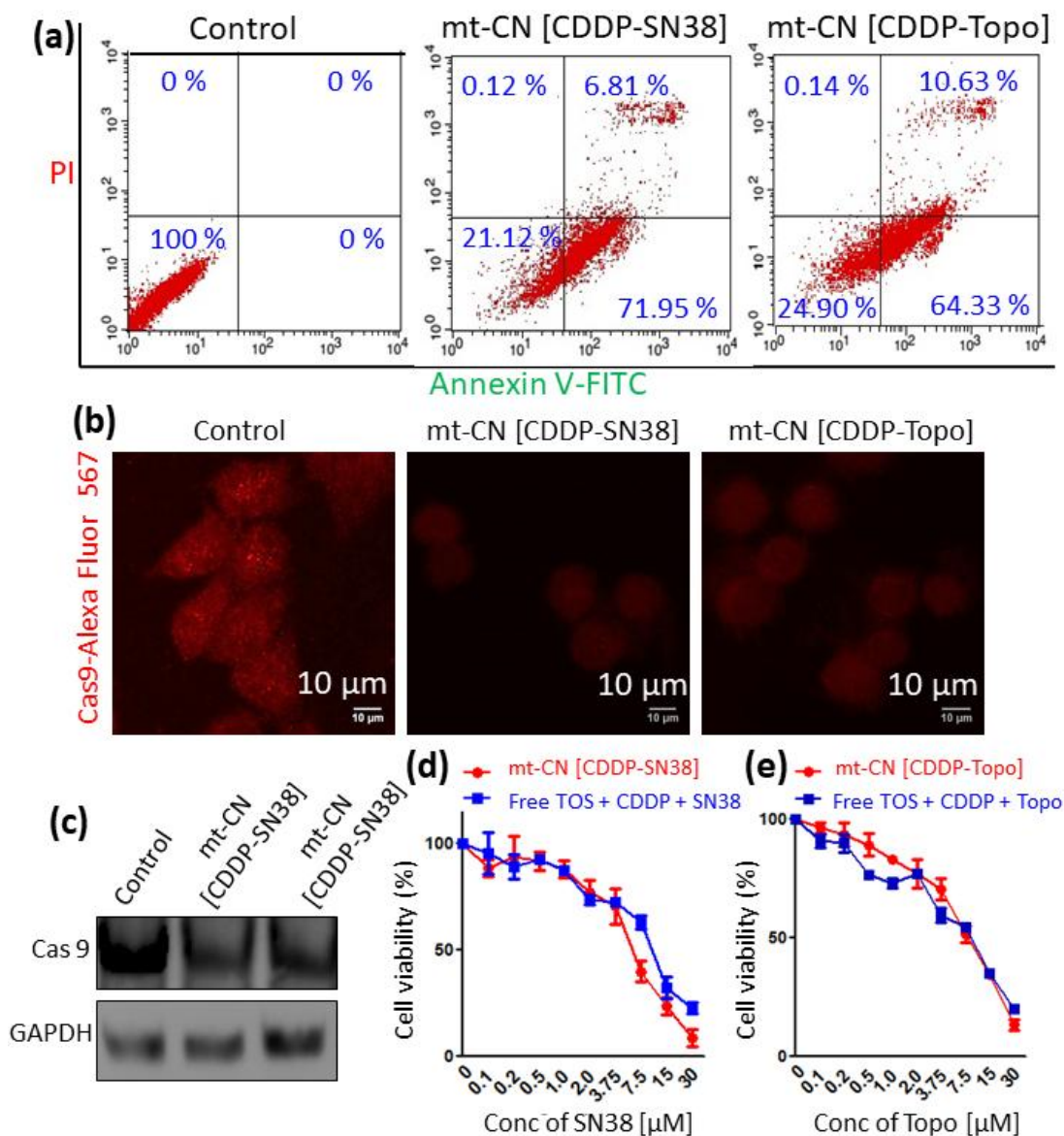


Figure 10: (a) Induction of apoptosis in MCF7 cells after treatment with mt-CN for 24 h, measured by flow cytometry analysis. (b) CLSM images of MCF7 cells after treatment with mt-CN for 24 h followed by staining caspase-9 with red fluorescent Alexa Fluor 567 labeled caspase-9 antibody. Scale = 10 μ m. (c) Western blot analysis of caspase-9 in MCF7 cells after treatment with mt-CN for 24 h. (d) Cell viability of MCF7 cells after treatment with mt-CN for 24 h by MTT assay.

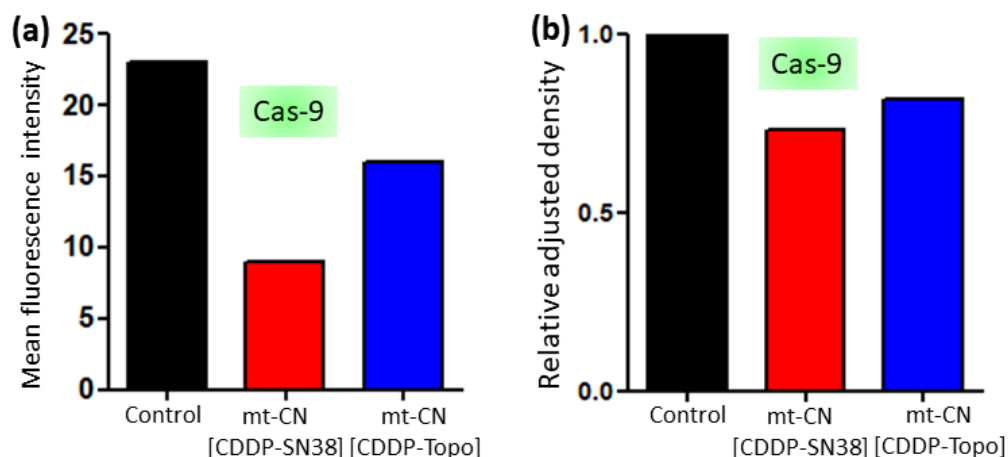


Figure 11 Quantification of (a) mean fluorescence intensity of caspase-9 from confocal microscopy and (b) expression of caspase-9 from gel electrophoresis in MCF7 cells after treatment with mt-CN for 24 h.

3a.3. Conclusion

In conclusion, we have engineered triphenylphosphine (TPP) coated mitochondria targeted Cerberus Nanoparticle (mt-CN) which can comprise DNA damaging agent (cisplatin) and Topoisomerase I inhibitor (SN38 or Topotecan) in a single nanoparticle for augmented efficacy. These positively charged sub 200 nm spherical nanoparticles can home into mitochondria of MCF7 breast cancer cells within 12 h. These mt-CN damaged mitochondrial DNA along with inhibition of mitochondrial Topoisomerase I (Top1mt) simultaneously leading to shutting down the mitochondrial translational machinery keeping nuclear translation unaffected. This co-targeting of mitochondrial DNA and Top1mt induced mitochondrial outer membrane permeabilization (MOMP) and mitochondrial transition pore (MTP) opening leading to mitochondrial damage. This mt-CN-mediated mitochondrial damage sequestered pro-apoptotic cytochrome c and generated reactive oxygen species (ROS) to induce apoptosis into MCF7 cells through caspase-9 cleavage. Finally, these mt-CN showed improved efficacy in MCF7 breast cancer cell killing compared to free drug combination. We anticipate that these novel Cerberus Nanoparticles can be used as platform to impair multiple targets specifically into mitochondria of tumor tissues as next-generation cancer therapeutics.

3a.4. Materials and Method

3a.4.1 Materials. α -tocopherylsuccinate, 5-bromopentanol, triphenylphosphine, cisplatin, Calcein AM, L- α -phosphatidylcholine (PC), JC 1 dye, TMRM and silicon wafer were procured from Sigma-Aldrich. SN38 and topotecan were bought from Selleck Chemicals. MitoTracker Red[®] FM, *SlowFade*[®] diamond antifade reagent and were obtained from Life Technologies. MCF7 cells were obtained from National Centre for Cell Science (NCCS), Pune. Anti-Caspase-9 primary antibody, HRP Goat anti-rat IgG, HRP Goat anti-mouse IgG, and Annexin V-FITC labeling solution were bought from Biolegend. Cytochrome c rabbit mAb, anti-rabbit IgG and HRP-linked antibody were obtained from CST. Rabbit anti-chicken IgG antibody, Alexa Fluor[®] 488 goat anti-rabbit IgG (H+L) antibody were purchased from Life technologies. Alexa Fluor 567-labeled secondary antibody was purchased from Invitrogen. H₂DCFDA was purchased from MitoBiogenesis[™]. Western Blot Cocktail and Anti-TOP1MT antibody were purchased from Abcam. The mitochondria isolation kit for cultured cells was bought from the Thermo Scientific.

3a.4.2. Synthesis of α -TOS-TPP conjugate (1). α -TOS-TPP conjugate (1) was synthesized in a two-step process starting from α -tocopherylsuccinate (α -TOS).⁵³ In short, α -TOS (200 mg, 0.38 mmol) was reacted with 5-bromopentanol (92 μ L, 0.7 mmol) in presence of DCC (100 mg, 0.4 mmol) and catalytic amount of DMAP for 3 h to obtain the corresponding ester which was further refluxed with triphenylphosphine in presence of potassium carbonate (K₂CO₃) as base to afford α -TOS-TPP conjugate (1) in 35 % yield.

3a.4.3. Synthesis of α -TOS-CDDP conjugate (2). α -TOS-CDDP conjugate (2) was synthesized by previously reported procedure.⁶⁴ Briefly, a solution of α -TOS (5 mg, 0.009 mmol) in 1 mL DMF was mixed with aquated cisplatin (500 μ L) and the reaction mixture was stirred for 24 h followed by solvent evaporation to obtain α -TOS-CDDP conjugate (2) in 89 % yield.

3a.4.4 Engineering of Cerberus Nanoparticle (mt-CN). 6.0 mg of L- α -phosphatidylcholine (PC), 1.0 mg of α -TOS-TPP conjugate (1), 1.0 mg of α -TOS-CDDP conjugate (2), 1.0 mg of SN38 or Topotecan and 0.6 mg of 1,2-distearoyl-*sn*-glycero-3-phosphoethanolamine-N-[amino(polyethylene glycol)2000] (DSPE-PEG) were dissolved in 5.0 mL DCM-methanol mixture. Solvent was evaporated thoroughly to form a thin uniform lipid film. The lipid film was aquated with 1 mL water for 1 h at 60 °C. The nanoparticles formed were passed through

Sephadex G-25 followed by extrusion through 200 nm filter. The Cerberus nanoparticles (mt-CNs) were stored at 4 °C for further use.⁶⁵

3a.4.5 Dynamic light scattering and FESEM. Hydrodynamic diameter and surface charge were determined by dynamic light scattering (DLS) by using Zetasizer Nano2590 (Malvern).⁶⁴ The size and morphology were visualized by field emission scanning electron microscopy (FESEM) by spotting the sample over silicon chip followed by gold coating and imaging in Carl Zeiss at 4 kV voltage.⁶⁴

3a.4.6 Determination of drug loading in mt-CN. A Calibration curve was plotted in the concentration range of 12.5-200 µM (for SN38) and 25-200 µM (for topotecan) by diluting the 1 mM standard stock solution of drugs in DMSO and water. The absorbance was measured at 387 nm and 405 nm for SN38 and topotecan respectively with respect to the corresponding solvent blank. A linear graph was plotted for absorbance (A) versus concentration (C). mt-CNs were dissolved in spectroscopic grade DMSO in 1 % dilution (in triplicate). Absorbance was measured at characteristic wavelength against the corresponding solvent blank in 200 µL quartz cuvette and from the calibration curve drug loading was measured in triplicate.^{53, 64}

3a.4.7 Stability of mt-CN. The stability of the mt-CNs was checked at 4 °C and 37 °C by DLS. 50 µL of mt-CN solution was diluted to 1 mL using de-ionized water and hydrodynamic diameter was recorded in triplicate. This was done for 7 days storing the nanoparticles at 4 °C. Similarly, the mt-CNs were incubated in DMEM cell culture media containing 10% FBS at 37°C for 3 days and hydrodynamic diameter was measured in triplicate in predetermined time points.⁶⁴

3a.4.8 Mitochondria localization. 2.0×10^4 MCF7 cells were seeded in a lab tek chamber slide 8 well (per well) and attached for 24 h. Cells were then treated with mt-CNs for 12 h. Cells were washed with PBS (pH = 7.4) and treated with MitoTracker Red® FM (200 nM) followed by incubation in dark at 37 °C for 25 min. Staining solution was removed and cells are washed with PBS. The cells were visualized by Zeiss LSM 710 confocal microscopy.⁵³

3a.4.9 Quantification of mt-DNA by polymerase chain reaction (PCR). 2×10^6 MCF7 cells were attached on a 6 well plate. Cells were then treated with mt-CNs for 24 h. A control was kept without adding the nanoparticles. Cells were then trypsinized and pelleted by centrifugation at 750 X g. The DNA isolation was performed from cell pellets using the Sigma GenElute Mammalian Genomic DNA Miniprep kit according to the manufacturer's protocol. The concentration of DNA in all samples was quantified by PicoGreen staining. Samples were

diluted in dd-H₂O to equal concentrations of 2 ng/μL. 10 ng of each template was inputted into the reaction.

Long-range polymerase chain reaction (PCR) was used to quantify the Mitochondrial DNA isolated from total DNA of the whole cell after treatment using the Elongase long range PCR enzyme kit (Invitrogen) with 2 mM Mg²⁺. A 10-Kb fragment and a shorter region of mtDNA (117 pb) were amplified. PCR reactions were limited to 14 and 16 cycles, to ensure that amplification process was still in the exponential phase. Primer sequences used for mtDNA analysis are:

Long range PCR: 5'-TCTAAGCCTCCTTATTCGAGCCGA-3' and 5'-TTTCATCATGCGGAGATGTTGGATGG-3'

Short range PCR: 5'-AAGTCACCCTAGCCATCATTCTAC-3' and 5'-GCAGGAGTAATCAGAGGTGTTCTT-3'

PCR conditions were: (1) 94 °C, 1 min; (2) 68 °C, 12 min and was repeated for 16 cycles; (3) 68 °C, 10 min for Long range PCR

3.a.4.10 Analysis of electron transport chain proteins. 3 x 10⁸ MCF7 cells were incubated in T75 flask overnight for attachment and then treated with mt-CNs for 24 h. A control was kept without adding the nanoparticles. After the treatment, media was removed and cells were trypsinized and washed with PBS by means of centrifugation at 750 X g for 4 min to obtain a cell pellet. The mitochondria were isolated from the cell pellet by mitochondria isolation kit using the protocol described by the manufacturer. The mitochondrial pellets were resuspended in RIPA buffer with protease inhibitors (Cell Signaling Technology) and placed on ice for 30 min with occasional vortexing. The total mitochondrial protein concentration was quantified using a 660 nm protein assay (Thermo Scientific). Mitochondrial protein lysates (15 μg) were loaded onto 4–15% polyacrylamide gel (Biorad) and standard Western blotting procedure was followed. For SDS-PAGE and Western Blot analysis, 7.5 μg of protein were boiled with 6 X SDS-PAGE loading buffer and samples were separated on precast NU-PAGE 10% Bis-Tris minigels (Novex). Western Blot analysis was performed in Western cocktail antibody. Chemiluminescence was used to detect immune-reactive proteins, and protein abundance was quantified based on band intensities using ImageQuant software.

3a.4.11 Detection of Mitochondrial Topoisomerase 1 (Top1mt) by immunostaining. 5 x 10⁴ MCF7 cells were seeded on a coverslip in a 6 well plate for attachment. Cells were then treated

with mt-CNs for 24 h. Cells were washed once PBS followed by treatment with 3.7% paraformaldehyde at 37 °C for 15 min. Cells were then washed again with PBS and were treated with blocking buffer at room temperature. Cells were then incubated in Top1mt primary antibody solution (1:100 dilution) at 37 °C for 3 h. Cells were further washed with blocking buffer. Cells were incubated with Alexa Fluor 488-labelled secondary antibody solution (1:500 dilution) at 37 °C for 40 min in dark. Cells were mounted on a glass slide using SlowFade® gold antifade reagent. The slides were visualized by using a CLSM (Zeiss LSM 710).

3a.4.12 Determination of mitochondrial outer membrane permeabilisation (MOMP):

2.0×10^4 MCF7 cells were attached in lab tek chamber slide 8 well and cells were treated with mt-CNs for 24 h.

3a.4.12.1 JC 1 assay. Cells were washed with PBS (pH = 7.4) and incubated with JC1 dye ($10 \mu\text{g mL}^{-1}$) at 37 °C for 20 min. The excess dye was aspirated and cells are washed thrice with PBS.

3a.4.12.2 TMRM assay. Cells were then washed with PBS and incubated with TMRM dye ($10 \mu\text{g mL}^{-1}$) for 20 min.

3a.4.12.3 Calcein AM assay. Cells were then washed twice with PBS and incubated with $1 \mu\text{M}$ Calcein AM and 1 mM CoCl_2 in modified Hanks' balanced solution supplemented with 10 mM Na-HEPES (pH = 7.4) without phenol red and sodium bicarbonate at 37 °C for 30 min. The cells are washed with PBS for the complete removal of Calcein AM and CoCl_2 .

Cells were finally subjected to confocal laser scanning microscopy using Zeiss LSM 710.⁵³

3a.4.13 Generation of Reactive Oxygen Species (ROS). 2.0×10^4 MCF7 cells were attached in a lab tek chamber slide 8 well. Cells were then treated with mt-CNs for 24 h. Cells were washed with PBS and incubated with DCFDA ($10 \mu\text{g mL}^{-1}$) for 20 min. The excess dye was removed and cells are washed with PBS. The cells were subjected to fluorescence imaging using a CLSM (Zeiss LSM 710).⁵³

3a.4.14 Release of Cytochrome C. 5×10^4 MCF7 cells were attached on a coverslip in a 6 well plate. Cells were then treated with mt-CNs for 24 h. Cells were washed with PBS and then treated with 3.7% paraformaldehyde for 15 min. Cells were then washed with PBS and were permeabilized by incubating in blocking buffer. Cells were then incubated in primary antibody solution (cytochrome c in 1:100 dilution) at for 3 h. Cells are washed thrice with blocking buffer followed by incubated in Alexa Fluor® 488 secondary antibody solution (1:500 dilution) at 37

°C for 40 min in dark. Cells were washed with PBS and mounted on a glass slide using SlowFade® gold antifade reagent. The cells were subjected to fluorescence imaging using a CLSM (Zeiss LSM 710).⁵³

3a.4.15 Apoptosis detection by flow cytometry. Detection of apoptosis by mt-CNs in MCF7 cells were performed using previously described method.⁵³ In short, 2×10^6 MCF7 cells were attached in 6 well plates and treated with mt-CNs for 24 hours. Cells were trypsinized and resuspended in 100 μ L of Annexin V binding buffer followed by treatment with 5 μ L of APC Annexin V and 10 μ L of propidium iodide solution. The apoptotic cells were quantified by using BD FACS Calibur.

3a.4.16 Caspase 9 activity. For immunostaining assay, 5×10^4 MCF7 cells were attached on a coverslip in a 6 well plate. Cells were treated with mt-CN for 24 h. Cells were washed and treated with 3.7% paraformaldehyde. Cells were then permeabilized by incubating in blocking buffer and incubated in Caspase 9 primary antibody solution (1:100 dilution) for 3 h. Cells are washed with blocking buffer incubated in Alexa Fluor 567 conjugated secondary antibody solution (1:500 dilution) at 37 °C for 40 min in dark. Cells were washed with PBS and mounted on a glass slide using SlowFade® gold antifade reagent. Cells were imaged using a CLSM (Zeiss LSM 710).

For western blot, after 24 h treatment with mt-CNs, cells were lysed and suspended in sample buffer. Proteins were separated using SDS-polyacrylamide gel electrophoresis (SDS-PAGE) and transferred onto the membrane (electro-blotting) and the proteins imaged using previously described method.⁵³ In short, blotted membrane was then blocked in freshly prepared TBS containing non-fat dry milk (5%) for 1 h with constant shaking at room temperature. Membrane was then rinsed with TBST and incubated in the Caspase-9 antibody (1:1000 dilution, except 1:2500 or GAPDH) overnight at 4 °C with gentle agitation (except 4 h for GAPDH). Membrane was then washed 3 times (15 min each) with TBST and incubated in anti- mouse HRP conjugated secondary antibody solution (1:500 dilution) for 45 min at room temperature with gentle agitation. Membrane was further washed thrice with TBST (5 min each). Protein detection was then performed by using Immobilon Western Chemiluminescent HRP Substrate (membrane was incubated in the substrate for 1 min). Images were acquired using GE Healthcare Lifesciences ImageQuant LAS 4000. After the acquisition, membrane was boiled in distilled

water for 5 min and re-probed for GAPDH protein. Further image processing and intensity calculations were performed using ImageJ software.

3a.4.17 Cell viability assay. 5×10^3 MCF7 cells were attached per well in 96-well plate. Cells were then treated with mt-CNs and free drug combinations in different concentrations (0.11, 0.23, 0.46, 0.92, 1.87, 3.75, 7.5, 15, 30 μ M) for 48 h. The cell viability was measured using the MTT assay described previously^{52, 53}. The percent cell viability was calculated considering the untreated cells as 100 % viability and the effectiveness of mt-CNs was compared with the free drug combinations.

3a.5. Reference

1. Siegel, R.; Miller, K.; Jemal, A. Cancer Statistics , 2015 . *CA Cancer J Clin.* **2015**, *65* , 87-108
2. Early Breast Cancer Trialists' Collaborative Group (EBCTCG). Effects of Chemotherapy and Hormonal Therapy for Early Breast Cancer on Recurrence and 15-Year Survival: An Overview of the Randomised Trials. *Lancet* **2005**, *365* , 1687–1717.
3. Henderson, I. C.; Berry, D. A.; Demetri, G. D.; Cirincione, C. T.; Goldstein, L. J.; Martino, S.; Ingle, J. N.; Cooper, M. R.; Hayes, D. F.; Tkaczuk, K. H.; Fleming, G.; Holland, J. F.; Duggan, D. B.; Carpenter, J. T.; Frei, E.; Schilsky, R. L.; Wood, W. C.; Muss, H. B.; Norton, L. Improved Outcomes from Adding Sequential Paclitaxel but Not from Escalating Doxorubicin Dose in an Adjuvant Chemotherapy Regimen for Patients with Node-Positive Primary Breast Cancer. *J. Clin. Oncol.* **2003**, *21* , 976–983.
4. Citron, M. L.; Berry, D. A.; Cirincione, C.; Hudis, C.; Winer, E. P.; Gradishar, W. J.; Davidson, N. E.; Martino, S.; Livingston, R.; Ingle, J. N.; Perez, E. A.; Carpenter, J.; Hurd, D.; Holland, J. F.; Smith, B. L.; Sartor, C. I.; Leung, E. H.; Abrams, J.; Schilsky, R. L.; Muss, H. B.; Norton, L. Randomized Trial of Dose-Dense versus Conventionally Scheduled and Sequential versus Concurrent Combination Chemotherapy as Postoperative Adjuvant Treatment of Node-Positive Primary Breast Cancer: First Report of Intergroup Trial C9741/Cancer and Leukemia Group B Trial 9741. *J. Clin. Oncol.* **2003**, *21* , 1431–1439.
5. McArthur, H. L.; Hudis, C. a. Breast Cancer Chemotherapy. *Cancer J.* **2007**, *13* , 141–147.

6. Aas, T.; Børresen, A. L.; Geisler, S.; Smith-Sørensen, B.; Johnsen, H.; Varhaug, J. E.; Akslen, L. A.; Lønning, P. E. Specific P53 Mutations are Associated with de Novo Resistance to Doxorubicin in Breast Cancer Patients. *Nat. Med.* **1996**, *2*, 811–814.
7. Meacham, C. E.; Morrison, S. J. Tumour Heterogeneity and Cancer Cell Plasticity. *Nature*, **2013**, *501*, 328-337.
8. Burrell, R. A.; McGranahan, N.; Bartek, J.; Swanton, C. The Causes and Consequences of Genetic Heterogeneity in Cancer Evolution. *Nature*, **2013**, *501*, 338-345.
9. Quail, D. F.; Joyce, J. A. Microenvironmental Regulation of Tumor Progression and Metastasis. *Nat. Med.* **2013**, *19*, 1423–1437.
10. Knight, Z. A.; Lin, H.; Shokat, K. M. Targeting the Cancer Kinome through Polypharmacology. *Nat. Rev. Cancer* **2010**, *10*, 130–137
11. Cunningham, R. M.; DeRose, V. J. Platinum Binds Proteins in the Endoplasmic Reticulum of *S. Cerevisiae* and Induces Endoplasmic Reticulum Stress. *ACS Chem. Biol.* **2017**, *12*, 2737–2745.
12. Galluzzi, L.; Larochette, N.; Zamzami, N.; Kroemer, G. Mitochondria as Therapeutic Targets for Cancer Chemotherapy. *Oncogene* **2006**, *25*, 4812–4830.
13. Clarke, H. J.; Chambers, J. E.; Liniker, E.; Marciniak, S. J. Endoplasmic Reticulum Stress in Malignancy. *Cancer Cell* **2014**, *25*, 563–573.
14. Wallace, D. C. Mitochondria and Cancer. *Nat. Rev. Cancer* **2012**, *12*, 685–698.
15. Fulda, S.; Galluzzi, L.; Kroemer, G. Targeting Mitochondria for Cancer Therapy. *Nat. Rev. Drug Discov.* **2010**, *9*, 447–464.
16. Sarosiek, K. A.; Ni Chonghaile, T.; Letai, A. Mitochondria: Gatekeepers of Response to Chemotherapy. *Trends Cell Biol.* **2013**, *23*, 612–619.
17. Nunnari, J.; Suomalainen, A. Mitochondria: In Sickness and in Health. *Cell* **2012**, *148*, 1145–1159.
18. Bowes, J.; Brown, A. J.; Hamon, J.; Jarolimek, W.; Sridhar, A.; Waldron, G.; Whitebread, S. Reducing Safety-Related Drug Attrition: The Use of in Vitro Pharmacological Profiling. *Nat. Rev. Drug Discov.* **2012**, *11*, 909–922
19. Bastard, K.; Smith, A. A. T.; Vergne-Vaxelaire, C.; Perret, A.; Zaparucha, A.; De Melo-Minardi, R.; Mariage, A.; Boutard, M.; Debard, A.; Lechaplais, C.; Pelle, C.; Pellouin, V.; Perchat, N.; Petit, J. L.; Kreimeyer, A.; Medigue, C.; Weissenbach, J.; Artiguenave, F.; De

- Berardinis, V.; Vallenet, D.; Salanoubat, M. Revealing the Hidden Functional Diversity of an Enzyme Family. *Nat. Chem. Biol.* **2014**, *10*, 42–49.
20. Chandel, N. S. Mitochondria as Signaling Organelles. *BMC Biol.* **2014**, *12*, 1-7.
21. Ward, P. S.; Thompson, C. B. Metabolic Reprogramming: A Cancer Hallmark Even Warburg Did Not Anticipate. *Cancer Cell* **2012**, *21*, 297–308
22. Kroemer, G.; Pouyssegur, J. Tumor Cell Metabolism: Cancer's Achilles' Heel. *Cancer Cell* **2008**, *13*, 472–482.
23. Vyas, S.; Zaganjor, E.; Haigis, M. C. Mitochondria and Cancer. *Cell* **2016**, *166*, 555–566.
24. Chatterjee, A.; Mambo, E.; Sidransky, D. Mitochondrial DNA Mutations in Human Cancer. *Oncogene* **2006**, *25*, 4663–4674.
25. Zanssen, S.; Schon, E. A. Mitochondrial DNA Mutations in Cancer. *PLoS Med.* **2005**, *2*, e401.
26. Hällberg, B. M.; Larsson, N.-G. Making Proteins in the Powerhouse. *Cell Metab.* **2014**, *20*, 226–240.
27. Rin Jean, S.; Tulumello, D. V.; Wisnovsky, S. P.; Lei, E. K.; Pereira, M. P.; Kelley, S. O. Molecular Vehicles for Mitochondrial Chemical Biology and Drug Delivery. *ACS Chem. Biol.* **2014**, *9*, 323–333.
28. Wisnovsky, S.; Lei, E. K.; Jean, S. R.; Kelley, S. O. Mitochondrial Chemical Biology: New Probes Elucidate the Secrets of the Powerhouse of the Cell. *Cell Chem. Biol.* **2016**, *23*, 917–927.
29. Ferrari, M. Cancer Nanotechnology: Opportunities and Challenges. *Nat. Rev. Cancer* **2005**, *5*, 161–171.
30. Kim, B. Y. S.; Rutka, J. T.; Chan, W. C. W. Nanomedicine. *N. Engl. J. Med.* **2010**, *363*, 2434–2443.
31. Peer, D.; Karp, J. M.; Hong, S.; Farokhzad, O. C.; Margalit, R.; Langer, R. Nanocarriers as an Emerging Platform for Cancer Therapy. *Nat. Nanotechnol.* **2007**, *2*, 751–760.
32. Kanasty, R.; Dorkin, J. R.; Vegas, A.; Anderson, D. Delivery Materials for siRNA Therapeutics. *Nat. Mater.* **2013**, *12*, 967–977.
33. Mitragotri, S.; Burke, P. A.; Langer, R. Overcoming the Challenges in Administering Biopharmaceuticals: Formulation and Delivery Strategies. *Nat. Rev. Drug Discov.* **2014**, *13*, 655–672.

34. Marrache, S.; Pathak, R. K.; Dhar, S. Detouring of Cisplatin to Access Mitochondrial Genome for Overcoming Resistance. *Proc. Natl. Acad. Sci.* **2014**, *111*, 10444–10449.
35. Qu, Q.; Ma, X.; Zhao, Y. Targeted Delivery of Doxorubicin to Mitochondria Using Mesoporous Silica Nanoparticle Nanocarriers. *Nanoscale* **2015**, *7*, 16677–16686.
36. Yoong, S. L.; Wong, B. S.; Zhou, Q. L.; Chin, C. F.; Li, J.; Venkatesan, T.; Ho, H. K.; Yu, V.; Ang, W. H.; Pastorin, G. Enhanced Cytotoxicity to Cancer Cells by Mitochondria-Targeting MWCNTs Containing platinum(IV) Prodrug of Cisplatin. *Biomaterials* **2014**, *35*, 748–759.
37. Feldhaeusser, B.; Platt, S. R.; Marrache, S.; Kolishetti, N.; Pathak, R. K.; Montgomery, D. J.; Reno, L. R.; Howerth, E.; Dhar, S. Evaluation of Nanoparticle Delivered Cisplatin in Beagles. *Nanoscale* **2015**, *7*, 13822–13830.
38. Han, M.; Vakili, M. R.; Soleymani Abyaneh, H.; Molavi, O.; Lai, R.; Lavasanifar, A. Mitochondrial Delivery of Doxorubicin via Triphenylphosphine Modification for Overcoming Drug Resistance in MDA-MB-435/DOX Cells. *Mol. Pharm.* **2014**, *11*, 2640–2649.
39. Zhou, J.; Zhao, W. Y.; Ma, X.; Ju, R. J.; Li, X. Y.; Li, N.; Sun, M. G.; Shi, J. F.; Zhang, C. X.; Lu, W. L. The Anticancer Efficacy of Paclitaxel Liposomes Modified with Mitochondrial Targeting Conjugate in Resistant Lung Cancer. *Biomaterials* **2013**, *34*, 3626–3638.
40. Wisnovsky, S. P.; Wilson, J. J.; Radford, R. J.; Pereira, M. P.; Chan, M. R.; Laposa, R. R.; Lippard, S. J.; Kelley, S. O. Targeting Mitochondrial DNA with a Platinum-Based Anticancer Agent. *Chem. Biol.* **2013**, *20*, 1323–1328.
41. Fonseca, S. B.; Pereira, M. P.; Mourta, R.; Gronda, M.; Horton, K. L.; Hurren, R.; Minden, M. D.; Schimmer, A. D.; Kelley, S. O. Rerouting Chlorambucil to Mitochondria Combats Drug Deactivation and Resistance in Cancer Cells. *Chem. Biol.* **2011**, *18*, 445–453.
42. Chamberlain, G. R.; Tulumello, D. V.; Kelley, S. O. Targeted Delivery of Doxorubicin to Mitochondria. *ACS Chem. Biol.* **2013**, *8*, 1389–1395.
43. Jean, S. R.; Ahmed, M.; Lei, E. K.; Wisnovsky, S. P.; Kelley, S. O. Peptide-Mediated Delivery of Chemical Probes and Therapeutics to Mitochondria. *Acc. Chem. Res.* **2016**, *49*, 1893–1902.
44. Jean, S. R.; Tulumello, D. V.; Riganti, C.; Liyanage, S. U.; Schimmer, A. D.; Kelley, S. O. Mitochondrial Targeting of Doxorubicin Eliminates Nuclear Effects Associated with Cardiotoxicity. *ACS Chem. Biol.* **2015**, *10*, 2007–2015.

45. Mourtada, R.; Fonseca, S. B.; Wisnovsky, S. P.; Pereira, M. P.; Wang, X.; Hurren, R.; Parfitt, J.; Larsen, L.; Smith, R. A. J.; Murphy, M. P.; Schimmer, A. D.; Kelley, S. O. Re-Directing An Alkylating Agent to Mitochondria Alters Drug Target and Cell Death Mechanism. *PLoS One* **2013**, *8*, e60253.
46. Zielonka, J.; Joseph, J.; Sikora, A.; Hardy, M.; Ouari, O.; Vasquez-Vivar, J.; Cheng, G.; Lopez, M.; Kalyanaraman, B. Mitochondria-Targeted Triphenylphosphonium-Based Compounds: Syntheses, Mechanisms of Action, and Therapeutic and Diagnostic Applications. *Chem. Rev.* **2017**, *117*, 10043–10120.
47. Kazak, L.; Reyes, A.; Holt, I. J. Minimizing the Damage: Repair Pathways Keep Mitochondrial DNA Intact. *Nat. Rev. Mol. Cell Biol.* **2012**, *13*, 659–671.
48. Wisnovsky, S.; Jean, S. R.; Kelley, S. O. Mitochondrial DNA Repair and Replication Proteins Revealed by Targeted Chemical Probes. *Nat. Chem. Biol.* **2016**, *12*, 567–573.
49. Douarre, C.; Sourbier, C.; Dalla Rosa, I.; Brata Das, B.; Redon, C. E.; Zhang, H.; Neckers, L.; Pommier, Y. Mitochondrial Topoisomerase I Is Critical for Mitochondrial Integrity and Cellular Energy Metabolism. *PLoS One* **2012**, *7*, e41094.
50. Zhang, H.; Barcelo, J. M.; Lee, B.; Kohlhagen, G.; Zimonjic, D. B.; Popescu, N. C.; Pommier, Y. Human Mitochondrial Topoisomerase I. *Proc. Natl. Acad. Sci.* **2001**, *98*, 10608–10613.
51. Khiati, S.; Rosa, I. D.; Sourbier, C.; Ma, X.; Rao, V. A.; Neckers, L. M.; Zhang, H.; Pommier, Y. Mitochondrial Topoisomerase I (Top1mt) Is a Novel Limiting Factor of Doxorubicin Cardiotoxicity. *Clin. Cancer Res.* **2014**, *20*, 4873–4881.
52. Smith, R. a J.; Porteous, C. M.; Gane, A. M.; Murphy, M. P. Delivery of Bioactive Molecules to Mitochondria in Vivo. *Proc. Natl. Acad. Sci. U. S. A.* **2003**, *100*, 5407–5412.
53. Mallick, A.; More, P.; Syed, M. M. K.; Basu, S. Nanoparticle-Mediated Mitochondrial Damage Induces Apoptosis in Cancer. *ACS Appl. Mater. Interfaces* **2016**, *8*, 13218–13231.
54. Blanco, E.; Shen, H.; Ferrari, M. Principles of Nanoparticle Design for Overcoming Biological Barriers to Drug Delivery. *Nat. Biotechnol.* **2015**, *33*, 941–951.
55. Matsumura, Y.; Maeda, H. A New Concept for Macromolecular Therapeutics in Cancer Chemotherapy: Mechanism of Tumoritropic Accumulation of Proteins and the Antitumor Agent Smancs. *Cancer Res.* **1986**, *46*, 6387–6392.

56. Marullo, R.; Werner, E.; Degtyareva, N.; Moore, B.; Altavilla, G.; Ramalingam, S. S.; Doetsch, P. W. Cisplatin Induces a Mitochondrial-ROS Response That Contributes to Cytotoxicity Depending on Mitochondrial Redox Status and Bioenergetic Functions. *PLoS One* **2013**, *8*, e81162.
57. Tait, S. W. G.; Green, D. R. Mitochondria and Cell Death: Outer Membrane Permeabilization and beyond. *Nat. Rev. Mol. Cell Biol.* **2010**, *11*, 621–632.
58. Petronilli, V.; Miotto, G.; Canton, M.; Brini, M.; Colonna, R.; Bernardi, P.; Di Lisa, F. Transient and Long-Lasting Openings of the Mitochondrial Permeability Transition Pore Can Be Monitored Directly in Intact Cells by Changes in Mitochondrial Calcein Fluorescence. *Biophys. J.* **1999**, *76*, 725–734
59. Floryk, D.; Houštěk, J. Tetramethyl Rhodamine Methyl Ester (TMRM) Is Suitable for Cytofluorometric Measurements of Mitochondrial Membrane Potential in Cells Treated with Digitonin. *Biosci. Rep.* **1999**, *19*, 27–34.
60. Jiang, X. J.; Wang, X. D. Cytochrome C-Mediated Apoptosis. *Annu. Rev. Biochem.* **2004**, *73*, 87–106.
61. Wu, D.; Yotnda, P. Production and Detection of Reactive Oxygen Species (ROS) in Cancers. *J. Vis. Exp.* **2011**, e3259.
62. Koczor, C. A.; Shokolenko, I. N.; Boyd, A. K.; Balk, S. P.; Wilson, G. L.; LeDoux, S. P. Mitochondrial DNA Damage Initiates a Cell Cycle Arrest by a Chk2-Associated Mechanism in Mammalian Cells. *J. Biol. Chem.* **2009**, *284*, 36191–36201.
63. Li, P.; Nijhawan, D.; Budihardjo, I.; Srinivasula, S. M.; Ahmad, M.; Alnemri, E. S.; Wang, X. Cytochrome c and dATP-Dependent Formation of Apaf-1/caspase-9 Complex Initiates an Apoptotic Protease Cascade. *Cell* **1997**, *91*, 479–489.
64. Mallick, A.; More, P.; Ghosh, S.; Chippalkatti, R.; Chopade, B. A.; Lahiri, M.; Basu, S. Dual Drug Conjugated Nanoparticle for Simultaneous Targeting of Mitochondria and Nucleus in Cancer Cells. *ACS Appl. Mater. Interfaces* **2015**, *7*, 7584–7598.
65. Palvai, S.; More, P.; Mapara, N.; Basu, S. Chimeric Nanoparticle: A Platform for Simultaneous Targeting of Phosphatidylinositol-3-Kinase Signaling and Damaging DNA in Cancer Cells. *ACS Appl. Mater. Interfaces* **2015**, *7*, 18327–18335.

Chapter 3b: Simultaneous targeting of mitochondrial DNA and mitochondrial Topoisomerase I by graphene oxide nanomaterials

Sections of this chapter represent the following work in progress:

Abhik Mallick, Aditi Nandi and Sudipta Basu. Simultaneous Targeting of Mitochondrial DNA and Mitochondrial Topoisomerase I by Graphene Oxide Nanomaterials. (Manuscript under preparation)

3b.1. Introduction

In the last few years, graphene and its derivative graphene oxide have been the main focus of research and have attracted great interest in nanomedicine because of its intrinsic properties.¹⁻² Graphene consists of a single layer of sp^2 hybridized carbon atoms arranged in a honeycomb 2D crystal lattice, whereas, Graphene oxide is a highly oxygenated derivative of graphene. It is composed of planar graphenes like patches which are separated by sp^3 hybridized carbon atoms bearing $-OH$, $-COOH$ and epoxy groups. Due to this unique structure and geometry, they possess amazing physical and chemical properties like 1) amphiphilicity, 2) negatively charged nature, 3) can be easily functionalized due to oxygenated groups, 4) planar surface endows it with capability to immobilize large number of materials such as metals, drugs (by Π - Π stacking interactions), biomolecules and imaging probes.³ Hence, it has great application as drug delivery system for water insoluble anticancer drugs, in gene therapy, tissue engineering and in bio-imaging and sensing system.⁴

Targeting subcellular organelles with graphene oxide has evolved to be an interesting anticancer therapeutic strategy in recent years.⁵ Specifically directing graphene oxide to mitochondria has been a major challenge in past few years due to its negative charge.⁶⁻⁷ The negative charge on GO can be converted into mitochondria targeting favorable positive charge by using polyethyleneimine (PEI), a cationic polymer, generally used for gene delivery.⁸⁻¹⁰

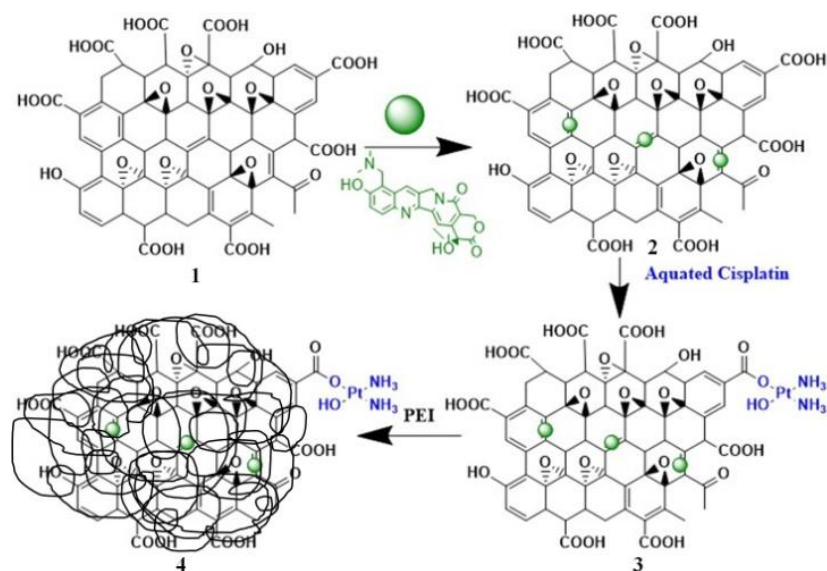
Inspired by the biomedical applications of graphene oxide and the targeting ability of polyethyleneimine directing nanomaterials to mitochondria,¹¹⁻¹² we have developed mitochondria targeting graphene oxide nanomaterial. Due to the aromatic structure and planar nature of graphene oxide, we could stack a water-soluble drug, topotecan (Topoisomerase 1 inhibitor), by Π - Π stacking interaction on its surface.¹³ We further used cisplatin (a nuclear DNA damaging drug) which coordinates with the $-COOH$ group of graphene oxide and thereby coated with polyethyleneimine to obtain mitochondria targeting graphene oxide nanomaterial. Interestingly, it was observed that stacking of topotecan onto graphene oxide maintained its sheet-like structure but, on the coordination of cisplatin to it converted its morphology into spherical particles of sizes < 200 nm.¹⁴ The shape of the nanomaterials was retained when coated with polyethyleneimine. The spherical shape and the size < 200 nm of the mitochondria targeting graphene oxide nanoparticle (GTCP) were confirmed by the FESEM. The presence of topotecan

in the mitochondria targeting graphene oxide nanoparticle (GTCP) was confirmed by the fluorescence emission quenching when stacked with graphene oxide. The presence of graphene oxide in the GTCP nanoparticle was confirmed by Raman spectroscopy through characteristic D and G bands. Finally, the presence of cisplatin was confirmed by Energy Dispersive Analysis Of X Rays (EDAX) studies. These mitochondria targeting graphene oxide nanoparticles (GTCP) damaged the mitochondrial DNA (mt-DNA) and mitochondrial Topoisomerase I (Top1mt) leading to mitochondrial outer membrane permeabilization (MOMP) and ROS generation. Finally, these GTCP nanoparticles induced enhanced cell death compared to the free drug combination. We envision that these GTCP nanoparticles could be translated into clinics in future as a platform technology for damaging multiple targets in mitochondria of cancer cells to overcome drug resistance.

3b.2. Result and Discussion

3b.2.1 Synthesis of mitochondria targeting graphene oxide conjugate (GTCP)

We have chosen Topotecan, a water soluble derivative of camptothecin to inhibit mitochondrial Topoisomerase I.



Scheme 1: Schematic diagram of mitochondria targeting graphene oxide conjugate synthesis.

(1) Graphene oxide, (2) Graphene oxide- topotecan (GT), (3) Graphene oxide-topotecan-cisplatin (GTC) and (4) Graphene oxide-topotecan-cisplatin- polyethyleneimine(GTCP)

Topotecan was stacked on graphene oxide (1) to obtain graphene oxide- topotecan (GT) composite (2) followed by coordination of cisplatin with the -COOH of the graphene oxide to form graphene oxide-topotecan-cisplatin (GTC) conjugate (3) (Scheme 1). Finally, GTC was coated with polyethyleneimine (PEI) to attain mitochondria targeting graphene oxide conjugate (GTCP) (4) (Scheme 1).

3b.2.2 Characterisation of mitochondria targeting graphene oxide nanoparticle (GTCP nanoparticles) The shape, size and morphology of graphene oxide composites (graphene oxide-topotecan and graphene oxide-topotecan-cisplatin conjugates) and mitochondria targeting graphene oxide nanoparticle (GTCP nanoparticle) were determined by field-emission scanning electron microscopy (FESEM, **Figure 1**). The FESEM images (**Figure 1**) clearly show that graphene oxide sheets self-assembled into spherical nanoparticles on addition of cisplatin having size of sub 200 nm diameter. The spherical shape of the graphene oxide-topotecan-cisplatin-NP (GTC) was retained after PEI coating confirmed by the FESEM image in Figure 1c. To confirm the stacking of topotecan on GO surface, we checked the quenching in fluorescence intensity of topotecan in the free-state and when stacked on GO surface. The fluorescence spectra of topotecan at room temperature shows a single unstructured band with emission max at 511 nm (**Figure 2a**) originated from the $\Pi-\Pi^*$ singlet state. When stacked onto GO surface, fluorescence of topotecan was quenched as seen from **Figure 2a**. The quenching of fluorescence of topotecan in GT and subsequently GTC and GTCP nanoparticle has occurred at a particular concentration. This fluorescence quenching clearly demonstrated that GTCP nanoparticle contained topotecan. The presence of GO in the GT, GTC and GTCP nanoparticle was characterized by Raman spectroscopy, which is an important and widely used tool for the characterization of carbon materials. The Raman spectrum recorded for GT, GTC and GTCP nanoparticle (**Figure 2b**) showed the characteristic D and G peaks for graphene oxide at 1355 cm^{-1} and 1605 cm^{-1} respectively.¹⁴ The G band arises due to C-C bond stretching and is common in all sp^2 hybridized carbon materials. The D band in the spectrum arises due to disorder in the sp^2 structure of graphene. Similar D and G band peaks are present in the Raman spectra of GT, GTC and GTCP nanoparticle, indicating that they contain graphene oxide. To calculate the amount of drugs loaded onto graphene oxide UV-Vis spectroscopic measurements were performed. The loading of cisplatin and topotecan in GTCP nanoparticle was found to be $514\text{ }\mu\text{g/mL}$ and $600\text{ }\mu\text{g/mL}$ respectively (Figure 2c). Drug loadings were determined from concentration vs absorbance

calibration graph at characteristic $\lambda_{\max} = 706 \text{ nm}$ and 387 nm for cisplatin and topotecan respectively. Finally, the presence of platinum (Pt) in the nanoparticles was determined by energy dispersive X-ray analysis (EDAX) (**Figure 2d**).

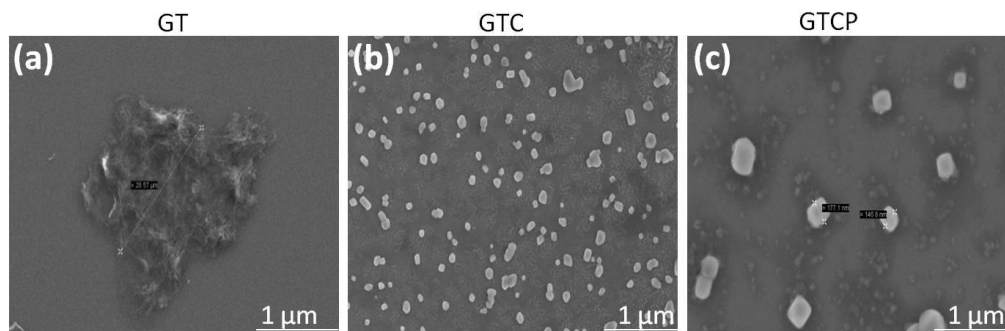


Figure 1: FESEM images of changes in morphology of GO composites from sheet to nanoparticle (a) GO-Top (GT), (b) GO-Top-Cis (GTC) and (c) GO-Top-Cis -PEI (GTCP).

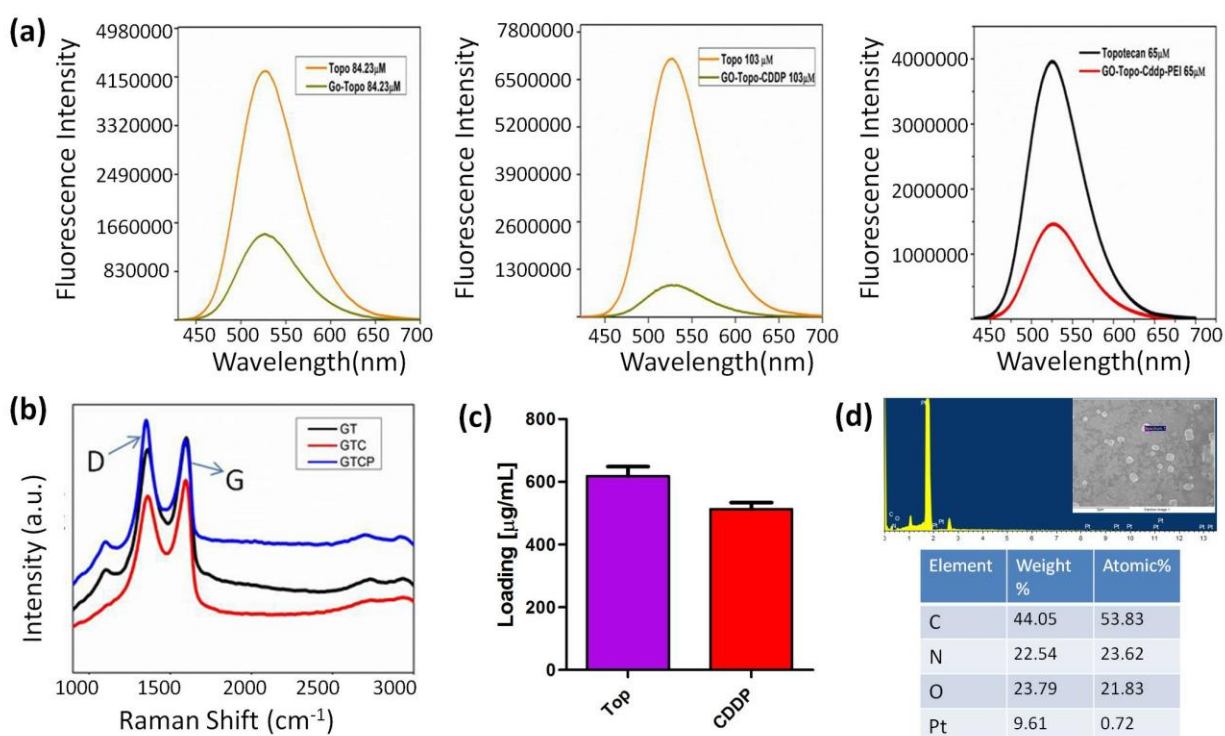


Figure 2: (a) Fluorescence spectra of topotecan in GO-Top (GT), GO-Top-Cis (GTC) and GO-Top-Cis -PEI (GTCP) and free drug kept at a fixed concentration $84.23 \mu\text{M}$, $103 \mu\text{M}$ and $65 \mu\text{M}$ respectively. (b) Resonance Raman spectra of GT, GTC and GTCP respectively (c) Drug loading of Top and Cisplatin in GTCP nanoparticle and (d) EDAX of GTCP nanoparticle.

For specific localization in mitochondria, the mitochondria targeting graphene oxide (GTCP) nanoparticle should bear high positive surface charge. Thus surface charge of the mitochondria targeting graphene oxide (GTCP) nanoparticle was evaluated by DLS measurement. It was found that GTCP nanoparticles has +26.1 mV surface charge. On contrary, graphene oxide and the graphene oxide composites such as GT and GTC, the surface charge was found to be -22.6 mV, -15.9 mV and -10.7 mV respectively (**Figure 3**). This zeta potential assay also indicated that PEI successfully covered the surface of the graphene oxide-topotecan-cisplatin nanoparticle to induce high positive surface charge for mitochondria targeting.

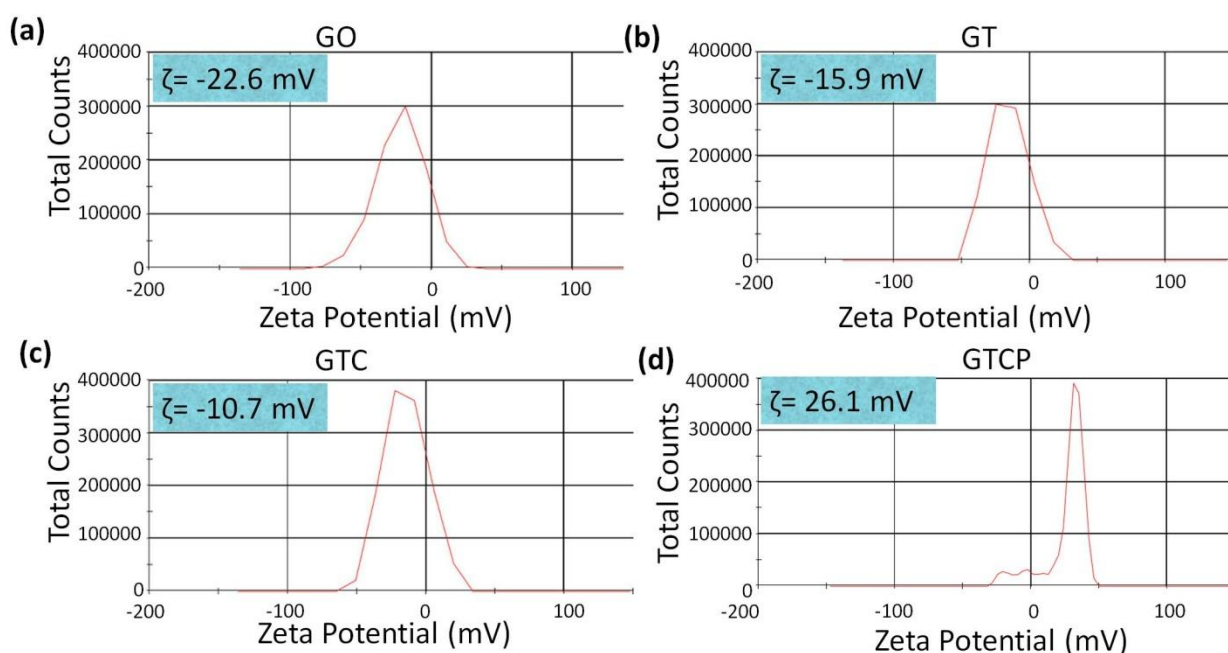


Figure 3: Evaluation of the surface charge by DLS. Zeta potential of (a) GO, (b) GO-Top (GT), (c) GO-Top-Cis (GTC) and (d) GO-Top-Cis -PEI (GTCP)

Although the usage of graphene oxide to deliver mitochondria targeting active agents is a novel strategy, one of the major problem of this strategy is the erratic distribution of the size of the nanomaterials when checked by dynamic light scattering (DLS). Thus the overall stability of these graphene oxide based system could not be confirmed.

The release kinetics data of cisplatin and π -stacked drug has been discussed in a recently published work from our group. We expect similar release profile in this case.¹⁴

3b.2.3 Mitochondrial outer membrane permeabilisation (MOMP):

3b.2.3.1 JC1 and TMRM assay : As explained in earlier chapters, JC1 and TMRM assay are performed to check the mitochondrial outer membrane permeabilisation (MOMP). To investigate the MOMP, we treated the HeLa cells with GTCP nanoparticle for 24 h followed by addition of JC1 dye. Non-nanoparticle treated HeLa cells were considered as control. The cells were visualized by confocal laser scanning microscopy (CLSM). Confocal images in **Figure 4a** clearly showed that there was a homogeneity in staining as red and green fluorescence for the control ($J_{\text{monomer}}/ J_{\text{aggregate}} = 1.03$). On the other hand, a major fluorescence shift from red to green ($J_{\text{monomer}}/ J_{\text{aggregate}} = 2.08$) was observed in GTCP nanoparticles treated cells due to the damaged mitochondria (Figure 5a). To visualize the effect of GTCP nanoparticles on the mitochondrial membrane potential, we treated HeLa cells with GTCP nanoparticles for 24 h and stained the cells with TMRM followed by confocal microscopy. From CLSM images in **Figure 4b**, we observed bright red fluorescence in the control cells due to the accumulation of TMRM in undamaged healthy mitochondria which was drastically decreased (nearly 2 fold) after treatment with GTCP nanoparticles (**Figure 5b**).

3b.2.3.2 Calcein AM assay: Calcein AM assay was performed to check the mitochondrial transition pore formation (discussed in earlier chapters). HeLa cells were treated with GTCP nanoparticles for 24 h and the cells were treated with Calcein AM in presence of CoCl_2 . The generation of green fluorescent Calcein after mitochondrial transition pore formation was further visualized by confocal microscopy. From CLSM images in **Figure 4c**, it was clear that GTCP nanoparticles increased the formation of green fluorescent Calcein compared to the non-nanoparticle treated control cells. Further quantification from CLSM, it was observed that GTCP nanoparticles increased the fluorescent intensity into the HeLa cells nearly 3 folds compared to control cells (Figure 5c). This Calcein AM assay clearly demonstrated that GTCP nanoparticles induced mitochondrial transition pore formation after damaging mitochondria in HeLa cells.

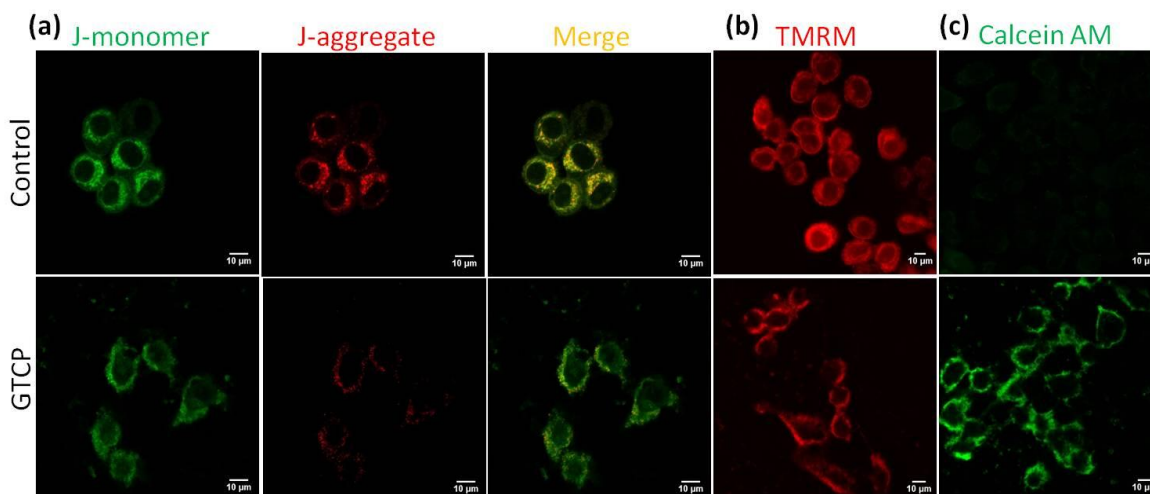


Figure 4: Mitochondrial damage induced by GTCP nanoparticle in HeLa cells was visualized by confocal microscopy through (a) JC1 assay (b) Calcein AM assay and (c) TMRM assay. Scale = 10 μ m.

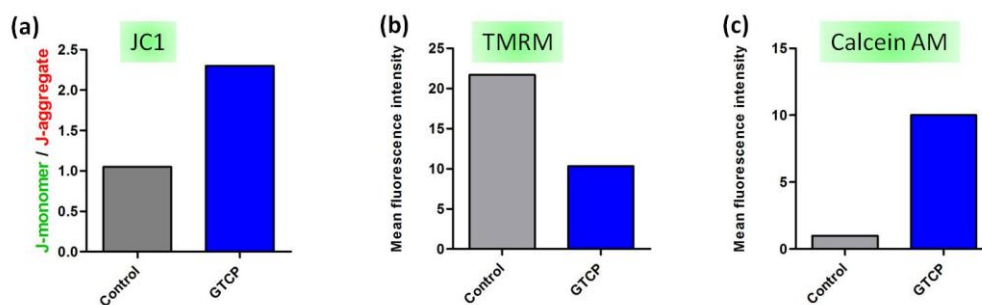


Figure 5: Confocal laser scanning microscopy based quantification of (a) J-monomer/J-aggregate in JC1 assay, (b) mean fluorescence intensity of Calcein AM and (c) mean fluorescence intensity of TMRM from HeLa cells after treatment with GTCP nanoparticle for 24 h.

3b.2.4. Generation of Reactive Oxygen Species (ROS): Reactive oxygen species are generated due to mitochondrial DNA damage. To observe the generation of ROS, we treated the HeLa cells with GTCP nanoparticles for 24 h followed by treatment with DCFDA for 30 min. The cells were further visualized by confocal microscopy. From CLSM images in **Figure 6(a)**, it was evident that GTCP nanoparticles induced much increased ROS generation compared to non-nanoparticle treated control cells. Further quantification from confocal images also confirmed that GTCP nanoparticles increased the fluorescence intensity nearly 5 folds compared to the fluorescence intensity in control cells (**Figure 6b**).

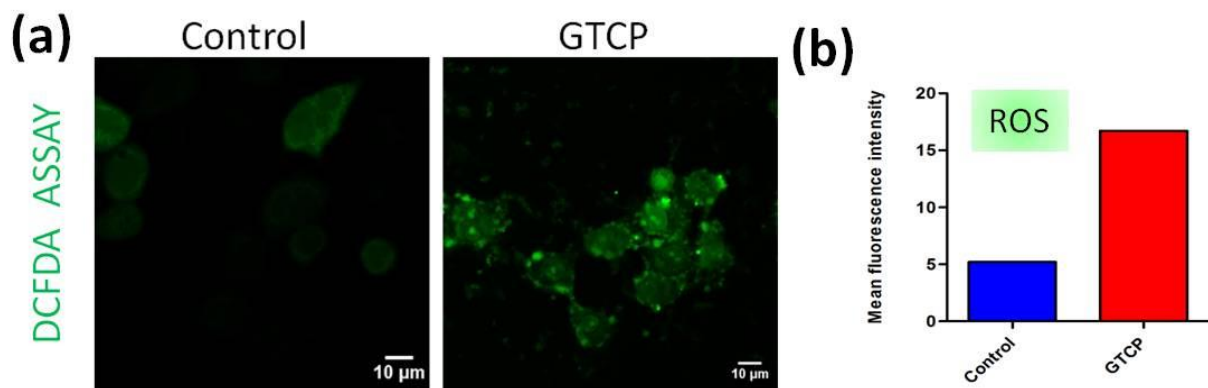


Figure 6: (a) CLSM images of HeLa cells after treatment with GTCP nanoparticle for 24 h to visualize generation of reactive oxygen species (ROS) by DCF assay. Scale = 10 μm . (b) Quantification of mean fluorescence intensity from confocal microscopy reactive oxygen species (ROS) in HeLa cells after treatment with GTCP nanoparticle for 24 h.

3b.2.5 Cell viability assay: We finally evaluated the effect of GTCP nanoparticle mediated mitochondrial damage in HeLa cell death. HeLa cells were treated with GTCP nanoparticle in a concentration dependent manner for 48 h and the cell viability was measured by MTT assay. The cells were treated with the GTCP nanoparticles in ten different concentration in triplicate and compared to the to the control after 48 hours using MTT reagent. This similar procedure was followed with the free drug combination. After 48 hours, GTCP nanoparticles showed much lower $\text{IC}_{50} = 6.5 \pm 0.54 \mu\text{m}$ (cell viability = $5.7 \pm 0.13\%$ at Topotecan concentration of $30\mu\text{m}$) compared to $\text{IC}_{50} = 10 \pm 0.78 \mu\text{m}$ (cell viability = $20.7 \pm 0.57\%$ at Topotecan concentration of $30\mu\text{m}$) for free drug combination . From this data, it is quite evident that the GTCP nanoparticles had a better cytotoxic effect in the human cervical cancer (HeLa) cell line at a higher concentration than the free drug combination after 48 hours.

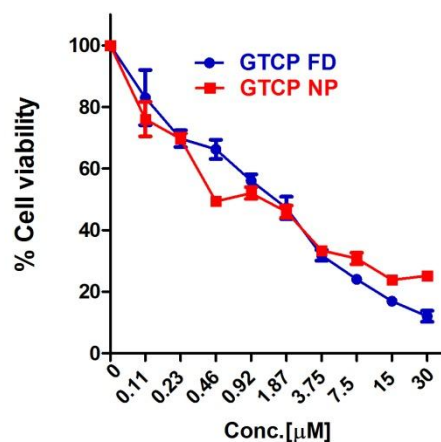


Figure 7: Cell viability of HeLa cells after treatment with GTCP nanoparticle for 48 h by MTT assay.

3b.3 Conclusion

In conclusion, we have successfully developed mitochondria targeting graphene oxide nanoparticle of size $<200\text{nm}$ which was characterised by electron microscopy and different spectroscopic methods. These mitochondria targeting graphene oxide nanoparticles (GTCP) damaged the mitochondrial DNA (mt-DNA) and mitochondrial Topoisomerase I (Top1mt) leading to mitochondrial outer membrane permeabilization (MOMP) and ROS generation. These mitochondria targeting graphene oxide nanoparticles (GTCP) induced enhanced cell death compared to the free drug combination. We envision that these GTCP nanoparticles could be translated into clinics in future as a platform technology for damaging multiple targets in mitochondria of cancer cells to overcome drug resistance.

3b.4. Materials and Methods

3b.4.1 Material. All commercially obtained compounds were used without further purification. Graphene oxide (4mg/ml), polyethyleneimine, JC 1 dye, TMRM, Calcein AM, sodium dodecyl sulfate (SDS), and silicon wafer for FE-SEM were bought from Sigma-Aldrich. Cisplatin and topotecan were bought from Selleck Chemicals. H_2DCFDA was purchased from MitoBiogenesis™. DMEM media and 3-(4, 5-dimethylthiazol-2-yl)-2,5-diphenyltetrazolium bromide (MTT) were purchased from HiMedia. 96 well plates, 6 well plates, 15 mL and 50 mL

graduated sterile centrifuge tubes and tissue culture flasks with filter cap sterile were purchased from Tarsons Product Pvt. Ltd. HeLa cells were obtained from National Centre for Cell Science (NCCS), Pune. The drug loading and cell viability assay were plotted using GraphPad Prism software. The laser scanning confocal microscopy was performed by Zeiss LSM 710 machine. Each sample was done in triplicate.

3b.4.2 Synthesis of mitochondria targeting graphene oxide nanomaterial : Graphene oxide (4 mg/mL, 250 μ L) was dispersed in distilled water (1 mL). Aqueous solution of topotecan (5 mg) in distilled water (1 mL) was prepared and added to the dispersed graphene oxide solution. The reaction was stirred in dark at room temperature overnight. To remove unreacted topotecan, the reaction mixture was dialysed against distilled water through dialysis membrane (MWCO= 1000 Dalton) for 24 hr. Further aquated cisplatin (5 mg/ml) was added to graphene oxide-topotecan conjugate (GT) and stirred at RT overnight. After completion of reaction, the mixture was again dialysed against distilled water through dialysis membrane (MWCO= 1000 Dalton) for 7 hr to remove excess of aquated cisplatin. Finally the graphene oxide-topotecan-cisplatin (GTC) obtained was coated polyethyleneimine (1mg/ml) by sonicating for 24 hr. The excess polyethyleneimine (PEI) was removed by centrifugation to obtain graphene oxide -topotecan-cisplatin-PEI (GTCP) conjugate.

3b.4.3 Determination of surface charge and shape of mitochondria targeting graphene oxide nanomaterial:

3b.4.3.1 Dynamic light scattering (DLS): The surface charge (zeta potential) of GT, GTC and GTCP was measured by dynamic light scattering (DLS) method using Zetasizer Nano2590 (Malvern, UK). 50 μ l of GT, GTC and GTCP solution was diluted to 1ml using DI water and 3 sets of 10 measurements each were performed at 90 degree scattering angle to get the average particle size.

3b.4.3.2 Field-Emission Scanning Electron Microscopy (FESEM) of mitochondria targeting graphene oxide nanomaterial: GT, GTC and GTCP in water was placed on a silicon chip without any dopant and it was allowed to dry at room temperature under vacuum desiccators for 2 hours. The silicon chip was then gold coated (30-40 nm thickness) using Quorum, Q150T- E5. The FESEM measurements were done using Carl Zeiss, Ultra plus, scanning electron microscope at an operating voltage of 4.0 KV.

3b.4.4 Raman Spectroscopy. Raman spectra were collected using a Lab RAM HR 800 (Horiba scientific) 532 nm excitation.

3b.4.5 Fluorescence Spectroscopy: Steady state fluorescence were recorded using a Flouromax-4 (HORIBA scientific, USA).

3b.4.6 Determination of drug loading: The drug loading of topotecan and cisplatin was checked according to the procedures discussed in **Chapter 3a**.

3b.4.7 Determination of mitochondrial outer membrane permeabilisation (MOMP)

3b.4.7.1 JC 1 assay: The JC1 assay was performed according to the procedures discussed in **Chapter 3a**.

3b.4.7.2 TMRM assay: The TMRM assay was performed according to the procedures discussed in **Chapter 3a**.

3b.4.7.3 Calcein AM assay: The Calcein AM assay was performed according to the procedures discussed in **Chapter 3a**.

3b.4.8 Generation of Reactive Oxygen Species (ROS): The generation of ROS was performed according to the procedures discussed in **Chapter 3a** by H₂DCFDA assay.

3b.4.9 Cell Viability assay: 5 x 10³ HeLa cells were seeded per well in 96-well microlitre plate and incubated overnight in a 5% CO₂ incubator at 37°C for attachment. Cells were then treated with GTC and GTCNP nanoparticles and their corresponding free drug combinations in different concentrations (0.11, 0.23, 0.46, 0.92, 1.87, 3.75, 7.5, 15, 30 µM) for 48 h. The cell viability was measured using the MTT assay described previously in **Chapter 2 and 3a**. The percent cell viability was calculated considering the untreated cells as 100 percent viability and the effectiveness of GTC and GTCNP nanoparticles was compared with the free drug combinations.

3b.5. References

- (1) Kostarelos, K.; Novoselov, K. S. Exploring the Interface of Graphene and Biology. *Science*. **2014**, *344*, 261–263.
- (2) Sydlík, S. A.; Jhunjhunwala, S.; Webber, M. J.; Anderson, D. G.; Langer, R. In Vivo Compatibility of Graphene Oxide with Differing Oxidation States. *ACS Nano* **2015**, *9*, 3866–3874.
- (3) Eigler, S.; Hirsch, A. Chemistry with Graphene and Graphene Oxide-Challenges for Synthetic Chemists. *Angew. Chemie Int. Ed.* **2014**, *53*, 7720–7738.

- (4) Kim, J.; Cote, L. J.; Huang, J. Two Dimensional Soft Material: New Faces of Graphene Oxide. *Acc. Chem. Res.* **2012**, *45*, 1356–1364.
- (5) Huang, J. G.; Leshuk, T.; Gu, F. X. Emerging Nanomaterials for Targeting Subcellular Organelles. *Nano Today* **2011**, *6*, 478–492.
- (6) Wei, Y.; Zhou, F.; Zhang, D.; Chen, Q.; Xing, D. A Graphene Oxide Based Smart Drug Delivery System for Tumor Mitochondria-Targeting Photodynamic Therapy. *Nanoscale* **2016**, *8*, 3530–3538.
- (7) Zhang, C.; Liu, Z.; Zheng, Y.; Geng, Y.; Han, C.; Shi, Y.; Sun, H.; Zhang, C.; Chen, Y.; Zhang, L.; Guo, Q.; Yang, L.; Zhou, X.; Kong, L. Glycyrrhetic Acid Functionalized Graphene Oxide for Mitochondria Targeting and Cancer Treatment In Vivo. *Small* **2017**, *1703306*, 1–16.
- (8) Kim, H.; Kim, W. J. Photothermally Controlled Gene Delivery by Reduced Graphene Oxide-Polyethylenimine Nanocomposite. *Small* **2014**, *10*, 117–126.
- (9) Kim, H.; Namgung, R.; Singha, K.; Oh, I. K.; Kim, W. J. Graphene Oxide-Polyethylenimine Nanoconstruct as a Gene Delivery Vector and Bioimaging Tool. *Bioconjug. Chem.* **2011**, *22*, 2558–2567.
- (10) Chen, B.; Liu, M.; Zhang, L.; Huang, J.; Yao, J.; Zhang, Z. Polyethylenimine-Functionalized Graphene Oxide as an Efficient Gene Delivery Vector. *J. Mater. Chem.* **2011**, *21*, 7736.
- (11) Ye, S.; Yang, P.; Cheng, K.; Zhou, T.; Wang, Y.; Hou, Z.; Jiang, Y.; Ren, L. Drp1-Dependent Mitochondrial Fission Mediates Toxicity of Positively Charged Graphene in Microglia. *ACS Biomater. Sci. Eng.* **2016**, *2*, 722–733.
- (12) M.; Liu, Z.; Zhang, W.; Dong, H.; Zhou, F.; Yu, J.; Wang, X.; Guo, Z. Mitochondrial Targeted Polyethylenimine Functionalized Graphene Oxide Nanocarrier and Its Anti-Tumor Effect on Human Lung Carcinoma Cells. *Nano* **2015**, *10*, 1550121.
- (13) Koninti, R. K.; Sengupta, A.; Gavvala, K.; Ballav, N.; Hazra, P. Loading of an Anti-Cancer Drug onto Graphene Oxide and Subsequent Release to DNA/RNA: A Direct Optical Detection. *Nanoscale* **2014**, *6*, 2937–2944.
- (14) Nandi, A.; Mallick, A.; More, P.; Sengupta, P.; Ballav, N.; Basu, S. Cisplatin-Induced Self-Assembly of Graphene Oxide Sheets into Spherical Nanoparticles for Damaging Sub-Cellular DNA. *Chem. Commun.* **2017**, *53*, 1409–1412.

Chapter 4: Dual drug conjugated nanoparticle for simultaneous targeting of mitochondria and nucleus in cancer cells

This chapter has been published as:

Abhik Mallick, Piyush More, Sougata Ghosh, Rohan Chipalkatti, Balu A. Chopade, Mayurika Lahiri, and Sudipta Basu. Dual drug conjugated nanoparticle for simultaneous targeting of mitochondria and nucleus in cancer cells. *ACS Appl. Mater. Interface*, **2015, 7, 7584-7598**

4.1. Introduction

Current cancer treatment relies on using drug combinations to inhibit multiple targets, maximize therapeutic outcomes and overcome drug resistance.^{1,2} As discussed in the earlier chapters, mitochondrion has emerged as an important alternative target in cancer therapeutics due to its diverse functions including cellular energy production by generating ATP via respiration, regulating danger signaling and containing mitochondrial DNA (mtDNA) as genomic material.^{3,4} As a result, routing the DNA damaging drugs and kinase inhibitors specifically into mitochondria by tagging mitochondria targeting peptides or triphenylphosphine (TPP) moiety has become an alternative strategy in cancer therapeutics.⁵⁻⁸ Recently, Lippard and coworkers developed mitaplatin and vitamin E analogues-Pt(IV) complexes as prodrugs for simultaneous targeting of nuclear DNA and mitochondria.^{9,10} However, targeting mitochondrial function by small molecule drugs would lead to severe side effects to the cancer patients considering mitochondria's critical role in governing cellular metabolism in healthy cells as well as diverse interconnected functions like autophagy and apoptosis.^{11,12} This challenge could be addressed by nanotechnology based platforms.

Nanotechnology based platforms have revolutionized cancer therapeutics in last decade by delivering small molecule drugs, siRNAs and therapeutic proteins specifically into tumors by using unique enhanced permeability and retention (EPR) effect or cancer biomarker driven active targeting.¹³⁻¹⁶ The nanovectors having size < 200 nm were found to be most effective in cancer therapy and diagnosis due to their preferential accumulation into tumor tissues compared to the healthy tissues.¹⁷ Several nanovectors including polymeric nanoparticles,¹⁸⁻²⁰ nanocell,²¹ layer-by-layer nanoparticles,²² graphene oxide,²³ gel-liposome²⁴ and carbon nanotubes²⁵ have been explored for effective dual drug delivery in cancer tissues to reduce the toxic side effects. However, nanoparticle mediated delivery of drugs to the specific sub-cellular compartments or organelles remains elusive due to the similarity in the structure and function of the organelles between healthy cells and cancer cells. Moreover, nanoparticle mediated selective targeting of organelles in cancer cells would lead to minimize the off-target toxicity in the healthy cells as well as overcome drug resistance. Recently, Dhar and coworkers developed TPP coated biocompatible PLGA-PEG based blended nanoparticles and gold nanoparticles to deliver different drugs selectively to mitochondria.^{26,27} Although, specific

targeting of mitochondria emerged as an interesting strategy to alter the bioenergetics of cancer cells, mitochondria depend on the nucleus and other cellular organelles for most of their proteins and lipids as well as their cellular functions.^{28,29} Moreover, nucleus is the most important cellular organelle, containing genomic materials (nuclear DNA, RNA and chromosomes) and regulates important functions like transcription, cell cycle and cell division in healthy cells as well as in cancer cells.³⁰

We hypothesize that dual drug conjugated nanoparticles would preferentially extravasate into tumor tissue through EPR effect and mediate simultaneous sub-cellular targeting of mitochondria and nucleus leading to more effective therapeutics in cancer. Aiming at this goal, we have chosen α -tocopheryl succinate (α -TOS) as mitochondria targeting drug, cisplatin and doxorubicin as different clinically approved nuclear DNA damaging drugs and paclitaxel as microtubule binding drug to disrupt the shape of the cellular nucleus. α -TOS is a redox silent analogue of vitamin E, which induces apoptosis in different types of cancers including prostate, breast, lung, colon, cervical, endometrial as well as hematopoietic cancers³¹⁻³³ by targeting the mitochondrial complex II and causing conformational changes in the pro-apoptotic protein Bak, leading to permeabilization of mitochondrial outer membrane (MOM) and subsequent production of cytochrome c.³⁴⁻³⁶ Moreover, α -TOS showed improved therapeutic efficacy in combination with cisplatin,³⁷ doxorubicin³⁸ and paclitaxel.³⁹ Although α -TOS shows broad antitumor effect without any toxicity to normal tissues,^{40,41} cisplatin, doxorubicin and paclitaxel show dose dependent nephrotoxicity, cardiotoxicity and neurotoxicity respectively to the patients.⁴²⁻⁴⁴

As a proof of concept, in this work, we have directly conjugated α -TOS with cisplatin, doxorubicin and paclitaxel without any additional linker (Figure 1a). We engineered sub 200 nm particles from these dual drug conjugates which were endocytosed into the acidic lysosomal compartments of HeLa cervical cancer cells temporally and released the dual drugs in a slow and sustained manner to target mitochondria and nucleus simultaneously (Figure 1b and Figure 1c). These dual drug conjugated nanoparticles showed cytotoxicity by inducing apoptosis through damaging mitochondrial outer membrane (MOM) to release cytochrome c as well as damaging nuclear DNA and tubulin to arrest the cell cycle. These dual drug conjugated nanoparticles have potential to simultaneous targeting of multiple sub-cellular organelles to escalate the therapeutic outcomes in modern cancer treatment.

4.2. Results and discussion

4.2.1 Synthesis and characterization of dual-drug conjugated nanoparticles.

4.2.1.1 Synthesis of dual-drug conjugates. The free carboxylic acid group of α -TOS (**1**) was directly conjugated with doxorubicin through amide linkage by using HBTU as coupling agent

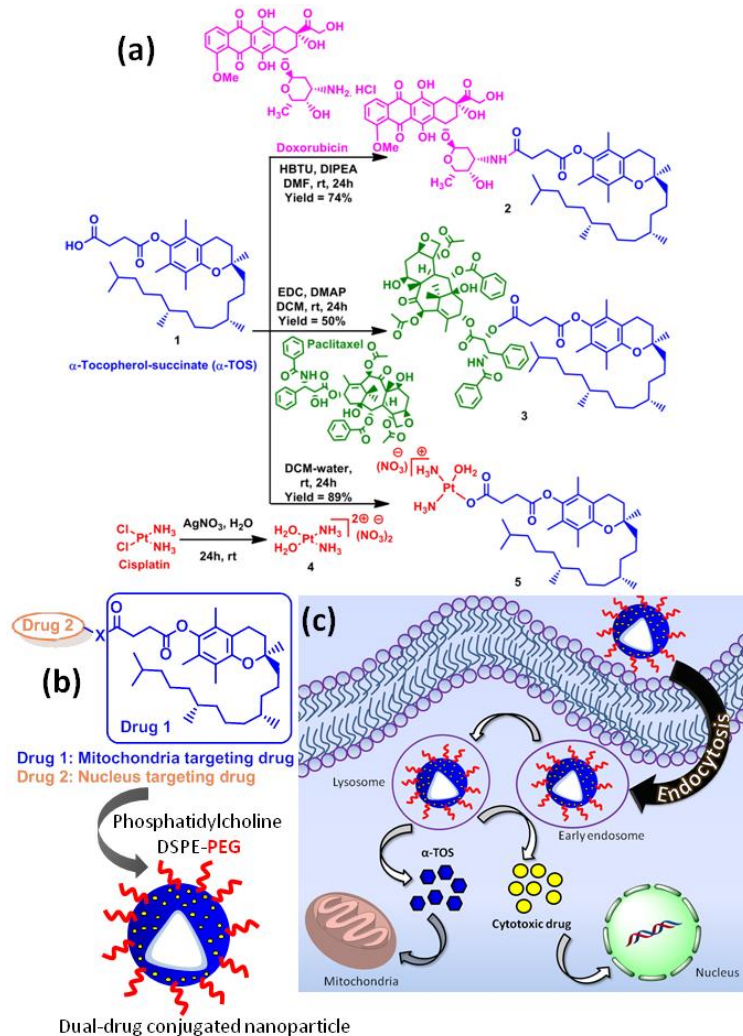


Figure 1. Schematic diagram of dual drug conjugate synthesis, nanoparticle engineering and cellular internalization. (a) Synthesis of dual drug conjugates from α -TOS and doxorubicin, paclitaxel and cisplatin by amide, ester and covalent coordinate conjugation respectively. (b) Schematic representation of dual drug conjugated nanoparticle synthesis by using phosphatidylcholine (PC) and DSPE-PEG. (c) Schematic diagram of internalization of dual drug conjugated nanoparticle into lysosomal compartment through endocytosis and target mitochondria and nucleus.

and DIPEA as base to obtain α -TOS-dox conjugate (**2**, **Figure 1a**) in 74% yield. α -TOS was conjugated through ester linkage with 2'-OH group of paclitaxel by using EDC as coupling agent and DIPEA as base in presence of DMAP as catalyst to obtain α -TOS-paclitaxel conjugate (**3**) (**Figure 1a**) in 50% yield. Finally, cisplatin (CDDP) was reacted with AgNO_3 to generate aquated $\text{cis-Pt}[(\text{NH}_3)_2(\text{OH}_2)_2]^{2+}$ (**4**)⁴⁵ which was further conjugated with α -TOS in 1:1 molar ratio by a monocarboxylato bond⁴⁶ to synthesize α -TOS-cisplatin conjugate (**5**) (**Figure 1a**) in 89% yield. The chemical structures of **2**, **3** and **5** were characterized by ¹H, ¹³C nuclear magnetic resonance spectroscopy (NMR), high-resolution mass spectroscopy (HR-MS) and MALDI-TOF (**Figure A1-A10**). Moreover, compound **5** showed characteristic monocarboxylato O-Pt peak at -1502 ppm in ¹⁹⁵Pt NMR spectroscopy (**Figure A11**).⁴⁷

4.2.1.2 Engineering of dual drug conjugated nanoparticles. We engineered nanoparticles from α -TOS-drug conjugates (**2**, **3** and **5**) by mixing it with phosphatidylcholine (PC) and 1,2-distearoyl-*sn*-glycero-3-phosphoethanolamine-N-[amino(polyethylene glycol)-2000] (DSPE-PEG) in 1:2:0.2 weight ratio using a lipid-film hydration method (**Figure 1b**).^{48, 49} We chose PC as it is biocompatible, biodegradable and a component of cell membrane. The nanoparticles were provided “stealth” capability by using DSPE-PEG to reduce opsonisation⁵⁰ and clearance by reticuloendothelial system (RES). This is not a spontaneous self-assembly. The TOS-drug conjugates were embedded in the PC to obtain a bilayer resulting in the formation of lipidic nanoparticles.

Mean drug loading in different dual drug conjugated nanoparticles was determined by UV-Vis spectroscopy to be = 2677.1 $\mu\text{g}/\text{mL}$ (α -TOS) and 217.7 $\mu\text{g}/\text{mL}$ (cisplatin) in α -TOS-CDDP-NP; 2116.2 $\mu\text{g}/\text{mL}$ (α -TOS) and 291.4 $\mu\text{g}/\text{mL}$ (doxorubicin) in α -TOS-Dox-NP; 784.3 $\mu\text{g}/\text{mL}$ (α -TOS) and 84.2 $\mu\text{g}/\text{mL}$ ($n = 3$) (paclitaxel) in α -TOS-Paclitaxel-NP (**Figure 2**), from a concentration vs absorbance calibration graph at characteristic $\lambda_{\text{max}} = 480 \text{ nm}$, 271 nm, 706 nm and 287 nm for doxorubicin, paclitaxel, cisplatin and α -TOS respectively (**Figure 3**). The mean hydrodynamic diameter of the dual drug conjugated nanoparticles were found to be = 163.3 nm, 186.3 nm and 167.9 nm ($n = 3$) having mean polydispersity index (PDI) = 0.152, 0.154 and 0.199 ($n = 3$) for α -TOS-Dox-NP, α -TOS-CDDP-NP and α -TOS-Paclitaxel-NP respectively by dynamic light scattering (DLS) (**Figure 4a**). The size, shape and morphology of the dual drug conjugated nanoparticle were characterized by field-emission scanning electron microscopy (FESEM, **Figure 4b**), transmission electron microscopy (TEM, **Figure**

4d) and atomic force microscopy (AFM, **Figure 4c**). DLS, FESEM, TEM and AFM data clearly demonstrated the dual drug conjugated nanoparticles were spherical in shape, having sub 200 nm diameter with a membrane thickness ~ 10 nm, which is suitable to accumulate into the tumor by EPR effect. Moreover, we confirmed the presence of Pt metal content in α -TOS-cisplatin-NP by energy-dispersive X-ray spectroscopy (EDX) measurements (**Figure 5**).

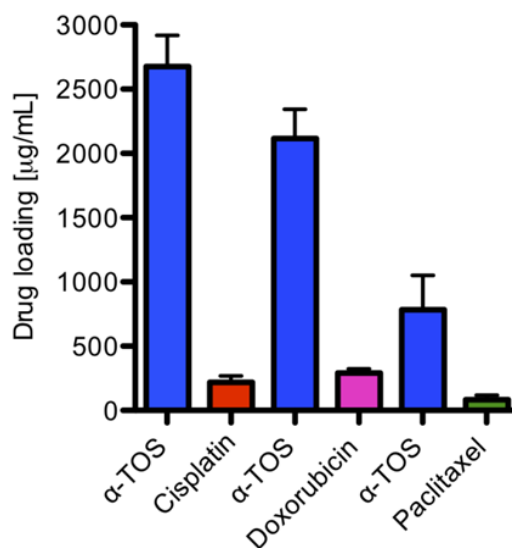


Figure 2: Loading of different drugs in dual-drug conjugated nanoparticles.

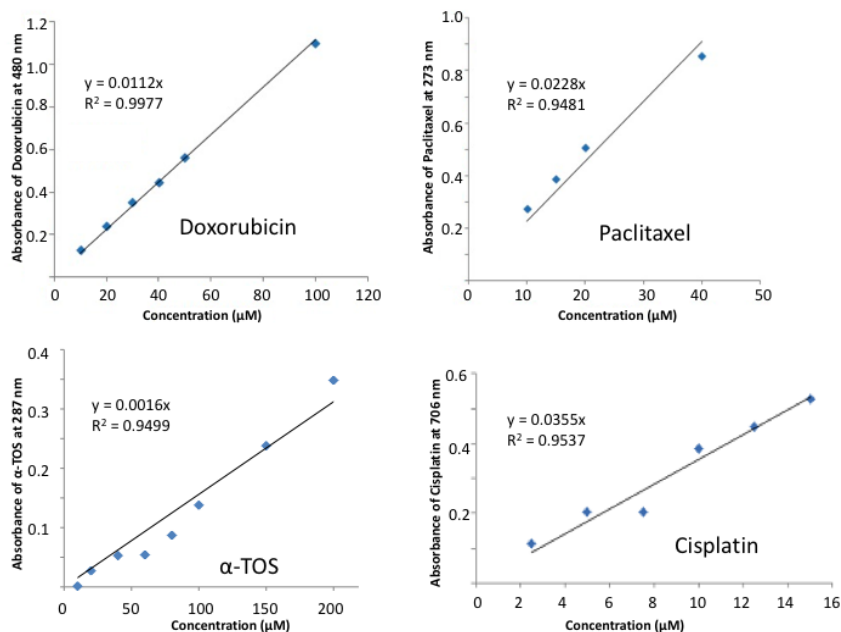


Figure 3: Concentration vs absorbance graph for Doxorubicin, Paclitaxel, α -TOS and Cisplatin at $\lambda_{\text{max}} = 480$ nm, 271 nm, 287 nm and 706 nm respectively.

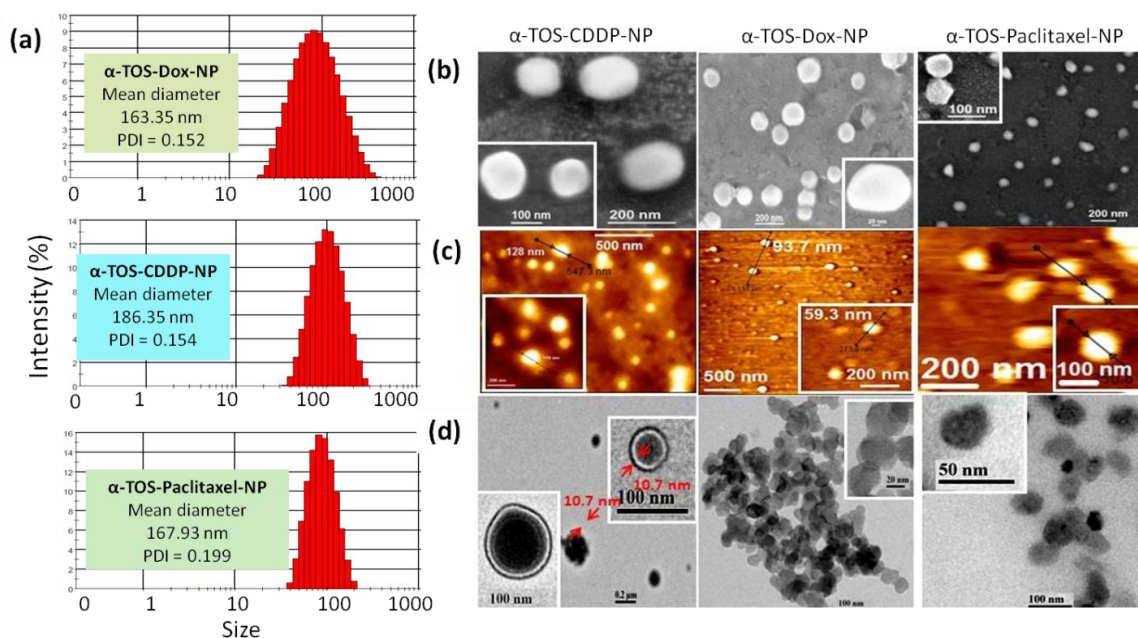


Figure 4: Characterization of dual drug conjugated nanoparticles. (a) Hydrodynamic diameter and polydispersity index (PDI) of dual drug conjugated nanoparticles determined by dynamic light scattering (DLS). (b) FESEM images of α -TOS-Dox-NP, α -TOS-CDDP-NP and α -TOS-Paclitaxel-NP respectively. (c) TEM images of α -TOS-Dox-NP, α -TOS-CDDP-NP and α -TOS-Paclitaxel-NP respectively. (d) AFM images of α -TOS-Dox-NP, α -TOS-CDDP-NP and α -TOS-Paclitaxel-NP respectively.

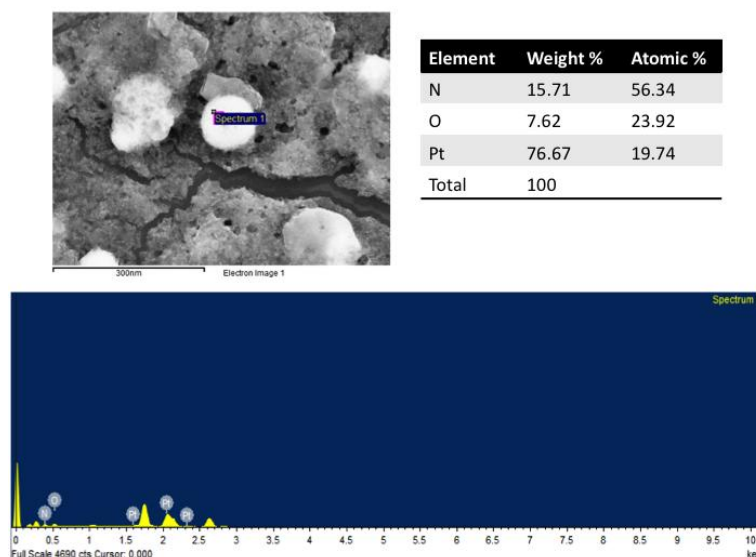


Figure 5: Determination of Pt metal content in α -TOS-CDDP-NP by energy dispersive X-ray spectroscopy (EDX).

4.2.1.3 Stability of dual drug conjugated nanoparticles. To use these dual drug conjugated nanoparticles in clinics, the nanoparticles should be stable for prolonged time at lower temperature storage conditions. We evaluated the stability of different nanoparticles by measuring the hydrodynamic diameter and PDI values at 4 °C for 14 days by using DLS (**Figure 6a**). α -TOS-Dox-NP showed change in size from 173.7 ± 0.9 nm (PDI = 0.152 ± 0.005) to 191.4 ± 5.6 nm (PDI = 0.350 ± 0.005) after 14 days. On the other hand, α -TOS-CDDP-NP demonstrated change in size from 176.3 ± 0.3 nm (PDI = 0.154 ± 0.008) to 197.6 ± 3.8 nm (PDI = 0.61 ± 0.23) over 14 days. Finally, α -TOS-Paclitaxel-NP increased in size from 185.0 ± 3.0 nm (PDI = 0.199 ± 0.009) to 175.3 ± 1.7 nm (PDI = 0.275 ± 0.25) in 14 days (mean \pm SEM, $n = 3$). Moreover, to be successful in the clinics, these dual drug conjugated nanoparticles should be stable inside the blood circulation at 37 °C to reach the tumor by EPR effect. Hence, we evaluated the stability of these nanoparticles at 37 °C in water. The hydrodynamic diameter of α -TOS-Dox-NP changed from 133.7 ± 0.7 nm to 144.1 ± 1.2 nm with a change in PDI value from 0.28 ± 0.04 to 0.47 ± 0.01 over 3 days (**Figure 6b**). Similarly, α -TOS-CDDP-NP changed its size from 152.5 ± 2.0 nm to 140.5 ± 3.4 nm with a change in PDI value from 0.37 ± 0.0 to 0.37 ± 0.01 over 3 days. Finally, α -TOS-Paclitaxel-NP demonstrated minimal change in size from 173.5 ± 2.0 nm (PDI = 0.11 ± 0.02) to 172.3 ± 2.2 nm (PDI = 0.48 ± 0.06) over 3 days. Further, we evaluated the stability these dual drug conjugated nanoparticles in phosphate buffer saline (PBS) at 37 °C for 3 days. α -TOS-CDDP-NP increased in size from 162.8 ± 1.8 nm (PDI = 0.28 ± 0.01) to 180.2 ± 2.8 nm (PDI = 0.54 ± 0.05) (**Figure 7a**). On the other hand, α -TOS-Dox-NP showed significant size increase from 147.2 ± 1.3 nm (PDI = 0.15 ± 0.02) to 190.3 ± 1.5 nm (PDI = 0.37 ± 0.05). Finally, α -TOS-Paclitaxel-NP also increased in size from 138.1 ± 1.3 (PDI = 0.14 ± 0.01) to 175.8 ± 5.7 nm (PDI = 0.31 ± 0.01) in PBS at 37°C. We finally, evaluated the stability of these nanoparticles in complete DMEM cell culture media with 10% fetal bovine serum (FBS) at 37 °C to mimic the blood circulation milieu. α -TOS-CDDP-NP showed a change in size from 152.0 ± 0.9 nm to 180.9 ± 2.8 nm with change in PDI from 0.51 ± 0.04 to 0.52 ± 0.07 over 48h (**Figure 7b**). Similarly, α -TOS-Dox-NP showed increase in size from 136.9 ± 1.4 nm to 189.9 ± 1.4 nm with the increase in PDI from 0.26 ± 0.02 to 0.46 ± 0.01 over 48 h. On the other hand, α -TOS-Paclitaxel-NP showed the increment in size from 127.3 ± 0.01 nm to 154.6 ± 3.0 nm with the change in PDI from 0.21 ± 0.01 to 0.31 ± 0.01 over 48 h. However, all three nanoparticles

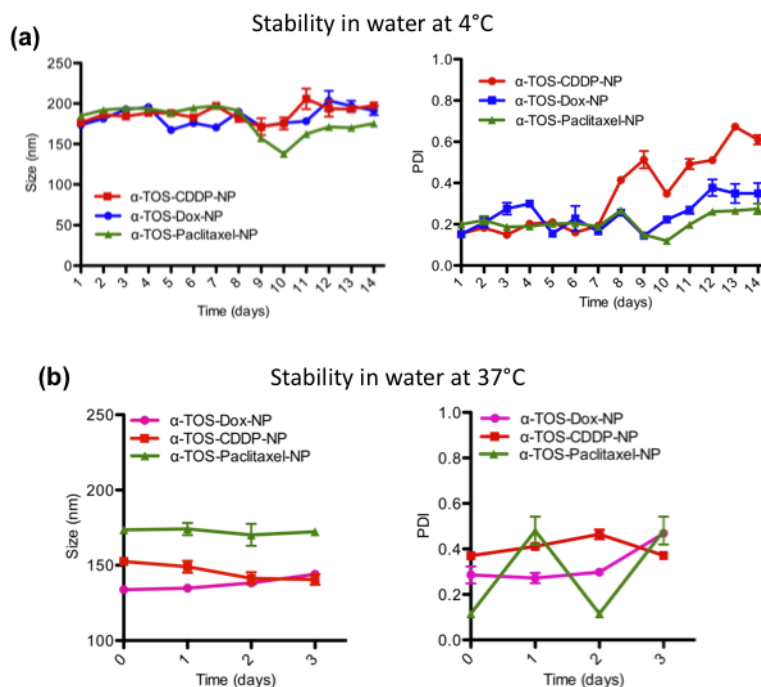


Figure 6: (a) Stability of dual drug conjugated nanoparticles in water over 14 days at 4 °C. (b) Stability of dual drug conjugated nanoparticles in water for 3 days at 37 °C determined by size and PDI values using DLS.

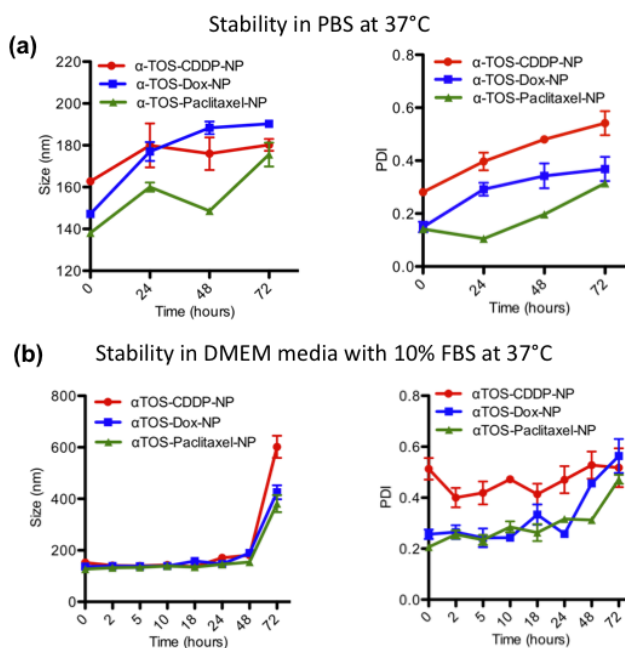


Figure 7: (a) Stability of dual drug conjugated nanoparticles in PBS over 72 h at 37 °C. (b) Stability of dual drug conjugated nanoparticles in DMEM cell culture media with 10% FBS for 72 h at 37 °C determined by size and PDI values using DLS.

showed considerable amount of aggregation at 72 h of incubation in DMEM with 10% FBS at 37 °C indicated by the huge increase in size of 601.8 ± 43.1 nm (PDI = 0.52 ± 0.07), 425.5 ± 27.0 nm (PDI = 0.56 ± 0.7) and 381.2 ± 33.1 nm (PDI = 0.47 ± 0.02) for α -TOS-CDDP-NP, α -TOS-Dox-NP and α -TOS-Paclitaxel-NP respectively. From the stability data, it was clear that all the nanoparticles were stable over 14 days at 4 °C as storage temperature. The nanoparticles were also stable at 37 °C in water as well as PBS for 3 days. Moreover, all the nanoparticles substantial stability in DMEM cell culture media with 10% FBS as blood circulation mimic for 48h, which was adequate to be accumulated into the tumor tissue through EPR effect.

4.2.1.4 Release of dual drugs from nanoparticles. To be effective in the clinics, the dual drug conjugated nanoparticles should release the drugs in a slow and sustained manner over a period of time. We evaluated the release of the drugs by using dialysis method⁴⁸ by incubating the nanoparticles in pH = 5.5 solution at 37 °C which mimics the lysosomal compartment in cancer cells.⁵¹ α -TOS-CDDP-NP released 45.9 ± 14.1 % cisplatin and 51.0 ± 5.5 % α -TOS at 72h (**Figure 8a**) whereas α -TOS-Dox-NP showed 58.6 ± 6.2 % release of α -TOS and only 29.5 ± 4.5 % release of doxorubicin at 72 h (**Figure 8b**). In the release kinetics experiment, doxorubicin was adsorbed in the dialysis membrane as well as precipitated out from the solution at pH = 5.5, which we suspected to be the reason for lower release of doxorubicin from the nanoparticle (**Figure 9a**). We solubilized the precipitate from the dialysis membrane in DMSO and identified it as doxorubicin by UV-Vis spectroscopy having characteristic $\lambda_{max} = 480$ nm (**Figure 9b**). Finally, α -TOS-Paclitaxel-NP demonstrated 78.5 ± 12.6 % release of paclitaxel at 72 h and 71.9 ± 21.6 % release of α -TOS at 36 h (**Figure 8c**). As control experiment, we also incubated the dual drug conjugated nanoparticles in physiological pH of 7.4 and quantified the dual drug release. At pH = 7.4, α -TOS-CDDP-NP released only 24.0 ± 2.4 % of cisplatin and 22.1 ± 2.1 % of α -TOS at 72 h and 48 h respectively (**Figure 8d**), whereas α -TOS-Dox-NP released 15.3 ± 1.0 % doxorubicin and 20.9 ± 3.6 % α -TOS at 72 h (**Figure 8e**). Finally, α -TOS-Paclitaxel-NP also demonstrated 18.8 ± 2.0 % and 26.4 ± 4.1 % release of paclitaxel and α -TOS at 72 h respectively (**Figure 8f**). We rationalized that amide, ester and monocarboxylato linkages in the α -TOS-Dox (**2**), α -TOS-Paclitaxel (**3**) and α -TOS-CDDP (**5**) conjugates respectively are more labile in pH = 5.5 compared to pH = 7.4 which triggered the enhanced dual drug release in acidic pH. We also identified the released free doxorubicin and paclitaxel after acidic hydrolysis from α -TOS-Dox-NP and α -TOS-Paclitaxel-

NP respectively by MALDI-TOF experiment (**Figure 10a-b**). The release profile data clearly showed higher dual drug release from nanoparticles in a slow and sustained manner over 72 h at pH = 5.5 compared to physiological pH = 7.4. All the data were evaluated as mean \pm SEM having $n = 3$.

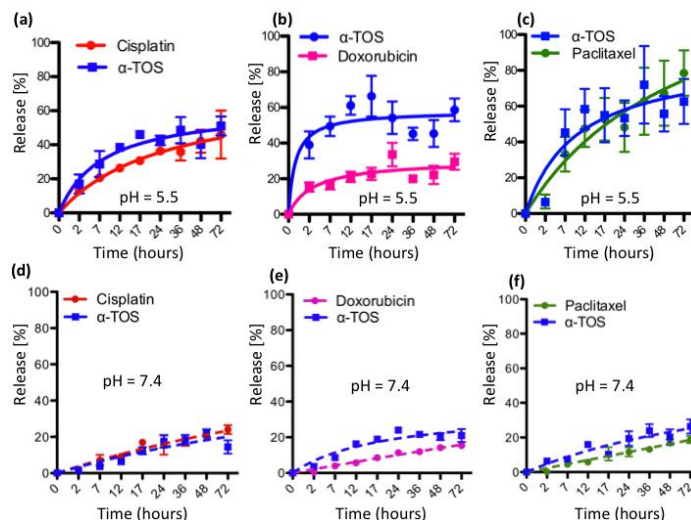


Figure 8: (a-c) Release of dual drugs from α -TOS-CDDP-NP, α -TOS-Dox-NP and α -TOS-Paclitaxel-NP respectively at pH = 5.5 which mimics the lysosomal compartments inside cancer cells. (d-f) Release of dual drugs from α -TOS-CDDP-NP, α -TOS-Dox-NP and α -TOS-Paclitaxel-NP respectively at pH = 7.4 which mimics the blood circulation environment *in vivo*.

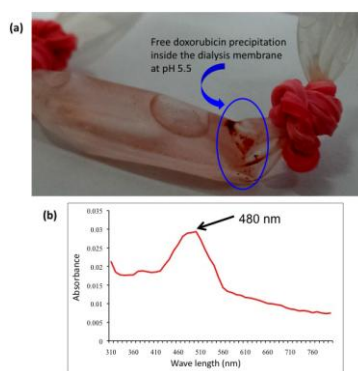


Figure 9: (a) Image of the dialysis membrane containing α -TOS-Dox-NP in pH = 5.5. The area of interest is showing the free doxorubicin precipitation. (b) UV-Vis spectra of free doxorubicin (dissolved in DMSO) precipitated in pH = 5.5 solution at $\lambda_{\max} = 480$ nm.

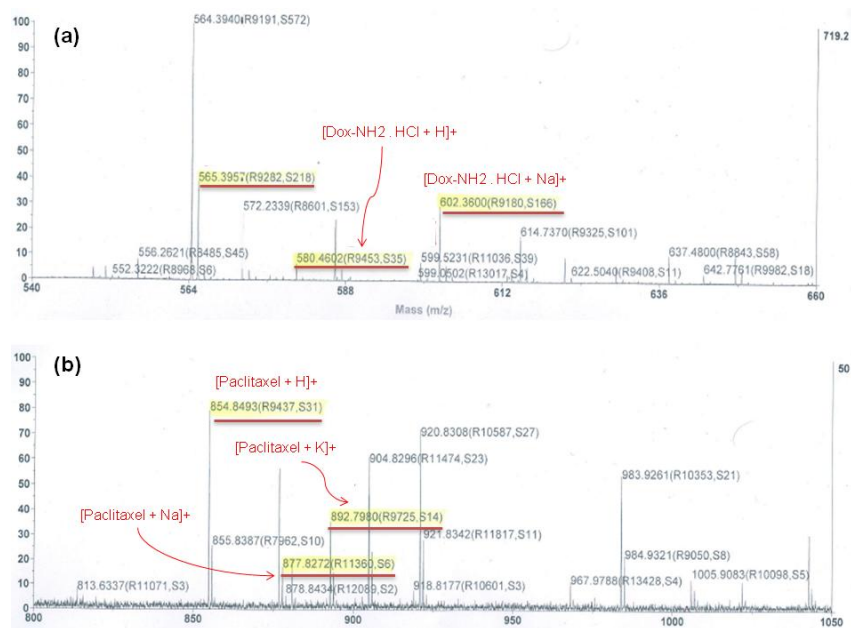


Figure 10: (a) MALDI-TOF traces of free doxorubicin released from α -TOS-Dox-NP at pH = 5.5. (b) MALDI-TOF traces of free paclitaxel released from α -TOS-Paclitaxel-NP at pH = 5.5.

4.2.2 In vitro cytotoxicity assay of dual-drug conjugated nanoparticles.

4.2.2.1 Cell viability assay. To determine the potential of our dual drug conjugated nanoparticles as cancer therapeutics, we evaluated the *in vitro* efficacy of the nanoparticles in HeLa cervical cancer cell line by cell viability assay. We incubated the HeLa cells with different nanoparticles in a dose dependent manner and evaluated the cell viability by using (3-(4,5-dimethylthiazol-2-yl)-2,5-diphenyl tetrazolium bromide)(MTT) at 48 h post treatment. The α -TOS-CDDP-NP showed $IC_{50} = 7.5 \mu M$ compared to $IC_{50} = 1.7 \mu M$ for free cisplatin and α -TOS combination (α -TOS: cisplatin = 6.5: 1) (**Figure 11a**). The α -TOS-CDDP-NP induced 93.9% HeLa cell death compared to 57.7% cell death induced by free cisplatin and α -TOS combination at 25 μM . On the other hand, α -TOS-Dox-NP demonstrated $IC_{50} = 6.8 \mu M$ compared to $IC_{50} = 2.7 \mu M$ for the free doxorubicin and α -TOS combination (α -TOS: doxorubicin = 7.4: 1) (**Figure 11b**). However, α -TOS-Dox-NP induced 72.6% cell death compared to 60.5% induced by free doxorubicin and α -TOS combination at 50 μM . Finally, α -TOS-Paclitaxel-NP showed $IC_{50} = 28.1 \mu M$ by inducing 71.7% cell death at 50 μM compared to $IC_{50} = 0.8 \mu M$ by inducing 57.4% cell death by free paclitaxel and α -TOS combination (α -TOS: paclitaxel = 15:1) (**Figure 11c**). Interestingly, all the different nanoparticles showed

improved efficacy in higher doses of drug combinations in contrast to the free drug treatments. We anticipate that different free drug combinations with α -TOS render drug resistance to HeLa cells.⁵² However, the exact mechanism needs to be explored. To understand the effect of dual drugs in cytotoxicity in HeLa cells, we used the Chou-Talalay method⁵³ to determine whether the drug combination effect was synergistic, additive or antagonistic. α -TOS-CDDP-NP and α -TOS-Dox-NP showed combination index (CI) values ranging from 0.05 to 0.62, which clearly indicated the strong synergistic effect (**Figure 12**). However, for α -TOS-Paclitaxel-NP showed CI values varied from 0.4 to 1.08 suggesting additive effect.

We also evaluated the effect of dual drug conjugates in HeLa cells. We incubated the HeLa cells with α -TOS-Dox (**2**), α -TOS-Paclitaxel (**3**) and α -TOS-CDDP (**5**) conjugates in a dose dependent manner and evaluated the cell viability by MTT assay at 48 h post-incubation. As controls, we treated the HeLa cells with free cisplatin, doxorubicin, paclitaxel and α -TOS individually. α -TOS-CDDP conjugate (**5**) showed $IC_{50} = 9.5 \mu\text{M}$ (cell viability = 23.0% at 50 μM) compared to $IC_{50} = 56 \mu\text{M}$ (cell viability = 56.1% at 50 μM) and $IC_{50} = 63.4$ (cell viability = 63.4% at 50 μM) for free cisplatin and free α -TOS respectively (**Figure 13a**). Similarly, α -TOS-Dox conjugate (**2**) showed $IC_{50} = 7.4 \mu\text{M}$ (cell viability = 23.1% at 50 μM) compared to $IC_{50} = 49 \mu\text{M}$ (cell viability = 34.6% at 50 μM) for free doxorubicin (**Figure 13b**). Finally, α -TOS-Paclitaxel conjugate (**3**) demonstrated $IC_{50} = 50 \mu\text{M}$ (cell viability = 50% at 50 μM) compared to $IC_{50} = 25.9 \mu\text{M}$ (cell viability = 42.2% at 50 μM) for free paclitaxel (**Figure 13c**). To evaluate the side effect of these dual drug conjugated nanoparticles in healthy cells, we treated HEK293 human embryonic kidney cells with different nanoparticles in a dose dependent manner for 24 h and 48 h post-incubation and quantified the cytotoxicity by MTT assay. At 24 h, α -TOS-CDDP-NP showed very high $IC_{50} = 63.9 \mu\text{M}$ compared to $IC_{50} = 14.6 \mu\text{M}$ and $IC_{50} = 89.9 \mu\text{M}$ for free cisplatin and free α -TOS respectively (**Figure 14a**). Similarly, α -TOS-Dox-NP also showed high $IC_{50} = 56.6 \mu\text{M}$ compared to $IC_{50} = 11 \mu\text{M}$ for free doxorubicin (**Figure 14b**). Finally, α -TOS-Paclitaxel-NP demonstrated $IC_{50} = 99.3 \mu\text{M}$ compared to $IC_{50} = 55.4 \mu\text{M}$ for free paclitaxel (**Figure 14c**). However, at 48 h, α -TOS-CDDP-NP showed $IC_{50} = 6.9 \mu\text{M}$ compared to $IC_{50} = 7.6 \mu\text{M}$ and $IC_{50} = 71.4 \mu\text{M}$ for free cisplatin and free α -TOS (**Figure 14d**). On the other hand, α -TOS-Dox-NP showed $IC_{50} = 7.1 \mu\text{M}$ compared to $IC_{50} = 3.3 \mu\text{M}$ for free doxorubicin (**Figure 14e**). Finally, α -TOS-Paclitaxel-NP demonstrated $IC_{50} = 29.9 \mu\text{M}$ compared to $IC_{50} = 11.3 \mu\text{M}$ for free paclitaxel (**Figure 14f**).

From these cell viability assays, it was clear that the dual drug conjugated nanoparticles induced enhanced cell death in a dose dependent manner compared to free drug combinations as well as compared to the dual drug conjugates at 48 h. Moreover, the dual drug conjugated nanoparticles showed negligible toxicity to the HEK293 non-cancerous embryonic kidney cells at 24 h. However, the dual drug conjugated nanoparticles showed toxicity to the HEK293 cells at 48 h post incubation, we anticipate that the nanoparticles would be homing specifically and selectively into the tumor tissues through the unique leaky vasculature (EPR effect) much earlier than 48 h in *in vivo* milieu. To evaluate the effect of phosphatidylcholine (PC) and DSPE-PEG in HeLa cell, we synthesized empty nanoparticles from PC and DSPE-PEG in 2:0.2 ratios in the same lipid film hydration method. We treated the HeLa cells with empty nanoparticle in different concentration and evaluated the cell viability by MTT assay. The empty nanoparticle showed no toxicity in HeLa cells at 1 mg/mL concentration (**Figure 15**).

4.2.2.2 Apoptosis assay by FACS. To confirm the potential of the nanoparticles in inducing apoptosis, we used fluorescence activated cell sorting (FACS) method to quantify the amount of cells undergoing apoptosis after treatment compared to the non treated cells. We treated the HeLa cells with different dual drug conjugated nanoparticles for 24 h and the cells were labelled with Annexin-V-FLUOS, which binds with externalized phosphatidylserine on the apoptotic cell surface. We further counterstained the cells with propidium iodide (PI) to distinguish between apoptotic and necrotic cells. Indeed, 39% and 47% cells were found in the early and late apoptosis stages respectively with 4% cells in necrotic stage with the treatment of α -TOS-CDDP-NP (**Figure 11d**). Similarly, 37% and 0.5% cells were found to be in early apoptotic and late apoptotic stages respectively in the treatment with α -TOS-Dox-NP. However, α -TOS-Paclitaxel-NP steered 27% and 7% cells into early and late apoptotic stages respectively. From this flow cytometric analysis, it was clear that the dual drug conjugated nanoparticles showed cytotoxicity into HeLa cells through induction of apoptosis.

4.2.2.3 Caspase assay. Induction of apoptosis in cells leads to the activation of a family of caspases including effector caspase-3 and initiator caspase-8 and caspase-9.⁵⁴⁻⁵⁶ We quantified the amount of caspase-3, caspase-8 and caspase-9 as markers of apoptosis by a colorimetric protease assay 24 h of post-treatment with different dual drug conjugated nanoparticles. Amount of caspase-3 was increased 1.1 ± 0.3 , 1.7 ± 0.5 and 3.4 ± 1.2 folds for α -TOS-CDDP-NP, α -TOS-Dox-NP and α -TOS-Paclitaxel-NP respectively (**Figure 16**). Similarly, caspase-8

activity was also increased to 2.5 ± 0.2 , 5.1 ± 1.3 and 1.5 ± 0.1 folds by α -TOS-CDDP-NP, α -TOS-Dox-NP and α -TOS-Paclitaxel-NP respectively. Finally, caspase-9 activity was increased significantly to 2.8 ± 0.7 , 2.9 ± 1.1 and 7.3 ± 0.8 folds by the treatment with α -TOS-CDDP-NP, α -TOS-Dox-NP and α -TOS-Paclitaxel-NP respectively. This caspase assay clearly demonstrated that different dual drug conjugated nanoparticles induced apoptosis in HeLa cells.

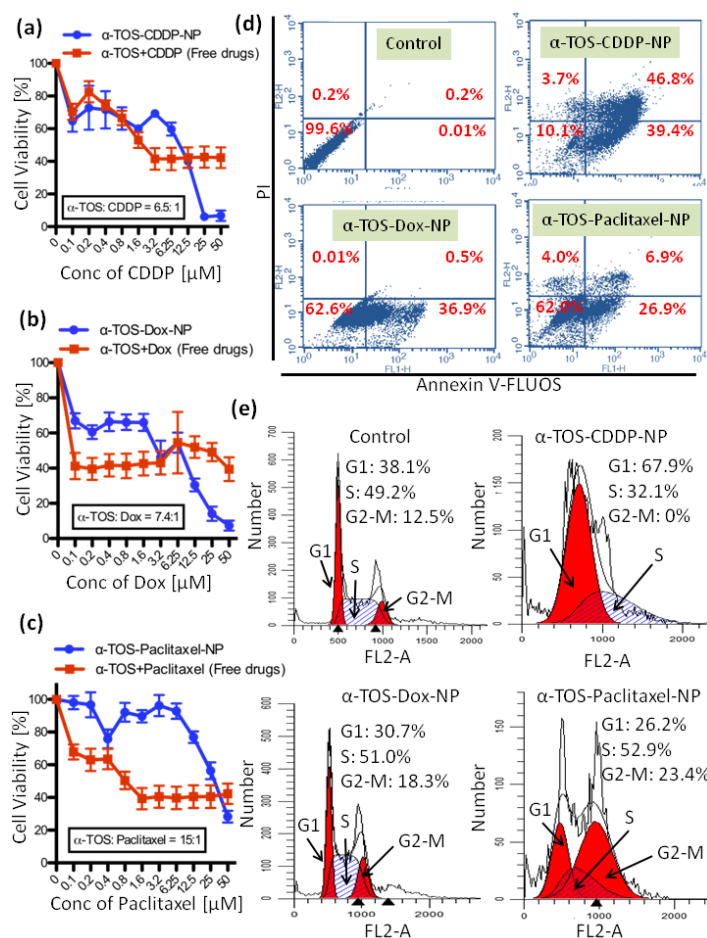


Figure 11. *In vitro* cytotoxicity assay of dual drug conjugated nanoparticles. (a-c) Dose dependent cell viability assay of α -TOS-CDDP-NP, α -TOS-Dox-NP and α -TOS-Paclitaxel-NP respectively in HeLa cells for 48 h. (d) Flow cytometric analysis of apoptosis induced by dual drug conjugated nanoparticles co-stained by PI and Annexin-V-FLUOS in HeLa cells for 24 h. Lower left: healthy cells; lower right: early apoptotic cells; upper right: late apoptotic cells and upper left: necrotic cells. The table shows the percentage of cells present in those areas. (e)

Cell cycle analysis by staining the DNA in HeLa cells with PI after 24h post incubation with different dual-drug conjugated nanoparticles.

4.2.2.4 Cell cycle analysis. To understand the mechanism of action further, we evaluated the effect of different dual drug conjugated nanoparticles on cell cycle. We analyzed the cell cycle arrest by using propidium iodide (PI)-labelled DNA in HeLa cells after 24 h post-treatment. The flow cytometry analysis showed that after α -TOS-CDDP-NP treatment, cells were in G1, S and G2-M phase as 67.9%, 32.1% and 0% respectively, whereas, non treated cells were found to be as 38.1%, 49.2% and 12.5% respectively (**Figure 11e**). Similarly, after α -TOS-Dox-NP treatment, 30.7%, 51.0% and 18.3% cells were found to be in G1, S and G2-M phase respectively. Finally, α -TOS-Paclitaxel-NP treated cells were found as 26.2%, 52.9% and 23.4% in G1, S and G2-M phase respectively. From this cell cycle analysis, it was evident that α -TOS-CDDP-NP arrested the cells in G1 phase whereas α -TOS-Dox-NP and α -TOS-Paclitaxel-NP arrested the HeLa cells in G2-M phase.

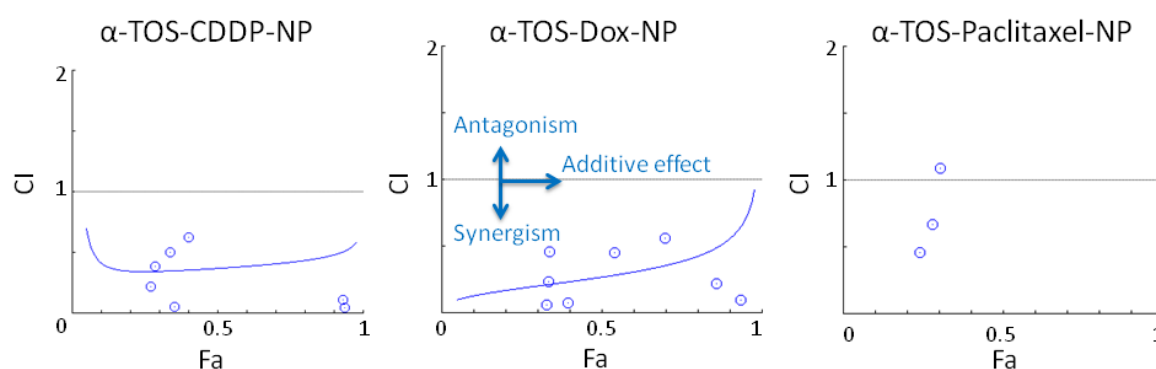


Figure 12: Chou-Talalay analysis of α -TOS-CDDP-NP, α -TOS-Dox-NP and α -TOS-Paclitaxel-NP in HeLa cells to determine synergistic, additive and antagonistic effects.

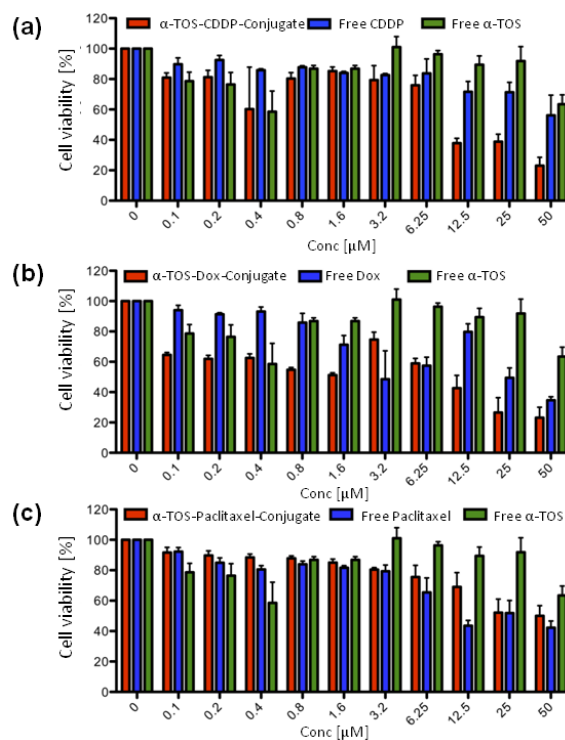


Figure 13: (a-c) MTT assay of α -TOS-CDDP conjugate, α -TOS-Dox conjugate and α -TOS-Paclitaxel conjugate respectively in HeLa cells at 48 h post treatment compared with free CDDP, free Dox, free Paclitaxel and free α -TOS.

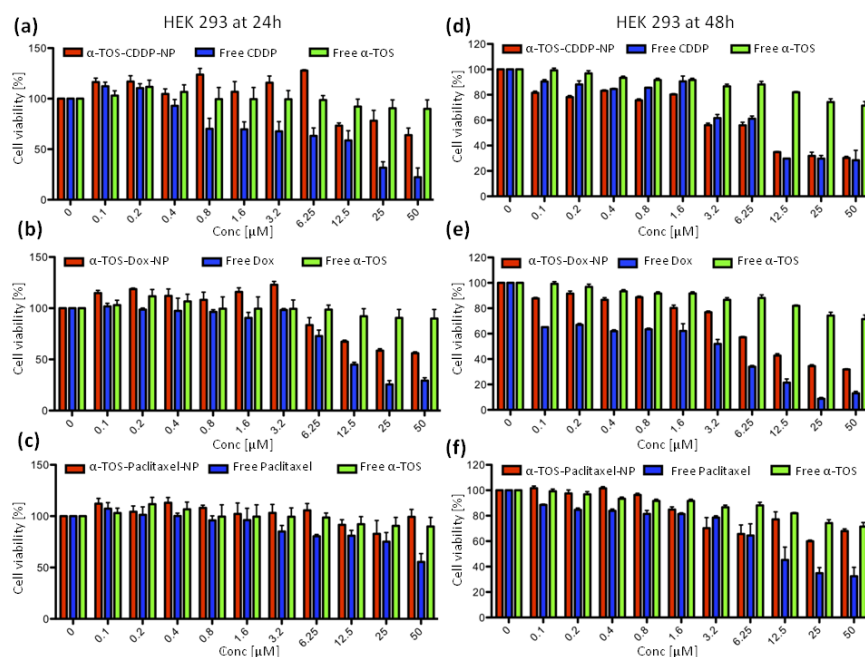


Figure 14: (a-c) MTT assay of α -TOS-CDDP-NP, α -TOS-Dox-NP and α -TOS-Paclitaxel-NP respectively in HEK293 cells at 24 h post treatment compared with free CDDP, free Dox, free

Paclitaxel and free α -TOS. (d-f) MTT assay of α -TOS-CDDP-NP, α -TOS-Dox-NP and α -TOS-Paclitaxel-NP respectively in HEK293 cells at 48 h post treatment compared with free CDDP, free Dox, free Paclitaxel and free α -TOS.

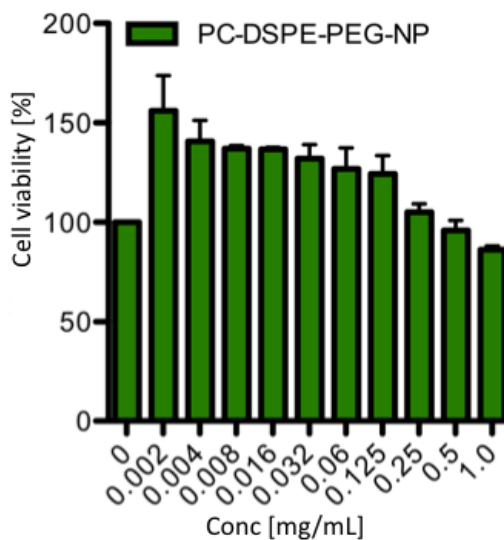


Figure 15: MTT assay of empty nanoparticle synthesized from PC and DSPE-PEG to show its non-toxic nature.

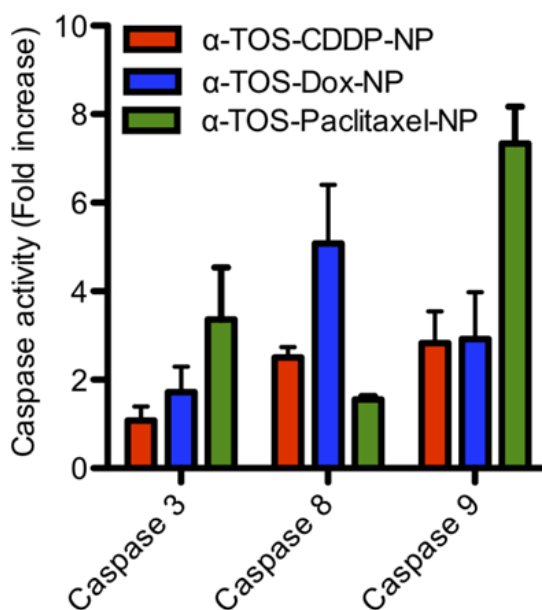


Figure 16: Quantification of caspase-3, caspase-8 and caspase-9 as makers of apoptosis in different dual-drug conjugated nanoparticle treatments at 24 h post-incubation.

4.2.3 Cellular internalization of dual drug conjugated nanoparticles. To visualize the temporal cellular internalization mechanism of the dual drug conjugated nanoparticles, we

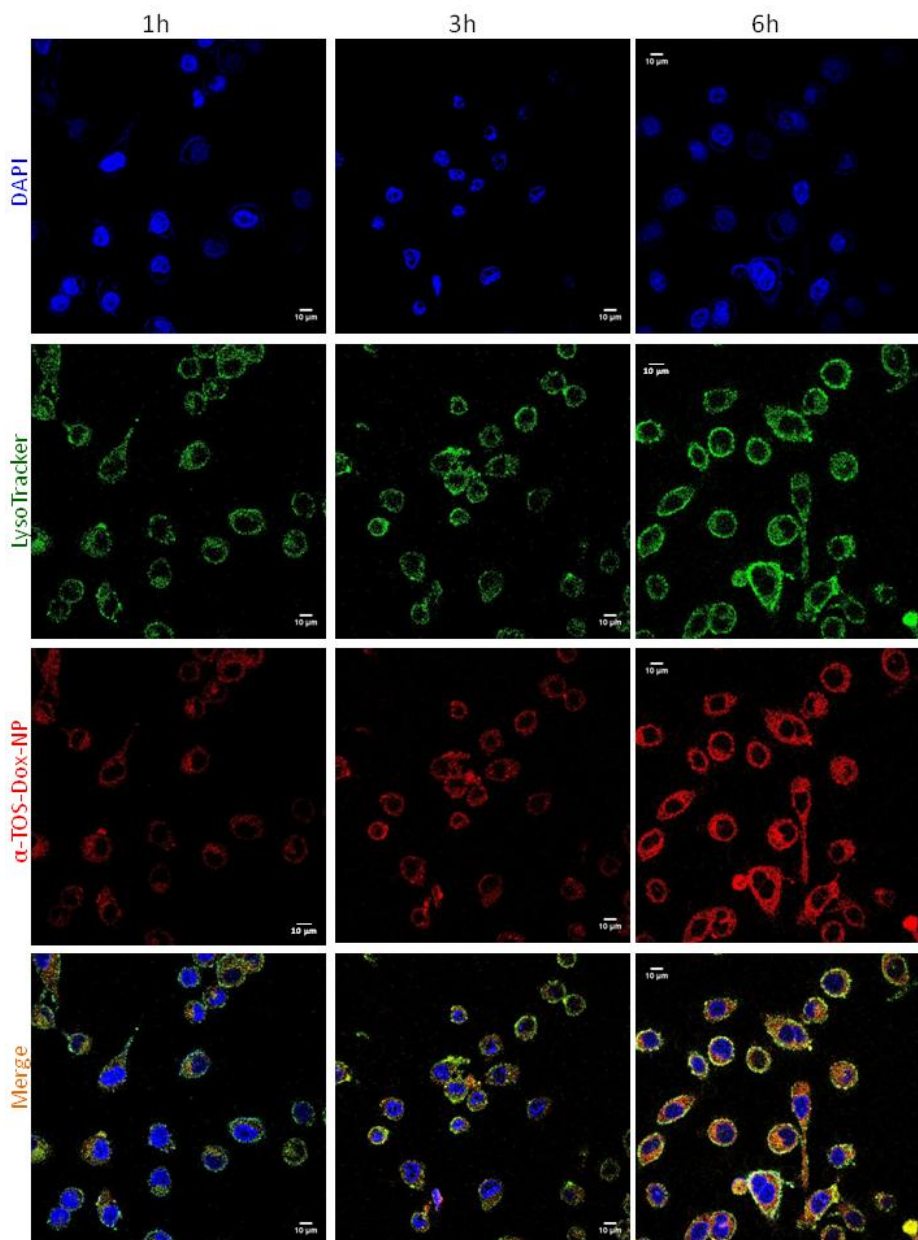


Figure 17. Cellular internalization of α -TOS-Dox-NP in HeLa cells in 1 h, 3 h and 6 h time points observed by confocal laser scanning microscopy (CLSM). Lysosomal compartments and nuclei were stained with LysoTrackerTM Green DND-26 (green) and DAPI (blue) respectively. Merged images (yellow) show the internalization of α -TOS-Dox-NP in lysosomal compartments. Scale bar = 10 μ m.

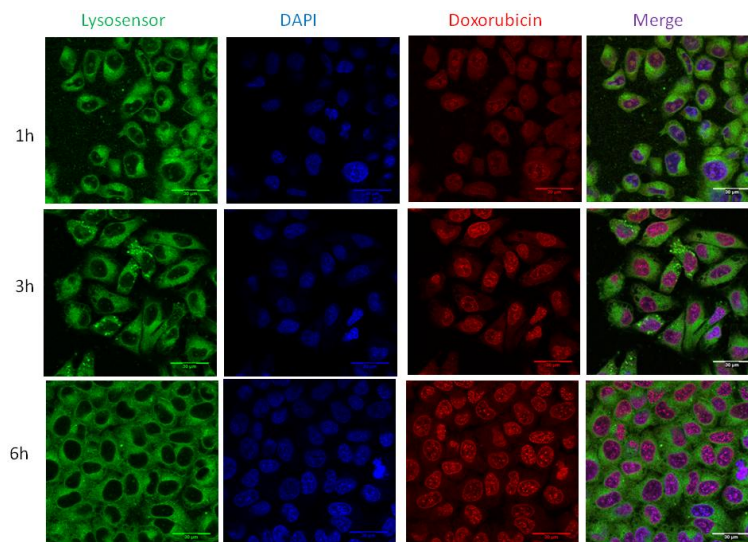


Figure 18: Confocal laser scanning microscopy (CLSM) images of free doxorubicin internalization into HeLa cells in 1 h, 3 h and 6 h. Lysosomal compartments and nucleus were stained with LysoSensor Green DND-153 (green) and DAPI (blue) respectively. In merged images, purple color indicated the localization of free doxorubicin (red) in nucleus in a time dependent manner. Scale bar = 30 μm .

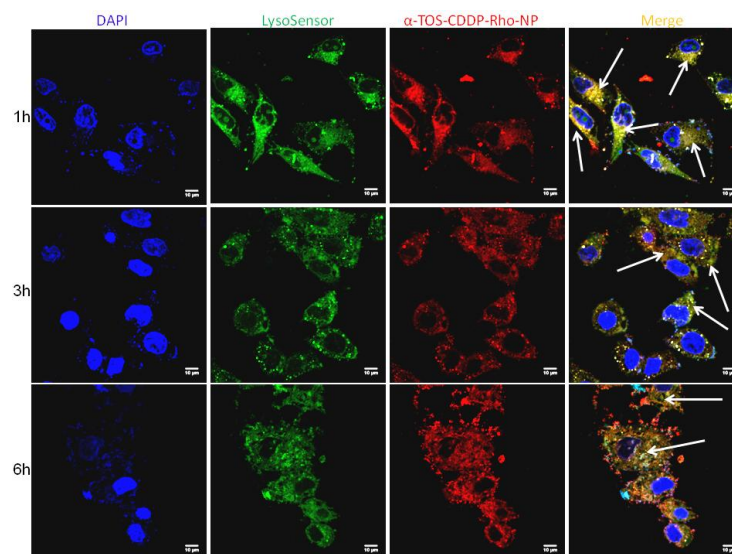


Figure 19: Confocal laser scanning microscopy (CLSM) images of α -TOS-CDDP-Rho-NP internalization into HeLa cells in 1 h, 3 h and 6 h. Lysosomal compartments and nucleus were stained with LysoSensor Green DND-153 (green) and DAPI (blue) respectively. In merged images, yellow color indicated the localization of α -TOS-CDDP-Rho-NP (red) in lysosomal compartments in a time dependent manner. Scale bar = 10 μm .

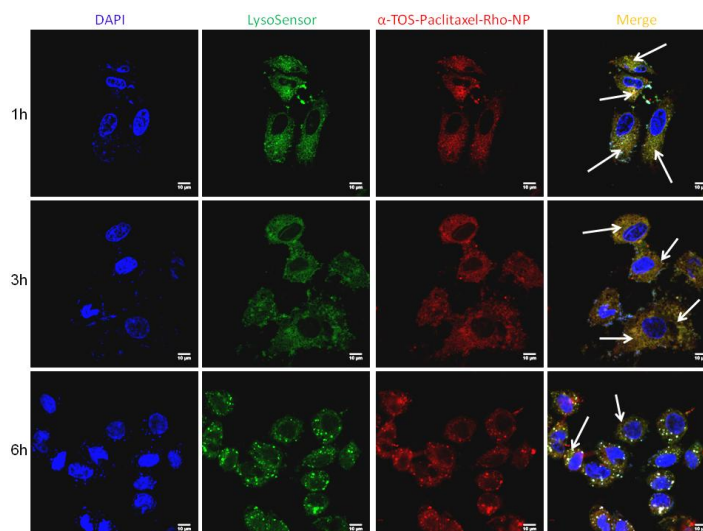


Figure 20: Confocal laser scanning microscopy (CLSM) images of α -TOS-Paclitaxel-Rho-NP internalization into HeLa cells in 1 h, 3 h and 6 h. Lysosomal compartments and nucleus were stained with LysoSensor Green DND-153 (green) and DAPI (blue) respectively. In merged images, yellow color indicated the localization of α -TOS-Paclitaxel-Rho-NP (red) in lysosomal compartments in a time dependent manner. Scale bar = 10 μ m.

Treatment Time		1h	3h	6h
Image Channels		C2(green) C3(red)	C2(green) C3(red)	C2(green) C3(red)
Pearsons' Correlation Coefficient	r	0.445	0.584	0.832
Manders Coefficients	M1 (fraction of C2 overlapping C3)	0.5214	0.5759	0.9398
	M2 (fraction of C3 overlapping C2)	0.5172	0.6396	0.9421
Percent volume colocalized		18.63%	21.52%	40.70%

Table 1: Quantification of colocalization of α -TOS-Dox-NP (red) into lysosomal compartments stained with LysoTracker Green DND-26 (green) in 1h, 3h and 6h time points.

Treatment Time		1h	3h	6h
Image Channels		C2(green) C3(red)	C2(green) C3(red)	C2(green) C3(red)
Pearsons' Correlation Coefficient	R	0.832	0.772	0.815
Manders Coefficients	M1 (fraction of C2 overlapping C3)	0.781	0.7947	0.8493
	M2 (fraction of C3 overlapping C2)	0.5833	0.6525	0.7
Percent volume colocalized		26.24%	31.85%	31.1%

Table 2: Quantification of colocalization of α -TOS-CDDP-Rho-NP (red) into lysosomal compartments stained with LysoSensor Green DND-153 (green) in 1h, 3h and 6h time points.

Treatment Time		1h	3h	6h
Image Channels		C2(green) C3(red)	C2(green) C3(red)	C2(green) C3(red)
Pearsons' Correlation Coefficient	r	0.72	0.763	0.726
Manders Coefficients	M1 (fraction of C2 overlapping C3)	0.7787	0.7884	0.77
	M2 (fraction of C3 overlapping C2)	0.7384	0.7371	0.8229
Percent volume colocalized		30.24%	28.02%	29.17%

Table 3: Quantification of colocalization of α -TOS-Paclitaxel-Rho-NP (red) into lysosomal compartments stained with LysoSensor Green DND-153 (green) in 1h, 3h and 6h time points.

treated the HeLa cells with red fluorescent α -TOS-Dox-NP (2 μ g/mL of doxorubicin concentration) for 1 h, 3 h and 6 h time points. We treated the cells with 2 μ g/mL of free

doxorubicin as control. We stained the low pH lysosomal compartments with LysoTrackerTM Green DND-26 (green) and nucleus with 4',6-diamidino-2-phenylindole (DAPI)(blue) respectively and imaged the cells by using high resolution confocal laser scanning microscopy (CLSM) (**Figure 17 and Figure 18**). From **Figure 17**, it was clear that α -TOS-Dox-NPs were internalized into the cells in a time dependent manner over 6 h and homed into the lysosomal compartments, which led the colocalization of red and green fluorescence resulting yellow color. We also quantified the amount of colocalization of green and red fluorescence through Pearson's correlation coefficient and Manders coefficients by CLSM. It was found that the % volume of colocalization increased from 1 h to 3 h to 6 h by 18.6% to 21.5% to 40.7% (**Table 1**). In contrast, free doxorubicin internalized into the cells within 3 h and directly localized into the nucleus, which led the colocalization of red and blue fluorescence resulting purple color (**Figure 18**). Interestingly, in free doxorubicin treatment, no colocalization of green and red was observed which clearly demonstrated that free doxorubicin was internalized into the cell through diffusion pathway and homed directly into nucleus.

To further visualize the internalization of α -TOS-CDDP-NP and α -TOS-Paclitaxel-NP, we encapsulated a red fluorescent dye rhodamine to synthesize α -TOS-CDDP-Rho-NP and α -TOS-Paclitaxel-Rho-NP respectively. We incubated the HeLa cells with α -TOS-CDDP-Rho-NP and α -TOS-Paclitaxel-Rho-NP for 1 h, 3 h and 6 h time points. We stained the lysosomal compartment and nucleus with LysoSensorTM Green DND-153 (green) and DAPI (blue) respectively. The CLSM images and colocalization quantification (**Figure 19 and Table 2**) clearly showed that α -TOS-CDDP-Rho-NP internalized into the lysosomal compartment within 1 h (26.2% colocalization) and retained for 6 h (31.1% colocalization). Similarly, α -TOS-Paclitaxel-Rho-NP also internalized into lysosomal compartments within 1 h (30.2% colocalization) and retained there for 6 h (29.2% colocalization) (**Figure 20 and Table 3**). The CLSM images and colocalization quantification data clearly showed that dual drug conjugated nanoparticles were internalized into the HeLa cells through endocytosis into the acidic lysosomal compartments in a temporal manner in contrast to the free drugs.

4.2.4 Targeting mitochondria by dual drug conjugated nanoparticles. We hypothesized that after internalization of dual drug conjugated nanoparticles into lysosomal compartments,

the individual drugs will be released to target mitochondria and nucleus. Hence, we evaluated the effect of dual drug conjugated nanoparticles on mitochondrial morphology. We treated

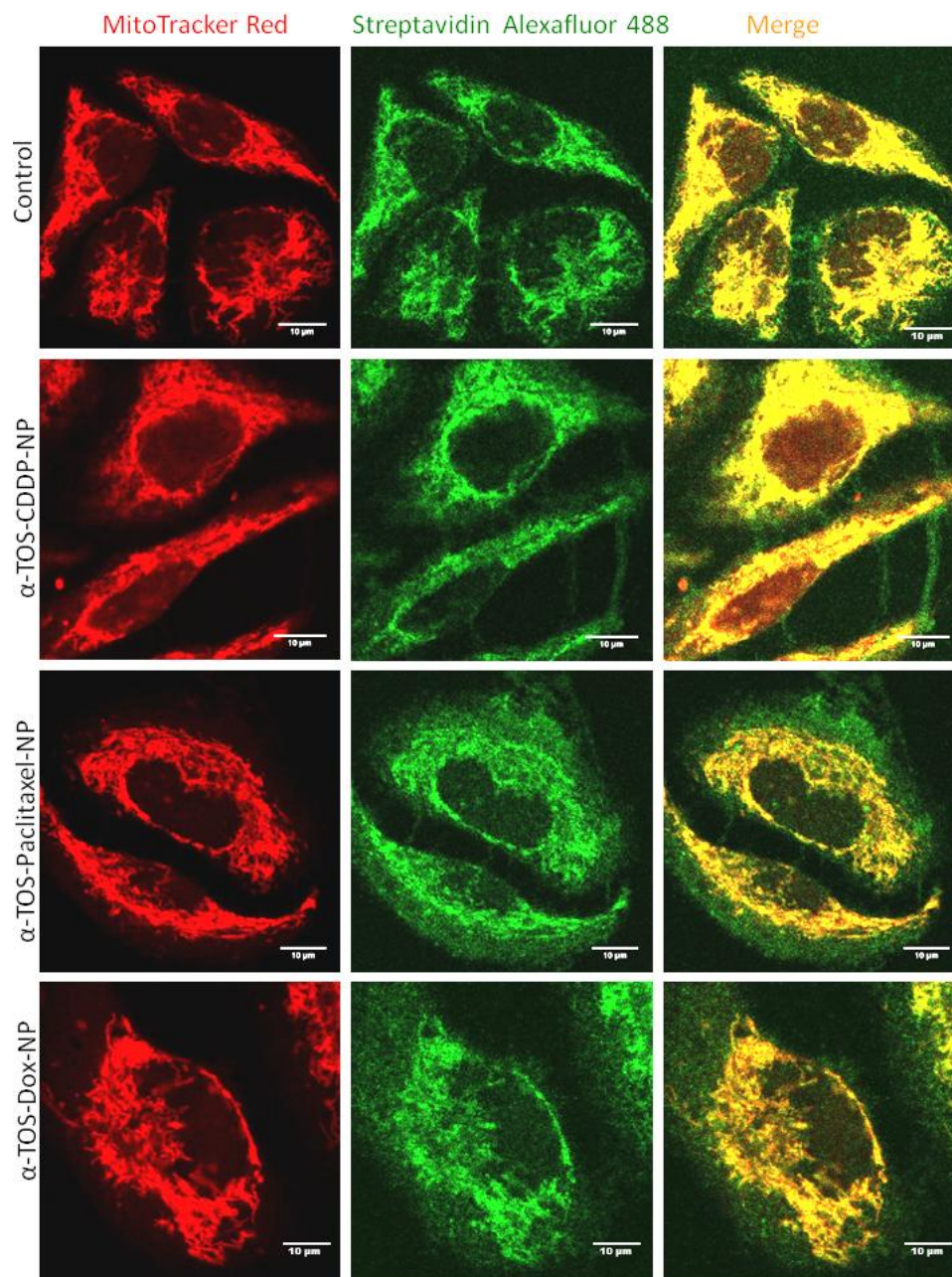


Figure 21. CLSM of mitochondria after treatment with individual dual drug conjugated nanoparticles for 24 h. Mitochondria were stained with MitoTracker Red CMXRos (red) and biotinylated proteins over-expressed on mitochondria were stained with Streptavidin Alexafluor 488 (green). CLSM images show the damage of mitochondrial morphology with different dual drug conjugated nanoparticle treatments. Scale bar = 10 μm.

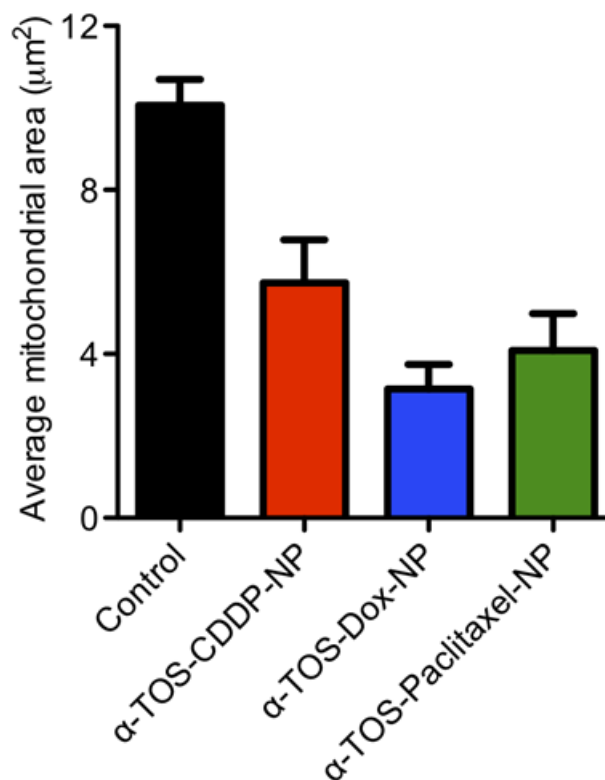


Figure 22: Quantification of mitochondrial area as the measure of mitochondrial fragmentation after the treatment with dual drug conjugated nanoparticles by CLSM.

HeLa cells with different dual drug conjugated nanoparticles individually for 24 h at their respective IC_{50} drug dosages and stained the mitochondria with red fluorescent MitoTracker Red CMXRos (**Figure 21**). We also co-stained the endogenous biotinylated proteins prevalent in mitochondria⁵⁷ by green fluorescent Streptavidin Alexafluor 488 and visualized the mitochondrial morphology change by CLSM. From **Figure 21**, it was clear that the non-treated control cells showed nice elongated mitochondrial morphology, which was visibly disrupted, leading to the mitochondrial fragmentation in different nanoparticle treated cells. Colocalization of MitoTracker Red CMXRos (red) and Streptavidin Alexafluor 488 (green) leading to yellow color in the merged images clearly demonstrated the lack of characteristic mitochondrial morphology by different nanoparticle treatments. Moreover, we quantified the average mitochondrial area by using ImageJ analysis software with the help of MitoMorphology macro, which allows to measure mitochondrial elongation, interconnectivity and morphology from epifluorescence images of cells stained for mitochondria.⁵⁸ The

mitochondrial average area for a non treated cell was found to be $10.1 \pm 0.6 \mu\text{m}^2$, whereas the average fragmented mitochondria area was found to be reduced to $5.7 \pm 1.0 \mu\text{m}^2$, $3.1 \pm 0.6 \mu\text{m}^2$ and $4.9 \pm 0.9 \mu\text{m}^2$ for α -TOS-CDDP-NP, α -TOS-Dox-NP and α -TOS-Paclitaxel-NP treated cells respectively ($n = 5$, mean \pm SEM) (**Figure 22**). From these CLSM images and quantification of the average mitochondrial area, it is clear that α -TOS from different dual drug conjugated nanoparticles targeted mitochondria and exhibited mitochondrial fragmentation.

One of the hallmarks of mitochondrial damage is the mitochondrial outer membrane permeabilization (MOMP) followed by release of cytochrome c from inter-membrane spaces (IMS).⁵⁹ We treated HeLa cells with different dual drug conjugated nanoparticles at their respective IC_{50} drug dosages for 24 h. The cells were then fixed and stained with green fluorescent Alexafluor 488 antibody specific for cytochrome c and visualized by CLSM. From **Figure 23a**, it is clear that α -TOS-CDDP-NP, α -TOS-Dox-NP and α -TOS-Paclitaxel-NP showed highly increased amount of cytochrome c expression in HeLa cells compared to non treated control cells. We also determined the expression of cytochrome c by western blot analysis using cytochrome c rabbit monoclonal antibody, after treatment of HeLa cells with different dual drug conjugated nanoparticles at their respective IC_{50} drug dosages for 24 h. From the Western blot images (**Figure 23b**), it was clear that all three dual drug conjugated nanoparticles increased the expression level of cytochrome c compared to the non treated control. Moreover, we also quantified the expression level of cytochrome c from the western blot, which clearly showed 1.1 fold, 1.5 fold and 1.5 fold increased expression of cytochrome c after the treatment with α -TOS-CDDP-NP, α -TOS-Dox-NP and α -TOS-Paclitaxel-NP respectively compared to the non treated control (**Figure 24**). From these CLSM images of mitochondrial morphology, cytochrome c release by inducing MOMP, western blot analysis and quantification, it was clear that the dual drug conjugated nanoparticles damaged mitochondria in the HeLa cancer cells.

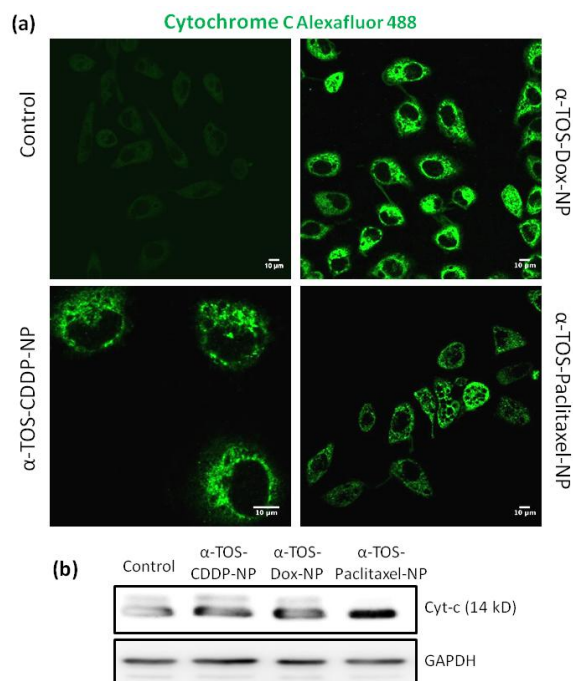


Figure 23. Characterization of mitochondrial damage by cytochrome c expression. (a) CLSM images of dual drug conjugated nanoparticle treated HeLa cells for 24 h at their respective IC_{50} drug dosages compared to non-treated control. Cells were stained with cytochrome c-Alexafluor 488 antibody (green). Scale bar = 10 μ m. (b) The expression of cytochrome c in HeLa cells after 24 h post incubation with dual drug conjugated nanoparticles determined by Western blot analysis.

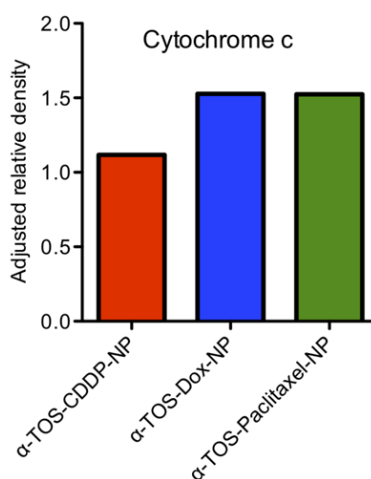


Figure 24: Quantification of cytochrome c expression from Western Blot analysis as a measure of mitochondrial damage after treatment with dual drug conjugated nanoparticles at 24 h post-incubation.

4.2.5 Targeting nucleus and microtubule by dual drug conjugated nanoparticle. Nucleus contains the genomic materials (DNA and RNA), regulates the gene expression and controls the replication of DNA during cell cycle. Hence damaging the DNA in the nucleus of the cancer cells would lead to inhibit the rapid cellular division. The DNA damage in the nucleus is followed by the phosphorylation of the histone H2AX in recruiting and localizing the DNA damage repairing proteins. Hence, γ H2AX has evolved as one of the important biomarkers to observe DNA damage.⁶⁰ To determine the effect of dual drug conjugated nanoparticles in nucleus we treated the HeLa cells with different dual drug conjugated nanoparticles in their respective IC₅₀ drug dosages for 24 h. We stained the cells with green fluorescent Alexafluor 488 antibody specific for γ H2AX and visualized the expression of γ H2AX by CLSM. From **Figure 25a**, it was clear that α -TOS-CDDP-NP inflicted high DNA damage in nucleus to induce elevated expression of γ H2AX compared to non treated control. α -TOS-Dox-NP induced lower level of γ H2AX expression compared to α -TOS-CDDP-NP treatment. It was reported that doxorubicin promoted histone eviction leading to induce lower expression of γ H2AX.⁶¹ Finally, we observed minimum expression γ H2AX after α -TOS-Paclitaxel-NP, which was expected as paclitaxel does not induce DNA damage directly.

We also evaluated the expression of γ H2AX by western blot analysis after 24 h incubation of HeLa cells with different dual drug conjugated nanoparticles in their respective IC₅₀ drug dosages. From the Western blot image (**Figure 25b**), it was clear that α -TOS-CDDP-NP induced highest level of γ H2AX expression compared to α -TOS-Dox-NP, α -TOS-Paclitaxel-NP as well as non-treated control. We also quantified the relative expression of γ H2AX in different dual drug conjugated nanoparticle treatments from western blot analysis. We observed 9.1 fold, 6.5 fold and 1.4 fold increases in γ H2AX expression induced by α -TOS-CDDP-NP, α -TOS-Dox-NP and α -TOS-Paclitaxel-NP respectively compared to the non-treated control (**Figure 26**).

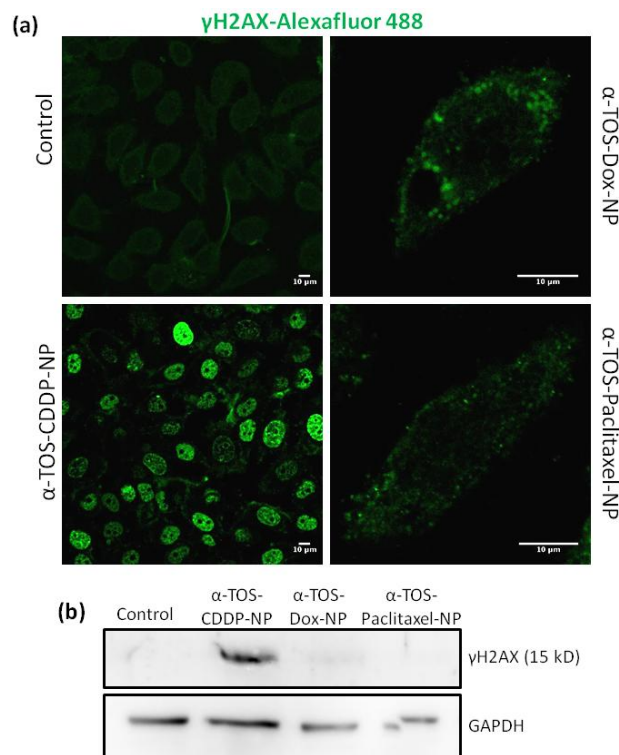


Figure 25: Characterization of nuclear damage by γ H2AX as DNA damage marker. (a) CLSM images of dual drug conjugated nanoparticle treatments to HeLa cells for 24 h at their respective IC_{50} drug dosages compared to non-treated control. Cells were stained with γ H2AX-Alexafluor 488 antibody (green). Scale bar = 10 μ m. (b) The expression of γ H2AX in HeLa cells after 24 h post incubation with dual drug conjugated nanoparticles determined by Western blot analysis.

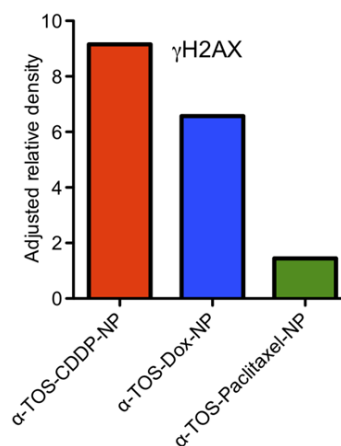


Figure 26: Quantification of γ H2AX expression from Western Blot analysis as a measure of DNA damage after treatment with dual drug conjugated nanoparticles at 24 h post-incubation.

Nuclear DNA damage triggers poly (ADP-ribose) polymerase (PARP) family of proteins which are involved in a number of cellular processes mainly DNA repair and apoptosis. Hence, PARP activation has emerged as one of the biomarkers for cellular DNA damage.⁶²

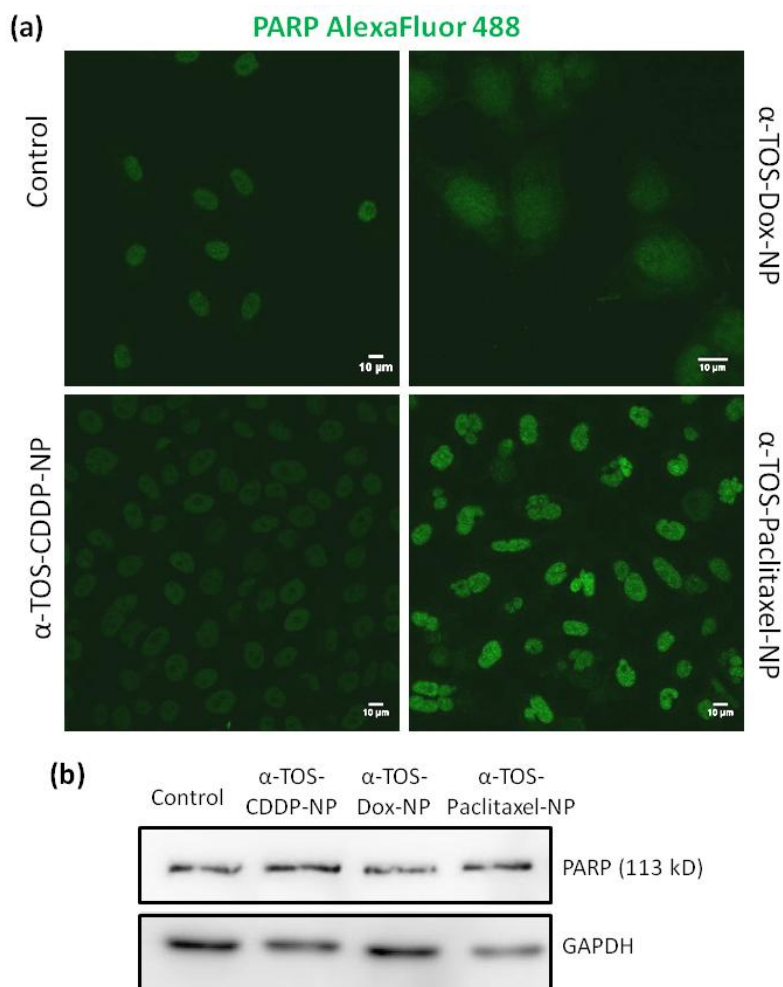


Figure 27. Characterization of nuclear damage by PARP as DNA damage repair marker. (a) CLSM images of dual drug conjugated nanoparticle treatments to HeLa cells for 24 h at their respective IC_{50} drug dosages compared to non-treated control. Cells were stained with PARP-Alexafluor 488 antibody (green). Scale bar = 10 μ m. (b) The expression of PARP (113 kDa) in HeLa cells after 24 h post incubation with dual drug conjugated nanoparticles determined by Western blot analysis.

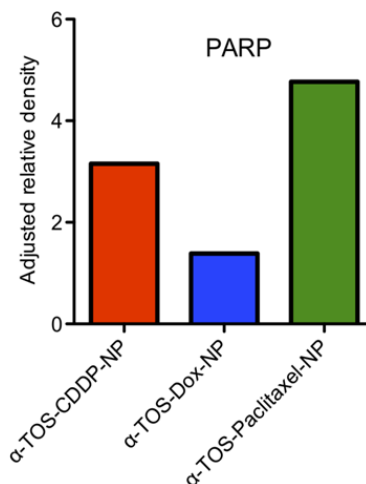


Figure 28: Quantification of PARP expression from Western Blot analysis as a measure of DNA damage repair after treatment with dual drug conjugated nanoparticles at 24 h post-incubation.

We treated the HeLa cells with different dual drug conjugated nanoparticles in their respective IC_{50} drug dosages for 24 h followed by staining with green fluorescent Alexafluor 488 antibody specific to PARP. We visualized the PARP expression by using CLSM. From **Figure 27a**, it was clear that interestingly α -TOS-Paclitaxel-NP induced highest PARP expression compared to α -TOS-CDDP-NP and α -TOS-Dox-NP. However, all the dual drug conjugated nanoparticles induced increased amount of PARP compared to non-treated cells. We further treated the HeLa cells with different dual drug conjugated nanoparticles and evaluated the expression of PARP by using western blot analysis. The Western blot image (**Figure 27b**) showed improved PARP expression after treatment with different nanoparticles compared to control cells. Moreover, the normalized PARP quantification from western blot clearly demonstrated that α -TOS-CDDP-NP, α -TOS-Dox-NP and α -TOS-Paclitaxel-NP induced 3.1 folds, 1.3 folds and 4.8 folds respectively (**Figure 28**).

Furthermore, we also observed the effect of different dual drug conjugated nanoparticles on morphology of the nucleus. We treated HeLa cells with dual drug conjugated nanoparticles with respective IC_{50} drug dosages for 24 h and stained the nucleus with blue fluorescent 4',6-diamidino-2-phenylindole (DAPI). We visualized the morphology of nucleus by CLMS. Only α -TOS-Paclitaxel-NP induced the fragmentation of nucleus (**Figure 29**, indicated by bold arrows). On the other hand, α -TOS-CDDP-NP and α -TOS-Dox-NP showed almost negligible

clustering of nucleus compared to the control (**Figure 29**). It was reported that paclitaxel and other microtubule binding drugs induce the clustering of nucleus.⁶³ Hence, it was clear that free paclitaxel released from α -TOS-Paclitaxel-NP was responsible for observed nuclear clustering. We also co-stained tubulin with green fluorescent tubulin Alexafluor 488 antibody and visualized the effect of dual drug conjugated nanoparticles. From **Figure 29** it was clear that only α -TOS-Paclitaxel-NP disrupted the typical elongated morphology of tubulin (indicated by thin arrows in **Figure 29**) into small fragments, whereas α -TOS-CDDP-NP and α -TOS-Dox-NP showed almost no tubulin damage compared to control. We anticipated this effect of α -TOS-Paclitaxel-NP compared to α -TOS-CDDP-NP and α -TOS-Dox-NP, as paclitaxel is known to bind with microtubule. From these CLSM, western blot analysis and protein expression quantification it was clear that all the dual drug conjugated nanoparticles damaged nuclear DNA as well as tubulin in HeLa cancer cells.

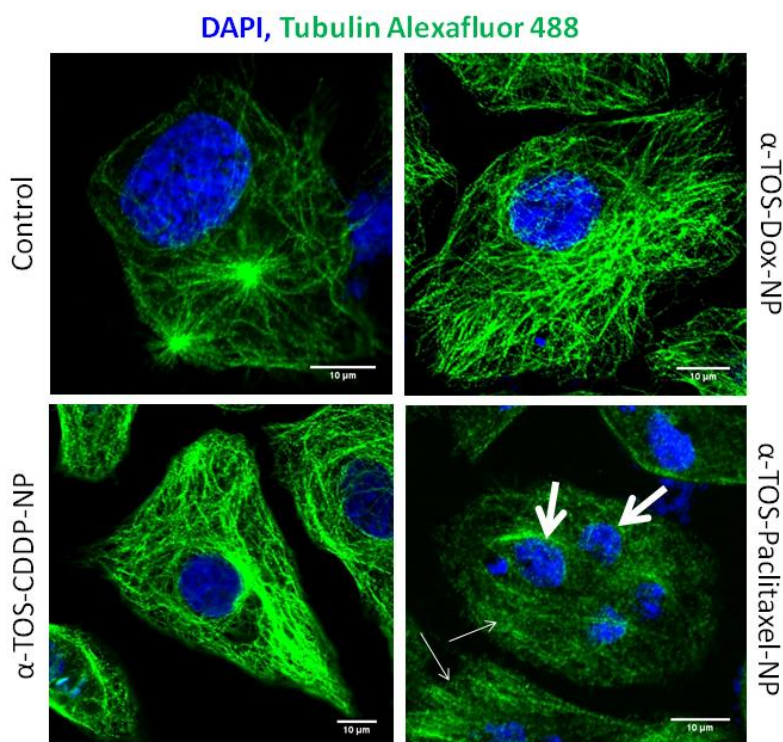


Figure 29. Characterization of nuclear fragmentation and tubulin damage after treatment with dual drug conjugated nanoparticles at 24 h post-incubation in HeLa cells. Nucleus was stained with DAPI (blue) and tubulin was stained with tubulin-Alexafluor 488 antibody. Nuclear

fragmentation is indicated by bold arrows and tubulin damage is indicated by thin arrows. Scale bar = 10 μm .

4.3. Conclusion

We have successfully developed dual drug conjugates by direct attachment of mitochondria damaging drug (α -TOS) and clinically approved DNA damaging drugs (cisplatin and doxorubicin) or microtubule binding drug (paclitaxel) without any additional linker strategy. We engineered sub 200 nm particles from those dual drug conjugates and characterized them by different electron microscopy (FESEM, TEM and AFM) techniques. These nanoparticles released the dual drugs in a slow and sustained manner over 3 days at pH = 5.5 mimicking the lysosomal compartments inside the tumor cells. Indeed these nanoparticles internalized into the lysosomal compartments in a time dependent manner through endocytosis in HeLa cervical cancer cells visualized by CLSM. These nanoparticles showed cytotoxicity by inducing apoptosis through arresting cell cycle. These nanoparticles damaged the mitochondrial morphology and released cytochrome c. These dual drug conjugated nanoparticles damaged the nucleus of HeLa cells and expressed DNA damaging marker γH2AX , DNA repair marker PARP. α -TOS-Paclitaxel-NP also damaged the tubulin of the HeLa cells. We anticipate that these dual drug conjugated nanoparticle strategy can be used as platform technology to conjugate different organelle damaging drugs and target them to illuminate the organelle cross talk in a diseased state like cancer. Moreover, these dual drug conjugated nanoparticles can be easily translated to the clinics to develop novel next generation multiple organelle damaging combination cancer therapeutics which can lead to reduced toxic side effects from the individual drugs, thus overcome drug resistance and providing a better quality of life to the cancer patients.

4.4. Materials and Methods

4.4.1 Materials: All reactions were performed under inert conditions unless otherwise indicated. All commercially obtained compounds were used without further purification. Ethyl

acetate, petroleum ether, dry dichloromethane (DCM), methanol, dry dimethyl formamide (DMF), alpha-tocopherol succinate, silver nitrate, sodium sulphate, sodium chloride, o-phenylenediamine, N-(3-Dimethylaminopropyl)-N'-ethylcarbodiimide hydrochloride (EDC), O-(Benzotriazol-1-yl)-N,N,N',N'-tetramethyluronium hexafluorophosphate (HBTU), N,N-dimethyl amino pyridine (DMAP), hydrochloric acid, chloroform-d (CDCl_3), dimethyl sulphoxide (DMSO-d₆), double distilled water, diisopropyl ethylamine (DIPEA), L-phosphatidylcholine, sephadex G-25, sodium dodecyl sulfate (SDS), paraformaldehyde, n-propyl gallate, glycerol, TritonTM X-100, ethyl alcohol and silicon wafer for FE-SEM were bought from Sigma-Aldrich. Paclitaxel, cisplatin and doxorubicin were bought from Selleck Chemicals. 1,2-Distearoyl-*sn*-Glycero-3-Phosphoethanolamine-N-[Amino(Polyethylene Glycol)2000] (DSPE-PEG) and the mini handheld extruder kit (including 0.2nm Whatman Nucleopore Track-Etch Membrane, whatman filter supports and 1.0 mL Hamiltonian syringes) were bought from Avanti Polar Lipids Inc. Analytical thin-layer chromatography (TLC) was performed using pre-coated silica gel aluminum sheets 60 F254 bought from EMD Laboratories. DMEM media and 3-(4, 5-dimethylthiazol-2-yl)-2,5-diphenyltetrazolium bromide (MTT), propidium iodide, RNase, MgCl_2 and DAPI were purchased from HiMedia. 96 well plates, 6 well plates, 15 mL and 50 mL graduated sterile centrifuge tubes and tissue culture flasks with filter cap sterile were purchased from Tarsons Product Pvt. Ltd. Annexin-V-FLUOS Staining Kit was purchased from Roche. LysoSensorTM Green DND-153, LysoTrackerTM Green DND-26, MitoTracker[®] Red CMXRos, Alexa Fluor[®] Fluorescent Streptavidin Conjugate, *SlowFade*[®] Gold Antifade Reagent and caspase-3, 8 and 9 protease assay kits were obtained from Life Technologies. Cytochrome c rabbit mAb, anti-rabbit IgG and HRP-linked antibody were obtained from CST. Anti-PARP antibody-clone 7A10, anti-phospho-histone H2AX (Ser139) antibody- clone JBW301, GAPDH antibody, goat anti-mouse IgG antibody, (H+L) HRP conjugate and rabbit anti-chicken IgG antibody. HRP conjugates were obtained from Merck Millipore. Alexa Fluor[®] 488 goat anti-mouse IgG (H+L) antibody and alexa fluor[®] 488 goat anti-rabbit IgG (H+L) antibody were purchased from Life technologies. HeLa and HEK293 cells were obtained from National Centre for Cell Science (NCCS), Pune. Spots on the TLC plates were visualized using alkanine permanganate or phosphomolybdic acid hydrate in methanol. ¹H (400 MHz) spectra were obtained on a Jeol-400 spectrophotometer. The chemical shifts are expressed in parts per million (ppm) using suitable

deuterated NMR solvents with reference to TMS at 0 ppm. The release kinetic data, drug loading, nanoparticle size and cell viability assay were plotted using GraphPad Prism software. The laser scanning confocal microscopy was performed by Zeiss LSM 710 machine. Each sample was done in triplicate. FACS analysis was performed using BD FACS Calibur™ flow cytometer.

4.4.2 Synthesis of α -tocopherol succinate-doxorubicin conjugate (2). α -tocopherol succinate (5 mg, 0.009 mmol, 1 equiv.) was dissolved in 1 mL dry DMF. After continuous stirring under inert condition at 0°C for 5 min, HBTU (15 mg, 0.014 mmol, 1.5 equiv) was added followed by addition of DIPEA (6 μ L, 0.037 mmol, 4 equiv.). The reaction mixture was cooled down for 10 min at 0°C and doxorubicin (6.55 mg, 0.011 mmol, 1.2 equiv) was added to it. The reaction was stirred at room temperature for 24 h. The reaction was then quenched with 0.1N HCl (10 mL) and H₂O (40 mL). The organic layer was extracted with DCM (2 X 20 mL). To remove dissolved salts present in the reaction mixture, wash with brine solution was given (2 X 30 mL). Anhydrous sodium sulphate (Na₂SO₄) was added to the organic layer to remove the trace amount of water present. Organic layer was then concentrated using rotary evaporator. Crude product was purified by silica gel (100-200 mesh size) column chromatography by using 1 % methanol in DCM to obtain product as a red colored solid. **Yield:** 7.4 mg (74.34 %).

Characterization of α -tocopheryl succinate-doxorubicin conjugate (2):

¹H NMR (400 MHz, CDCl₃): δ = 8.05-8.03 (dd, J = 7.6 Hz, 0.8 Hz, 1H), 7.81-7.76 (t, J = 8 Hz, 1H), 7.40-7.38 (d, J = 8 Hz, 1H), 5.97-5.95 (d, 8Hz, 1H), 5.50-5.49 (d, J = 4 Hz, 1H), 5.30 (s, 3H), 4.77(s, 2H), 4.17-4.12 (dd, 8Hz, 2H), 4.08 (s, 3H), 3.65 (s,1H), 3.26 (m,1H), 3.05-3.00 (m, 1H) 2.99-2.94 (m, 1H), 2.91-2.85 (m, 1H), 2.57-2.53 (m, 4H), 2.36-2.32 (m, 2H), 2.19-2.16 (m, 2H), 2.07-2.05 (s, 3H), 1.96 (s, 3H), 1.92 (s, 4H), 1.82-1.73 (m, 8H),1.55-1.47 (m, 5H), 1.28-1.21 (m, 19H), 1.15-1.14 (m, 4H), 0.87-0.83 (m, 12H).

¹³C NMR (100 MHz, CDCl₃): δ = 214.1, 187.3, 186. 9, 171.9, 170.8, 161.2, 156.35, 155.8, 149.5, 140.3, 135.9, 135.7, 133.7, 126.7, 125.0, 123.2, 121.1, 120.0, 118.5, 117.5, 111.7, 111.6, 100.8, 77.5, 77.2, 76.8, 75.2, 69.8, 69.2, 67.3, 65.7, 56.8, 53.6, 45.6, 39.5, 37.6, 37.4, 35.9, 34.2, 32.9, 32.9, 32.1, 31.2, 29.8, 29.5, 29.3, 28.1, 24.9, 24.6, 22.9, 22.8, 21.2, 20.7, 19.9, 19.8, 17.0, 14.3, 13.1, 12.3, 11.9, 1.2.

HRMS (ESI): m/z: for C₆₀H₈₁NO₁₅Na⁺ [M+Na]⁺ : calculated =1078.5504, observed=1078.5502.

MALDI-TOF: m/z: for $C_{60}H_{81}NO_{15}K^+$ $[M+K]^+$: calculated =1094.5243, observed=1094.6461.

4.4.3 Synthesis of α -tocopherol succinate-paclitaxel conjugate (3). α -tocopherol succinate (1) (2.5 mg, 0.0047 mmol, 1 equiv.) was dissolved in 1 mL dry dichloromethane (DCM) under inert atmosphere and cooled to 0°C. Subsequently, N-(3-dimethylaminopropyl)-N'-ethylcarbodiimide hydrochloride (EDC) (0.99 mg, 0.005 mmol, 1.1 equiv), diisopropylethylamine (DIPEA) (2.4 μ L, 0.014 mmol, 3 equiv) and 4-(dimethylamino)pyridine (DMAP) (0.06 mg, 0.00047 mmol, 0.1 equiv) were added to the reaction mixture with continuous stirring under inert condition. After 30 min, paclitaxel (4.33 mg, 0.005 mmol, 1.1 equiv) was added into the reaction mixture. The reaction was monitored by TLC. After 24 h, the reaction was quenched with 0.1 N HCl (1mL), water (5 mL) and diluted with DCM (10 mL). The organic layer was extracted with DCM (2 X 15 mL) and washed with brine solution (10 mL). The organic layer was dried over anhydrous sodium sulphate (Na_2SO_4). Organic solvent was then evaporated using rotary evaporator and the crude product was purified using silica gel (100-200 mesh size) column chromatography with 30% ethyl acetate in petroleum ether to obtain the pure compound. **Yield:** 3 mg (50.14%).

Characterization of α -tocopheryl succinate-paclitaxel conjugate (3)

1H NMR (400 MHz, $CDCl_3$): δ = 8.15-8.09 (m, 2H), 7.75-7.72 (m, 1H), 7.62-7.60 (m, 1H), 7.53-7.48 (m, 4H), 7.37 (m, 2H), 7.18 (m, 3H), 6.99-6.97 (m, 1H), 6.77-6.74 (m, 1H) 6.32-6.27 (m, 2H), 5.87-5.76 (m, 1H), 5.70-5.63 (m, 2H), 5.42-5.25 (m, 2H), 5.02-4.88 (m, 3H), 4.49-4.38 (m, 1H), 4.33-4.27 (m, 2H), 4.21-4.12 (m, 2H), 3.89-3.79 (m, 1H), 2.95-2.90 (m, 2H), 2.83-2.75 (m, 1H), 2.61-2.53 (m, 3H), 2.39-2.29 (m, 9H), 2.25-2.23 (m, 4H), 2.08-2.01 (m, 11H), 1.69-1.61 (m, 14H), 1.33-1.11 (m, 16H), 0.89-0.83 (m, 12H).

^{13}C NMR (100 MHz, $CDCl_3$): δ = 204.0, 174.7, 173.5, 171.4, 169.9, 167.2, 162.3, 161.3, 149.6, 147.2, 144.2, 142.9, 140.3, 139.4, 133.8, 132.9, 132.1, 130.4, 129.2, 128.6, 124.6, 123.2, 119.2, 117.6, 114.2, 95.8, 92.3, 90.5, 86.3, 84.7, 81.1, 79.3, 77.5, 77.2, 76.8, 75.3, 72.3, 71.9, 67.1, 62.2, 61.7, 58.7, 52.8, 45.6, 43.3, 39.5, 37.6, 34.2, 33.9, 32.9, 32.1, 31.6, 30.3, 29.8, 29.5, 29.3, 28.1, 27.4, 25.0, 24.6, 22.8, 21.2, 20.7, 19.9, 19.8, 14.6, 14.3, 13.1, 12.3, 11.9, 9.7.

HRMS (ESI): m/z: for $C_{80}H_{103}NO_{15}Na^+$ $[M+Na]^+$: calculated=1388.7073, observed=1388.7102.

MALDI TOF: m/z: for $C_{80}H_{103}NO_{15}K^+$ $[M+K]^+$: calculated=1404.6812, observed=1405.0453.

4.4.4 Synthesis of aquated cisplatin (4). 50 mg of cisplatin was dissolved in 10 mL of water and 28 mg of silver nitrate was added to the solution. Reaction mixture was then stirred at room temperature under dark conditions for 24 h. Reaction mixture turned milky white and was centrifuged for 15 to 20 minutes to precipitate silver chloride. The supernatant is then filtered through 0.2 μ m filter and compound was obtained for further reaction.

4.4.5 Synthesis of α -tocopherol succinate-cisplatin conjugate (5). α -tocopherol succinate (**1**) (5 mg, 0.009 mmol, 1 equiv) was dissolved in 1 mL DMF and aquated cisplatin (**4**)(500 μ L = 2.5 mg, 0.009 mmol, 1 equiv) was added to it. It was kept for stirring for 24 hours. After 24 h, solvent was evaporated by rotary evaporator. **Yield:** 6.5 mg (89.0%).

Characterization of α -tocopheryl succinate-cisplatin conjugate (5):

1H NMR (400 MHz, $CDCl_3$): δ = 4.62 (s, 4H), 3.39-3.34 (s, 6H), 2.83-2.75 (m, 2H), 2.59-2.56 (m, 2H), 2.00 (s, 3H), 1.91 (s, 3H), 1.89 (s, 3H), 1.75-1.71 (m, 2H), 1.54-1.46 (m, 3H), 1.39-1.35 (m, 4H), 1.24-1.21 (m, 10H), 1.14-1.09 (m, 3H), 1.05-1.02 (m, 4H), 0.84-0.80 (m, 12H).

^{13}C NMR (100 MHz, $CDCl_3$): δ = 173.5, 171.1, 162.3, 148.5, 140.3, 126.4, 125.0, 121.7, 117.3, 74.7, 40.1, 39.9, 39.7, 39.5, 39.3, 39.1, 38.9, 38.8, 32.1, 31.9, 28.8, 28.5, 27.4, 24.2, 23.7, 22.6, 22.5, 20.3, 19.9, 19.6, 12.7, 11.8, 11.6.

^{195}Pt NMR: δ = -1502.26.

MALDI TOF: m/z: for $C_{80}H_{103}NO_{15}Na^+$ $[M+Na]^+$: calculated=861.0041, observed=861.1266; m/z: for $C_{80}H_{103}NO_{15}K^+$ $[M+K]^+$: calculated=876.9703, observed=876.6498.

4.4.6 General procedure of synthesizing dual drug conjugated nanoparticles and rhodamine loaded nanoparticles. 10.0 mg of L- α -phosphatidylcholine (PC), 5.0 mg of dual-drug conjugates (**2**, **3** and **5**) and 1 mg of 1,2-distearoyl-*sn*-glycero-3-phosphoethanolamine-N-[amino(polyethylene glycol)2000] (DSPE-PEG) (1 mg of Rhodamine was added for the synthesis of α -TOS-CDDP-Rho-NP and α -TOS-Paclitaxel-Rho-NP) were dissolved in 5.0 mL DCM. Solvent was evaporated into a thin and uniform film with the help of a rotary evaporator. After thorough drying with vacuum pump dual-drug conjugate film was hydrated with 1.0 ml H_2O for 2 h at 60°C. It was passed through Sephadex G-25 column and extruded through 200 nm Whatmann polycarbonate membrane at 65°C to obtain sub 200 nm particles.

The dual-drug conjugated nanoparticles, α -TOS-CDDP-Rho-NP and α -TOS-Paclitaxel-Rho-NP were stored at 4°C for further use.

4.4.7 General procedure for quantification of drug loading. A Calibration curve was plotted in the concentration range of 2.5 to 100 μ M (for α -TOS), 10-40 μ M (for paclitaxel) and 10-100 μ M (for doxorubicin) by diluting the 1 mM standard stock solution of drugs in dimethyl sulfoxide (DMSO). The absorbance was measured at 287 nm, 271 nm and 490 nm for α -TOS, paclitaxel and doxorubicin respectively against the corresponding solvent blank. The linearity was plotted for absorbance (A) against concentration (C). For drug loading in nanoparticles, prepared nanoparticles were dissolved in spectroscopic grade DMSO in 5%, 10% and 15% dilution. Absorbance was measured at characteristic wavelength against the corresponding solvent blank in 200 μ L quartz cuvette and from the calibration curve drug loading was measured in triplicate. For the quantification of cisplatin, a different strategy was followed since it is not itself UV active. For the calibration curve, 1 mM stock was prepared by dissolving cisplatin into 1.2 mg/ mL solution of o-phenylenediamine in DMF and heated at 100°C for 4 h, till the solution turned deep green in colour. Range of further dilutions from 2.5 μ M to 15 μ M was obtained by diluting stock solution with DMF. The absorbance was measured at 706 nm (which is characteristic λ_{max} for cisplatin) against DMF as blank. Linear relationship was obtained by plotting the absorbance values (A) against corresponding concentrations (C). For drug loading in nanoparticles, prepared nanoparticles (100 μ L) were dissolved in 500 μ L o-phenylene diamine (1.2 mg /mL of spectroscopic grade DMF). Then it was heated at 100°C for 4 h until greenish yellow color appears. From the stock of the greenish yellow solution, 5%, 10%, 15% dilutions were prepared. Absorbance was measured at characteristic wavelength against the corresponding solvent blank in 200 μ L quartz cuvette and from the calibration curve drug loading was measured in triplicate in the similar way as the above.

4.4.8 Determination of size distribution of nanoparticles by dynamic light scattering (DLS). The mean particle size of the dual-drug conjugated nanoparticles was measured by dynamic light scattering (DLS) method using Zetasizer Nano2590 (Malvern, UK). 50 μ L of nanoparticle solution was diluted to 1mL using DI water and 3 sets of 10 measurements each were performed at 90 degree scattering angle to get the average particle size.

4.4.9 Field-Emission Scanning Electron Microscopy (FESEM) of dual-drug conjugated nanoparticles. 5 μL of dual-drug conjugated nanoparticles in water was placed on a silicon chip without any dopant and it was allowed to dry at room temperature under vacuum desiccators for 2 hours. The silicon chip was then gold coated (30-40 nm thickness) using Quorum, Q150T- E5. The FESEM measurements were done using Carl Zeiss, Ultra plus, scanning electron microscope at an operating voltage of 4.0 KV.

4.4.10 Atomic Force Microscopy (AFM) of dual-drug conjugated nanoparticles. 5 μL of dual-drug conjugated nanoparticles in water was placed on mica sheet and dried under the vacuum desiccators for 2 h. Shape and size of dual-drug conjugated nanoparticles were determined using NanoWizard Atomic Force Microscopy (AFM).

4.4.11 Transmission Electron Microscopy (TEM) of dual-drug conjugated nanoparticles. 15 μL of nanoparticles in water was placed on a TEM copper grid. After 30 min, this sample drop was wicked off by using filter paper and then 15 μL of freshly prepared 0.25% uranyl acetate (2.5 mg uranyl acetate in 1 mL dd water) solution was placed on the TEM copper grid. After 1 min, uranyl acetate solution was wicked off and the sample was washed three times with 15 μL dd water each time. The sample was dried overnight on a clean dust free surface under a funnel. The dual-drug conjugated nanoparticles were imaged using Tecnai T300 HR-TEM and Tecnai G2 20-Twin LR-TEM instruments.

4.4.12 Stability of the nanoparticles at 4°C and 37°C by dynamic light scattering (DLS). The stability of the nanoparticles was checked at 4°C and 37°C by Dynamic Light Scattering method using Zetasizer Nano2590 (Malvern, UK). 200 μL of nanoparticles solution was diluted to 1 mL using DI water and 3 sets of 10 measurements each were performed at 90 degree scattering angle to get the average particle size. This was done for 14 days keeping the nanoparticles at 4°C (refrigerator) and 37°C (incubator) to check its stability at shelf (for storage purpose) as well as in blood circulation temperature. Similarly, the nanoparticles were incubated in DMEM cell culture media containing 10% FBS (or in PBS) at 37°C for 3 days and size and PDI values were measured in predetermined time points.

4.4.13 General procedure for determining the drug release profile. Concentrated 250 μL dual-drug conjugated nanoparticles were suspended in 250 μL pH = 5.5 solution (or pH = 7.4 solution) and sealed in a dialysis membrane (MWCO = 2000 Dalton for cisplatin, paclitaxel and doxorubicin release). The dialysis bags were incubated in 10 mL pH = 5.5 solution (or pH

= 7.4 solution) at room temperature with gentle shaking. A 400 μL portion of the aliquot was collected from the incubation medium at predetermined time intervals and the released dual drugs were quantified by UV-VIS spectrophotometer.

4.4.14 Cell viability assay. 5000 cells (HeLa and HEK293 cells) were seeded per well in 96-well microtitre plate and incubated overnight in a 5% CO_2 incubator at 37°C for attachment. Cells were then treated with dual-drug conjugated nanoparticles and free drug combinations in different concentrations (0.1, 0.2, 0.4, 0.8, 1.6, 3.2, 6.4, 12.5, 25, 50 μM) for 48 h. Free drugs were dissolved in DMSO to make a stock solution of 5 mM concentration. Serial dilutions of free drugs in DMSO were made from this stock solution and $2\mu\text{L}$ of each free drug solution was added to cells to obtain desired final concentrations. 20 μL of MTT reagent (5 mg/mL) was added to each well and incubated for 4 h at 37°C . Formazan crystals were then solubilized in 100 μL of the solubilization buffer (10 % SDS in 0.01 M HCl) and incubated overnight. Absorbance was measured with spectrophotometer at 550 nm. The percent cell viability was calculated considering the untreated cells as 100 percent viability and the effectiveness of dual-drug conjugated nanoparticles was compared with the free drug combinations.

4.4.15 FACS analysis for apoptosis detection. For apoptosis detection, 2×10^6 HeLa cells were incubated in 6 well plates overnight for attachment and then treated with nanoparticles for 24 hours at their respective IC_{50} values. After the treatment, media was removed and cells were trypsinized and washed twice with PBS by means of centrifugation at 750 rpm for 4 min. Cell pellet was then re-suspended in 100 μL of Annexin-V-FLUOS labeling solution (Annexin-V-FLUOS Staining Kit from Roche) and incubated in 500 μL of incubation buffer at 25°C for 15 mins. Cells were then passed through cell strainer to get uniform cell suspension and analyzed using BD FACS CaliburTM to detect the apoptosis.

4.4.16 Caspase activity assay. Caspase activities for caspase-3, caspase-8 and caspase-9 were assayed using Caspase-3, 8 and 9 colorimetric protease assay kit from Life TechnologiesTM. Caspase-3, caspase-8 and caspase-9 recognize the amino acid sequence- DEVD (Asp-Glu-Val-Asp), IETD (Ile-Glu-Thr-Asp) and LEHD (Leu-Glu-His-Asp) respectively. After treating the HeLa cells with dual-drug conjugated nanoparticles for 24 h, 3×10^6 cells were centrifuged and resuspended in 50 μL chilled cell lysis buffer and incubated in ice for 10 min. Cell lysates were then centrifuged at 10,000 x g for 1 min and supernatant was collected for assaying the caspase activities. Total protein concentration was estimated using protein estimation kit by

bradford protein assay (GeNei™ Merck) and cytosol extracts were diluted to a concentration of 50 µg protein per 50 µL of cell lysis buffer. 50 µL of 2X reaction buffer was added to each 50 µL sample followed by addition of 5 µL substrate specific for each caspase and incubated at 37°C in dark for 2 h. Substrates consist of a chromophore, *p*-nitroanilide (*p*NA) and the amino acid sequence of the respective caspase cleavage site. Upon proteolytic cleavage of substrate by caspase, generated free *p*NA was measured spectrophotometrically at 405 nm. Fold increase in caspase activity was calculated by direct comparison to the level of control absorbance.

4.4.17 Cell cycle analysis. 2×10^6 HeLa cells were seeded in a 6 well plate and allowed to attach overnight in a 5% CO₂ incubator at 37°C. Cells were treated with dual-drug conjugated nanoparticles at a concentration corresponding to the IC₅₀ value of respective drugs for 24 h. After the treatment, the cells were harvested and washed with 1 mL PBS (pH = 7.4) and then centrifuged at 850 rpm for 4 min. Supernatant was discarded and cells were fixed in 70% ice-chilled ethyl alcohol for 30 min at -20°C. Fixed cells were centrifuged at 850 rpm for 4 min. Fixing solution was aspirated and 1 mL ice-chilled PBS was added. Cells were again centrifuged at 850 rpm for 4 min and resuspended in 0.5 mL of the staining solution (50 µL 1 mg mL⁻¹ propidium iodide, 50 µL 1 mg mL⁻¹ RNase and 400 µL PBS). Cells were then analyzed using BD Accuri™ C6 flow cytometer.

4.4.18 Confocal laser scanning microscopy (CLSM) studies.

4.4.18.1 Cellular internalization. 5×10^4 HeLa cells were seeded on a cover slip in a 6 well plate and incubated overnight in a 5% CO₂ incubator at 37°C for attachment. Cells were then first washed with PBS (pH = 7.4) and then treated with α-TOS-Dox-NP (at a concentration equivalent to 2 µg mL⁻¹ of doxorubicin) and free doxorubicin (2 µg mL⁻¹) for 1, 3 and 6 h. Cells were then washed twice with PBS and fixed with 500 µL of paraformaldehyde (3.7% in PBS, pH = 6.9) by incubating for 10 min at 4°C. The paraformaldehyde was aspirated and cells are washed trice with PBS. Low pH lysosomes were stained with 50 nM LysoTracker™ Green DND-26 (Invitrogen) by incubating the cells at 37°C for 45 min. The cells were then washed three times to remove the unbound LysoTracker™ Green DND-26 followed by staining the cells for nuclei with 2 µg mL⁻¹ DAPI (HiMedia) by incubating at 37°C for 20 min. Then cells were washed three times with PBS and mounted on a glass slide using 5 µL *SlowFade*® Gold Antifade Reagent. The slides were subjected to fluorescence imaging using a CLSM (Zeiss LSM 710).

4.4.18.2 Mitochondrial imaging. 5×10^4 HeLa cells were seeded on a cover slip in a 6 well plate and incubated overnight in a 5% CO₂ incubator at 37°C for attachment. Cells were then treated with dual-drug conjugated nanoparticles at a concentration corresponding to the IC₅₀ value of respective drugs for 24 h. Cells were then washed twice with PBS (pH = 7.4) and treated with MitoTracker Red CMXRos at a concentration of 200 nM in PBS and incubated in dark at 37°C for 25 min. Staining solution was aspirated and cells are washed thrice with PBS and then fixed with 3.7% paraformaldehyde at 37°C for 15 min. Fixing solution was discarded and cells are permeabilized with PBS containing 0.2% TritonX. 200 µL of Alexa Fluor® 488 streptavidin conjugate ($2 \mu\text{g mL}^{-1}$) was added to the cells and incubated for 90 min at 37°C in dark. Cells were washed thrice with PBS and mounted on a glass slide using *SlowFade*® gold antifade reagent. The slides were subjected to fluorescence imaging using a CLSM (Zeiss LSM 710).

4.4.18.3 General procedure for immunostaining to visualize cytochrome c, γ H2AX, PARP and tubulin. 5×10^4 HeLa cells were seeded on a coverslip in a 6 well plate and incubated overnight in a 5% CO₂ incubator at 37°C for attachment. Cells were then treated with dual-drug conjugated nanoparticles at corresponding IC₅₀ concentration for 24 h. Cells were washed once with PBS and then fixed with 3.7% paraformaldehyde at 37°C for 15 min. Cells were then washed twice with PBS (pH = 7.4) and were permeabilized by incubating in blocking buffer (PBS containing 0.3% tween and 5% FBS) at room temperature. Cells were then incubated in primary antibody solution (cytochrome c, γ H2AX, PARP in 1:100 dilution and tubulin in 1:2500 dilutions) at 37°C for 3 hr. Cells are washed thrice with blocking buffer. Then cells were incubated in fluorochrome conjugated secondary antibody solution (1:500 dilution) at 37°C for 40 min in dark. Cells were washed thrice with PBS and mounted on a glass slide using *SlowFade*® gold antifade reagent. The slides were subjected to fluorescence imaging using a CLSM (Zeiss LSM 710).

4.4.19 General procedure for Western blot analysis. After 24 hours of dual-drug conjugated nanoparticle treatment in their corresponding IC₅₀ concentrations, HeLa cells were lysed and suspended in sample buffer. Proteins were separated using SDS-polyacrylamide gel electrophoresis (SDS-PAGE) and then proteins were transferred onto the membrane (electroblotting). Blotted membrane was then blocked in freshly prepared TBS containing

nonfat dry milk (5%) for 1 hour with constant agitation at room temperature. Membrane was then rinsed once with TBST and then incubated in the primary antibody solution (1:1000 dilution, except 1:2500 for GAPDH) overnight at 4°C with gentle agitation (except 4 hours for GAPDH). Membrane was then washed 3 times (15 min each) with TBST and then incubated in HRP conjugated secondary antibody solution (1:500 dilution) for 45 min at room temperature with gentle agitation. Membrane was again washed thrice with TBST (5 min each). Protein detection was then followed by using Immobilon Western Chemiluminescent HRP Substrate (membrane was incubated in the substrate for 1 min). Images were acquired using GE Healthcare Lifesciences ImageQuant LAS 4000. After the acquisition, membrane was boiled in distilled water for 5 min and again was re-probed for GAPDH gene. Further image processing and intensity calculations were performed using ImageJ software.

4.5. Appendices

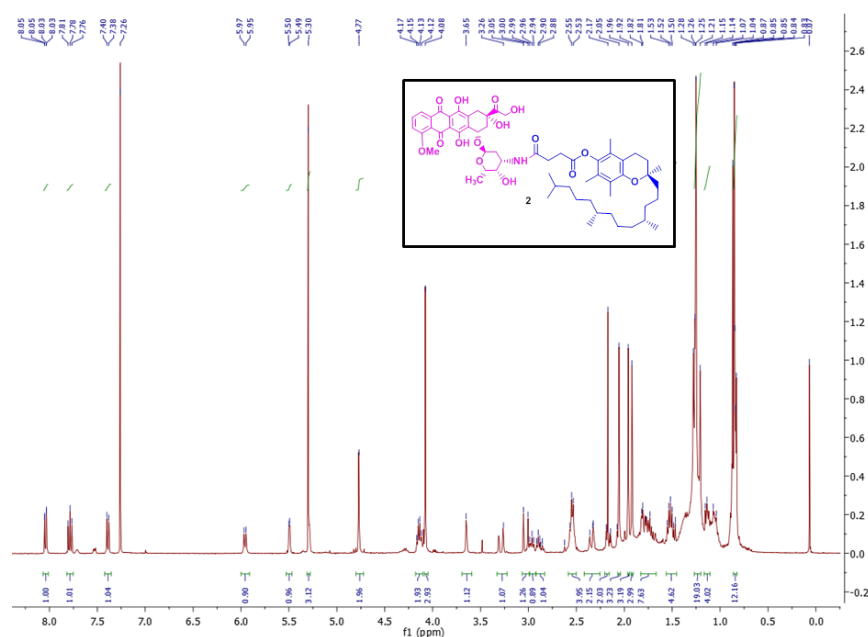


Figure A1: ^1H NMR spectra of α -TOS-Doxorubicin conjugate (**2**)

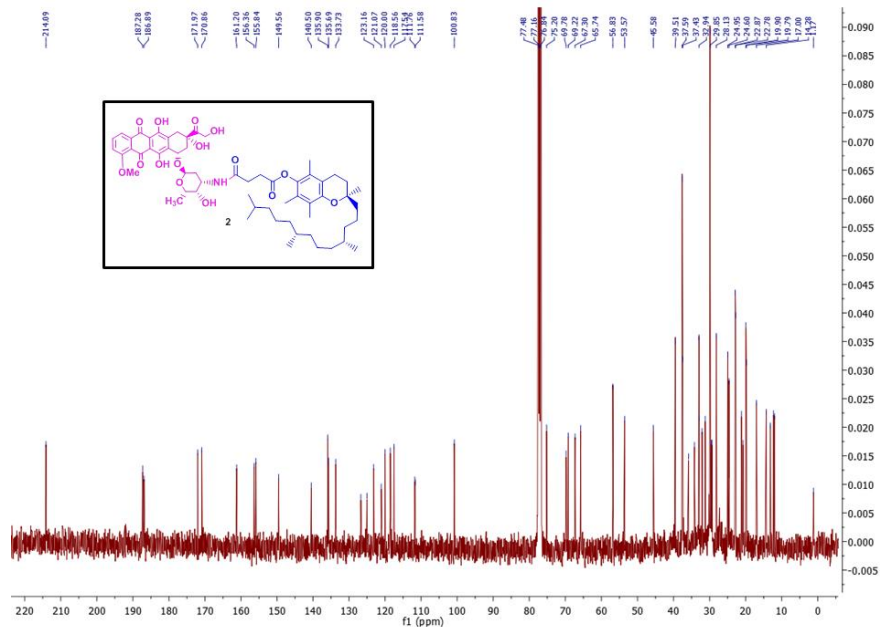


Figure A2: ^{13}C NMR spectra of α -TOS-Doxorubicin conjugate (2).

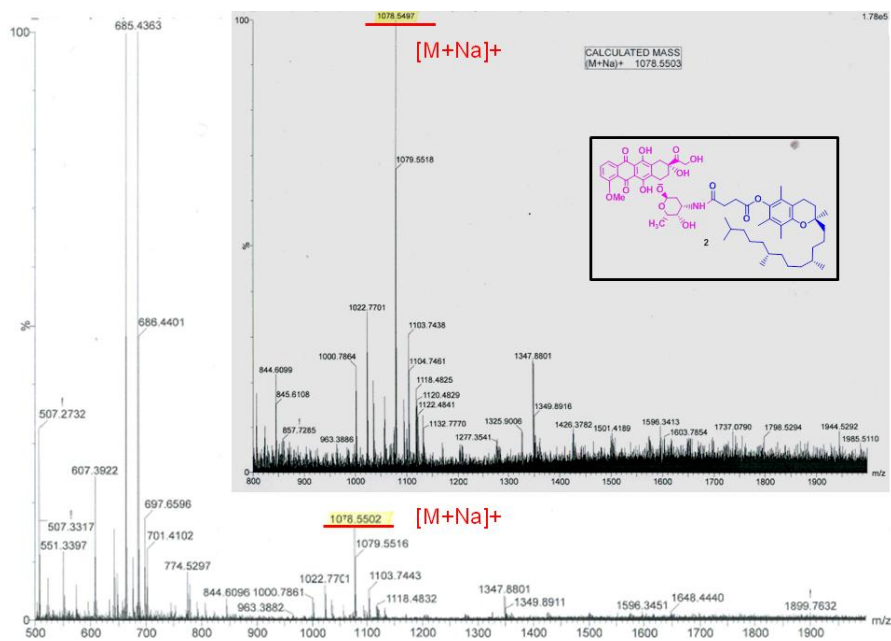


Figure A3: HR-MS and MALDI-TOF (inset) spectra of α -TOS-Doxorubicin conjugate (2).

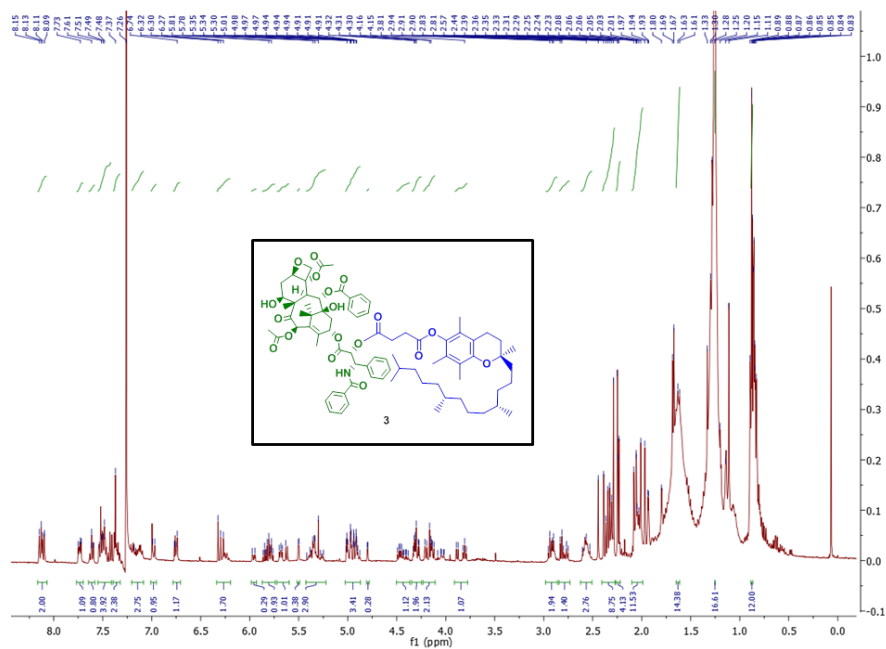


Figure A4: ^1H NMR spectra of α -TOS-Paclitaxel conjugate (3).

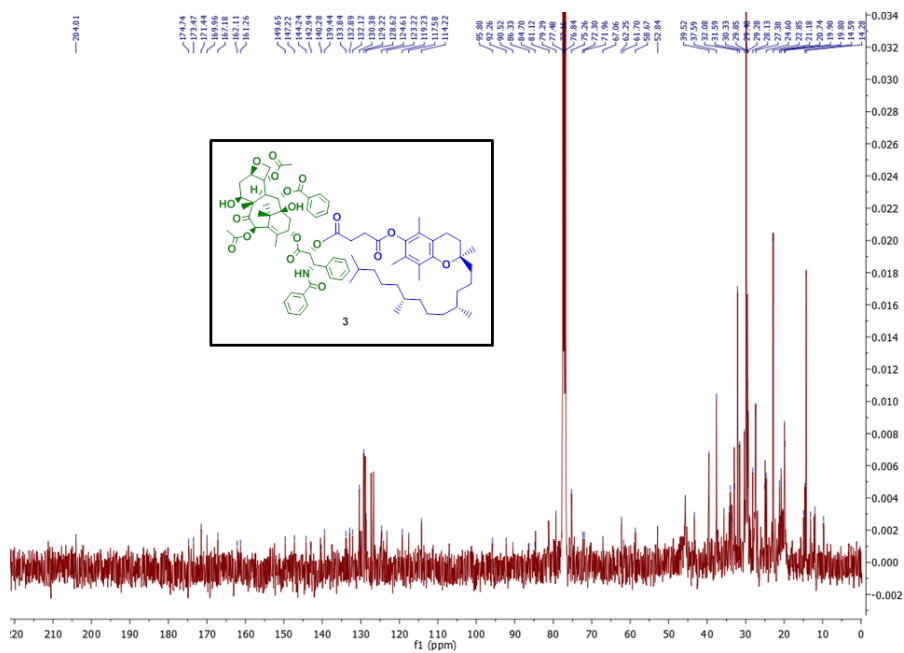


Figure A5: ^{13}C NMR spectra of α -TOS-Paclitaxel conjugate (3).

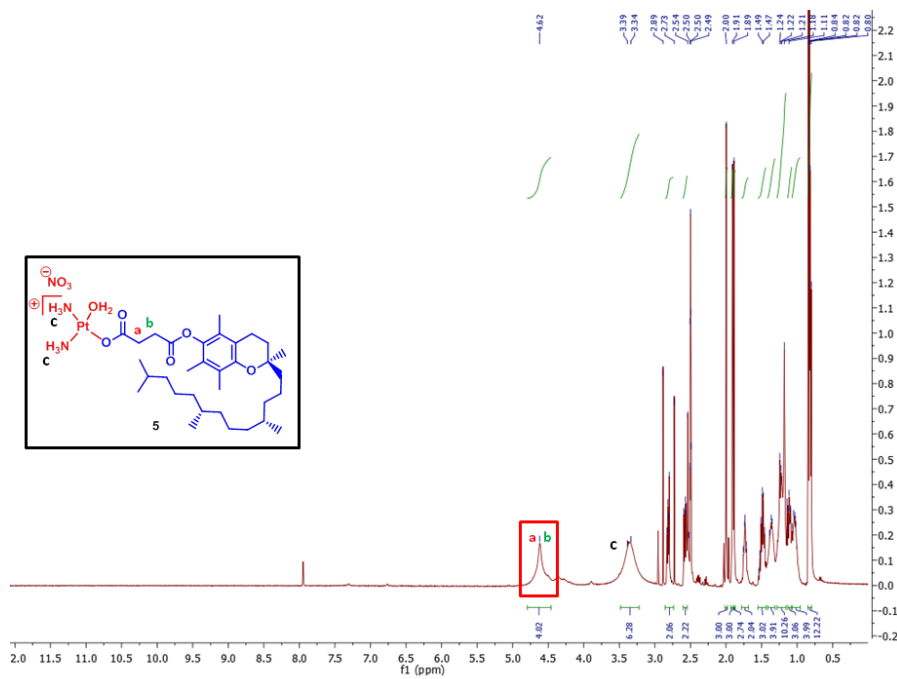


Figure A8: ^1H NMR spectra of α -TOS-cisplatin conjugate (5).

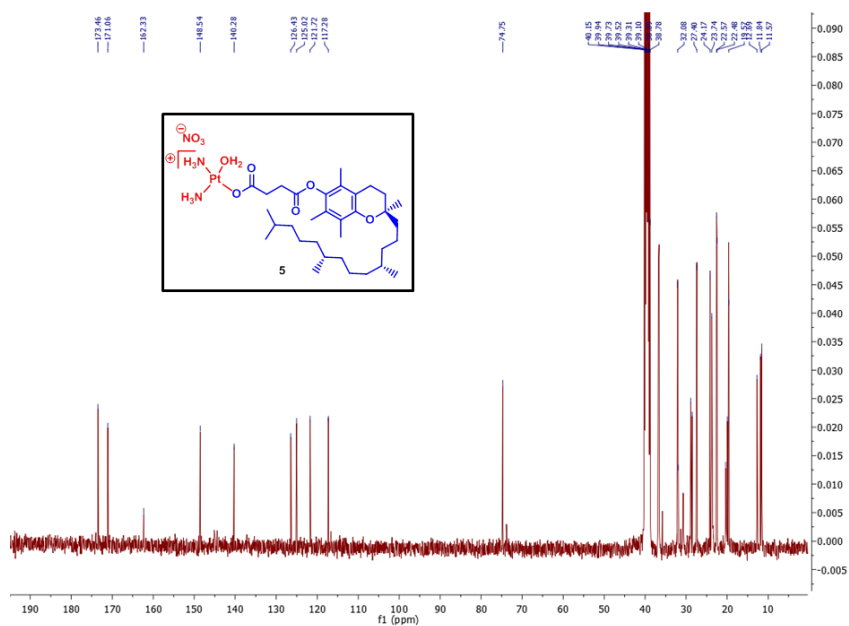


Figure A9: ^{13}C NMR spectra of α -TOS-cisplatin conjugate (5).

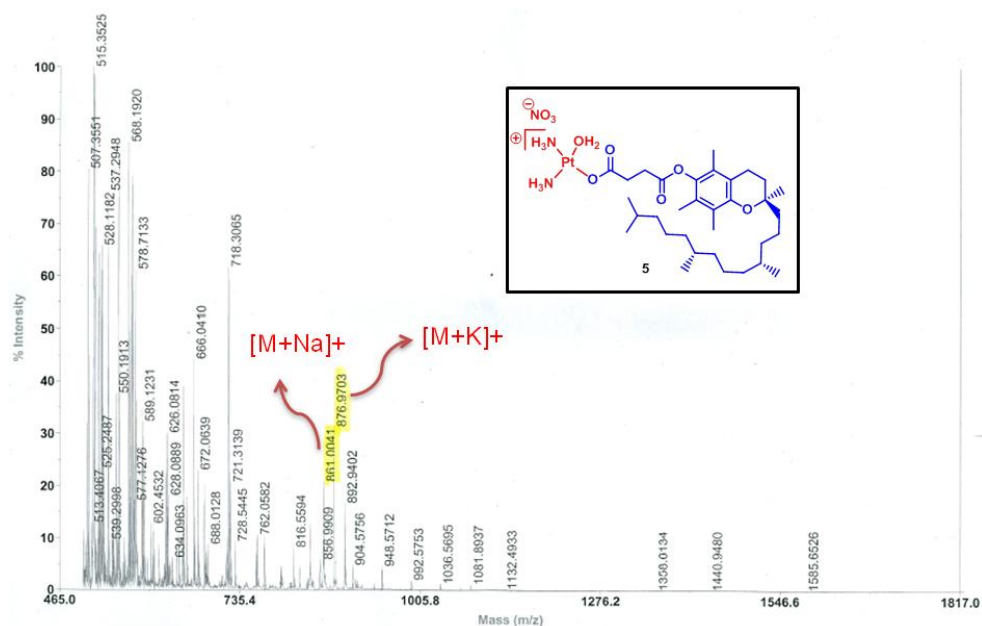


Figure A10: HR-MS spectra of α -TOS-cisplatin conjugate (5).

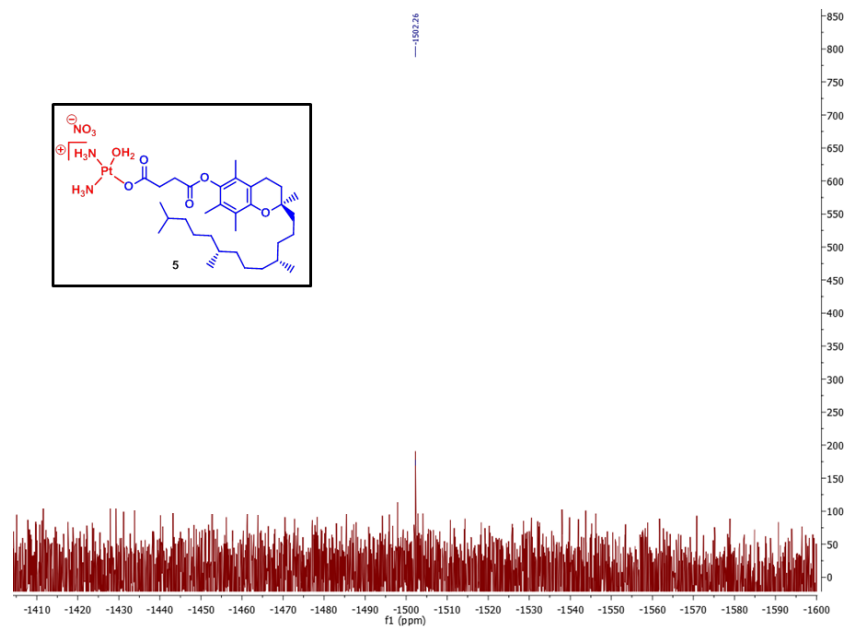


Figure A11: ^{195}Pt NMR spectra of α -TOS-cisplatin conjugate (5).

4.6. References

- (1) Jia, J.; Zhu, F.; Ma, X.; Cao, Z. W.; Li, Y. X.; Chen, Y. Z. Mechanisms of Drug Combinations: Interaction and Network Perspectives. *Nat. Rev. Drug Discov.* **2009**, *8*, 111-128.
- (2) Al-Lazikani, B.; Banerji, U.; Workman, P. Combinatorial Drug Therapy for Cancer in the Post-Genomic Era. *Nat. Biotech.* **2012**, *30*, 679-692.
- (3) Nummari, J.; Suomalainen, A. Mitochondria: in Sickness and in Health. *Cell* **2012**, *148*, 1145-1159.
- (4) Galluzzi, L.; Kepp, O.; Kroemer, G. Mitochondria: Master Regulators of Danger Signalling. *Nat. Rev. Mol. Cell Biol.* **2012**, *13*, 780-788.
- (5) Chamberlain, G. R.; Tulumello, D. V.; Kelley, S. O. Targeted Delivery of Doxorubicin to Mitochondria. *ACS Chem. Biol.* **2013**, *8*, 1389–1395.
- (6) Wisnovsky, S. P.; Wilson, J. J.; Radford, R. J.; Pereira, M. P.; Chan, M. R.; Laposa, R. R.; Lippard, S. J.; Kelley, S. O. Targeting Mitochondrial DNA with a Platinum-Based Anticancer Agent. *Chem. Biol.* **2013**, *20*, 1323-1328.
- (7) Marrache, S.; Pathaka, R. K.; Dhar, S. Detouring of Cisplatin to Access Mitochondrial Genome for Overcoming Resistance. *Proc. Natl. Acad. Sci. USA.* **2014**, *111*, 10444-10449.
- (8) Pathak, R. K.; Marrache, S.; Harn, D. A.; Dhar, S. Mito-DCA: a Mitochondria Targeted Molecular Scaffold for Efficacious Delivery of Metabolic Modulator Dichloroacetate. *ACS Chem. Biol.* **2014**, *9*, 1178–1187.
- (9) Dhar, S.; Lippard, S. J. Mitaplatin, a Potent Fusion of Cisplatin and the Orphan Drug Dichloroacetate. *Proc. Natl. Acad. Sci. USA.* **2009**, *106*, 22199-22204.
- (10) Suntharalingam, K.; Song, Y.; Lippard, S. J. Conjugation of Vitamin E Analog α -TOS to Pt(IV) Complexes for Dual-Targeting Anticancer Therapy. *Chem. Commun.* **2014**, *50*, 2465-2468.
- (11) Ward, P. S.; Thompson, C. B. Metabolic Reprogramming: a Cancer Hallmark Even Warburg Did Not Anticipate. *Cancer Cell* **2012**, *21*, 297-308.
- (12) Guo, J. Y.; Xia, B.; White, E. Autophagy-Mediated Tumor Promotion. *Cell* **2013**, *155*, 1216-1219.

- (13) Peer, D.; Karp, J. M.; Hong, S.; Farokhzad, O. C.; Margalit, R.; Langer, R. Nanocarriers as an Emerging Platform for Cancer Therapy. *Nat. Nanotechnol.* **2007**, *2*, 751-760.
- (14) Castanotto, D.; Rossi, J. J. The Promises and Pitfalls of RNA-Interference-Based Therapeutics. *Nature* **2009**, *457*, 426-433.
- (15) Matsumura, Y.; Maeda, H. A New Concept for Macromolecular Therapeutics in Cancer Chemotherapy: Mechanism of Tumor-tropic Accumulation of Proteins and the Antitumor Agent Smancs. *Cancer Res.* **1986**, *46*, 6387–6392.
- (16) Ruoslahti, E.; Bhatia, S. N.; Sailor, M. J. Targeting of Drugs and Nanoparticles to Tumors. *J. Cell Biol.* **2010**, *188*, 759-68.
- (17) Couvreur, P.; Vauthier, C. Nanotechnology: Intelligent Design to Treat Complex Disease. *Pharm. Res.* **2001**, *74*, 1417-1450.
- (18) Kolishettia, N.; Dhar, S.; Valencia, P. M.; Lin, L. Q.; Karnik, R.; Lippard, S. J.; Langer, R.; Farokhzad, O. C. Engineering of Self-Assembled Nanoparticle Platform for Precisely Controlled Combination Drug Therapy. *Proc. Natl. Acad. Sci. USA.* **2010**, *107*, 17939–17944.
- (19) Wang, H.; Zhao, Y.; Wu, Y.; Hu, Y.; Nan, K.; Nie, N.; Chen, H. Enhanced Anti-Tumor Efficacy by Co-Delivery of Doxorubicin and Paclitaxel with Amphiphilic Methoxy PEG-PLGA Copolymer Nanoparticles. *Biomaterials* **2011**, *32*, 8281-8290.
- (20) Liao, L.; Liu, J.; Dreaden, E. C.; Morton, S. W.; Shopsowitz, K. E.; Hammond, P. T.; Johnson, J. A. A Convergent Synthetic Platform for Single-Nanoparticle Combination Cancer Therapy: Ratiometric Loading and Controlled Release of Cisplatin, Doxorubicin, and Camptothecin. *J. Am. Chem. Soc.* **2014**, *136*, 5896–5899.
- (21) Sengupta, S.; Eavarone, D.; Capila, I.; Zhao, G.; Watson, N.; Kiziltepe, T.; Sasisekharan, R. Temporal Targeting of Tumour Cells and Neovasculature with a Nanoscale Delivery System. *Nature* **2005**, *436*, 568-572.
- (22) Deng, Z. J.; Morton, S. W.; Ben-Akiva, E.; Dreaden, E. C.; Shopsowitz, K. E.; Hammond, P. T. Layer-By-Layer Nanoparticles for Systemic Codelivery of an Anticancer Drug and siRNA for Potential Triple-Negative Breast Cancer Treatment. *ACS Nano* **2013**, *7*, 9571–9584.
- (23) Zhang, L.; Xia, J.; Zhao, Q.; Liu, L.; Zhang, Z. Functional Graphene Oxide as a Nanocarrier for Controlled Loading and Targeted Delivery of Mixed Anticancer Drugs. *Small* **2010**, *6*, 537–544.

- (24) Jiang, T.; Mo, R.; Bellotti, A.; Zhou, J.; Gu, Z. Gel–Liposome-Mediated Co-Delivery of Anticancer Membrane-Associated Proteins and Small-Molecule Drugs for Enhanced Therapeutic Efficacy. *Adv. Funct. Mater.* **2014**, *24*, 2295–2304.
- (25) Chin, C. F.; Yap, S. Q.; Li, J.; Pastorin, G.; Ang, W. H. Ratiometric Delivery of Cisplatin and Doxorubicin Using Tumour-Targeting Carbon-Nanotubes Entrapping Platinum(IV) Prodrugs. *Chem. Sci.* **2014**, *5*, 2265-2270.
- (26) Marrache, S.; Dhar, S. Engineering of Blended Nanoparticle Platform for Delivery of Mitochondria-Acting Therapeutics. *Proc. Natl. Acad. Sci. USA.* **2012**, *109*, 16288-16293.
- (27) Marrache, S.; Dhar, S. The Energy Blocker Inside the Power House: Mitochondria Targeted Delivery of 3-Bromopyruvate. *Chem. Sci.*, **2014**, *6*, 1832-1845.
- (28) Singh, K. K.; Kulawiec, M.; Still, I.; Desouki, M. M.; Geradts, J.; Matsui, S. Inter-Genomic Cross Talk Between Mitochondria and the Nucleus Plays an Important Role in Tumorigenesis. *Gene* **2005**, *354*, 140-146.
- (29) Rowland, A. A.; Voeltz, G. K. Endoplasmic Reticulum–Mitochondria Contacts: Function of the Junction. *Nat. Rev. Mol. Cell Biol.* **2012**, *13*, 607-615.
- (30) Bernhard, W.; Granboulan, N. The Fine Structure of the Cancer Cell Nucleus. *Exp. Cell Res.* **1963**, *24*, 19-53.
- (31) Neuzil, J.; Webe, T.; Shroder, A.; Lu, M.; Ostermann, G.; Gellert, N.; Mayne, G. C.; Olejnicka, B.; Negre-Salvayre, A.; Sticha, M.; Coffe, R. J.; Weber, C. Induction of Cancer Cell Apoptosis by Alpha-Tocopheryl Succinate: Molecular Pathways and Structural Requirements. *FASEB J.* **2001**, *15*, 403-415.
- (32) Prasad, K. N.; Edwards-Prasad, J. Activation of Extracellular Signal-Regulated Kinase and c-Jun-NH(2)-Terminal Kinase but not p38 Mitogen-Activated Protein Kinases is Required for RRR-Alpha-Tocopheryl Succinate-Induced Apoptosis of Human Breast Cancer Cells. *Cancer Res.* **2001**, *61*, 6569-6576.
- (33) Zhang, Y.; Ni, J.; Messing, E. M.; Chang, E.; Yang, C. R.; Yeh, S. Vitamin E Succinate Inhibits the Function of Androgen Receptor and the Expression of Prostate-Specific Antigen in Prostate Cancer Cells. *Proc. Natl. Acad. Sci. USA.* **2002**, *99*, 7408-7413.
- (34) Prochazka, L.; Dong, L.; Valis, K.; Freeman, R.; Ralph, S. J.; Turanek, J.; Neuzil, J. Alpha-Tocopheryl Succinate Causes Mitochondrial Permeabilization by Preferential Formation of Bak Channels. *Apoptosis* **2010**, *15*, 782-794.

- (35) Dong, L. F.; Low, P.; Dyason, J. C.; Wang, X. F.; Prochazka, L.; Witting, P. K.; Freeman, R.; Swettenham, E.; Valis, K.; Liu, J.; Zobalova, R.; Turanek, J.; Spitz, D. R.; Domann, F. E.; Scheffler, I. E.; Ralph, S. J.; Neuzil, J. Alpha-Tocopheryl Succinate Induces Apoptosis by Targeting Ubiquinone-Binding Sites in Mitochondrial Respiratory Complex II. *Oncogene* **2008**, *27*, 4324-4335.
- (36) Dong, L.; Freeman, R.; Liu, J.; Zobalova, R.; Marin-Hernandez, A.; Stantic, M.; Rohlena, J.; Valis, K.; Rodriguez-Enriquez, S.; Butcher, B.; Goodwin, J.; Brunk, U. T.; Witting, P. K.; Moreno-Sanchez, R.; Scheffler, I. E.; Ralph, S. J.; Neuzil, J. Suppression of Tumor Growth In Vivo by the Mitocan Alpha-Tocopheryl Succinate Requires Respiratory Complex II. *Clin. Cancer Res.* **2009**, *15*, 1593-1600.
- (37) Kruspig, B.; Zhivotovsky, B.; Gogvadze, V. Contrasting Effects of α -Tocopheryl Succinate on Cisplatin- and Etoposide-Induced Apoptosis. *Mitochondrion* **2013**, *13*, 533-538.
- (38) Zhang, X.; Peng, X.; Yu, W.; Hou, S.; Zhao, Y.; Zhang, Z.; Huang, X.; Wua, K. Alpha-Tocopheryl Succinate Enhances Doxorubicin-Induced Apoptosis in Human Gastric Cancer Cells Via Promotion of Doxorubicin Influx and Suppression of Doxorubicin Efflux. *Cancer Lett.* **2011**, *307*, 174-181.
- (39) Kanai, K.; Kikuchi, E.; Mikami, S.; Suzuki, E.; Uchida, Y.; Kodaira, K.; Miyajima, A.; Ohigashi, T.; Nakashima, J.; Oya, M. Vitamin E Succinate Induced Apoptosis and Enhanced Chemosensitivity to Paclitaxel in Human Bladder Cancer Cells In Vitro and In Vivo. *Cancer Sci.* **2010**, *101*, 216-223.
- (40) Neuzil, J.; Weber, T.; Gellert, N.; Weber, C. Selective Cancer Cell Killing by Alpha-Tocopheryl Succinate. *Br. J. Cancer.* **2001**, *84*, 87-89.
- (41) Crispen, P. L.; Uzzo, R. G.; Golovine, K.; Makhov, P.; Pollack, A.; Horwitz, E. M.; Greenberg, R. E.; Kolenko, V. M. Vitamin E Succinate Inhibits NF-KappaB and Prevents the Development of a Metastatic Phenotype in Prostate Cancer Cells: Implications for Chemoprevention. *Prostate* **2007**, *67*, 582-590.
- (42) Yao, X.; Panichpisal, K.; Kurtzman, N.; Nugent, K. Cisplatin Nephrotoxicity: a Review. *Am. J. Med. Sci.* **2007**, *334*, 115-124.
- (43) Octavia, Y.; Tocchetti, C. G.; Gabrielson, K. L.; Janssens, S.; Crijns, H. J.; Moens, A. L. Doxorubicin-Induced Cardiomyopathy: from Molecular Mechanisms to Therapeutic Strategies. *J. Mol. Cell. Cardiol.* **2012**, *52*, 1213-25.

- (44) Rowinsky, E. K.; Chaudhry, V.; Cornblath, D. R.; Donehower, R. C. Neurotoxicity of Taxol. *J. Natl. Cancer Inst. Monogr.* **1993**, *15*, 107-115.
- (45) Aronov, O.; Horowitz, A. T.; Gabizon, A.; Gibson, D. Folate-Targeted PEG as a Potential Carrier for Carboplatin Analogs. Synthesis and In Vitro Studies. *Bioconjugate Chem.* **2003**, *14*, 563-574.
- (46) Brown, S. D.; Nativo, P.; Smith, J-A.; Stirling, D.; Edwards, P. R.; Venugopal, B.; Flint, D. J.; Plumb, J. A.; Graham, D.; Wheate, N. J. Gold Nanoparticles for the Improved Anticancer Drug Delivery of the Active Component of Oxaliplatin. *J. Am. Chem. Soc.* **2010**, *132*, 4678-4684.
- (47) Still, B. M.; Kumar, P. G.; Aldrich-Wright, J. R.; Price, W. S. 195Pt NMR-Theory and Application. *Chem. Soc. Rev.* **2007**, *36*, 665-686.
- (48) Sengupta, P.; Basu, S.; Soni, S.; Pandey, A.; Roy, B.; Oh, M. S.; Chin, K. T.; Paraskar, A. S.; Sarangi, S.; Connor, Y.; Sabbisetti, V. S.; Koppam, J.; Kulkarni, A.; Muto, K.; Amarasiriwardena, C.; Jayawardene, I.; Lupoli, N.; Dinulescu, D.; Bonventre, J. V.; Mashelkar, R. A.; Sengupta, S. Cholesterol-Tethered Platinum II-Based Supramolecular Nanoparticle Increases Antitumor Efficacy and Reduces Nephrotoxicity. *Proc. Natl. Acad. Sci. USA.* **2012**, *109*, 11294-11299.
- (49) Li, K.; Liu, B. Polymer-Encapsulated Organic Nanoparticles for Fluorescence and Photoacoustic Imaging. *Chem. Soc. Rev.* **2014**, *43*, 6570-6597.
- (50) Harris, J. M.; Chess, R. B. Effect of Pegylation on Pharmaceuticals. *Nat. Rev. Drug Discov.* **2003**, *2*, 214-221.
- (51) Gilleron, J.; Querbes, W.; Zeigerer, A.; Borodovsky, A.; Marsico, G.; Schubert, U.; Manygoats, K.; Seifert, S.; Andree, C.; Stöter, M.; Epstein-Barash, H.; Zhang, L.; Kotliansky, V.; Fitzgerald, K.; Fava, E.; Bickle, M.; Kalaidzidis, Y.; Akinc, A.; Maier, M.; Zerial, M. Image-Based Analysis of Lipid Nanoparticle-Mediated siRNA Delivery, Intracellular Trafficking and Endosomal Escape. *Nat. Biotech.* **2013**, *31*, 638-646.
- (52) Prochazka, L.; Koudelka, S.; Dong, L. -F.; Stursa, J.; Goodwin, J.; Neca, J.; Slavik, J.; Ciganek, M.; Masek, J.; Kluckova, K.; Nguyen, M.; Turanek, J.; Neuzil, J. Mitochondrial Targeting Overcomes ABCA1-Dependent Resistance of Lung Carcinoma to α -Tocopheryl Succinate. *Apoptosis* **2013**, *18*, 286-299.

- (53) Chou, T. –C. Drug Combination Studies and Their Synergy Quantification Using the Chou-Talalay Method. *Cancer Res.* **2010**, *70*, 440-446.
- (54) Mariño, G.; Niso-Santano, M.; Baehrecke, E. H.; Kroemer, G. Self-Consumption: the Interplay of Autophagy and Apoptosis. *Nat. Rev. Mol. Cell Biol.* **2014**, *15*, 81-94.
- (55) Kruidering, M.; Evan, G. I. Caspase-8 in Apoptosis: the Beginning of "the End"? *IUBMB Life* **2000**, *50*, 85–90.
- (56) Li, P.; Nijhawan, D.; Budihardjo, I.; Srinivasula, S. M.; Ahmad, M.; Alnemri, E. S.; Wang, X. Cytochrome c and dATP-Dependent Formation of Apaf-1/Caspase-9 Complex Initiates an Apoptotic Protease Cascade. *Cell* **1997**, *91*, 479–489.
- (57) Chapman-Smith, A.; Cronan Jr., J. E. In Vivo Enzymatic Protein Biotinylation. *Biomol. Eng.* **1999**, *16*, 119-125.
- (58) Dagda, R. K.; Cherra III, S. J.; Kulich, S. M.; Tandon, A.; Park, D.; Chu, C. T. Loss of PINK1 Function Promotes Mitophagy Through Effects on Oxidative Stress and Mitochondrial Fission. *J. Biol Chem.* **2009**, *284*, 13843-13855.
- (59) Tait, S. W. G.; Green, D. R. Mitochondria and Cell Death: Outer Membrane Permeabilization and Beyond. *Nat. Rev. Mol. Cell Biol.* **2010**, *11*, 621-632.
- (60) Kuo, L. J.; Yang, L. –X. γ -H2AX-A Novel Biomarker for DNA Double-Strand Breaks. *In Vivo* **2008**, *22*, 305-310.
- (61) Pang, B.; Qiao, X.; Janssen, L.; Velds, A.; Groothuis, T.; Kerkhoven, R.; Nieuwland, M.; Ovaa, H.; Rottenberg, S.; van Tellingen, O.; Janssen, J.; Huijgens, P.; Zwart, W.; Neefjes, J. Drug-Induced Histone Eviction from Open Chromatin Contributes to the Chemotherapeutic Effects of Doxorubicin. *Nat. Commun.* **2013**, *4*, 1908-1920.
- (62) Curtin, N. J. DNA Repair Dysregulation from Cancer Driver to Therapeutic Target. *Nat. Rev. Cancer* **2012**, *12*, 801-817.
- (63) Theodoropoulos, P. A.; Polioudaki, H.; Kostaki, O.; Derdas, S. P.; Georgoulas, V.; Dargemont, C.; Georgatos, S. D. Taxol Affects Nuclear Lamina and Pore Complex Organization and Inhibits Import of Karyophilic Proteins into the Cell Nucleus. *Cancer Res.* **1999**, *59*, 4625-4633.